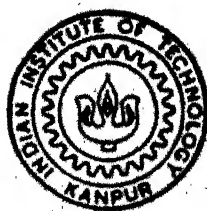


# CONTROL OF METAL - LIGAND ORBITAL INTERACTIONS AND DINUCLEAR OXO-BRIDGED CORE FORMATION WITH TRIDENTATE NITROGENOUS LIGANDS

*by*

**SAMIRAN MAHAPATRA**



DEPARTMENT OF CHEMISTRY

**INDIAN INSTITUTE OF TECHNOLOGY KANPUR**

SEPTEMBER, 1992

CHM

1992

D

MAH

CON

# **CONTROL OF METAL - LIGAND ORBITAL INTERACTIONS AND DINUCLEAR OXO-BRIDGED CORE FORMATION WITH TRIDENTATE NITROGENOUS LIGANDS**

*A Thesis Submitted  
in Partial Fulfilment of the Requirements  
for the Degree of*

**DOCTOR OF PHILOSOPHY**

*by*

**SAMIRAN MAHAPATRA**

*to the*

**DEPARTMENT OF CHEMISTRY**

**INDIAN INSTITUTE OF TECHNOLOGY KANPUR**

**SEPTEMBER, 1992**

✓ CHM-1992-D-MAH-CON

2 4 JUN 1994 /chem

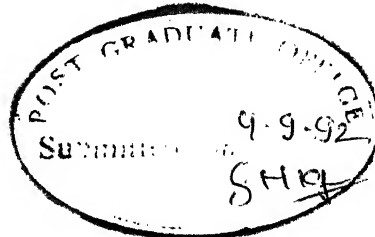
CENTRAL LIBRARY  
I I T KANPUR

**Acc. No. A. 11795E**

TH  
541.2242  
M277C

*Dedicated to  
my parents  
as a token of  
Love and Respect*





## STATEMENT

I hereby declare that the matter embodied in this thesis is the result of investigations carried out by me in the Department of Chemistry, Indian Institute of Technology, Kanpur, India under the supervision of Dr. R. N. Mukherjee.

In keeping with the general practice of reporting scientific observations, due acknowledgements have been made wherever the work described is based on the findings of other investigators.

*Samiran Mahapatra*

Samiran Mahapatra

I.I.T. Kanpur

September, 1992

DEPARTMENT OF CHEMISTRY  
INDIAN INSTITUTE OF TECHNOLOGY, KANPUR  
INDIA


CERTIFICATE - I

This is to certify that Mr. Samiran Mahapatra (Roll Number 8910768) has satisfactorily completed all the courses required for the Ph.D. degree program and obtained C.P.I. of 10.00.


These courses include:

CHM 605 Principles of Organic Chemistry  
CHM 645 Principles of Inorganic Chemistry  
CHM 625 Principles of Physical Chemistry  
CHM 624 Modern Physical Methods in Chemistry  
CHM 646 Bio Inorganic Chemistry  
CHM 668 Advanced Inorganic Chemistry II  
CHM 800 General Seminar  
CHM 801 Special Seminar  
CHM 900 Post Graduate Research

Mr. Samiran Mahapatra successfully completed his Ph.D. qualifying examination in September 1991.

  
(S. S. Katiyar)  
Head

Department of Chemistry  
I.I.T. Kanpur


  
(Y. D. Vankar)

Convenor  
Departmental Post Graduate  
Committee  
Department of Chemistry  
I.I.T. Kanpur

v

## CERTIFICATE -II

It is certified that the work contained in the thesis entitled "Control of Metal-Ligand Orbital Interactions and Dinuclear Oxo-Bridged Core Formation with Tridentate Nitrogenous Ligands" by Mr. S. Mahapatra, has been carried out under my supervision and that this work has not been submitted elsewhere for a degree.

  
Signature of Supervisor  
(Dr. R. N. Mukherjee)  
Chemistry  
I.I.T. Kanpur

September, 1992

## ACKNOWLEDGEMENTS

It is a great privilege for me to record my profound gratitude to Dr. R. N. Mukherjee who inspired and encouraged me through his scholarly guidance, constructive suggestions, critical comments, and detailed instructions at every stage of my research program. I am really indebted to him for his untiring efforts in providing me a good spadework in my research career. His dynamism, thoroughness and relentless adherence to the strictures of scientific rationale have really been exemplary.

I am highly indebted to Dr. P. K. Bharadwaj, Prof. S. Sarkar, Prof. N. Sathyamurthy, Dr. J. Iqbal, Dr. S. Manogaran and other faculty members in this department for their valuable suggestions and encouragement from time to time.

I owe a lot to my labmates for various help and the nice homogeneous association I had with them. My special thank goes to Dr. Nishi Gupta who introduced me to the ways and language of laboratory discipline and helped me in various other ways in the completion of my work. I thank my colleague, friend Manabendra Ray for lively discussions I had with him in arriving at meaningful interpretation of the experimental results. I am grateful to him for his various help regarding computational work. I would like to express my thanks to other labmates, Dr. K. Ramesh and Dr. Z. Shirin for useful discussions and various helps in the lab, Mr. Tapan K. Lal for his help in the steric effect/electronic effect project, and Mr. Anil K. Barik who never allowed us a dull moment in the lab. I also thank Anupam Talapatra, Subhasish Mukerjee, Debnath Bhuniya, and Pampa Das for various help during the course of their stay in this laboratory.

Prof. S. Mitra (TIFR, Bombay) for variable temperature magnetic susceptibility measurements. I am also thankful to Dr. A. K. Nigam (TIFR, Bombay) and Prof. D. C. Khan (IIT, Kanpur) for Mössbauer measurements and Dr. Raja Roy (CDRI, Lucknow) for 400 MHz  $^1\text{H}$  NMR measurements. I would also like to thank Prof. Ray J. Butcher (Howard University, Washington, D.C.) for X-ray structure.

I extend my sincere thanks to Mr. Nayab Ahmed, Mr. D. K. Kannauzia and Mr. N. Jayaraman for helping me in recording NMR, EPR, and IR spectra respectively. I thank Mr. Bhaskar Chaudhury for his help regarding nonlinear least-squares fitting program.

I thank Mr. L. P. Tripathi, Mr. B. N. Shukla, Mr. Katiyar and Mr. K. K. Bajpai of this department for all the help I got from them. I also thank Mr. V. K. Gupta for tracing of figures.

It is my privilege to thank my friends Dinu, Shanti, Sujoy and Tapan who enlivened many hours which would have been unbearably dull. I also thank Subrata, Ravikanth, Damodar, Tamilarasu, Bhisma, Shaji, Naren, Samar, Indrani, Beena and Bedamati of this department who made my stay at IIT Kanpur a memorable one.

I also like to take this opportunity to thank Mrs. Mukherjee for making my stay here homely and lively.

I find myself at a loss for words in expressing my heartfelt gratitude to my adored parents, sisters, and other family members for providing tremendous moral support and encouragement for completion of my work.

Finally, I thank Council of Scientific and Industrial Research, New Delhi, India for financial assistance.

## SYNOPSIS

The thesis entitled "Control of Metal-Ligand Orbital Interactions and Dinuclear Oxo-Bridged Core Formation with Tridentate Nitrogenous ligands", has been divided into seven chapters.

Chapter 1 (Introduction) presents an overview of the known chelate chemistry of tridentate nitrogenous ligands. Also included is a very brief outline of the biological implications of the oxo-bridged diiron and dimanganese units. This chapter also describes the scope of the present work which stems from the following facts: (i) there were no reports on systematic studies of identification of steric effect over electronic in a closely related group of complexes; (ii) number of high-spin iron(II) and cobalt(II) complexes with  $M^{II}N_6$  coordination sphere are limited; moreover  $M^{III}/M^{II}$  redox potential data for these two couples with non-porphyrin nitrogenous ligands are rather restricted, (iii)  $(\mu\text{-oxo})\text{bis}(\mu\text{-carboxylato})\text{diiron(III)}$  unit is now known to be present at the active sites of an emerging group of non-heme iron containing proteins and enzymes. In recent years a quite extensive research is on to synthesize low-molecular-weight structural and/or electronic structural analogues for better understanding of the structure-function relationships in these proteins, (iv) a comprehensive electrochemical study on  $(\mu\text{-oxo})\text{bis}(\mu\text{-carboxylato})\text{diruthenium(III)}$  was not done although several compounds were reported having similar core structure, (v)  $\text{bis}(\mu\text{-oxo})\text{dimanganese(IV,III)}$  core is believed to be present

in the water-oxidizing enzyme in photosystem II; model studies of this core structure are of considerable current interest. Each of these problems has been dealt with in subsequent chapters.

Chapter 2 describes the effect of methyl substituents adjacent to donor atoms on the complexing properties of a novel family of three tridentate ( $N_3$ ) pyridylpyrazole ligands. In the course of this investigation a series of grossly octahedral manganese(II) ( $S = 5/2$ ), iron(II) ( $S = 2$ ), cobalt(II) ( $S = 3/2$ ), nickel(II) ( $S = 1$ ), and ruthenium(II) ( $S = 0$ ) complexes embracing the  $M^{II}N_6$  coordination sphere has been synthesized. The metal coordination environments in iron(II), cobalt(II), nickel(II), and ruthenium(II) complexes have been revealed by  $^1H$  NMR spectroscopy. From an analysis of their ligand field spectral behavior an estimate of  $Dq$  values has been made for these three ligands toward iron(II), cobalt(II), and nickel(II). It has been observed that increased steric crowding progressively decreases the value of  $Dq$  for these tridentate ligands in their grossly octahedral complexes. This underscores the fact that within these three ligands more the methyl substituents near the donor site weaker the strength of their ligand fields. Cyclic voltammetric experiments in MeCN solution neatly demonstrate that for first-row transition metals (Mn, Fe, and Co), the potentials for  $M^{III}/M^{II}$  redox couple increase with increasing methyl substituents near donor site. This is a clear demonstration of the predominance of steric over electronic effect; but the trend is opposite in the case of second-row transition metal like ruthenium. Due to its larger size it overrides the steric effect.

Chapter 3 describes the solid state structure of a representative iron(II) bis-chelate determined by three-dimensional X-ray diffraction, which shows a severely distorted octahedral coordination with the longest Fe-N (pyridine) bond distance among all known high-spin  $\text{Fe}^{\text{II}}\text{N}_6$  systems. This highly distorted solid state structure is retained in solution as revealed by its  $^1\text{H}$  NMR study.

Chapter 4 deals with a new iron(II) spin-equilibrium system with singlet ( $^1\text{A}_1$ )  $\rightleftharpoons$  quintet ( $^5\text{T}_2$ ) transition utilizing the unsubstituted tridentate ligand used in Chapter 2. This interesting behavior has been characterized by variable-temperature magnetic susceptibility and Mössbauer spectral measurements.

Chapter 5 describes the synthesis, characterization, and reactivity of a group of novel  $(\mu\text{-oxo})\text{bis}(\mu\text{-carboxylato})\text{diiron(III)}$  and  $(\mu\text{-oxo})\text{bis}(\mu\text{-diphenylphosphato})\text{diiron(III)}$  complexes with tridentate  $\text{N}_3$ -capping ligands, 2-pyridylethyl-(2-pyridylmethyl)amine(HL) and its N-methylated derivative(MeL). These complexes exhibit infrared, absorption, and Mössbauer spectral features characteristic of triply-bridged diiron(III) complexes as well as non-heme oxo-bridged proteins with similar core. These complexes are antiferromagnetically coupled which has been confirmed by variable-temperature magnetic susceptibility measurements. The lability of bridging acetate groups has been demonstrated by exchange with diphenylphosphate and deuterioacetate as revealed by absorption and  $^1\text{H}$  NMR studies respectively.

Chapter 6 describes the synthesis, characterization, and a novel reactivity property of a triply bridged diruthenium(III) complex having  $[\text{Ru}^{\text{III}}_2(\mu\text{-O})(\mu\text{-OAc})_2]^{2+}$  core with MeL as capping



ligand. The purplish-blue diamagnetic complex exhibits in MeCN solution two oxidative responses due to  $\text{Ru}^{\text{IV}}\text{Ru}^{\text{III}}/\text{Ru}^{\text{III}}_2$  and  $\text{Ru}^{\text{IV}}_2/\text{Ru}^{\text{IV}}\text{Ru}^{\text{III}}$  couples respectively, and two reductive responses due to  $\text{Ru}^{\text{III}}_2/\text{Ru}^{\text{III}}\text{Ru}^{\text{II}}$  and  $\text{Ru}^{\text{III}}\text{Ru}^{\text{II}}/\text{Ru}^{\text{II}}_2$  couples respectively. The red one-electron oxidized species, generated chemically and/or electrochemically is very sensitive toward moisture giving back the blue diruthenium(III) complex. The intense purplish-blue and red colors are due to the charge-transfer transitions involving  $\{\text{Ru}_2(\mu\text{-O})\}^{4+}$  and  $\{\text{Ru}_2(\mu\text{-O})\}^{5+}$  ions respectively.

Chapter 7 describes a novel triply bridged mixed-valance dinuclear manganese complex containing the  $[\text{Mn}_2(\mu\text{-O})_2(\mu\text{-OAc})]^{2+}$  core with MeL as capping ligand. The complex is strongly anti-ferromagnetically coupled which has been revealed from variable temperature magnetic susceptibility experiments. The frozen solution ESR spectrum of the complex at 77 K exhibits sixteen  $^{55}\text{Mn}$  hyperfine pattern centered near  $g \approx 2.0$ . A well-resolved quasireversible oxidative response due to  $\text{Mn}^{\text{IV}}_2/\text{Mn}^{\text{IV}}\text{Mn}^{\text{III}}$  couple and an irreversible reductive response due to  $\text{Mn}^{\text{IV}}\text{Mn}^{\text{III}}/\text{Mn}^{\text{III}}_2$  couple were observed in MeCN solution. The one-electron oxidized species generated chemically and/or electrochemically is stable in MeCN solution. Unlike dimanganese(IV,III) complex, the oxidized product did not give ESR spectrum at 77 K.

# CONTENTS

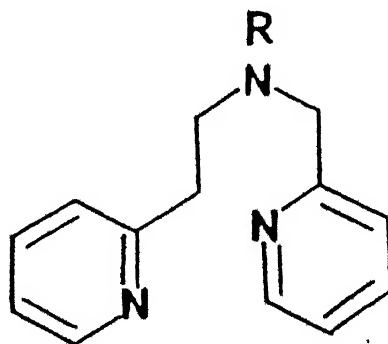
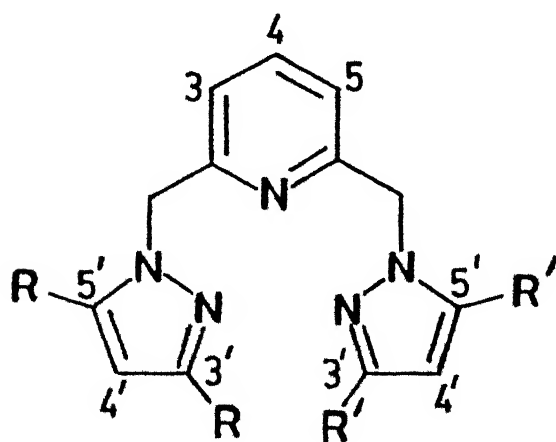
STATEMENT		iii
CERTIFICATE - I		iv
CERTIFICATE - II		v
ACKNOWLEDGEMENTS		vi
SYNOPSIS		viii
CHAPTER 1	Introduction	1
CHAPTER 2	Consequences of Incremental Steric Crowding at the $M^{II}N_6$ (M = Mn, Fe, Co, Ni, and Ru) Coordination Sphere with Tridentate Pyridyl-pyrazole Ligands. Predominance of Steric over Electronic Effects	23
CHAPTER 3	Solution and Crystal Structure of Sterically Hindered Iron(II) Bis Chelate with Unsymmetrically Methyl Substituted Ligand $H_2Me_2bpp$	106
CHAPTER 4	Magnetic and Mössbauer Spectroscopic Characterization of Singlet $\rightleftharpoons$ Quintet Transition in a Six-Coordinate Iron(II) Complex of a Tridentate Pyridylpyrazole Ligand	122
CHAPTER 5	Triply Bridged Diiron(III) Complexes with $[Fe_2(\mu-O)(\mu-X)_2]^{2+}$ Cores {X = $MeCO_2$ , $PhCO_2$ or $(PhO)_2PO_2$ }	142
CHAPTER 6	Triply Bridged Diruthenium Complexes with $\{Ru_2^{III}(\mu-O)(\mu-O_2CMe)_2\}^{2+}$ and $\{Ru^{IV}Ru^{III}(\mu-O)(\mu-O_2CMe)_2\}^{3+}$ Cores: Synthesis, Spectra, and Electrochemistry	177
CHAPTER 7	New Mixed Valence Binuclear Complex Containing the $\{Mn^{IV}(\mu-O)_2(\mu-OAc)Mn^{III}\}^{2+}$ Core: A Synthetic Model for the Active Site of Photosystem II.	195
REFERENCES		216
APPENDIX		238
UTURE SCOPE OF THIS WORK		244

## CHAPTER 1

### INTRODUCTION

#### 1.1 Purpose of the Present Investigation

The primary concern of this thesis is a neat demonstration of the versatility in the use of five potentially tridentate nitrogenous pyridine-pyrazole rich ligands, I - V, to develop an interesting transition metal chemistry as well as studies related to synthetic analogue approach of bioinorganic chemistry.



R = R' = H : H<sub>4</sub>bpp (I)

R = H, R' = Me : H<sub>2</sub>Me<sub>2</sub>bpp (II)

R = R' = Me : Me<sub>4</sub>bpp (III)

R = H : HL (IV)

R = Me : MeL (V)

## 1.2 Scope of the Work

In what follows we summarize (Table 1.1) the known chelate chemistry utilizing a wide variety of selected tridentate nitrogenous ligands. This background information allows one to appreciate the uniqueness of the ligands chosen in the present work. The design of a new organic molecule capable of acting as a potential ligand to metal ions deserves an attention on its own merit but the ultimate challenge lies in the fruitful use of those organic molecules to develop new interesting chemistry of greater importance to chemists in general and inorganic chemists in particular.

The chemistry which we shall be describing in the subsequent chapters using the ligands I - V could be classified in two categories. We discuss them one after another.

### 1.2.1 Consequences of Steric over Electronic Effect or vice versa

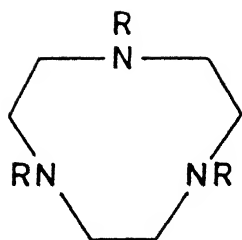
In this section we consider the ligands  $R_4bpp$  (I-III) to explore the possibility of fine tuning of the extent of metal-ligand orbital overlap to observe the effect of steric factor over electronic or the vice versa as a function of metal ions, viz., Mn(II), Fe(II), Co(II), Ni(II), and Ru(II). The results obtained from this investigation are presented in Chapters 2, 3, and 4.

#### 1.2.1.1 Steric/Electronic Effect

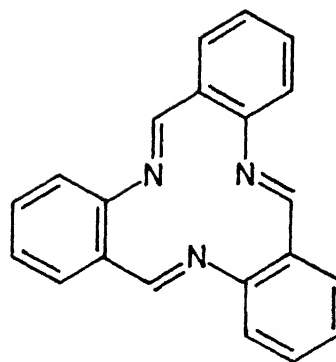
For a given metal ion in a fixed stereochemistry, substituents on the ligand framework can affect the metal-centered redox potentials due to two factors, viz., electronic and steric. Examples of tuning of the redox potentials in a closely related

**Table 1.1: A Selected Listing of Tridentate Nitrogen-Containing Ligands and their Chemistry**

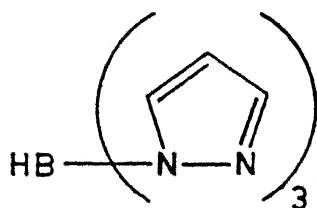
Ligands	Comments	References
1,4,7 triazacyclo- nonane (TACN) and N,N',N''-trimethyl- 1,4,7 triazacyclo- nonane (MTACN)	Ligand syntheses  Extensive chemistry using these ligands	1,2  3
Tribenzo[1,5,9]- triazacyclodode- cine (TRI)	Synthesis, absorption and infra- red spectra, $\mu_{\text{eff}}$ of nickel(II) complexes	4
Hydrotris(1-pyra- zoly1) borate(-) (HBpz <sub>3</sub> ) and its substituted derivatives	Extensive chemistry using these ligands  Syntheses of ligand and bis- chelates of cobalt(II) and iron(II); Electrochemistry  Syntheses of first transition metal complexes: spectroscopy and X-ray structure	5  6,7  8,9
Hydrotris triazoly1 borate(-) (HBTz <sub>3</sub> )	Synthesis of cobalt(II) bis- complex	10
Bis(pyrazoly1ethyl) amine (BPEA)	Extensive copper chemistry	11
Tris(1-pyrazoly1)- methane (TPM)	Ligand synthesis and gold(III) complexes  Syntheses and reactivity studies on ruthenium aqua complexes using this ligand	12  13



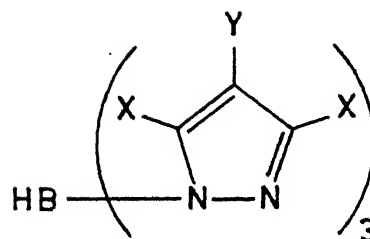
R = H : TACN.  
R = Me : MTACN



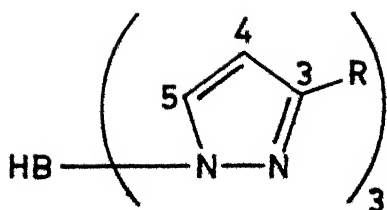
TRI



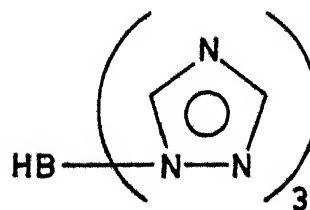
HBpz<sub>3</sub>



X = Y = Me  
X = Me, Y = H  
X = H, Y = Cl  
X = H, Y = i-Pr  
X = H, Y = n-Bu



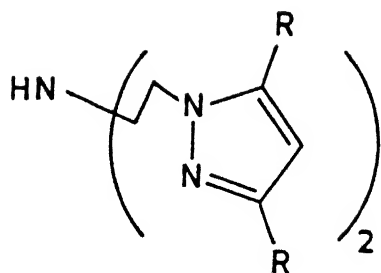
R = t-Bu  
R = Ph



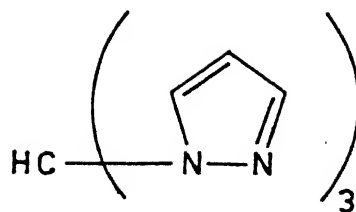
HBtz<sub>3</sub>

Table 1.1 (contd.)

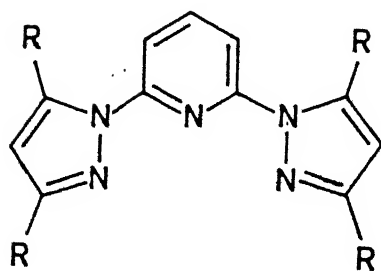
Ligands	Comments	References
Bis(pyrazolyl)-pyridine (BPPY) and its methyl derivatives	Mixed- and bis-chelates of ruthenium(II); spectroelectrochemical correlation	14
6-(N-pyrazolyl)-2,2'-bipyridine (PBPY) and its methyl derivative	Syntheses of ligands and ruthenium(II) bis complexes; $^1\text{H}$ and $^{13}\text{C}$ NMR assignments, absorption spectra and electrochemistry	15
6-(N-pyrazolylmethyl)-2,2'-bipyridine (PMBPY) and its methyl derivative	Syntheses of ruthenium(II) complex; dangling arm, $^1\text{H}$ and $^{13}\text{C}$ NMR spectra, coordination induced effect, absorption spectra, electrochemistry	15
Tris(N-methylimidazol-2-yl)methoxy methane (TIMM)	Synthesis, spectroscopy and X-ray structure of dimeric copper(I) complex	16
Tris(N-methylimidazol-2-yl)methanol (TIM)	Synthesis and X-ray structure of gold(III) complex; dangling arm	17
Bis(N-methylimidazol-2-yl)pyridyl-2-ylmethanol (BIPM)	Gold(III) complex: Fluxional behavior	18
Bis(benzimidazolyl)pyridine (BBP)	Mono and bis chelates of iron(II) and iron(III): spin cross over, absorption spectra, magnetism and electrochemistry	19
	Copper(II) mono and bis chelates: Infrared, Absorption, ESR spectra and X-ray	20,21



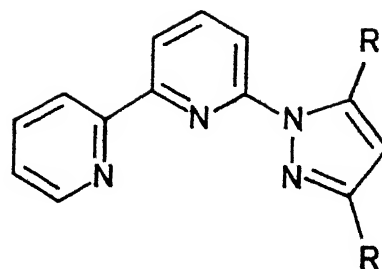
R = H : BPEA  
R = Me: MBPEA



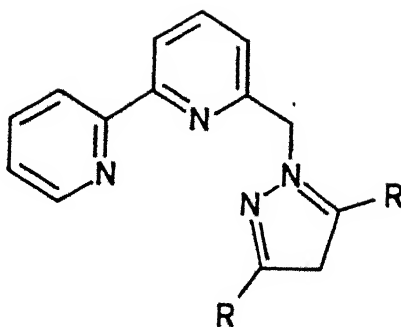
TPM



BPPY  
R = H or Me

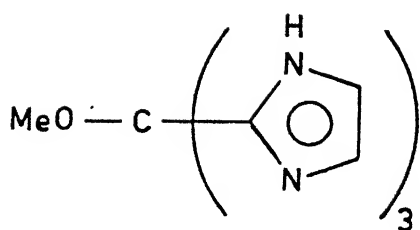


PBPY  
R = H or Me

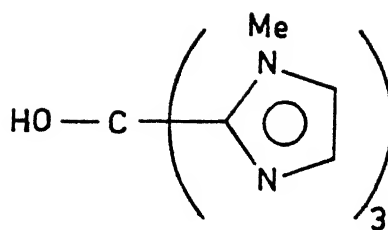


PMBPY  
R = H or Me

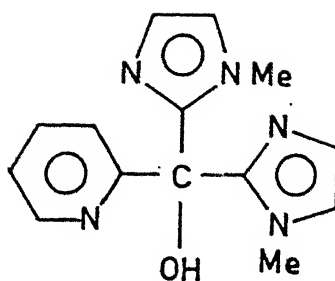




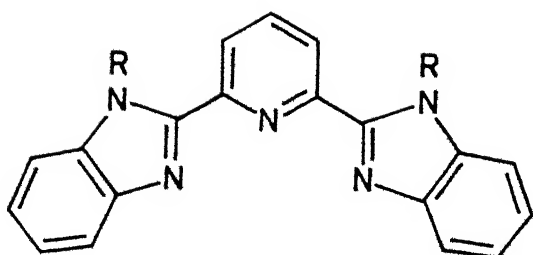
TIMM



TIM

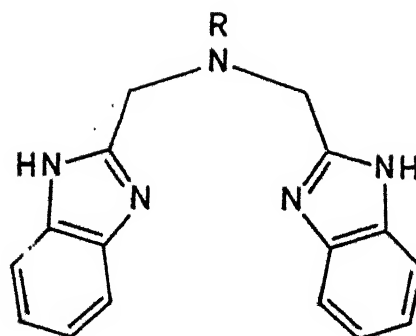


BIPM



BBP

R = H or Me

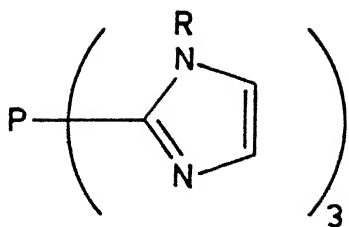


BBA

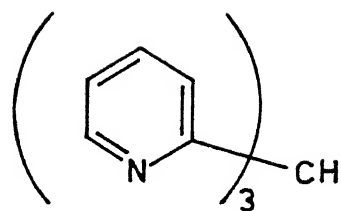
R = H or Me

Table 1.1 (contd.)

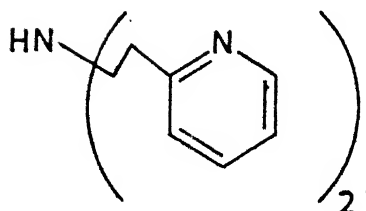
Ligands	Comments	References
Bis(benzimidazolyl-methyl)amine (BBA) and its methyl derivative	( $\mu$ -oxo)bis( $\mu$ -carboxylato) diiron(III) core  Mono chelates of manganese(II) and iron(II)	22  23
Tris(imidazol-2-yl)-phosphine (TIP) and its N-methyl analogue (TMIP)	Ligand synthesis  ( $\mu$ -oxo)bis( $\mu$ -carboxylato) diiron(III) and dimanganese(III) cores	24  26,27
Di-(2-pyridyl-ethyl)amine (DPA)	Copper complexes: Hemocyanin modelling	11
Bis(2-pyridylmethyl)amine (BPA) and its methyl derivative	Low-spin iron(II) and nickel(II) complexes	27
Tris(2-pyridyl)methane (TPME)	Synthesis of ligand and stability constants of zinc(II), copper(II), nickel(II) complexes	12
2,2':6',2''-terpyridine (TPY)	Coordination chemistry of TPY with various metal ions	28
3-phenyl-2,2':6',2''-terpyridine (PhTPY)	Syntheses, spectroscopy and electrochemistry of complexes type $M^{II}LCl_2$ ( $M = Mn, Co, Ni, Cu$ and $Zn$ ) and $M^{II}L_2^{2+}$ ( $M = Mn, Fe, Co, Ni, Cu$ and $Zn$ )	29-31



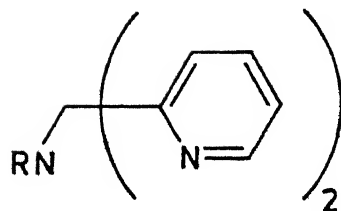
R = H : TIP  
R = Me : TMIP



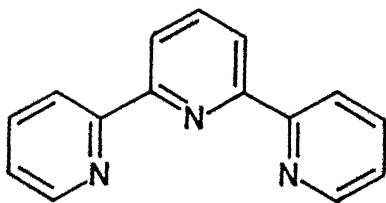
TPME



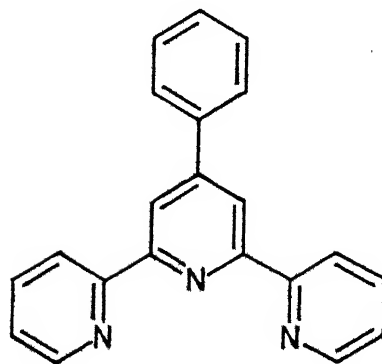
DPA



BPA  
R = H or Me



TPY



PhTPY

group of complexes by remote polar substituents are numerous.<sup>32-37</sup> On the other hand, relatively little is known<sup>38,39</sup> about ligand induced steric factors, especially for metal-centered redox reactions. It can be argued, however, that relatively few attempts have been made to vary ligand structure systematically so that steric effects can be identified. Difficulty in synthesizing these complexes may be the major reason to limit the study.

#### 1.2.1.2 Spin-State Equilibrium

A thermally driven spin-state transition between the high-spin state (HS) and the low-spin state (LS) has received considerable attention over the last twenty five years.<sup>40,41</sup> First-row transition-metal complexes with electronic configurations  $d^4$ - $d^7$  have been found to exhibit such transitions because in these systems two electronic states of differing spin multiplicity become nearly equienergetic and thermal population of the excited state is possible.<sup>42</sup> The experimental realization of an equilibrium of this type is determined by the availability of a complex for which the low-spin and high-spin ground states are separated by only a few hundred reciprocal centimeters.

#### Design of New Spin-Equilibrium Systems<sup>43</sup> -

One of the effective ways to design a new system exhibiting spin-transition is to fine tune the extent of metal-ligand orbital overlap by manipulating steric characteristics of the ligands so that their ligand field strengths lie near the critical value where the high-spin/low-spin transition occurs.

(a) Ligand Design: It is possible to design new spin-

equilibrium systems through carefully planned ligand syntheses. As for example, generally iron(II)-imine complexes are low-spin whereas most of the iron(II) complexes of aliphatic amine ligands are high-spin. Hence, 2-pyridylmethylaniline could be argued to be a good candidate for a ligand giving an intermediate field strength, since it is both an amine and an imine.

Changing the number of chelate rings in the resulting complex offers an alternative possibility for variations in the ligand field strength.

Another strategy of achieving intermediate ligand field strength is to introduce steric bulk near the donor site. Typically a ligand forming low-spin complex is modified by introducing bulky groups. This prevents the donor atoms from coming close to the central metal atom which causes spin pairing, and in turn a situation with longer M-N bonds is favored, facilitating population of antibonding  $e_g$  orbitals.

(b) Anion and Solvent Effects: It seems to be a general trend that polar solvents of crystallization will stabilize the low-spin forms. It has been somewhat more difficult to rationalize the influence of the counter ions on the spin state. There is no correlation between the size and charge of an anion and the spin state of the salts, so the lattice energy does not seem to contribute significantly to the ligand field.

### 1.2.2 Syntheses and Reactivity Studies on Oxo-bridged Dinuclear Complexes

We describe here the use of ligands HL (IV) and MeL (V) as potential facially capping agents to develop a rich chemistry of oxo-bridged dinuclear complexes with additional carboxylato bridge(s) of the types, viz., ( $\mu$ -oxo)bis( $\mu$ -carboxylato)diiron(III), ( $\mu$ -oxo)bis( $\mu$ -carboxylato)diruthenium(III), and bis( $\mu$ -oxo)( $\mu$ -carboxylato)dimanganese(IV,III). We discuss in this section the relevance of these structural types to non-heme metallobiomolecules. Chapters 5-7 deal with the above dinuclear core formation.

#### 1.2.2.1 Oxo-Bridged Diiron Complexes. Relevance to Non-heme Iron Proteins

In recent years, extensive studies have suggested that proteins containing oxo-bridged dinuclear iron centers are widespread in biology. The structure of prototypical hemerythrin, an oxygen transport protein from marine invertebrates<sup>44-48</sup> reveals the presence of two bridging carboxylate ligands in addition to an oxo bridge. Subsequent spectroscopic experiments strongly implicated the presence of a similar unit in ribonucleotide reductase,<sup>49-53</sup> purple acid phosphatase,<sup>54</sup> methane monooxygenase,<sup>55,56</sup> and very recently discovered rubrerythrin.<sup>57,58</sup> It is to be noted that the three-dimensional X-ray structure of ribonucleotide reductase has also been reported recently.<sup>53</sup>

The available structural and spectroscopic data indicate a high degree of congruence in the dinuclear iron sites in these proteins, yet they exhibit an amazing variety of biological functions: O<sub>2</sub> transport, O<sub>2</sub> activation and insertion into an

unactivated C-H bond, phosphate ester hydrolysis, and electron transfer (Table 1.2). In fact, it can be argued that the  $\text{Fe}_2\text{O}$  unit constitutes the most versatile iron center yet encountered in biology. The more familiar heme centers are capable of both electron transfer and  $\text{O}_2$  binding and activation, while iron-sulfur clusters are known to participate in electron transfer, but not directly in  $\text{O}_2$  chemistry. It now appears as if proteins containing  $\text{Fe}_2\text{O}$  unit are capable of all these functions. Dinuclear oxo-bridged iron centers have also been suggested to be important for initiating the formation of the polynuclear iron core in the iron storage protein ferritin.<sup>59</sup> Among these oxo-bridged non-heme iron proteins and enzymes, hemerythrin is the one which has been studied most thoroughly. An overview of its structure-function relationship is presented below. In Chapter 5 we shall be dealing with the synthetic analogue approach of its active sites. Chemistry of a similar core with ruthenium will be discussed in Chapter 6.

#### 1.2.2.1.1 Hemerythrin<sup>44-48</sup>

Hemerythrin (Hr) is an oxygen-binding protein containing two non-heme iron atoms per subunit.<sup>44-46</sup> The most detailed information on the structure and function of hemerythrin has come from X-ray crystallographic studies.<sup>60-67</sup> The dinuclear iron center is located roughly in the center of the four antiparallel  $\alpha$ -helices. In the metazido form, both irons are octahedrally coordinated and bridged by an oxide ion. The protein provides two bridging carboxylate groups from the side chains of an aspartate and a glutamate residue and five imidazole ligands from histi-

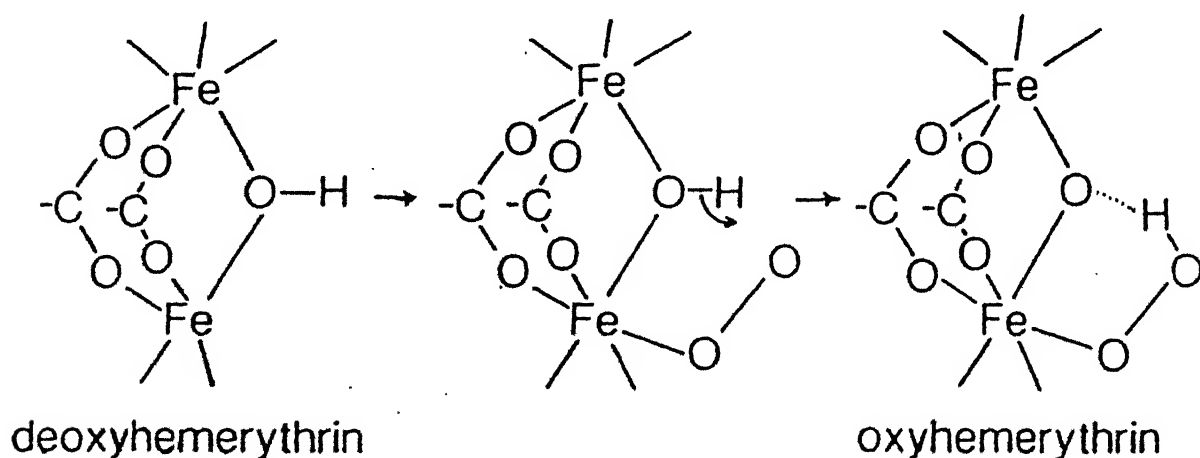
**Table 1.2: Polyyron Oxo Proteins: Occurence and Biological Function**

Proteins	Biological Function	Occurence
Hemerythrin	Oxygen transport	Marine invertebrates
Ribonucleotide Reductase	Reduction of ribo- to deoxy-ribonucleotides	Viruses, bacteriophages, prokaryotes
Purple Acid Phosphatases, Uteroferrin	Phosphate ester hydrolysis	Mammals, plants
Methane Mono-oxygenase	Methane oxidation	Methanotrophic bacteria
Ferritin	Iron storage	Most life forms



dines. One iron is coordinated by three histidines, the other by two and the second iron's coordination is completed by a monodentate azide ligand (Figure 1.1). Two helices provide ligands to one iron, while the other two  $\alpha$ -helices furnish ligands to the second iron.

A mechanism for the conversion of deoxyHr to oxyHr that is consistent with the spectroscopic (Mössbauer, Resonance Raman, MCD, EXAFS, and  $^1\text{H}$  NMR) and magnetic data on the respiratory protein has been proposed.<sup>47</sup> Thus, the reversible dioxygen binding reaction of Hr may be viewed as oxidative addition and



reductive elimination of  $\text{O}_2$  to the diiron center. Since dioxygen binding is pH independent, internal proton transfer from the bridging hydroxide in deoxyHr to the hydroperoxide in oxyHr is postulated.<sup>68</sup>

DeoxyHr can be oxidized chemically in the absence of dioxygen to produce metHr. One electron oxidation of deoxyHr or one electron reduction of metHr produces the semimet levels,

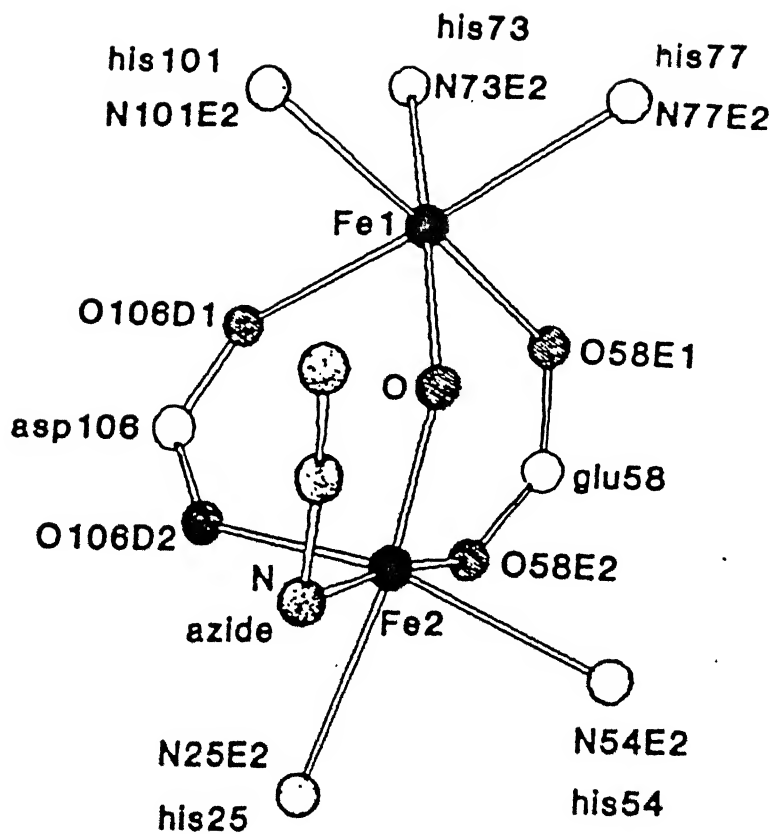


Figure 1.1 Structure of dinuclear Iron center of metazldohemerythrin

intermediate between deoxy and met form. There are however two types of semimet forms : (semimet)<sub>O</sub> and (semimet)<sub>R</sub>, which are found to exhibit distinct spectroscopic properties.<sup>69,70</sup> A scheme showing the interconversion of the various forms of Hr and their probable structures is displayed in Figure 1.2.<sup>71</sup>

#### 1.2.2.2 Bis( $\mu$ -oxo)dimanganese(IV,III) Complexes. Relavance to the Active Site of Photosystem II

There has been an intense research interest in the chemistry of higher oxidation states of manganese because of their great importance in biological systems<sup>72-76</sup> and in catalytic oxidative processes.<sup>77-79</sup> Manganese can adopt a wide variety of oxidation states, this ability is certainly related to the redox function of the metal ion in biological systems as well as in catalytic oxidative processes.

By far the most important role of manganese in nature is its direct involvement in the photocatalytic, four-electron oxidation of water to dioxygen in green plant photosynthesis, an essential process for the maintenance of life. In 1937 Pirson first discovered the requirement of manganese in photosynthesis by showing that plants grown in a Mn-deficient medium lost their water oxidation capacity.<sup>80</sup> During the next four decades, several researchers showed that two photosystems, photosystem I (PSI) and photosystem II (PSII), were involved in photosynthesis and that O<sub>2</sub> evolution and manganese were localized at PSII.

It is believed to catalyze the following reaction:



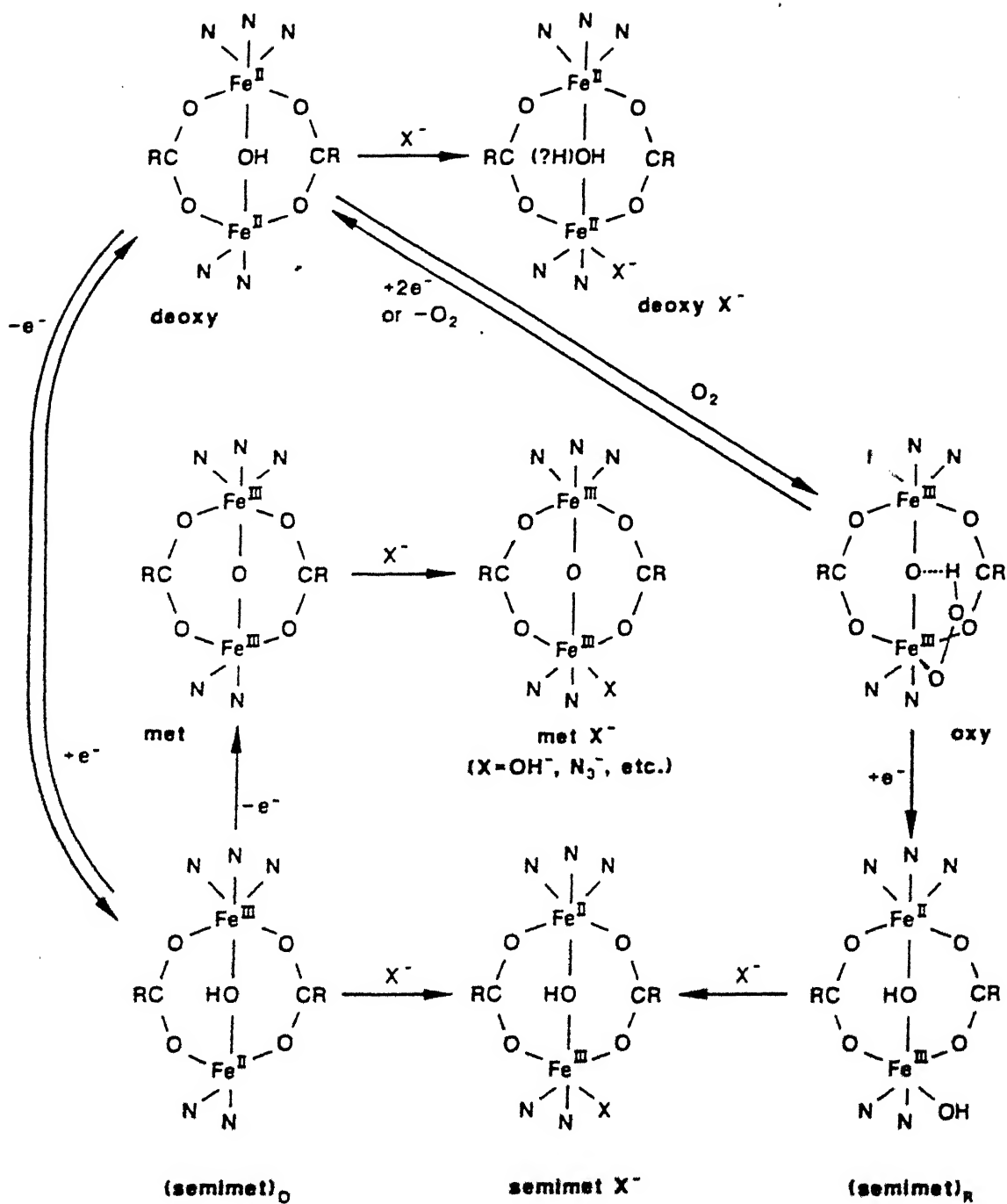
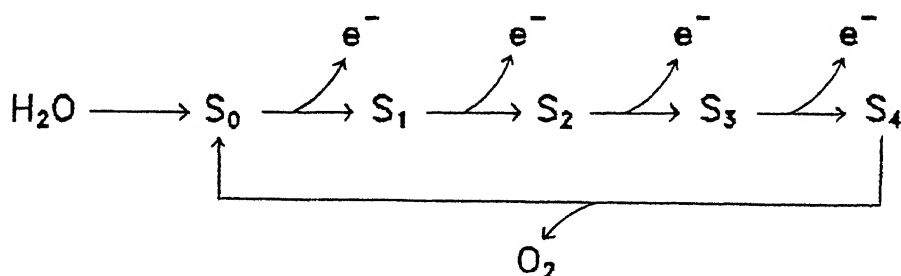


Figure 1.2 Interconversion of the various forms of hemerythrin

In a classical flash study, Kok and coworkers<sup>81</sup> showed that  $O_2$ -evolving complex of PSII is oxidized sequentially in a four-quantum, four one-electron oxidative processes, the steps being named  $S_0$ - $S_4$ , with  $S_0$  representing the totally reduced form.



Manganese in the photosynthetic apparatus is believed to function in three main ways:<sup>82</sup> (i) by acting as a template to hold two molecules of water in close proximity making oxygen-oxygen bond formation as facile as possible, (ii) by stabilizing oxidizing equivalents as described above, mainly because of the availability of different oxidation states in manganese, and (iii) by making the bound water more acidic so that  $H^+$  loss is more facile.

Two mechanisms for photosynthetic water oxidation have been put forward recently. The first, proposed by Brudvig and Crabtree,<sup>74</sup> utilizes a ' $Mn_4O_6$  adamantane'-like complex and a ' $Mn_4O_4$  cubane'-like assembly (Figure 1.3). The cubane is oxidized in one-electron steps starting from  $S_0$  to  $S_4$ . During  $S_2 \rightarrow S_3$  advance, two molecules of water are incorporated into the cubane which rearranges to give  $Mn_4O_6$  adamantane complex. In the next step, O-O bond forms from two of the bridging oxides and  $O_2$  is

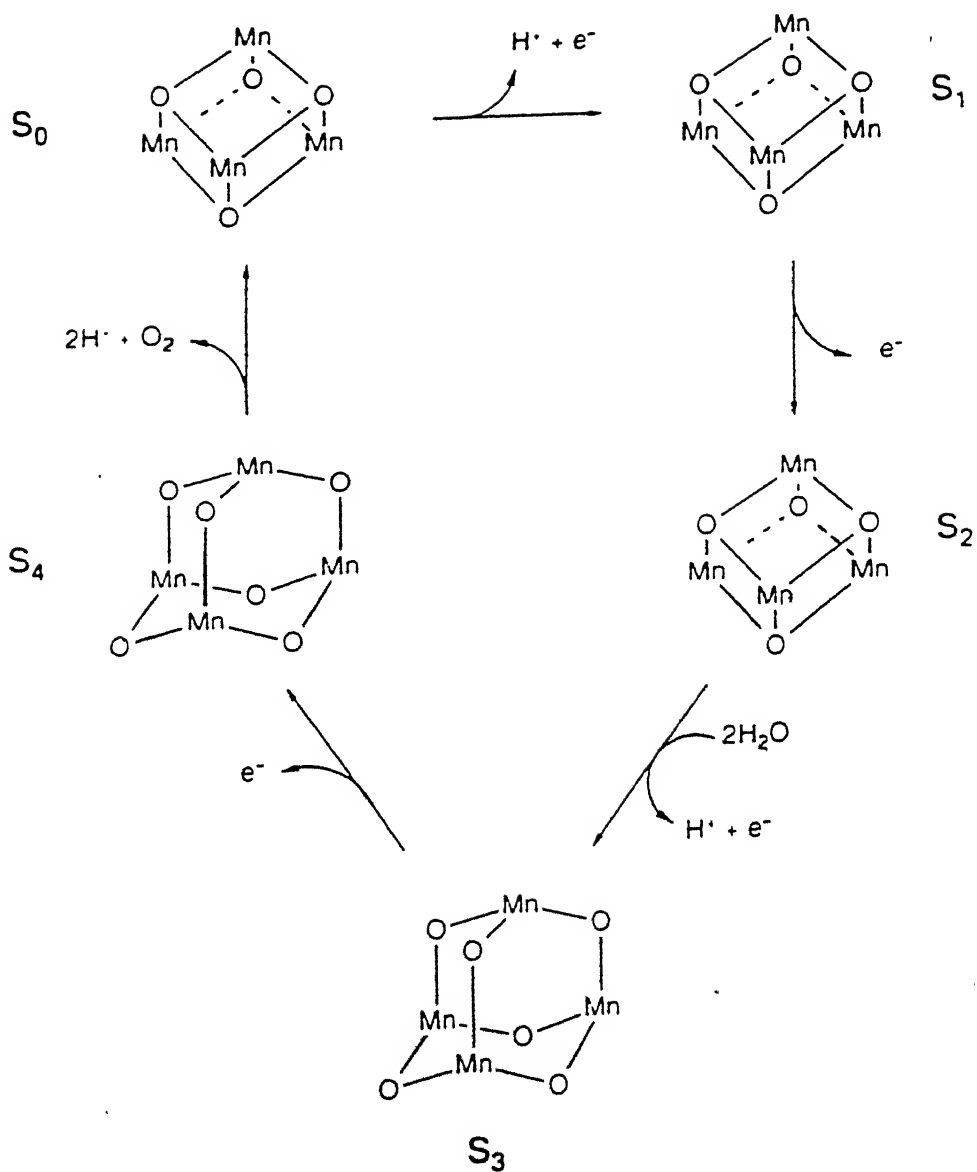


**Figure 1.3** Schematic representation of mechanism of water oxidation proposed by Brudvig and Crabtree

subsequently released. The plausible oxidation state of manganese was given to be:  $S_0$ , 3Mn(III), Mn(IV);  $S_1$ , 2Mn(III), 2Mn(IV);  $S_2$ , 3Mn(IV), Mn(III);  $S_3$ , 4Mn(IV); and  $S_4$ , 3Mn(IV), Mn(V).

The second scheme, the 'double-pivot' mechanism proposed by Vincent and Christou,<sup>75</sup> was reported in 1987. Figure 1.4 illustrates this mechanism for water oxidation. According to this model, during  $S_0 \rightarrow S_1$  and  $S_1 \rightarrow S_2$  transitions, manganese(III) centers of  $Mn_4O_2$  is oxidized through two one-electron processes. Further oxidation from  $S_2 \rightarrow S_3$  results structural changes. Oxygen atoms derived from water move towards each other initiating bond formation, there is a concomitant movement of manganese atoms apart from each other and transfer of electrons to Mn. The authors suggested the following oxidation states at each  $S_n$  levels:  $S_0$ , Mn(II), 3Mn(III);  $S_1$ , 4Mn(III);  $S_2$ , 3Mn(III), Mn(IV); and  $S_3$ , 2Mn(III), 2Mn(IV).

In Chapter 7 we will encounter the synthetic analogue approach of the active sites of photosystem II.

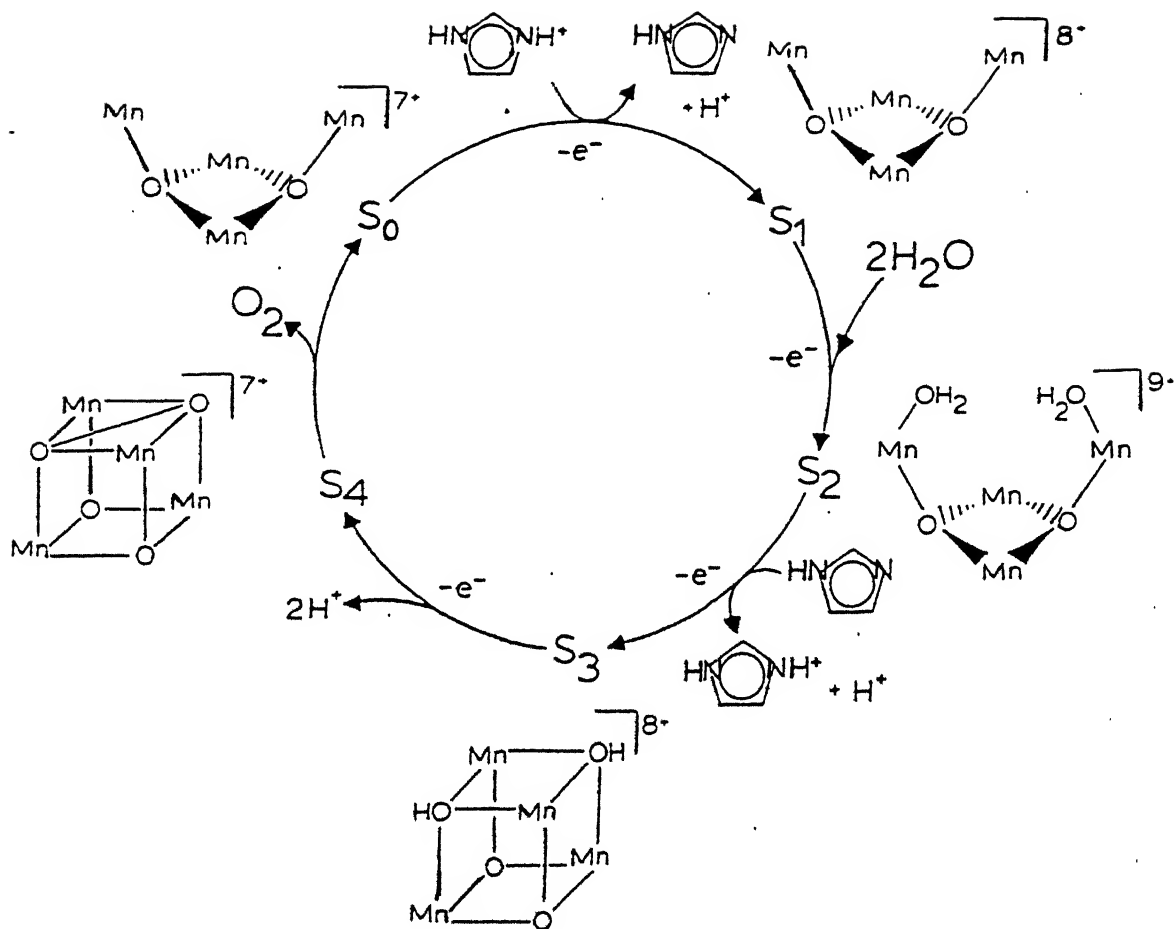


**Figure 1.4 Schematic representation of mechanism of water oxidation proposed by Vincent and Christou**



## CHAPTER 2

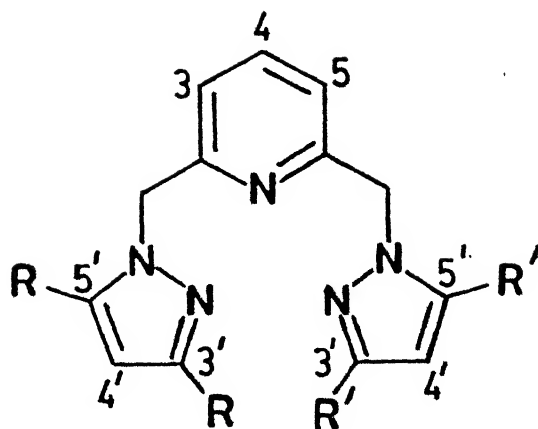
Consequences of Incremental Steric Crowding at the  $M^{II}N_6$  ( $M = Mn, Fe, Co, Ni, \text{ and } Ru$ ) Coordination Sphere with Tridentate Pyridylpyrazole Ligands. Predominance of Steric over Electronic Effects or vice versa\*

\*A part of this work has been published/accepted for publication in

- (i) J. Chem. Soc. Dalton Trans. 1991, 2911.
- (ii) J. Chem. Soc. Dalton Trans. 1992, in press.
- (iii) Polyhedron 1992, 11, in press.
- (iv) Indian J. Chem. 1992, 31A, in press.

In this chapter we investigate the effect of incremental increase in the number of methyl groups near donor site(s) of a given set of ligands  $R_4\text{bpp}$  (I-III) on the metal-ligand orbital interactions in selected bis chelate transition-metal complexes. If one compares the  $pK_a$  values<sup>83</sup> of pyrazole (2.52) and 3,5-dimethylpyrazole (4.12), on electronic grounds one is left with the notion that  $\text{H}_2\text{Me}_2\text{bpp}$  (II) and  $\text{Me}_4\text{bpp}$  (III) would be better as ligands. If the observed effect turns out to be just the opposite one then one is ought to believe that the effect of the methyl substituents are not at all of the usual electron-donating type. In contrast, there could be repulsion of the chelate rings around a given metal ion caused by the interligand steric factors and hence the opposite effect. Obviously, to monitor either of the effects one has to invoke suitable metal ions and also suitable experimental techniques. We decided to use mainly two easily available techniques, namely, absorption spectroscopy (ligand field transition) and electrochemistry (cyclic voltammetry). As an absorption spectroscopic probe we have chosen the metal ions: iron(II), cobalt(II), and nickel(II). For latter experiments we decided to concentrate on those metal ions which have well-defined redox states, such as, Mn(II), Fe(II), Co(II), and Ru(II).

Let us consider the basis for the choice of the ligands  $R_4\text{bpp}$  (I-III) for this purpose. Nitrogen-containing heterocycles in general and imidazole, pyrazole, and pyridine in particular have been used extensively in the construction of ligands<sup>5,14,84-113</sup>. Derivatization of the heterocycles is a



$H_4\text{bpp} : R = R' = H \quad (\text{I})$

$H_2Me_2\text{bpp} : R = H; R' = Me \quad (\text{II})$

$Me_4\text{bpp} : R = R' = Me \quad (\text{III})$

crucial factor in designing and controlling subtle electronic and steric effects on the properties and reactivity of the resulting complexes while keeping the rest of the molecule fixed. Imidazole and pyrazole are good candidates<sup>5,14,107-113</sup> in this regard to be incorporated into chelating ligands. Pyridine is incorporated into chelates using either vinyl pyridine or 2(6)-bis(chloromethyl)pyridine, precursors which however unfortunately offer limited possibilities for derivatizing the heterocycle.

Specifically, the reason for choosing the ligands  $R_4bpp$  (I-III) also includes the following points. First to examine whether or not incremental incorporation of ligand steric crowding still gives rise to bis-chelates as is known<sup>114</sup> for the ligand  $H_4bpp$ (I). Secondly, the number of high-spin iron(II) and cobalt(II) complexes having  $MN_6$  coordination sphere is limited.<sup>115-127</sup> Additionally, Lever has pointed out recently<sup>128</sup> that the high-spin  $Fe^{III}/Fe^{II}$  redox potential data-base with non-porphyrin nitrogenous ligands is rather restricted so giving an impetus to the present study. Thirdly, the striking difference between our ligands I-III and Jameson's ligands (BPPY) is that in the former case there are additional methylene groups intervening the non-ligating pyrazole nitrogens and the pyridine ring. Our objective is to squeeze the pyrazole nitrogen atoms into the metal coordination sphere and pronounce the substituent induced steric effect near donor site.

For brevity, we present below the results of our investigation on  $[M(R_4bpp)_2]^{2+}$  species having  $M^{II}N_6$  coordination unit in the order iron, nickel, cobalt, manganese, and ruthenium.

## 2.1 Experimental Section

### 2.1.1 Solvents and Reagents

Solvents and reagents were obtained from commercial sources and used without further purification unless otherwise stated. Water was deionized and then distilled from alkaline permanganate. Acetonitrile was dried by distillation over  $\text{CaH}_2$ . For electrochemical experiments (see below) further purification was achieved by  $\text{KMnO}_4/\text{Li}_2\text{CO}_3$  treatment<sup>129</sup> followed by distillation over  $\text{P}_4\text{O}_{10}$ . Chloroform was made acid free by washing first with sodium bicarbonate solution then by five to six times with water followed by keeping over anhydrous calcium chloride for 24 h and distilled. N,N'-dimethylformamide (DMF) was kept over alumina (neutral) for a day and then vacuum distilled. Ethanol and methanol were distilled from  $\text{Mg}(\text{OC}_2\text{H}_5)_2$  and  $\text{Mg}(\text{OCH}_3)_2$  respectively. Diethyl ether was dried first with anhydrous  $\text{CaCl}_2$  and then refluxed with and distilled over sodium. Benzene was first stirred with concentrated sulfuric acid until it was free from thiophene. To remove acid it was then shaken twice with water, once with 10%  $\text{Na}_2\text{CO}_3$  solution, again with water, and finally dried over anhydrous  $\text{CaCl}_2$  and stored over sodium. Tetra-n-butylammonium perchlorate (TBAP) was prepared from tetra-n-butylammonium bromide and 70% aqueous perchloric acid. This was recrystallized from ethanol and dried in vacuo. Dinitrogen was purified by bubbling through an alkaline dithionite reducing solution.<sup>130</sup>

### 2.1.2 Measurements

IR spectra were recorded in KBr disks with the help of a Perkin Elmer 1320 or M-580 IR spectrophotometer. Electronic

spectra were measured with a Perkin Elmer Lambda 2 spectrophotometer. The  $^1\text{H}$  NMR spectra were obtained on either a PMX-60 JEOL (60 MHz) instrument or a Brüker WP-80 (80 MHz) NMR spectrometers using  $\text{CDCl}_3$  or  $\text{CD}_3\text{CN}$  solutions. The 400 MHz NMR spectra were measured in  $\text{CD}_3\text{CN}$  on a Brüker WM-400 (400 MHz) NMR spectrometer. This was obtained by the Analytical Facilities, Regional Sophisticated Instrumentation Center, Lucknow, India. Solution magnetic susceptibility measurements were made by the usual NMR method<sup>131</sup> with a PMX-60 Jeol (60 MHz) or Brüker WP-80 spectrometer and made use of the paramagnetic shift of the methyl protons of acetonitrile and the TMS reference as the measured NMR parameter using the Equation 2.1

$$\text{Mass susceptibility } \chi_m = \frac{3 \Delta f}{2\pi f m} + \chi_o + \frac{\chi_o(d_o - d_s)}{m} \quad (2.1)$$

where  $\Delta f$  is the frequency separation between the two TMS or solvent peaks in Hz,  $f$  is the frequency at which the proton resonances are being studied in Hz,  $m$  is the mass of substance contained in 1 mL of solution,  $\chi_o$  is the mass susceptibility of the solvent,  $d_o$  is the density of the solvent and  $d_s$  that of solution. Final term involved in Equation 2.1 is negligible for the highly paramagnetic substances.

The temperature of the NMR probe was determined<sup>132</sup> using  $\text{CH}_3\text{OH}$  proton signals using Equation 2.2

$$T = 435.5 - 1.193 (\Delta f) - 29.3 (\Delta f \times 10^{-2})^2 \quad (2.2)$$

where  $\Delta f$  is the frequency difference between the peak positions

of  $-\text{CH}_3$  and  $-\text{OH}$  protons, in Hz. Solvent susceptibilities<sup>133</sup> and diamagnetic corrections<sup>134</sup> were taken from literature tabulations.

Variable-temperature magnetic susceptibility measurements were made on powdered samples over the temperature range  $8.0 < T < 300$  K by the Faraday method using a locally built susceptometer in Professor S. Mitra's laboratory, Chemical Physics Group, Tata Institute of Fundamental Research (TIFR), Bombay, India. The measurements were started at  $\sim 8.0$  K and the sample was heated and held at the desired temperature during the measurement. This process was continued until the sample was attained at room temperature. Effective magnetic moments were calculated from  $\mu_{\text{eff}} = 2.828 [\chi_M T]^{1/2}$ , where  $\chi_M$  is the corrected molar susceptibility. Diamagnetic corrections were made for the sample holder and for the diamagnetic contribution of the complex being measured. All measurements were made at a fixed field strength and field dependence of the magnetic susceptibility was not studied.

X-Band EPR spectra were recorded with a Varian E-109 C spectrometer fitted with a quartz Dewar for measurements at liquid dinitrogen temperature. The spectra were calibrated with the help of DPPH ( $g = 2.0037$ ). Solution electrical conductivity measurements were made with an Elico (Hyderabad, India) Type CM-82 T conductivity bridge.

Cyclic voltammetric measurements were performed by using the PAR Model 370-4 electrochemistry system incorporating the following: Model 174A polarographic analyzer; Model 175 universal programmer; Model RE-0074 X-Y recorder. Differential pulse

voltammetric experiments were carried out using the Model 174A polarographic analyzer. Potentials are reported at  $-25^{\circ}\text{C}$  referenced to an aqueous saturated calomel electrode (SCE) and are uncorrected for junction potentials. The solutions were  $\sim 10^{-3}$  M in complex and 0.2 M in supporting electrolyte, TBAP. In acetonitrile and DMF solutions at a scan rate of  $50 \text{ mV s}^{-1}$  the above condition was found to give best performance with platinum and glassy carbon electrodes for the  $[\text{Fe}(\eta\text{-C}_5\text{H}_5)_2]^+ / [\text{Fe}(\eta\text{-C}_5\text{H}_5)_2]$  couple. At a platinum electrode the  $E_f$  [ $E_f = 0.5(E_{pa} + E_{pc})$ ] and the peak-to-peak separation ( $\Delta E_p$ ) values are: MeCN, 0.40 V (80 mV); DMF, 0.49 V (80 mV).<sup>135</sup>

A PAR G0021 glassy carbon electrode or a planar platinum-inlay electrode (Beckman Model 39273) was used as the working electrode. A sealed all-glass cell was used; measurements were made under an atmosphere of dry dinitrogen. The auxiliary electrode, which consisted of a platinum flag sealed in soft glass, and the reference electrode were separated from the working solution by means of fritted bridge filled with the same solvent and supporting electrolyte. Uncompensated solution resistance in the cell configuration was minimized by placing the tip of the reference electrode as close to the working electrode as possible.

## 2.2 Syntheses of Ligands

The tridentate ligands,  $R_4\text{bpp}$  were prepared by phase-transfer catalyzed reactions of 2,6-bis(chloromethyl)pyridine with pyrazole and its derivatives. 2,6-Bis(hydroxymethyl)pyridine<sup>136</sup>, 2,6-bis(chloromethyl)pyridinehydrochloride,<sup>137</sup> and 2,6-



bis(pyrazol-1-ylmethyl)pyridine ( $H_4bpy$ )<sup>114</sup> were prepared by using similar procedures as outlined in the literature. The various steps of the syntheses of  $R_4bpy$  ligands are summarized in Scheme I.

### 2.2.1 2,6-Bis(chloroformyl) pyridine<sup>136</sup>

A solution of 31 g (0.186 mol) of 2,6-pyridinedicarboxylic acid in 200 mL of thionyl chloride was heated to reflux for 10 h. Thionyl chloride was distilled off and the mixture was cooled to give solid (m.p. 56°C) product (yield 36 g, 95%).

### 2.2.2 Dimethyl 2,6-pyridine dicarboxylate<sup>136</sup>

2,6-Bis(chloroformyl)pyridine (36 g, 0.18 mol) was cooled in an ice bath and to it absolute methanol (250 mL) was added dropwise. The resulting mixture was heated to reflux for 30 min, and ~150 mL methanol was distilled off. The solution was cooled in an ice bath, and the white crystals formed were filtered, washed with cold (0°C) methanol and dried in vacuo to yield 34 g (94%) of the diester (mp 117°C).

### 2.2.3 2,6-Bis(hydroxymethyl) pyridine<sup>136</sup>

A suspension of 30 g (0.154 mol) of the diester in 420 mL of absolute ethanol was stirred and cooled in an ice bath as 27 g (0.71 mol) of sodium borohydride was added in portions over a period of 15 min. The mixture was stirred at 0°C for 1 h. The ice bath was removed and the mixture was stirred at 25°C for 3 h, after which it was heated to reflux on steam bath for 10 h. The solvent was distilled in vacuo, the residue was mixed with 120 mL acetone and heated on a steam bath (60°C) for 1 h. The solvent was distilled in vacuo and the residue was mixed with 36 mL (15%)



aqueous potassium carbonate and heated on a steam bath for 1 h. The solvent was distilled off in vacuo and the product was extracted several times with chloroform to give 18 g (yield, 83%) of diol (mp 116°C).

#### 2.2.4 2,6-Bis(chloromethyl) pyridine hydrochloride<sup>137</sup>

2,6-Bis(hydroxymethyl)pyridine (10.50 g, 0.075 mol) was cooled to 0°C on an ice bath and was kept for 30 min. Thionyl chloride (160 mL) was added slowly using a dropping funnel. The reaction mixture was warmed (60°C) with stirring for 4 h, after which it was kept overnight at room temperature. Dry and cold benzene (480 mL) was added drpwise to the reaction mixture kept in an ice bath, until the completion of precipitation. White product was filtered, washed with cold dry benzene and dried in vacuo (yield 12.00 g, ~75%).

#### 2.2.5 2-Chloromethyl-6-(pyrazol-1-ylmethyl)pyridine

This was prepared with a modified method as described in the literature.<sup>114</sup> A mixture of 2,6-bis(chloromethyl)pyridine (5.00 g, 0.024 mol), pyrazole (1.60 g, 0.024 mol), benzene (700 mL), 40% aqueous sodium hydroxide (120 mL) and 40% aqueous tetra-n-butyl-ammonium hydroxide (3 mL) was refluxed with stirring for 6 h and then stirred at room temperature overnight. The organic layer was separated, dried over anhydrous sodium sulphate and evaporated under reduced pressure to yield an oil shown by <sup>1</sup>H NMR to be a 1:1 mixture of two isomers. The crude product (oil) was purified by column chromatography on silica gel by using 40% Et<sub>2</sub>O / 60% n-hexane mixture as eluent to give the desired product (yield, 28%). <sup>1</sup>H NMR: 7.6 (m, 3H; H<sub>4</sub>, H<sub>3'</sub>, H<sub>5'</sub>), 7.4 (d, 1H; H<sub>3</sub>), 6.8

(d, 1H; H5), 6.3 (t, 1H, H4'), 5.5 (s, 2H; NCH<sub>2</sub>), 4.7 ppm (s, 2H; CH<sub>2</sub>Cl). The <sup>1</sup>H NMR spectrum of this unsymmetrical precursor is displayed in Figure 2.1.

#### 2.2.6 2,6-Bis(pyrazol-1-ylmethyl)pyridine (H<sub>4</sub>bpp)<sup>114</sup>

A mixture of 2,6-bis(chloromethyl)pyridine (2.50 g, 0.012 mol), pyrazole (1.60 g, 0.024 mol), benzene (300 mL), 40% aqueous sodium hydroxide (60 mL) and 40% aqueous tetrabutylammonium hydroxide (30 drops) was refluxed with stirring for 8 h and then stirred at room temperature overnight. The organic layer was separated, dried over anhydrous sodium sulphate and evaporated under reduced pressure to yield 2,6-Bis(pyrazol-1-ylmethyl)pyridine as an oil (yield 2.54 g, 90%).

#### 2.2.7 2-(pyrazol-1-ylmethyl)-6-(3,5-dimethyl-pyrazol-1-ylmethyl)pyridine (H<sub>2</sub>Me<sub>2</sub>bpp)

A mixture of 2-chloromethyl-6-(pyrazol-1-ylmethyl)pyridine (0.5 g, 2.41 mmol), pyrazole (0.23 g, 2.40 mmol), benzene (70 mL), 40% aqueous sodium hydroxide (12 mL) and 40% aqueous tetra-n-butylammonium hydroxide (6 drops) was refluxed with stirring for 8 h and then stirred at room temperature overnight. The organic layer was separated, dried over anhydrous sodium sulphate and evaporated under reduced pressure to yield 2-(pyrazol-1-ylmethyl)-6-(3,5-dimethyl-pyrazol-1-ylmethyl)pyridine as an oil (yield 0.60 g, 93%).

#### 2.2.8 2,6-Bis(3,5-dimethylpyrazol-1-ylmethyl)pyridine (Me<sub>4</sub>bpp)

This was prepared following similar procedure described for 2,6-bis(pyrazol-1-ylmethyl)pyridine (H<sub>4</sub>bpp) using 3,5-dimethyl pyrazole instead of unsubstituted pyrazole (yield, 90%) (mp 115°C).

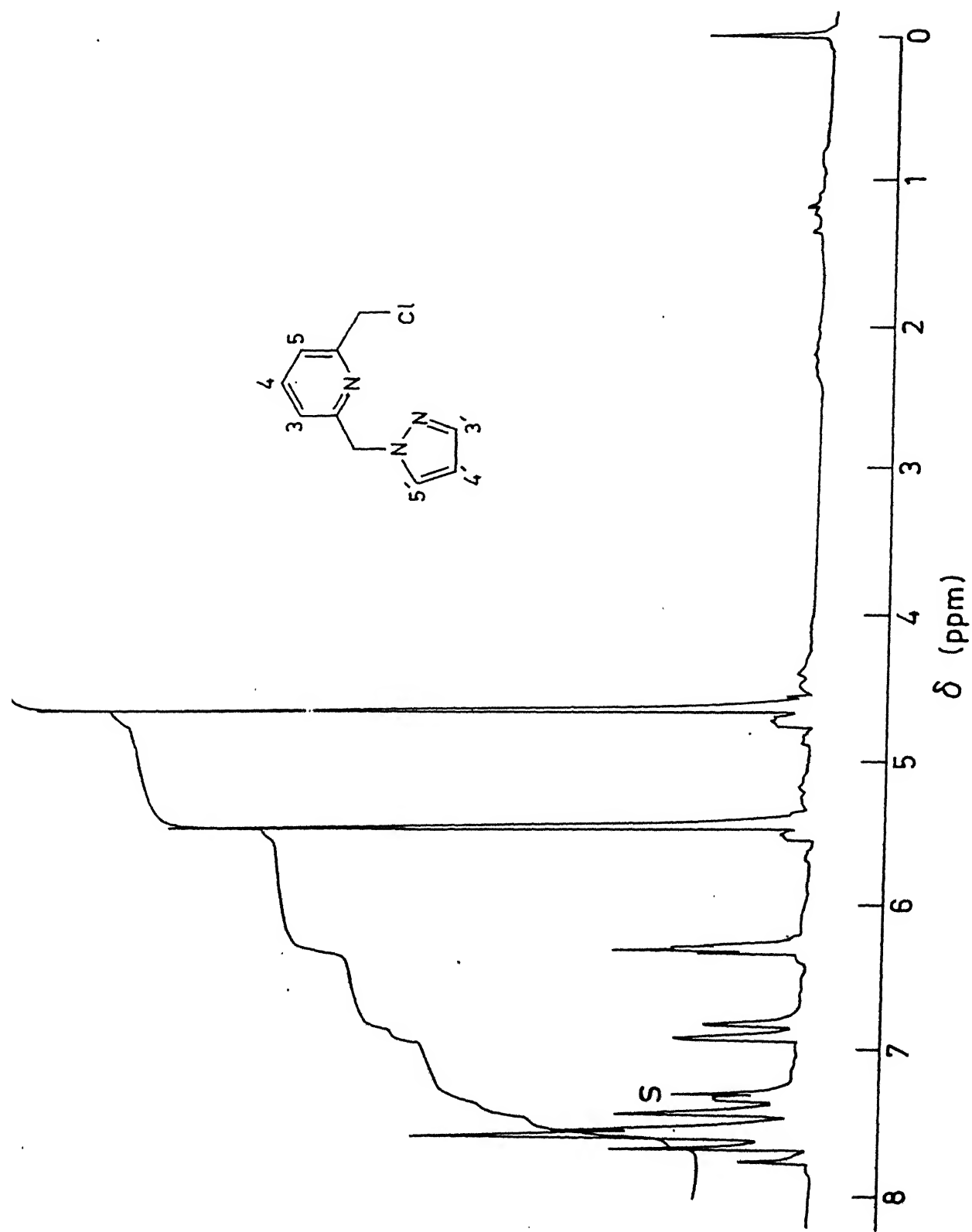


Figure 2.1  $^1\text{H}$  NMR spectrum of 2-chloromethyl-6-(pyrazol-1-ylmethyl)pyridine in  $\text{CDCl}_3$

The  $^1\text{H}$  NMR spectral data for  $\text{H}_4\text{bpp}$ ,  $\text{H}_2\text{Me}_2\text{bpp}$ , and  $\text{Me}_4\text{bpp}$  in  $\text{CDCl}_3$  are set out in Table 2.1. The spectra of the unsymmetrical ligand,  $\text{H}_2\text{Me}_2\text{bpp}$  and the tetramethyl derivative,  $\text{Me}_4\text{bpp}$  are shown in Figures 2.2 and 2.3 respectively.

## 2.3 Syntheses of complexes

### 2.3.1 $[\text{Mn}(\text{H}_4\text{bpp})_2](\text{ClO}_4)_2 \cdot 2\text{H}_2\text{O}$

To a 5 mL solution of the ligand  $\text{H}_4\text{bpp}$  (0.13 g, 0.55 mmol) in MeCN was added dropwise a solution of  $\text{Mn}(\text{ClO}_4)_2 \cdot 6\text{H}_2\text{O}$  (0.10 g, 0.28 mmol) in MeCN (5 mL) and stirred for 15 min. To the resulting solution 10 mL of diethyl ether was added and kept at  $-0^\circ\text{C}$  for 24 h. The cream colored crystalline compound that separated was filtered, washed with diethyl ether and finally dried in vacuo (yield 0.15 g, 70%).

### 2.3.2 $[\text{Mn}(\text{H}_2\text{Me}_2\text{bpp})_2](\text{ClO}_4)_2 \cdot 2\text{H}_2\text{O}$

To an ethanolic solution (5 mL) of the ligand  $\text{H}_2\text{Me}_2\text{bpp}$  (0.15 g, 0.55 mmol) was added an aqueous solution (5 mL) of  $\text{Mn}(\text{ClO}_4)_2 \cdot 6\text{H}_2\text{O}$  (0.100 g, 0.28 mmol). Immediate precipitation of light orange material had occurred. The crude product was recrystallized from ethanol-water (1:1) (yield 0.17 g, 76%).

### 2.3.3 $[\text{Mn}(\text{Me}_4\text{bpp})_2](\text{ClO}_4)_2 \cdot 2\text{H}_2\text{O}$

This was synthesized using a similar method as described above for the ligand  $\text{H}_2\text{Me}_2\text{bpp}$ .

### 2.3.4 $[\text{Mn}(\text{H}_4\text{bpp})\text{Cl}_2]$

An ethanolic solution (20 mL) of the ligand  $\text{H}_4\text{bpp}$  (0.20 g, 0.84 mmol) was added dropwise to an ethanolic solution (20 mL) of  $\text{MnCl}_2 \cdot 4\text{H}_2\text{O}$  (0.17 g, 0.84 mmol). The mixture was stirred at  $60^\circ\text{C}$

Table 2.1:  $^1\text{H}$  NMR Data<sup>a</sup> of  $\text{R}_4\text{bpp}$  Ligands

Ligands	$\text{H}^3, \text{H}^5$	$\text{H}^4$	$\text{H}^{3'}$ (or Me)	$\text{H}^{5'}$ (or Me)	$\text{H}^{4'}$	$\text{CH}_2$
$\text{H}_4\text{bpp}$	6.8 (d, $J=8.0$ Hz)	7.5 (m)	7.5 (m)	7.5 (m)	6.2 (t, $J=2.0$ Hz)	4.5 (s)
$\text{H}_2\text{Me}_2\text{bpp}$	6.7 (t, $J=8.0$ Hz)	7.5 (m)	7.5 (m)	7.5 (m)	6.3 (t, $J=2.0$ Hz)	5.2 (s)
			2.1 <sup>b</sup> (s)	2.2 <sup>c</sup> (s)	5.8 <sup>d</sup> (s)	5.4 (s)
$\text{Me}_4\text{bpp}$	6.6 (d, $J=8.0$ Hz)	7.4 (q, $J=7.5$ Hz)	2.2 (s)	2.3 (s)	5.9 (s)	5.3 (s)

<sup>a</sup> Symbols: s = singlet; d = doublet; t = triplet; m = multiplet.

<sup>b</sup>  $\text{Me}^{3''}$

<sup>c</sup>  $\text{Me}^{5''}$

<sup>d</sup>  $\text{H}^{4''}$

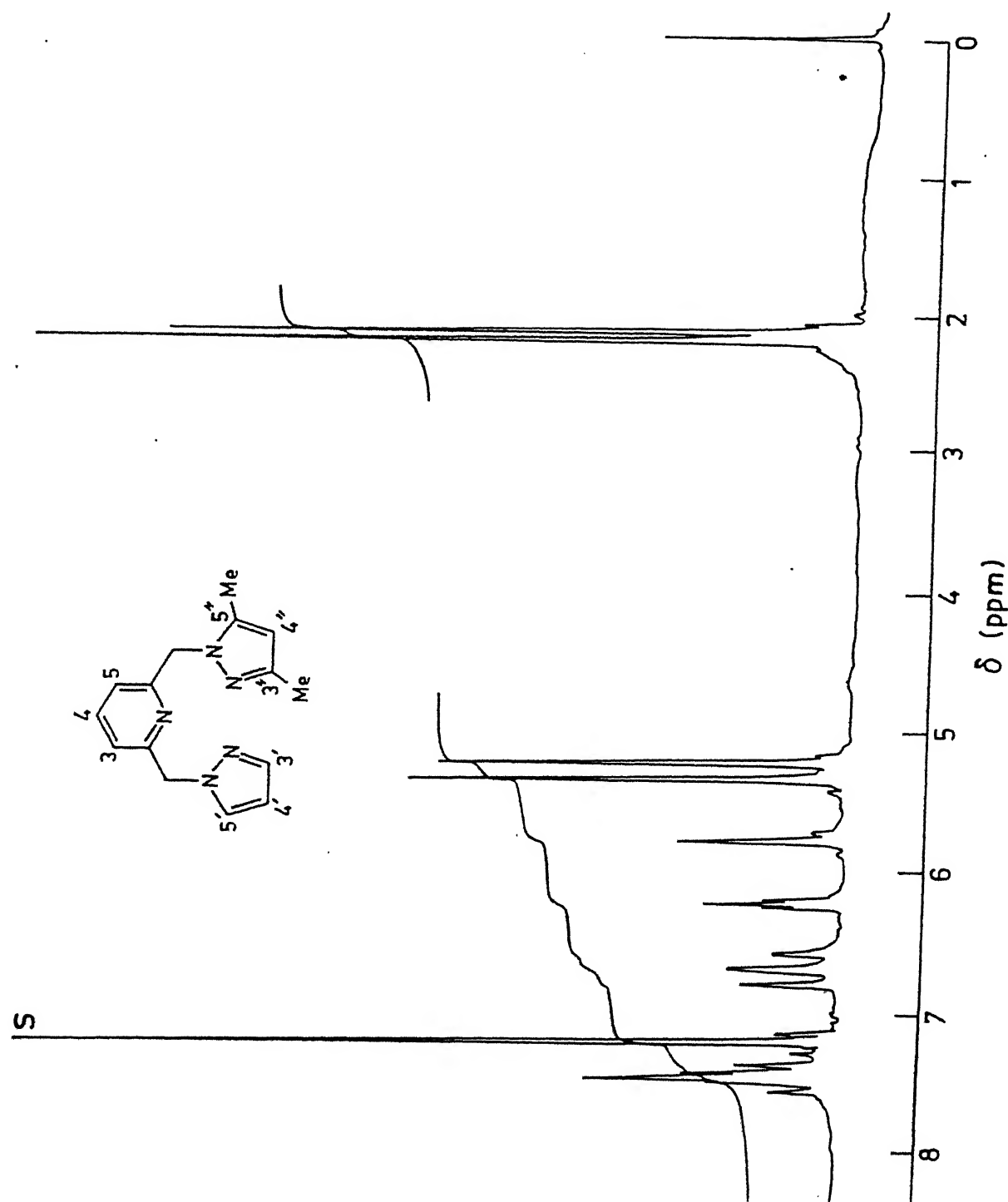


Figure 2.2  $^1\text{H}$  NMR spectrum of 2-(3,5-dimethylpyrazol-1-ylmethyl)-6-(pyrazol-1-ylmethyl)pyridine ( $\text{H}_2\text{Me}_2\text{bpp}$ ) in  $\text{CDCl}_3$



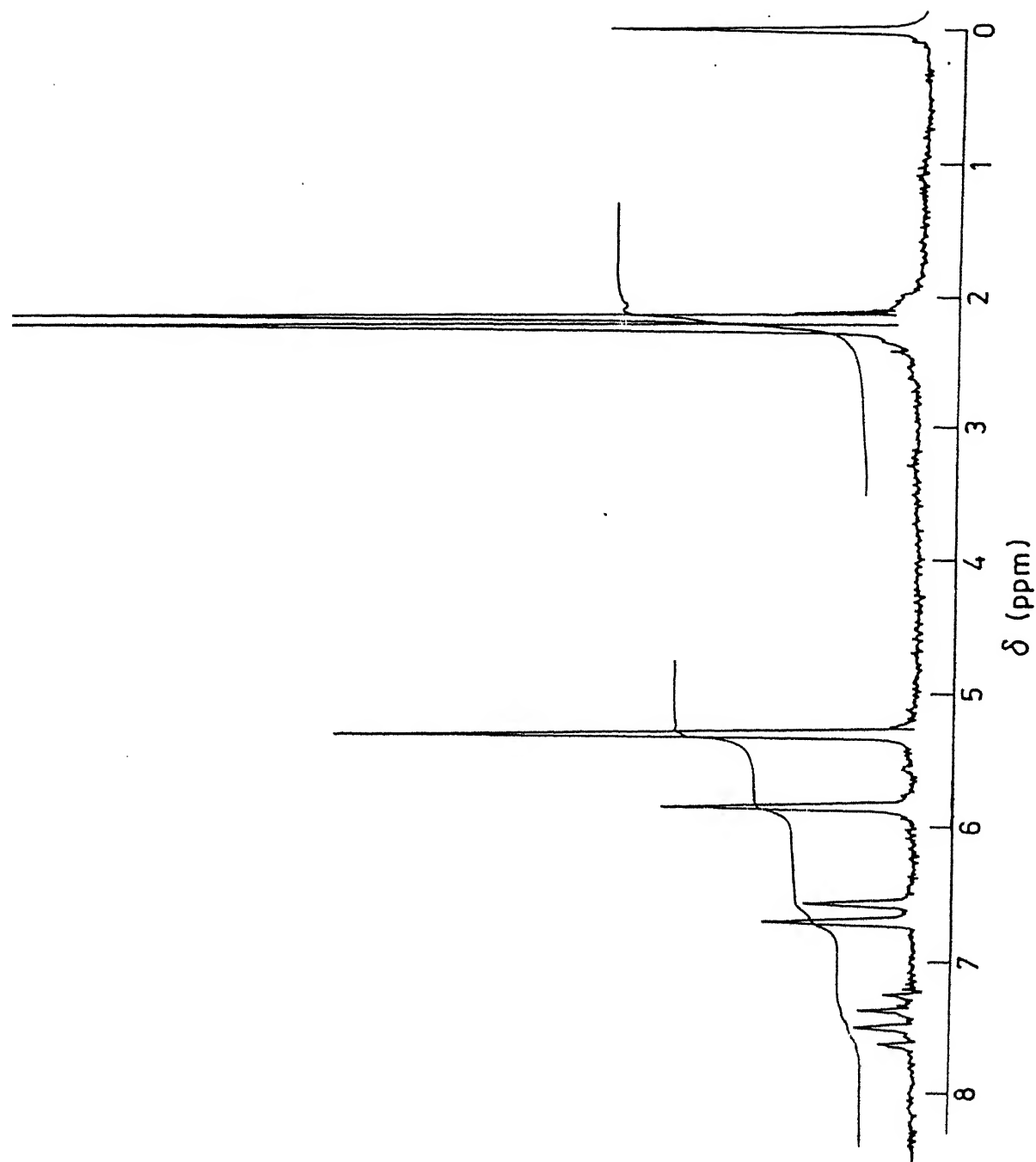


Figure 2.3  $^1\text{H}$  NMR spectrum of 2,6-bis(3,5-dimethylpyrazol-1-ylmethyl)pyridine (Me<sub>4</sub>bpp) in  $\text{CDCl}_3$

for 45 min and the resulting solution was kept at 0°C for 3 h to give white microcrystalline product. The compound was filtered and washed with ethanol followed by chloroform and finally air dried (yield 0.25 g, 80%).

### 2.3.5 [Mn(Me<sub>4</sub>bpp)Cl<sub>2</sub>]

This was prepared similarly following the method as described above.

### 2.3.6 [Fe(R<sub>4</sub>bpp)<sub>2</sub>](ClO<sub>4</sub>)<sub>2</sub>

The iron(II) bis-chelates of the ligands H<sub>4</sub>bpp, H<sub>2</sub>Me<sub>2</sub>bpp, and Me<sub>4</sub>bpp were prepared according to the reported procedure<sup>114</sup> using H<sub>4</sub>bpp.

The microanalytical data for the manganese and iron complexes are given in Table 2.2.

### 2.3.7 [Co(H<sub>4</sub>bpp)<sub>2</sub>](ClO<sub>4</sub>)<sub>2</sub>·H<sub>2</sub>O

To a 5 mL ethanolic solution of the ligand H<sub>4</sub>bpp (0.10 g, 0.42 mmol) was added a 5 mL aqueous solution of CoCl<sub>2</sub>·6H<sub>2</sub>O (0.05 g, 0.21 mmol). The mixture was stirred at room temperature for 30 min, after which time a saturated aqueous solution (1 mL) of sodium perchlorate was added. The pale yellow microcrystalline solid was collected, washed with ethanol-water (1:1), and dried under vacuum (yield 0.11 g, 68%).

### 2.3.8 [Co(H<sub>2</sub>Me<sub>2</sub>bpp)<sub>2</sub>](ClO<sub>4</sub>)<sub>2</sub>·H<sub>2</sub>O.

To a stirred solution of H<sub>2</sub>Me<sub>2</sub>bpp (0.15 g, 0.56 mmol) in 10 mL ethanol was added a 5 mL aqueous solution of Co(ClO<sub>4</sub>)<sub>2</sub>·6H<sub>2</sub>O (0.10 g, 0.27 mmol). The mixture was stirred for 1 h and kept at room temperature for slow evaporation. Orange crystals were

Table 2.2: Microanalytical Data of Manganese(II) and Iron(II) Complexes

Compounds	Empirical Formula	Analysis <sup>a</sup>		
		% C	% H	% N
[Fe(H <sub>4</sub> bpp) <sub>2</sub> ] (ClO <sub>4</sub> ) <sub>2</sub> ·2H <sub>2</sub> O	C <sub>26</sub> H <sub>28</sub> Cl <sub>2</sub> N <sub>10</sub> O <sub>9</sub> Fe	41.60 (41.55)	3.68 (3.73)	18.67 (18.65)
[Fe(H <sub>2</sub> Me <sub>2</sub> bpp) <sub>2</sub> ] (ClO <sub>4</sub> ) <sub>2</sub> ·2H <sub>2</sub> O	C <sub>30</sub> H <sub>30</sub> Cl <sub>2</sub> N <sub>10</sub> O <sub>10</sub> Fe	43.60 (43.64)	4.57 (4.61)	16.95 (16.97)
[Fe(Me <sub>4</sub> bpp) <sub>2</sub> ] (ClO <sub>4</sub> ) <sub>2</sub> ·2H <sub>2</sub> O	C <sub>34</sub> H <sub>46</sub> Cl <sub>2</sub> N <sub>10</sub> O <sub>10</sub> Fe	46.80 (46.32)	4.97 (5.22)	15.67 (15.89)
[Mn(H <sub>4</sub> bpp) <sub>2</sub> ] (ClO <sub>4</sub> ) <sub>2</sub> ·2H <sub>2</sub> O	C <sub>26</sub> H <sub>30</sub> Cl <sub>2</sub> N <sub>10</sub> O <sub>10</sub> Mn	40.50 (40.63)	3.80 (3.91)	18.50 (18.23)
[Mn(H <sub>2</sub> Me <sub>2</sub> bpp) <sub>2</sub> ] (ClO <sub>4</sub> ) <sub>2</sub> ·2H <sub>2</sub> O	C <sub>30</sub> H <sub>38</sub> Cl <sub>2</sub> N <sub>10</sub> O <sub>10</sub> Mn	43.80 (43.68)	4.80 (4.61)	16.90 (16.99)
[Mn(Me <sub>4</sub> bpp) <sub>2</sub> ] (ClO <sub>4</sub> ) <sub>2</sub> ·2H <sub>2</sub> O	C <sub>34</sub> H <sub>46</sub> Cl <sub>2</sub> N <sub>10</sub> O <sub>10</sub> Mn	46.20 (46.36)	5.40 (5.23)	16.00 (15.91)
[Mn(H <sub>4</sub> bpp)Cl <sub>2</sub> ]	C <sub>13</sub> H <sub>13</sub> Cl <sub>2</sub> N <sub>5</sub> Mn	42.90 (42.74)	3.60 (3.56)	19.10 (19.18)
[Mn(Me <sub>4</sub> bpp)Cl <sub>2</sub> ]	C <sub>17</sub> H <sub>21</sub> Cl <sub>2</sub> N <sub>5</sub> Mn	48.20 (48.46)	5.04 (4.99)	16.60 (16.63)

<sup>a</sup> Calculated values in parentheses.

collected after 48 h, washed with ethanol-water (1:1), and dried under vacuum (yield 0.14 g, 62%).

### 2.3.9 $[\text{Co}(\text{Me}_4\text{bpp})_2](\text{ClO}_4)_2 \cdot \text{H}_2\text{O}$

This complex was synthesized following a similar method as described above for the ligand  $\text{H}_2\text{Me}_2\text{bpp}$  (yield 75%).

### 2.3.10 $[\text{Ni}(\text{R}_4\text{bpp})_2](\text{ClO}_4)_2$

The nickel(II) bis-chelates of the ligands  $\text{H}_4\text{bpp}$ ,  $\text{H}_2\text{Me}_2\text{bpp}$ , and  $\text{Me}_4\text{bpp}$  were prepared according to the reported procedure<sup>114</sup> using  $\text{H}_4\text{bpp}$ .

The microanalytical data for the cobalt and nickel complexes are given in Table 2.3.

### 2.3.11 $(\text{H}_4\text{bpp})\text{RuCl}_3 \cdot 3\text{H}_2\text{O}$

An ethanolic solution (10 mL) of  $\text{H}_4\text{bpp}$  (0.18 g, 0.76 mmol) was added dropwise to a vigorously stirred ethanolic solution (15 mL) of  $\text{RuCl}_3 \cdot 3\text{H}_2\text{O}$  (0.20 g, 0.76 mmol). The mixture was stirred for 1 h at room temperature and the greenish-brown powder that separated was filtered off and washed with ethanol followed by acetone and finally dried in vacuo (yield 0.27 g, 72%).

Electronic spectrum (in DMSO),  $\lambda$ , nm ( $\epsilon$ ,  $\text{M}^{-1}\text{cm}^{-1}$ ): 369 (4450), 460 (sh) (3260), 600 (sh) (657). Molar conductance,  $\Lambda_{\text{M}} = 36 \Omega^{-1}\text{cm}^2 \text{mol}^{-1}$ .  $\mu_{\text{eff}}$  (in DMF) = 1.98 B.M.

### 2.3.12 $[\text{Ru}(\text{H}_4\text{bpp})_2](\text{ClO}_4)_2 \cdot \text{H}_2\text{O}$

Two different synthetic procedures were followed to prepare this compound.

**Method A:** An aqueous solution (10 mL) of  $\text{RuCl}_3 \cdot 3\text{H}_2\text{O}$  (0.100 g, 0.38 mmol) and  $\text{H}_4\text{bpp}$  (0.220 g, 0.92 mmol) was refluxed under

**Table 2.3:** Microanalytical Data of Cobalt(II) and Nickel(II) Complexes

Compounds	Empirical Formula	Analysis <sup>a</sup>		
		% C	% H	% N
[Co(H <sub>4</sub> bpp) <sub>2</sub> ] (ClO <sub>4</sub> ) <sub>2</sub> ·H <sub>2</sub> O	C <sub>26</sub> H <sub>28</sub> N <sub>10</sub> O <sub>9</sub> Cl <sub>2</sub> Co	40.36 (41.60)	3.71 (3.73)	18.20 (18.67)
[Co(H <sub>2</sub> Me <sub>2</sub> bpp) <sub>2</sub> ] (ClO <sub>4</sub> ) <sub>2</sub> ·H <sub>2</sub> O	C <sub>30</sub> H <sub>36</sub> N <sub>10</sub> O <sub>9</sub> Cl <sub>2</sub> Co	44.32 (44.67)	4.58 (4.47)	16.40 (17.37)
[Co(Me <sub>4</sub> bpp) <sub>2</sub> ] (ClO <sub>4</sub> ) <sub>2</sub> ·H <sub>2</sub> O	C <sub>34</sub> H <sub>44</sub> N <sub>10</sub> O <sub>9</sub> Cl <sub>2</sub> Co	47.05 (47.33)	5.31 (5.10)	16.16 (16.24)
[Ni(H <sub>4</sub> bpp) <sub>2</sub> ] (ClO <sub>4</sub> ) <sub>2</sub>	C <sub>26</sub> H <sub>26</sub> N <sub>10</sub> O <sub>8</sub> Cl <sub>2</sub> Ni	42.70 (42.45)	3.49 (3.54)	19.01 (19.03)
[Ni(H <sub>2</sub> Me <sub>2</sub> bpp) <sub>2</sub> ] (ClO <sub>4</sub> ) <sub>2</sub>	C <sub>30</sub> H <sub>34</sub> N <sub>10</sub> O <sub>8</sub> Cl <sub>2</sub> Ni	45.72 (45.46)	4.25 (4.30)	17.73 (17.68)
[Ni(Me <sub>4</sub> bpp) <sub>2</sub> ] (ClO <sub>4</sub> ) <sub>2</sub>	C <sub>34</sub> H <sub>42</sub> N <sub>10</sub> O <sub>8</sub> Cl <sub>2</sub> Ni	48.35 (48.12)	5.02 (4.96)	16.59 (16.52)

<sup>a</sup>Calculated values in parentheses

dinitrogen atmosphere for 1 h.<sup>5</sup> The ruthenium was then reduced by the addition of sodium hypophosphite solution [1.8 mL ; prepared by neutralizing 30%  $\text{H}_3\text{PO}_2$  (1.2 mL) with 2.0 M NaOH (3.4 mL)] Concentrated HCl (8 drops) was then added to the green solution and was further refluxed for 2 h and finally filtered. The complex was precipitated as brownish-green microcrystalline solid by dropwise addition of a saturated aqueous solution of sodium perchlorate. The compound was recrystallized from ethanol-water (1:1); (yield 0.08 g, 51%).

**Method B:** A suspension of  $(\text{H}_4\text{bpp})\text{RuCl}_3 \cdot 3\text{H}_2\text{O}$  (0.10 g, 0.20 mmol) and  $\text{H}_4\text{bpp}$  (0.05 g, 0.20 mmol) in water (10 mL) was refluxed for 30 min under dinitrogen atmosphere. After the addition of sodium hypophosphite solution (1.2 mL ; prepared as described above) it was further refluxed for 2 h and filtered. The desired complex was precipitated and recrystallized as described above (yield 0.78 g, 48%). Both the methods gave similar microanalysis.

#### 2.3.13 $[\text{Ru}(\text{H}_4\text{bpp})(\text{Me}_4\text{bpp})](\text{ClO}_4)_2 \cdot \text{H}_2\text{O}$

This complex was prepared by a procedure similar to that described above (Method B) for  $[\text{Ru}(\text{H}_4\text{bpp})_2](\text{ClO}_4)_2 \cdot \text{H}_2\text{O}$ , using  $\text{Me}_4\text{bpp}$  as ligand in place of  $\text{H}_4\text{bpp}$  (yield 48%).

The microanalytical data for the ruthenium complexes are given in Table 2.4.

Table 2.4: Microanalytical Data of Ruthenium(II) Complexes

Compounds	Empirical Formula	Analysis <sup>a</sup>		
		% C	% H	% N
[Ru(H <sub>4</sub> bpp) <sub>2</sub> ] (ClO <sub>4</sub> ) <sub>2</sub> ·H <sub>2</sub> O	C <sub>26</sub> H <sub>28</sub> Cl <sub>2</sub> N <sub>10</sub> O <sub>9</sub> Ru	39.20 (39.20)	3.60 (3.50)	17.60 (17.60)
[Ru(H <sub>2</sub> Me <sub>2</sub> bpp) <sub>2</sub> ] (ClO <sub>4</sub> ) <sub>2</sub> ·H <sub>2</sub> O	C <sub>30</sub> H <sub>28</sub> Cl <sub>2</sub> N <sub>10</sub> O <sub>9</sub> Ru	43.60 (43.64)	4.57 (4.61)	16.95 (16.97)
[Ru(Me <sub>4</sub> bpp) <sub>2</sub> ] (ClO <sub>4</sub> ) <sub>2</sub> ·H <sub>2</sub> O	C <sub>34</sub> H <sub>44</sub> Cl <sub>2</sub> N <sub>10</sub> O <sub>9</sub> Ru	46.80 (46.32)	4.97 (5.22)	15.67 (15.89)
[Ru(H <sub>4</sub> bpp)(H <sub>2</sub> Me <sub>2</sub> - bpp)](ClO <sub>4</sub> ) <sub>2</sub> ·H <sub>2</sub> O	C <sub>26</sub> H <sub>28</sub> Cl <sub>2</sub> N <sub>10</sub> O <sub>9</sub> Ru	41.60	3.68	18.67
[Ru(H <sub>4</sub> bpp)(Me <sub>4</sub> - bpp)](ClO <sub>4</sub> ) <sub>2</sub> ·H <sub>2</sub> O	C <sub>26</sub> H <sub>28</sub> Cl <sub>2</sub> N <sub>10</sub> O <sub>9</sub> Ru	41.60	3.68	18.67
[Ru(H <sub>2</sub> Me <sub>2</sub> bpp)(Me <sub>4</sub> - bpp)](ClO <sub>4</sub> ) <sub>2</sub> ·H <sub>2</sub> O	C <sub>26</sub> H <sub>28</sub> Cl <sub>2</sub> N <sub>10</sub> O <sub>9</sub> Ru	41.60	3.68	18.67

<sup>a</sup> Calculated values in parentheses.

## 2.4 Results and Discussion

### 2.4.1 Bis chelates of Iron(II) with FeN<sub>6</sub> Coordination

#### 2.4.1.1 Synthesis and Characterization of [Fe(R<sub>4</sub>bpp)<sub>2</sub>]<sup>+</sup> Complexes

The bis-ligand complexes were readily obtained when methanolic solutions of the ligands and aqueous solutions of iron(II) perchlorate were mixed. An interesting observation is that the color of the complexes varies from light green, [Fe(H<sub>4</sub>bpp)<sub>2</sub>]<sup>2+</sup> to yellowish brown, [Fe(H<sub>2</sub>Me<sub>2</sub>bpp)<sub>2</sub>]<sup>2+</sup> to yellow [Fe(Me<sub>4</sub>bpp)<sub>2</sub>]<sup>2+</sup>.

The iron(II) complexes display the  $\nu$ (OH) bands at 3400 cm<sup>-1</sup> and  $\nu$ (ClO<sub>4</sub><sup>-</sup>) absorptions at 1100 and 620 cm<sup>-1</sup> in their IR spectra. These complexes are highly soluble in polar organic solvents. In MeCN solutions they show the expected<sup>138</sup> 1:2 electrolytic behavior (Table 2.5). Measurements of susceptibilities in MeCN solutions (Evans' method<sup>131</sup>) of the iron complexes, [Fe(R<sub>4</sub>bpp)<sub>2</sub>]<sup>2+</sup> gave the effective magnetic moments,  $\mu_{\text{eff}}$  ~5.40 whereas solid state magnetic moment ranges from 4.9-5.2  $\mu_B$  (Table 2.5). These magnetic data clearly establish<sup>139</sup> the high-spin electronic configuration (S = 2).

#### 2.4.2.2 Solution Structure of the High-spin Fe<sup>II</sup>N<sub>6</sub> Coordination Sphere by <sup>1</sup>H NMR Spectra

To elucidate the coordination geometry of these high-spin pseudooctahedral iron(II) complexes we have undertaken a <sup>1</sup>H NMR study on [Fe(H<sub>4</sub>bpp)<sub>2</sub>](ClO<sub>4</sub>)<sub>2</sub>·H<sub>2</sub>O and [Fe(Me<sub>4</sub>bpp)<sub>2</sub>](ClO<sub>4</sub>)<sub>2</sub>·2H<sub>2</sub>O focusing on paramagnetically shifted<sup>140,141</sup> resonances. The observed narrower ligand proton chemical shifts (Figures 2.4 and



Table 2.5: Molar Conductance, Magnetic Moment and Electronic Spectral data of the Iron(II) Complexes in MeCN at 298 K

Compounds	$\Lambda_M^a$ ( $\Omega^{-1}\text{cm}^2\text{mol}^{-1}$ )	$\mu_{\text{eff}}(\text{B.M.})^b$	$\lambda$ , nm ( $\epsilon$ , $\text{M}^{-1}\text{cm}^{-1}$ )
$[\text{Fe}(\text{H}_4\text{bpp})_2](\text{ClO}_4)_2 \cdot 2\text{H}_2\text{O}$	284	5.40 (4.90) <sup>c</sup>	931 (4), 781 (5), 543 (17), 415 (840), 368(sh) (600), 304(sh) (1200), 262 (10750)
$[\text{Fe}(\text{H}_2\text{M}_2\text{bpp})_2](\text{ClO}_4)_2 \cdot 2\text{H}_2\text{O}$	281	5.43	955 (6), 813(7), 360 (460), 262(11 150)
$[\text{Fe}(\text{Me}_4\text{bpp})_2](\text{ClO}_4)_2 \cdot 2\text{H}_2\text{O}$	294	5.44 (5.11) <sup>c</sup>	962 (7), 852(8), 365 (340), 265(sh) (10 700), 245(sh) (14 100)

<sup>a</sup> Expected 1:2 electrolyte range 220-300  $\Omega^{-1}\text{cm}^2\text{mol}^{-1}$ .

<sup>b</sup> Measured in MeCN solution (298 K) using Evans' method.

<sup>c</sup> Room temperature solid state values in parentheses

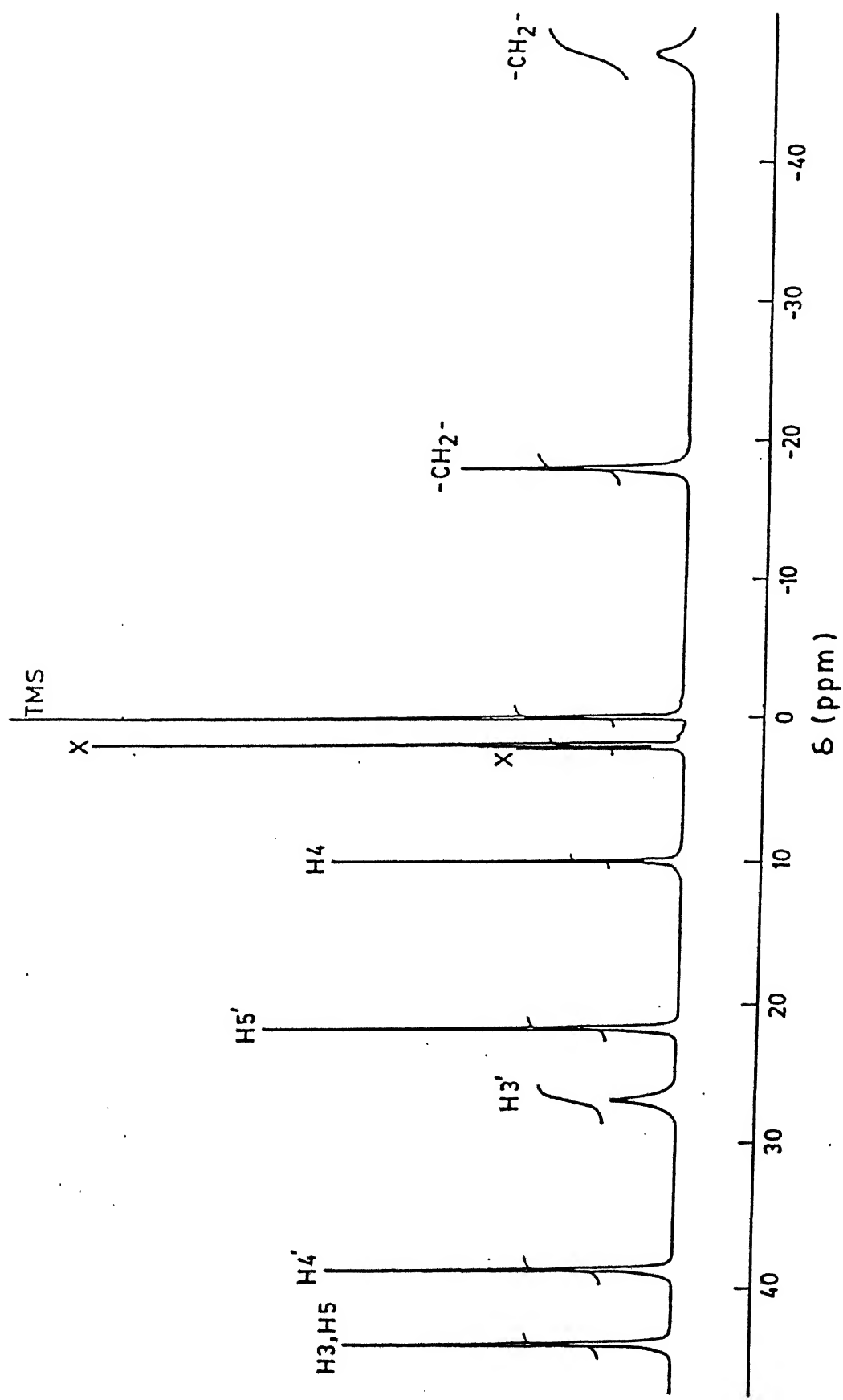


Figure 2.4 400 MHz  $^1\text{H}$  NMR spectrum of  $[\text{Fe}(\text{H}_4\text{bpp})_2](\text{ClO}_4)_2 \cdot \text{H}_2\text{O}$  in  $\text{CD}_3\text{CN}$   
(solvent and water peaks marked by x)

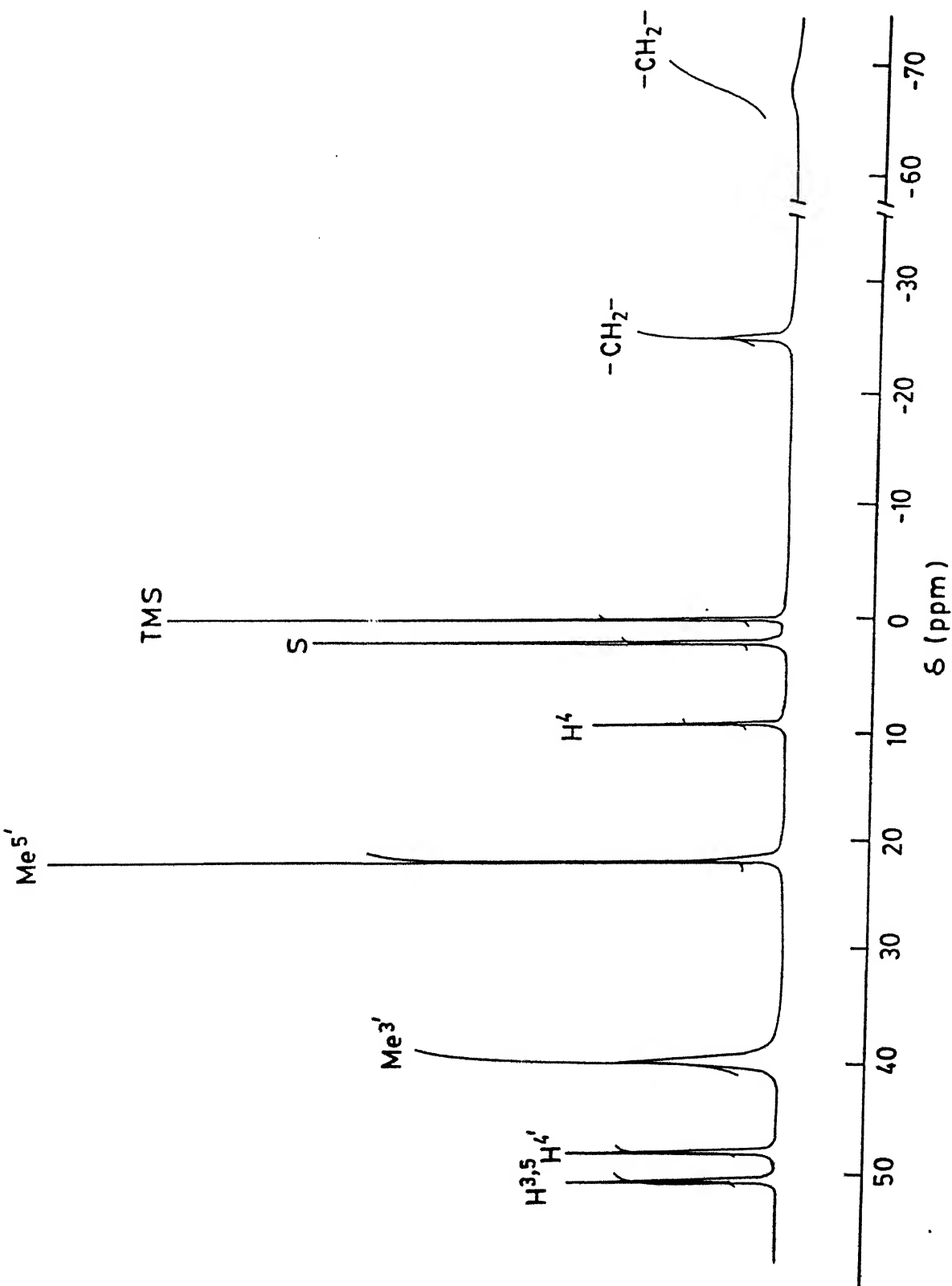


Figure 2.5 400 MHz  $^1\text{H}$  NMR spectrum of  $[\text{Fe}(\text{Me}_4\text{bpp})_2](\text{ClO}_4)_2 \cdot 2\text{H}_2\text{O}$  in  $\text{CD}_3\text{CN}$

2.5) point towards shorter electron spin-lattice relaxation time,  $T_{1e}$ . The  $T_{1e}$ 's tend to broaden the ligand NMR resonances according to<sup>140,141</sup>  $T_1^{-1} \propto T_{1e}r^{-6}$  where  $T_1$  is the  $^1H$  spin-lattice relaxation time and  $r$  is the length of the Fe-H distance vector. Thus a proton farthest removed (most distant) from the paramagnetic center is expected to exhibit comparatively sharper signal and to give rise to smallest observed chemical shift from a diamagnetic reference. We mean the free ligand proton resonances as the diamagnetic reference. In this work we have assigned resonances (Table 2.6) by a combination of the expected behavior for paramagnetically shifted resonances as outlined above and integrated area ratios.

The resonances at ~10 ppm are consistent with their assignments as the para protons ( $H^4$ ) of the pyridine rings. A comparative analysis of the spectra of  $[Fe(H_4bpp)_2]^{2+}$  and  $[Fe(Me_4bpp)_2]^{2+}$  clearly establishes the resonances at ~20 ppm are due to 5' protons (methyl groups) of pyrazole rings. Comparatively broad resonances at ~ 27 ppm for  $[Fe(H_4bpp)_2]^{2+}$  and at ~ 40 ppm for  $[Fe(Me_4bpp)_2]^{2+}$  in the relative intensity ratio of 1:3 are assignable as 3' protons (methyl groups) of pyrazole rings. The two upfield resonances of relative intensity 1:1 is assigned as the methylene protons. The most upfield resonances are the broadest in the spectra of both the compounds and is supposed to have the shortest  $T_1$ 's as expected in the  $CH_2$  protons, which are the closest to the iron center. Now we are left with only two resonances at ~ 39 and ~ 44 ppm in the case of  $[Fe(H_4bpp)_2]^{2+}$  and at ~48 and 50 ppm in the spectrum of  $[Fe(Me_4bpp)_2]^{2+}$ . It is expected that the pyridine ring protons  $H^3$  and  $H^5$  and pyrazole

**Table 2.6:** Proton NMR Chemical Shifts Relative to TMS for  
High-spin Pseudooctahedral Iron(II) Complexes

Compounds		int <sup>a</sup>	assignments
$[\text{Fe}(\text{H}_4\text{bpp})_2]$ $(\text{ClO}_4)_2 \cdot \text{H}_2\text{O}$	$[\text{Fe}(\text{Me}_4\text{bpp})_2]$ $(\text{ClO}_4)_2 \cdot 2\text{H}_2\text{O}$		
44.0	50.0	4	$\text{H}^3, \text{H}^5$
39.0	47.5	4	$\text{H}^{4'}$
27.0	39.5	4,12	$\text{H}^{3'}, \text{CH}_3$
22.0	21.5	4,12	$\text{H}^{5'}, \text{CH}_3$
10.0	9.0	2	$\text{H}^4$
-18.0	-25.0	4	$\text{CH}_2$
-48.0	-68.0	4	$\text{CH}_2$

<sup>a</sup> Relative intensity

CENTRAL LIBRARY  
I. I. T. KANPUR

Acc. No. A. 117955

ring proton  $H^{4'}$  would experience similar effects since they are almost the same distance from the iron center. We tentatively assign the most downfield resonances due to pyridine  $H^3$  and  $H^5$  protons and the other left one is due to pyrazole  $H^{4'}$  proton.

The singlet nature of all the pyridine and pyrazole ring proton resonances is consistent with two equivalent chelate rings, reflecting grossly octahedral symmetry of these high-spin iron(II) complexes in  $CD_3CN$  solution. However, the occurrence of two methylene proton resonances is indicative of a nonplanar chelate ring conformations as observed in the solid-state structures of  $[Fe(H_2Me_2bpp)_2](ClO_4)_2$  (Chapter 3) and  $[Ni(H_4bpp)_2](ClO_4)_2$ .<sup>114</sup>

An octahedral high-spin Fe(II) generally give rise to<sup>140</sup> both contact and dipolar contributions to isotropic shifts (i.e., the observed chemical shift minus a reference diamagnetic shift). The resonance for 3' protons (methyl groups) would also be the broadest signal if the dipolar interactions were primarily responsible for the line broadening. At this level of available experimental results we cannot elucidate the relative contributions of  $\sigma$ - and  $\pi$ -spin delocalization mechanism in these complexes.

#### 2.4.1.3 Absorption Spectra

The spectra of the iron(II) complexes in MeCN solutions have two weak broad bands in the near-IR region (780-970 nm) assignable as d-d transitions (Figure 2.6, Table 2.5). These bands are considered to arise from the  $^5T_2 \rightarrow ^5E$  transition of high-spin octahedral iron(II). These split bands are due to<sup>142,143</sup>

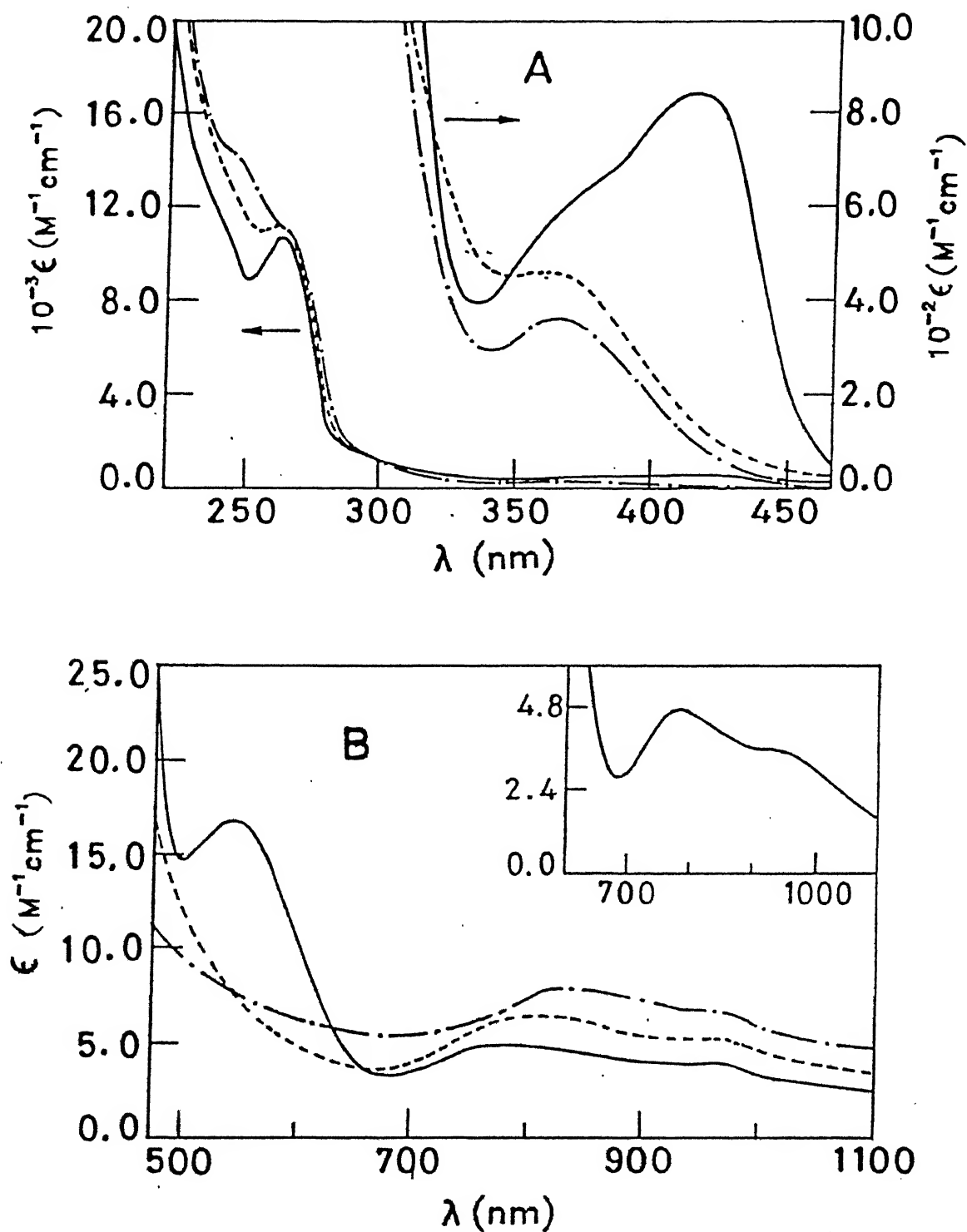


Figure 2.6 Electronic spectra of  $[\text{Fe}(\text{H}_4\text{bpp})_2](\text{ClO}_4)_2 \cdot \text{H}_2\text{O}$  (—),  $[\text{Fe}(\text{H}_2\text{Me}_2\text{bpp})_2](\text{ClO}_4)_2 \cdot 2\text{H}_2\text{O}$  (---), and  $[\text{Fe}(\text{Me}_4\text{bpp})_2](\text{ClO}_4)_2 \cdot 2\text{H}_2\text{O}$  (-.-) in MeCN (A) High energy region (B) Low energy region. Inset shows expansion for  $\text{Fe}(\text{H}_4\text{bpp})_2^{2+}$  in the

a combination of a dynamic Jahn-Teller effect in the electronic excited states and the lowering of metal site symmetry. In fact, the  $\text{Fe}^{\text{II}}\text{N}_6$  coordination sphere has a distorted octahedral geometry (Section 2.4.1.2). The spectral behavior observed in this work is well documented<sup>43,144-146</sup> in the case of most high-spin six-coordinate complexes of iron(II). The energy of these bands increases in the order  $[\text{Fe}(\text{H}_4\text{bpp})_2]^{2+} > [\text{Fe}(\text{H}_2\text{Me}_2\text{bpp})_2]^{2+} > [\text{Fe}(\text{Me}_4\text{bpp})_2]^{2+}$  (Figure 2.6, Table 2.5). This clearly demonstrates a monotonous decrease in the strength of the ligand fields as the number of methyl groups near the donor atom increases. The complex  $[\text{Fe}(\text{H}_4\text{bpp})_2]^{2+}$  exhibits an additional ligand field band at  $\sim 540$  nm. The origin of which is not clearly known to us.

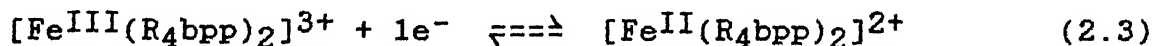
The iron(II) complexes exhibit metal-to-ligand charge transfer (MLCT) transitions in addition to the ligand field transitions (Figure 2.6, Table 2.5). Moderately intense bands are seen in the range 360-370 nm. We find that increasing the inclination of the pyrazole meanplanes to the pyridine meanplane on passing the ligands from  $\text{H}_4\text{bpp} \rightarrow \text{H}_2\text{Me}_2\text{bpp} \rightarrow \text{Me}_4\text{bpp}$  has only a small effect on the energy of the MLCT absorption. A closer examination of the values of molar extinction coefficients reveals that the values decrease with an increase in the number of methyl groups in the ligands. We think that a different "bite" of a 565 tridentate heterocyclic ligand and associated changes in metal-ligand orbital overlaps is likely the reason behind this effect. Apparently the overlap between Fe(II) (donor) and pyrazole/pyridine (acceptor) orbitals is relatively small (Chapter 3) to allow appreciable intensity for the MLCT transition in the absence of mixing with available low-energy  $\pi \rightarrow \pi^*$  transitions.



Interestingly, the complex  $[\text{Fe}(\text{H}_4\text{bpp})_2]^{2+}$  exhibits an additional MLCT transition at 415 nm (the origin of this transition has been considered in Chapter 4). Intraligand transitions are also observed at still higher energies.

#### 2.4.1.4 Electrochemistry

To investigate the effect of incorporating substituents into the two pyrazole rings on the  $\text{Fe}^{\text{III}}/\text{Fe}^{\text{II}}$  redox potentials of these high-spin iron(II) bis-ligand complexes, cyclic voltammetry was utilized. In acetonitrile solutions all the complexes undergo reversible electron-transfer reactions (Equation 2.3) at high potentials (Figure 2.7, Table 2.7).



The electron stoichiometry was identified by comparing the current heights of  $[\text{Fe}(\eta\text{-C}_5\text{H}_5)_2]^+ / [\text{Fe}(\eta\text{-C}_5\text{H}_5)_2]$  redox process. The peak-to-peak separations ( $\Delta E_p$ ) are characteristic of reversible  $1\text{e}^-$  transfer in equation 2.3 (Table 2.7).

The trend in the formal potentials of  $[\text{Fe}(\text{H}_2\text{Me}_2\text{bpp})_2]^{2+}$  and  $[\text{Fe}(\text{Me}_4\text{bpp})_2]^{2+}$  is completely unexpected as one would predict values less positive for the methyl substituted complex than the unsubstituted complex based on the electron releasing properties of methyl substituents (Figure 2.7, Table 2.7).

The observed opposite effect can be rationalized by considering the predominance of steric crowding at the 3-position(s) over the electronic contribution prevailing at the 5-position(s) in the ligands  $\text{H}_2\text{Me}_2\text{bpp}$  and  $\text{Me}_4\text{bpp}$ . If two methyl groups replace the hydrogens in the 3-positions of two pyrazole

Table 2.7: Electrochemical Data<sup>a,b</sup> of Fe<sup>III</sup>/Fe<sup>II</sup> Couple in MeCN

Compound	$E_{pa}(V)$	$E_{pc}(V)$	$E_f(V)$	$\Delta E_p$	$E_p(DPV)(V)$
$[Fe(H_4bpp)_2](ClO_4)_2 \cdot 2H_2O$	1.10	1.02	1.06	80	1.06
$[Fe(H_2M_2bpp)_2](ClO_4)_2 \cdot 2H_2O$	1.20	1.12	1.16	80	1.16
$[Fe(Me_4bpp)_2](ClO_4)_2 \cdot 2H_2O$	1.26	1.18	1.22	80	1.21

<sup>a</sup> $E_p(DPV) = E_f - \Delta E/2$ . Meaning of the other symbols given in text.

<sup>b</sup>Scan rate: 50 mV s<sup>-1</sup> (for cyclic voltammetry) and 5 mV s<sup>-1</sup> (for DPV); platinum working electrode; reference electrode SCE; supporting electrolyte, TBAP; drop time 0.5 s; modulation amplitude,  $\Delta E = 25$  mV.

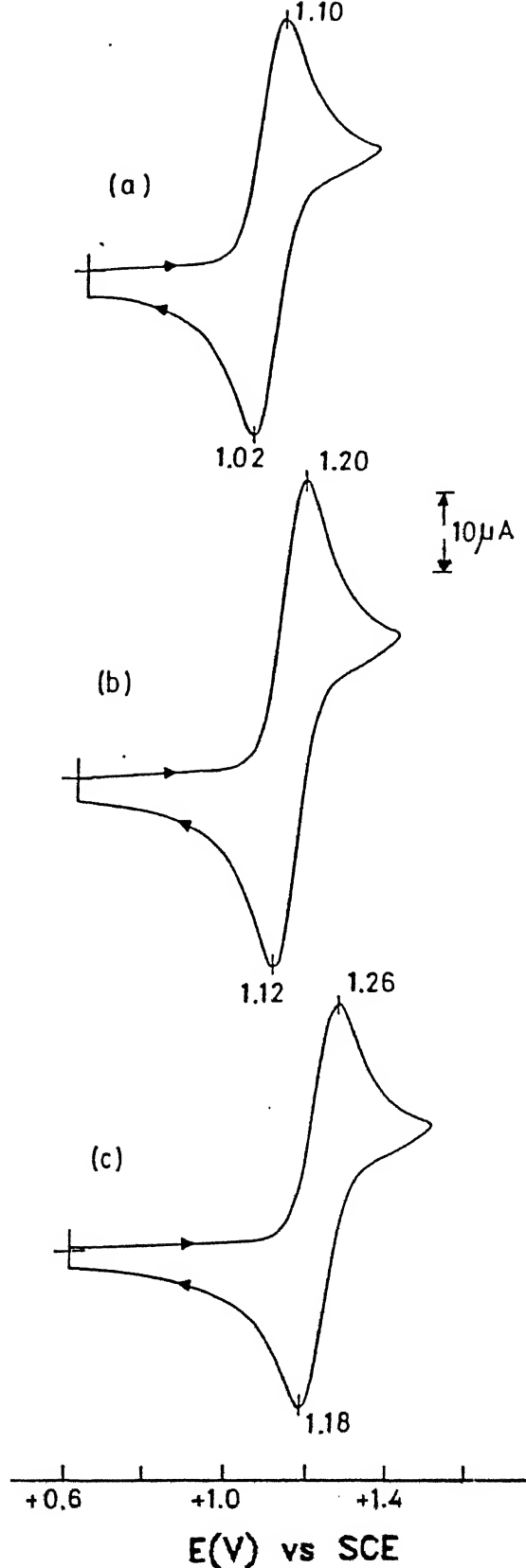


Figure 2.7 Cyclic voltammograms of (a)  $[\text{Fe}(\text{H}_4\text{bpp})_2]^{2+}$  (b)  $[\text{Fe}(\text{H}_2\text{Me}_2\text{bpp})_2]^{2+}$  and (c)  $[\text{Fe}(\text{Me}_4\text{bpp})_2]^{2+}$  in MeCN at a platinum electrode; scan rate 50 mV s<sup>-1</sup>

rings, some crowding between the two methyl groups occurs with a resulting tilt of the two pyrazole rings in the nonplanar ligand superstructure (Section 2.4.1.2). This causes a less favorable orientation of the coordinating nitrogen atoms and thus may make  $\text{H}_2\text{Me}_2\text{bpp}$  and  $\text{Me}_4\text{bpp}$  poorer donors overall than  $\text{H}_4\text{bpp}$  (Section 2.4.1.3) even though the 3-Me groups are electron donating. As the methyl substituents at the 5-positions are farther away from the donor site they are expected to contribute only the electronic effect.

Electrochemical studies have been made<sup>38</sup> on sterically hindered  $\text{CuN}_4$  complexes of tripodal ligands. The ligands used were tris[2-(1-pyrazolyl)ethyl]amine and its 3,5-dimethylpyrazolyl and 3,5-di-~~tert~~-butylpyrazolyl derivatives. The unusual electrochemical result like ours was rationalized as a result of pronounced environmental effects. The geometrical preference is not a priori in the iron(III) and iron(II) oxidation states but it is<sup>147</sup> in copper(II) and copper(I) oxidation states. Thus unusual electrochemical behavior in our complexes demands special attention.

The paucity of  $\text{Fe}^{\text{III}}/\text{Fe}^{\text{II}}$  redox potentials in high-spin iron(II) complexes having  $\text{Fe}^{\text{II}}\text{N}_6$  coordination sphere limit us to compare our  $E_f$  values with other systems. The iron(II) oxidation state in  $[\text{Fe}(\text{H}_4\text{bpp})_2]^{2+}$  is stabilized by more than 100 mV<sup>117</sup> compared to  $[\text{Fe}(\text{py})_3\text{tren}]^{2+}$  {(py)<sub>3</sub>tren = tris[4-(2-pyridyl)-3-aza-3-butenyl]amine} and ~200 mV<sup>127</sup> compared to the complex using hydrotris(3-phenylpyrazol-1-yl)borate as ligand having identical coordination sphere and spin-state.

## 2.4.2 Bis Chelates of Nickel(II) with $\text{NiN}_6$ Coordination

The nickel(II) complexes  $[\text{Ni}(\text{H}_4\text{bpp})_2]^{2+}$ ,  $[\text{Ni}(\text{H}_2\text{Me}_2\text{bpp})_2]^{2+}$ , and  $[\text{Ni}(\text{Me}_4\text{bpp})_2]^{2+}$  were chosen for a better evaluation of the magnitude of the ligand field splitting parameter  $10Dq$ .

### 2.4.2.1 Synthesis and Characterization of $[\text{Ni}(\text{R}_4\text{bpp})_2]^{2+}$ complexes

The bis-ligand complexes were readily obtained when ethanolic solution of the ligands and aqueous solution of nickel(II) perchlorate were mixed. The complexes are blue colored crystalline solids.

The nickel(II) complexes are highly soluble in polar organic solvents. In MeCN solutions they show the expected<sup>138</sup> 1:2 electrolytic behavior (Table 2.8). Measurements of susceptibilities in MeCN solutions (Evans' method)<sup>131</sup> of the nickel complexes,  $[\text{Ni}(\text{R}_4\text{bpp})_2]^{2+}$  gave the effective magnetic moments,  $\mu_{\text{eff}} \sim 3.00 \mu_B$  (Table 2.8).

### 2.4.2.2 Absorption Spectra

The absorption spectral results of nickel(II) bis-chelates in acetonitrile solution are in Tables 2.8 and the spectra of  $[\text{Ni}(\text{R}_4\text{bpp})_2]^{2+}$  ( $\text{R}=\text{H}, \text{Me}$ ) are shown in Figure 2.8. The spectra of the nickel(II) complexes consist of two principal crystal field bands,  ${}^3\text{A}_{2g} \rightarrow {}^3\text{T}_{2g} (\nu_1)$  and  ${}^3\text{A}_{2g} \rightarrow {}^3\text{T}_{1g}(\text{F}) (\nu_2)$ . The low energy transitions are more or less symmetrical revealing that the bonding geometry about the central nickel atom (symmetrical octahedral) observed in the solid state structure<sup>114</sup> of  $[\text{Ni}(\text{H}_4\text{bpp})_2](\text{ClO}_4)_2$  is retained in solution. The  ${}^3\text{A}_{2g} \rightarrow {}^3\text{T}_{2g}$  transitions are observed at 868 nm, 903 nm, and 932 nm for  $[\text{Ni}(\text{H}_4\text{bpp})_2]^{2+}$ ,  $[\text{Ni}(\text{H}_2\text{Me}_2\text{bpp})_2]^{2+}$ , and  $[\text{Ni}(\text{Me}_4\text{bpp})_2]^{2+}$  respec-

**Table 2.8:** Molar Conductance, Magnetic Moment and Electronic Spectral Data of Nickel(II) Complexes in MeCN at 298 K.

Compound	$\Lambda_M(\Omega^{-1}\text{cm}^2\text{mol}^{-1})^a$	$\mu_{\text{eff}}(\text{B.M.})^b$	$\lambda, \text{nm} (\epsilon, \text{M}^{-1}\text{cm}^{-1})$
$[\text{Ni}(\text{H}_4\text{bpp})_2](\text{ClO}_4)_2$	282	2.99	868 (9), 538 (11), 272 (sh) (7 050), 265 (9 400), 224 (13 900)
$[\text{Ni}(\text{H}_2\text{Me}_2\text{bpp})_2](\text{ClO}_4)_2$	275	-	903 (10), 556 (sh) (25), 378 (sh) (268), 266 (10 100), 218 (24 250)
$[\text{Ni}(\text{Me}_4\text{bpp})_2](\text{ClO}_4)_2$	281	2.96	932 (11), 583 (15), 370 (sh) (33), 265 (9 900), 223 (11 600)

<sup>a</sup>Expected range for 1:2 electrolyte, 220-300  $\Omega^{-1}\text{cm}^2\text{mol}^{-1}$ .

<sup>b</sup>Measured in MeCN using Evans' method.

**Table 2.9:** Visible Spectral Data for the Nickel(II) Complexes in MeCN at 298 K

Compound	${}^3\text{T}_{2g} \leftarrow {}^3\text{A}_{2g}$		${}^3\text{T}_{1g}(\text{F}) \leftarrow {}^3\text{A}_{2g}$		$Dq, \text{cm}^{-1}$	$B, \text{cm}^{-1}$
	$\lambda, \text{nm}$	$\epsilon, \text{M}^{-1}\text{cm}^{-1}$	$\lambda, \text{nm}$	$\epsilon, \text{M}^{-1}\text{cm}^{-1}$		
$[\text{Ni}(\text{H}_4\text{bpp})_2](\text{ClO}_4)_2$	868	9	538	11	1152	976
$[\text{Ni}(\text{H}_2\text{Me}_2\text{bpp})_2](\text{ClO}_4)_2$	903	10	556(sh)	25	1107	987
$[\text{Ni}(\text{Me}_4\text{bpp})_2](\text{ClO}_4)_2$	932	11	583	15	1073	853

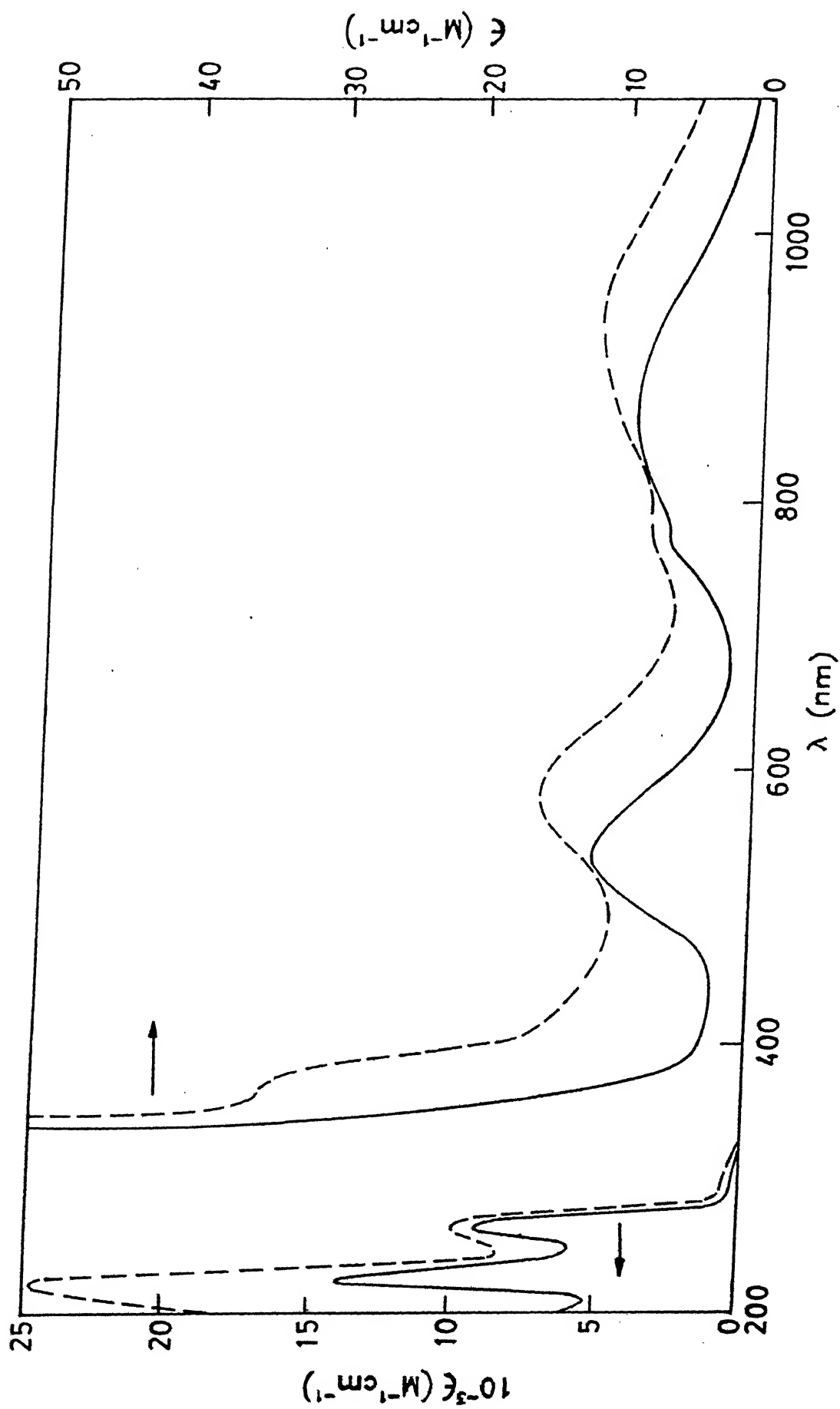


Figure 2.8 Electronic spectra of  $[\text{Ni}(\text{H}_4\text{bpp})_2](\text{ClO}_4)_2$  (—) and  $[\text{Ni}(\text{Me}_4\text{bpp})_2](\text{ClO}_4)_2$  (---) in MeCN

tively (Tables 2.8 and 2.9). From the energies of the transitions the values for the ligand field splitting parameter  $Dq$  are estimated as  $1152\text{ cm}^{-1}$ ,  $1107\text{ cm}^{-1}$ , and  $1073\text{ cm}^{-1}$  for ligands  $H_4bpp$ ,  $H_2Me_2bpp$ , and  $Me_4bpp$  respectively. A most interesting result of the spectral study is the gradual  $\sim 790\text{ cm}^{-1}$  reduction in  $10Dq$  value in going from  $[Ni(H_4bpp)_4]^{2+}$  to  $[Ni(Me_4bpp)_4]^{2+}$  complex. The iron complexes give rise to similar trend (Section 2.4.1.2). Such an effect is clearly not explainable on the basis of electronic effects, and is best attributed to the steric effect of methyl groups adjacent to the donor atom. This behavior has been noted previously<sup>116</sup> for other nickel(II) complexes having  $NiN_6$  coordination sphere. Examination of molecular models provides some support for a steric interpretation (interligand repulsion) that would cause an increase in the metal-ligand bond distance with an accompanying decrease in ligand field strength.

The highest energy transition,  $^3A_{2g} \rightarrow ^3T_{1g}(P)$  ( $\nu_3$ ) is obscured by the intraligand absorptions for  $[Ni(H_4bpp)_2]^{2+}$  and  $[Ni(H_2Me_2bpp)_2]^{2+}$ , but a shoulder is observed in the case of  $[Ni(Me_4bpp)_2]^{2+}$ . Considering the following equations<sup>148</sup> the Racah interelectronic repulsion parameter,  $B$  was calculated to be 976, 987, and  $853\text{ cm}^{-1}$  for  $H_4bpp$ ,  $H_2Me_2bpp$ , and  $Me_4bpp$  respectively (Table 2.9).

$$\nu_1 = 10Dq \quad (2.4)$$

$$\nu_2 = 7.5B + 15Dq - \frac{1}{2}(225B^2 + 100Dq^2 - 180Dq.B)^{\frac{1}{2}} \quad (2.5)$$

$$\nu_3 = 7.5B + 15Dq + \frac{1}{2}(225B^2 + 100Dq^2 - 180Dq.B)^{\frac{1}{2}} \quad (2.6)$$



In addition to the three spin-allowed transitions, a spin-forbidden transition  ${}^3A_{2g} \rightarrow {}^1E_g(D) (\gamma')$  is located at  $13\,000\text{ cm}^{-1}$ . Using the values of  $Dq$  and  $B$ ,  ${}^3A_{2g} \rightarrow {}^3T_{1g} (P)$  transition ( $\gamma_3$ ) is predicted to be  $23\,294\text{ cm}^{-1}$  (for  $H_4bpp$ ),  $26\,455\text{ cm}^{-1}$  (for  $H_2Me_2bpp$ ) and  $27\,837\text{ cm}^{-1}$  (for  $Me_4bpp$ ).

#### 2.4.2.3 ${}^1H$ NMR spectra

An attempt was made to determine the coordination geometry of  $[Ni(R_4bpp)_2]^{2+}$  ( $R = H, Me$ ) in  $CD_3CN$  by means of  ${}^1H$  NMR spectroscopy. The complexes give rise to paramagnetically shifted resonances ranging from  $+60$  to  $-20$  ppm relative to TMS (Figure 2.9). Assignments of the resonances (Table 2.10) are made by comparison with the available data on coordinated pyridine ring proton resonances,<sup>119,149-151</sup> as well as the spectra of  $[Fe(R_4bpp)_2]^{2+}$  ( $R = H, Me$ ).

Since octahedrally coordinated nickel(II) complexes are magnetically isotropic, the observed isotropic shifts can be attributed predominantly to contact interactions. On this basis the isotropic shifts should provide direct evidence of the mechanism of spin delocalization in  $[Ni(H_4bpp)_2]^{2+}$  and  $[Ni(Me_4bpp)_2]^{2+}$  complexes. The contact shifts observed for the pyridine protons reflect the dominance of a  $\sigma$ -delocalization mechanism<sup>140</sup>. Such a mechanism, cannot however explain the upfield shifts of the methylene protons. Nevertheless, it can be explained on the basis of an indirect spin-polarization mechanism.<sup>149,150</sup> According to this mechanism, spin density will alternate in sign along a  $\sigma$ -bonded network, starting from the donor atom which possesses positive spin. Nuclei experiencing

**Table 2.10: Proton NMR Chemical Shifts Relative to TMS for Nickel(II) Bis Chelates**

$[\text{Ni}(\text{H}_4\text{bpp})_2](\text{ClO}_4)_2$			$[\text{Ni}(\text{Me}_4\text{bpp})_2](\text{ClO}_4)_2$		
$\delta(\text{ppm})$	int <sup>a</sup>	assignment	$\delta(\text{ppm})$	int <sup>a</sup>	assignment
55.0	4	H <sup>3</sup> , H <sup>5</sup>	49.5	4	H <sup>3</sup> , H <sup>5</sup>
47.0	4	H <sup>4'</sup>	43.5	4	H <sup>4'</sup>
44.5	4	H <sup>5'</sup>	19.6	2	H <sup>4</sup>
32.0	4	H <sup>3'</sup>	-1.0	12	Me <sup>5'</sup>
17.6	2	H <sup>4</sup>	-4.5	4	CH <sub>2</sub>
- 5.5	4	CH <sub>2</sub>	-7.0	12	Me <sup>3'</sup>
-10.5	4	CH <sub>2</sub>	-10.0	4	CH <sub>2</sub>

<sup>a</sup> Relative intensity

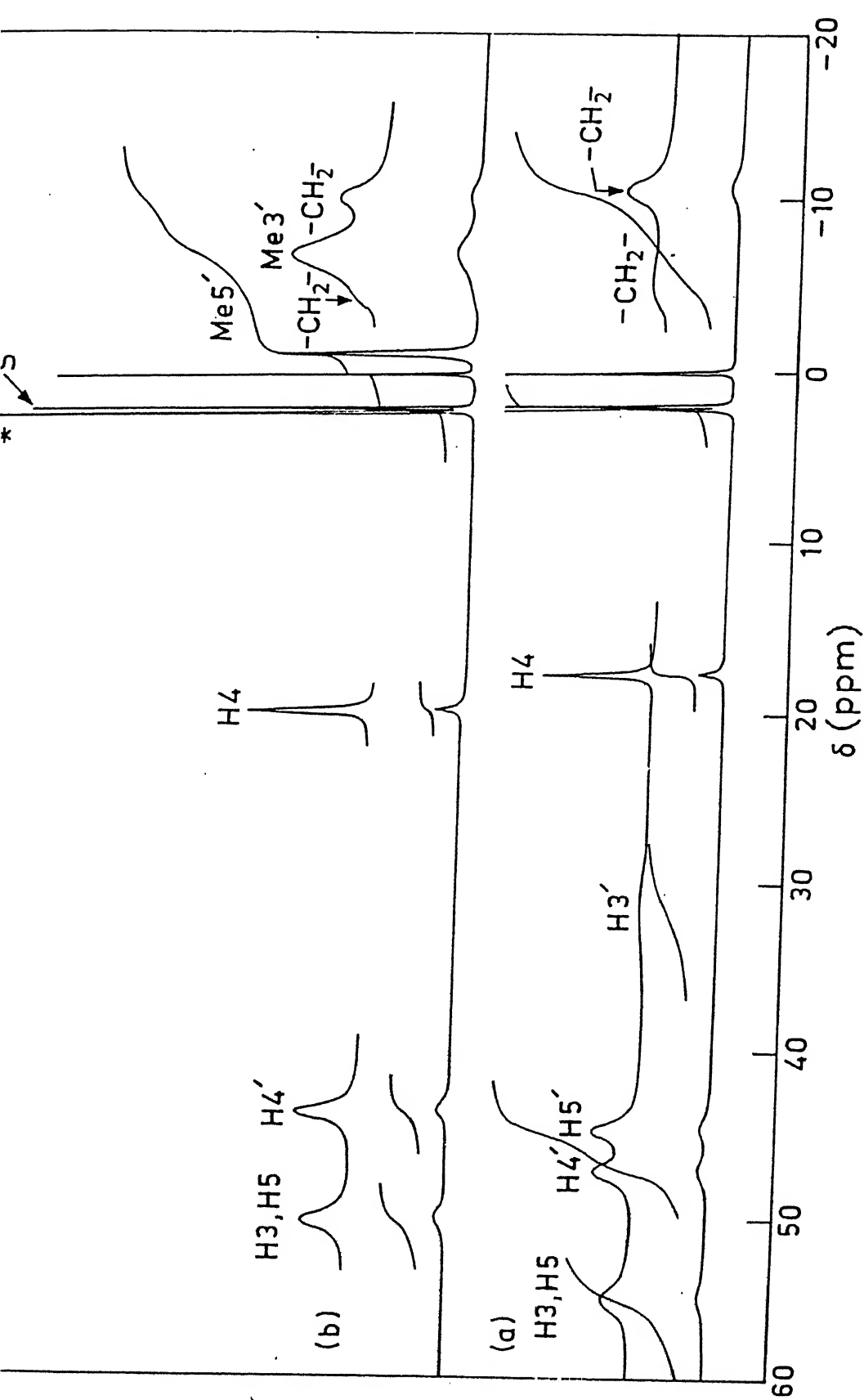


Figure 2.9 400 MHz  $^1\text{H}$  NMR spectra of (a)  $[\text{Ni}(\text{H}_4\text{bpp})_2](\text{ClO}_4)_2$  and (b)  $[\text{Ni}(\text{Me}_4\text{bpp})_2](\text{ClO}_4)_2$  in  $\text{CD}_3\text{CN}$  (solvent and water peaks marked by  $S$  and  $*$  respectively).

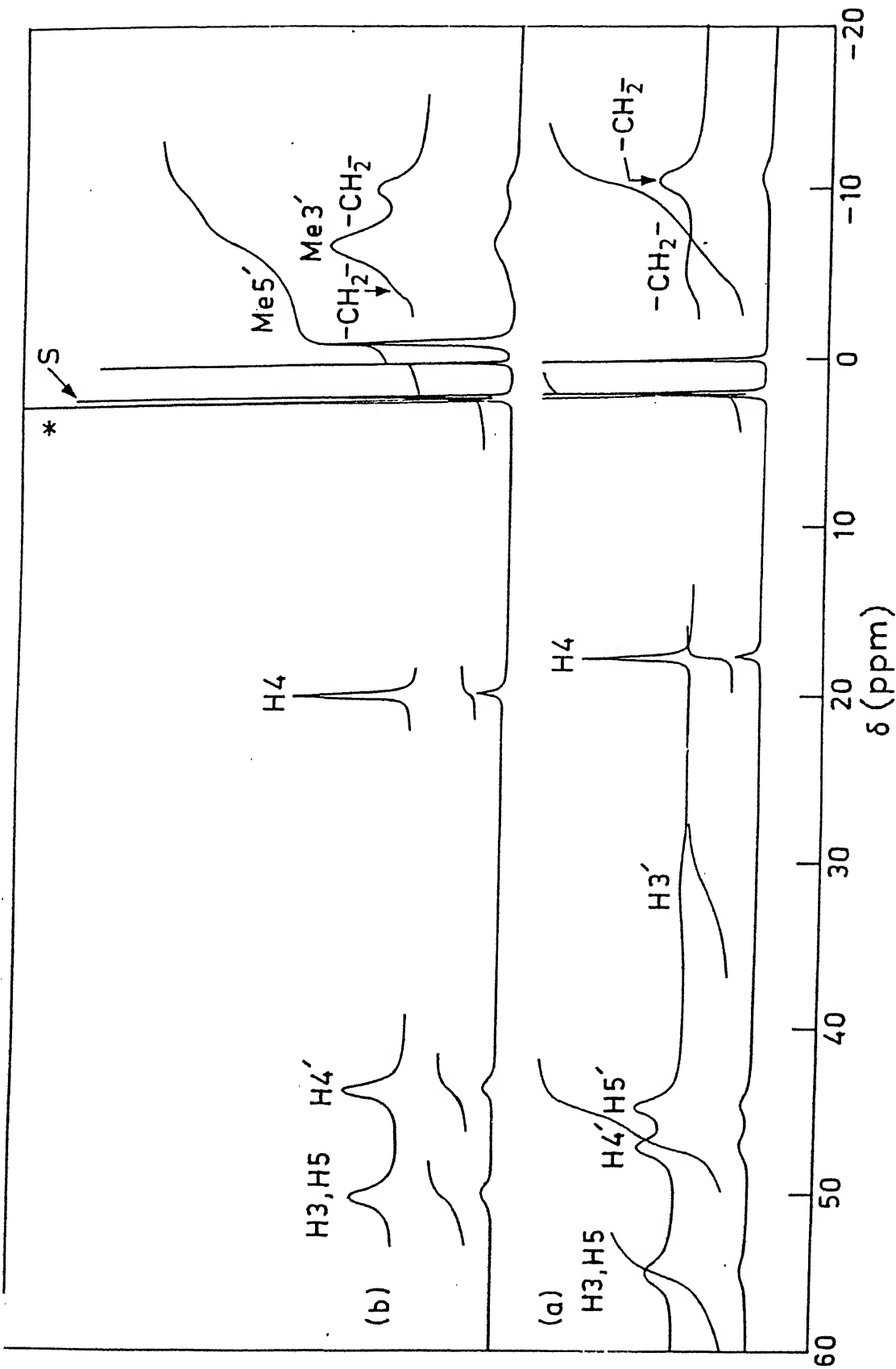


Figure 2.9 400 MHz  $^1\text{H}$  NMR spectra of (a)  $[\text{Ni}(\text{H}_4\text{bpp})_2](\text{ClO}_4)_2$  and (b)  $[\text{Ni}(\text{Me}_4\text{bpp})_2](\text{ClO}_4)_2$  in  $\text{CD}_3\text{CN}$  (solvent and water peaks marked by  $S$  and  $*$  respectively).

positive spin density will exhibit low field chemical shift. By contrast the nuclei with negative spin density display upfield shifts. Other broad upfield resonances in the spectrum of  $[\text{Ni}(\text{Me}_4\text{bpp})_2]^{2+}$  are assigned to the pyrazole 3- and 5- methyl proton resonances. Such shifts are probably due to interaction of the methyl protons of one pyrazole ring with the  $\pi$  network of the other adjacent ring resulting in significant shielding.<sup>119,149,150</sup> As expected, the resonance for the pyrazole  $\text{H}^3$  proton is very broad in the spectrum of  $[\text{Ni}(\text{H}_4\text{bpp})_2]^{2+}$ . Since  $\text{H}_4\text{bpp}$  and  $\text{Me}_4\text{bpp}$  do not possess low-lying vacant orbitals (Section 2.4.5.2), it is not expected that the observed shifts would be indicative of  $\pi$ -delocalization mechanism.

The observed single set of resonances for all the pyridine and pyrazole proton resonances is indicative of two equivalent chelate rings and this reflects a grossly octahedral symmetry of the complexes in solution (Section 2.4.1.2). However, the doublet feature for the methylene proton resonances is consistent with a nonplanar chelate ring conformations as in the solid state structure<sup>114</sup> of  $[\text{Fe}(\text{H}_2\text{Me}_2\text{bpp})_2]^{2+}$  (Chapter 3),  $[\text{Ni}(\text{H}_4\text{bpp})_2]^{2+}$  as well as in the  $^1\text{H}$  NMR spectra of  $[\text{Fe}(\text{R}_4\text{bpp})_2]^{2+}$  ( $\text{R} = \text{H}$  and  $\text{Me}$ ).

#### 2.4.3 Bis Chelates of Cobalt(II) with $\text{CoN}_6$ Coordination

As cobalt(II) complexes are expected to exhibit ligand field transitions and are also capable of providing well defined redox behavior, we have chosen cobalt(II) bis chelates for further substantiation of the predominance of steric over electronic effect.

#### 2.4.3.1 Synthesis and Selected Properties

The synthetic method reported herein for the preparation of  $[\text{Co}(\text{R}_4\text{bpp})_2](\text{ClO}_4)_2$  is relatively straight forward. The reaction of  $\text{CoCl}_2 \cdot 4\text{H}_2\text{O}$  or  $\text{Co}(\text{ClO}_4)_2 \cdot 6\text{H}_2\text{O}$  with the appropriate tridentate ligand in aqueous ethanol, affords complexes with 1:2 metal-to-ligand ratio having the general formula  $[\text{Co}(\text{R}_4\text{bpp})_2](\text{ClO}_4)_2 \cdot \text{H}_2\text{O}$  (when  $\text{CoCl}_2 \cdot 4\text{H}_2\text{O}$  was used a saturated aqueous solution of  $\text{NaClO}_4 \cdot \text{H}_2\text{O}$  was added to isolate the desired product). The orange to pale yellow complexes are indefinitely stable in air. The complexes are 1:2 electrolytic<sup>138</sup> in MeCN solution (Table 2.11).

#### 2.4.3.2 Magnetic Susceptibility

Solution-state magnetic susceptibility measurements using Evans' method reveal that magnetic moments of  $[\text{Co}(\text{R}_4\text{bpp})_2]^{2+}$  are in the range 4.78-4.86  $\mu_B$ , which is within the accepted range of 4.7-5.2  $\mu_B$  for high-spin octahedral cobalt(II) complexes with a ground term  $^4T_{1g}$ .<sup>143</sup> The solid-state magnetic behavior of a representative complex  $[\text{Co}(\text{H}_4\text{bpp})_2](\text{ClO}_4)_2 \cdot \text{H}_2\text{O}$  has been examined as a function of temperature (8-300 K) and displayed in Figure 2.10. Unlike the behavior for corresponding iron(II) complex (Chapter 4) there is no indication for temperature-induced spin transition in this complex. The complex is uniformly high-spin ( $S=3/2$ ). The magnetic susceptibility of  $[\text{Co}(\text{H}_4\text{bpp})_2](\text{ClO}_4)_2 \cdot \text{H}_2\text{O}$  was found to adhere closely to the Curie-Weiss law ( $C = 3.38$  emu K/mol;  $\theta = -6.25$  K). Room-temperature solid-state magnetic moments of  $[\text{Co}(\text{R}_4\text{bpp})_2](\text{ClO}_4)_2 \cdot \text{H}_2\text{O}$  are in good agreement with the solution phase data. Variable temperature magnetic susceptibility data are given in Table 2.12.

**Table 2.11: Molar Conductance, Magnetic Moment and Electronic Spectral Data of Cobalt(II) Complexes in MeCN at 298 K.**

Compound	$\Lambda_M (\Omega^{-1} \text{cm}^2 \text{mol}^{-1})^a$	$\mu_{\text{eff}} (\text{B.M.})$	$\lambda, \text{nm} (\epsilon, \text{M}^{-1} \text{cm}^{-1})$
$[\text{Co}(\text{H}_4\text{bpp})_2](\text{ClO}_4)_2 \cdot \text{H}_2\text{O}$	270	4.78 <sup>b</sup> (5.07) <sup>c</sup>	934 (11), 539 (sh) (11), 510 (sh) (18), 479 (26), 435 (sh) (21), 302 (sh) (1 670), 265 (11 100)
$[\text{Co}(\text{H}_2\text{Me}_2\text{bpp})_2](\text{ClO}_4)_2 \cdot \text{H}_2\text{O}$	260	4.86 <sup>b</sup>	992 (14), 655 (sh) (12), 545 (sh) (31), 485 (sh) (70), 308 (sh) (2 330), 265 (10 900)
$[\text{Co}(\text{Me}_4\text{bpp})_2](\text{ClO}_4)_2 \cdot \text{H}_2\text{O}$	263	4.80 <sup>b</sup> (5.20) <sup>c</sup>	1050 (11), 537 (sh) (16), 486 (31), 310 (sh) (2 400), 267 (11 600)

<sup>a</sup>Expected range for 1:2 electrolyte, 220-300  $\Omega^{-1} \text{cm}^2 \text{mol}^{-1}$ .

<sup>b</sup>Measured in MeCN using Evans' method.

<sup>c</sup>Room temperature solid state values in parentheses

**Table 2.12: Variable Temperature Magnetic Susceptibility Data  
for  $[\text{Co}(\text{H}_4\text{bpp})_2](\text{ClO}_4)_2 \cdot \text{H}_2\text{O}$**

T (K)	$\chi_M$ ( $\text{cm}^3\text{mol}^{-1}$ )	$1/\chi_M$ ( $\text{cm}^{-3} \text{mol}$ )	$\mu_{\text{eff}}(\text{B.M.})$
8.8	0.3650	2.738	5.07
11.8	0.2727	3.667	5.07
20.0	0.1636	6.113	5.12
40.0	0.0896	11.161	5.35
60.0	0.0624	16.026	5.47
80.0	0.0475	21.053	5.51
100.0	0.0382	26.178	5.53
120.0	0.0319	31.348	5.53
140.0	0.0271	36.900	5.44
160.0	0.0231	43.290	5.38
180.0	0.0201	49.751	5.38
200.0	0.0182	54.945	5.39
220.0	0.0161	62.112	5.32
240.0	0.0146	68.493	5.30
260.0	0.0132	75.758	5.24
280.0	0.0120	83.333	5.18
295.2	0.0111	90.090	5.12



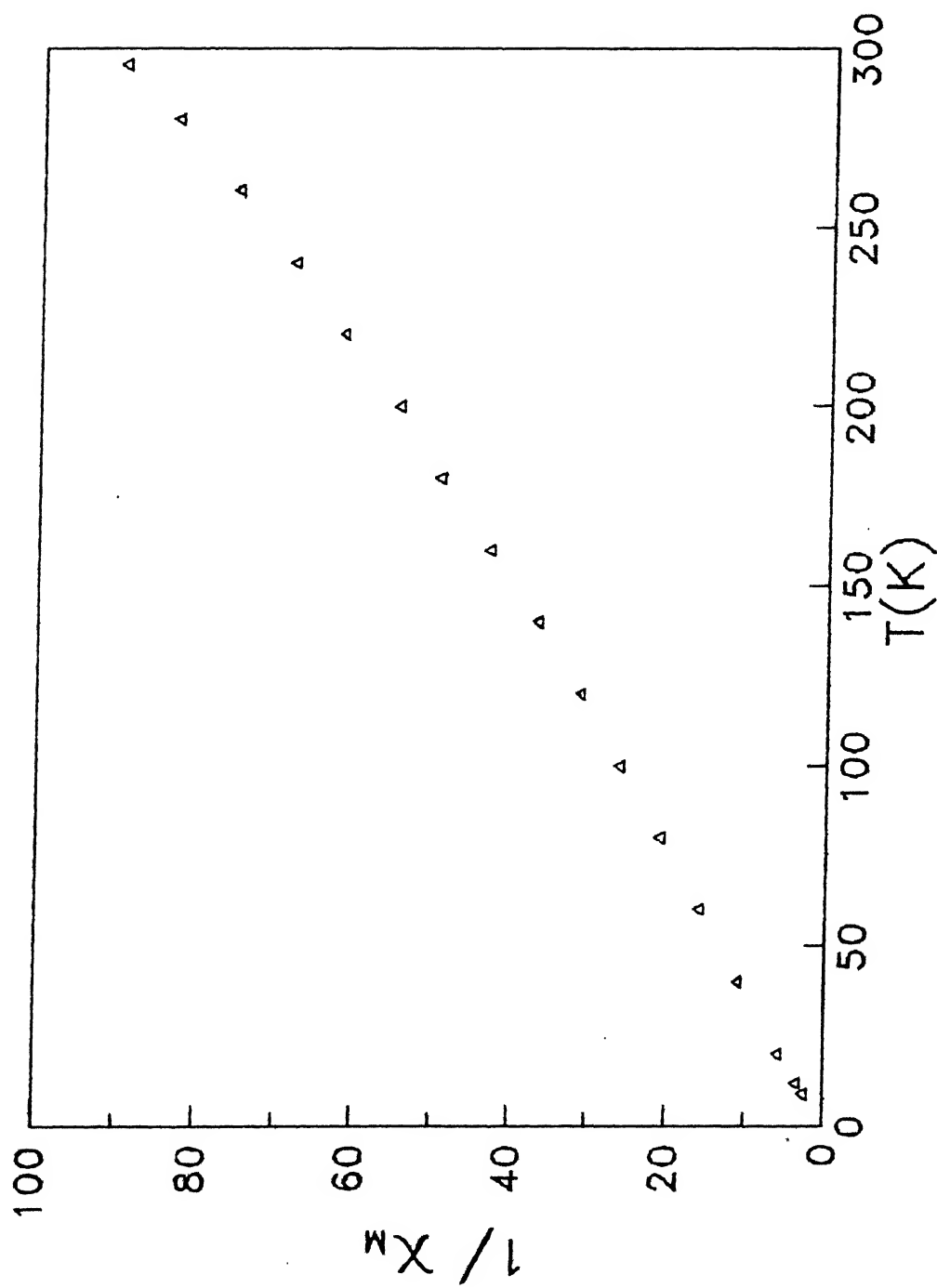


Figure 2.10 Inverse molar susceptibility of  $[\text{Co}(\text{H}_4\text{bpp})_2](\text{ClO}_4)_2 \cdot 2\text{H}_2\text{O}$  as a function of temperature

### 2.4.3.3 Ligand Field Spectra

The absorption spectral properties of these cobalt(II) complexes were examined in MeCN solutions and the behavior of  $[\text{Co}(\text{H}_4\text{bpp})_2]^{2+}$  is displayed in Figure 2.11 and data are presented in Table 2.11. The spectra of these complexes are similar to those observed for octahedral high-spin cobalt(II) complexes.<sup>143</sup> The comparatively low molar absorption coefficient of the bands of d-d origin also indicates octahedral coordination. Under the influence of an octahedral crystal field, it is expected that the free-ion terms ( $^4\text{F}$  and  $^4\text{P}$ ) split into  $^4\text{T}_{1\text{g}}(\text{F})$ ,  $^4\text{T}_{2\text{g}}$ ,  $^4\text{A}_{2\text{g}}$  and  $^4\text{T}_{1\text{g}}(\text{P})$  giving three spin-allowed transitions. In the present complexes the number of d-d transitions are more due to low symmetry in the ligand field component.

The d-d bands that are observed for octahedral Co(II) complexes occur as follows:  $\nu_1$  at 930-1050 nm ( $\epsilon \sim 10$ ) and  $\nu_2$  at 480-490 nm ( $\epsilon \sim 40$ ). Three spin-allowed d-d transitions are expected for octahedral Co(II) unless the field strength of the ligands is such that the  $^4\text{A}_{2\text{g}}$  and  $^4\text{T}_{1\text{g}}(\text{P})$  terms have the same energy. Typical values of  $\nu_1$ ,  $\nu_2$ , and  $\nu_3$  for octahedral cobalt(II) are 8 000, 20 000 and 22 000  $\text{cm}^{-1}$  respectively. The assignment of  $\nu_1$  to the  $^4\text{T}_{1\text{g}}(\text{F}) \rightarrow ^4\text{T}_{1\text{g}}(\text{F})$  transition is unequivocal; however, depending upon the  $\text{Dq/B}$  ratio,  $\nu_2$  may be either  $^4\text{T}_{1\text{g}}(\text{F}) \rightarrow ^4\text{T}_{1\text{g}}(\text{P})$  or  $^4\text{T}_{1\text{g}}(\text{F}) \rightarrow ^4\text{A}_{2\text{g}}$ . If the assignment is made as

$$\nu_1 : ^4\text{T}_{1\text{g}}(\text{F}) \rightarrow ^4\text{T}_{2\text{g}}(\text{F}) \quad 934 \text{ nm} \quad (2.7)$$

$$\nu_2 : ^4\text{T}_{1\text{g}}(\text{F}) \rightarrow ^4\text{T}_{1\text{g}}(\text{P}) \quad 479 \text{ nm} \quad (2.8)$$

where the energies are taken for  $[\text{Co}(\text{H}_4\text{bpp})_2]^{2+}$  complex, then

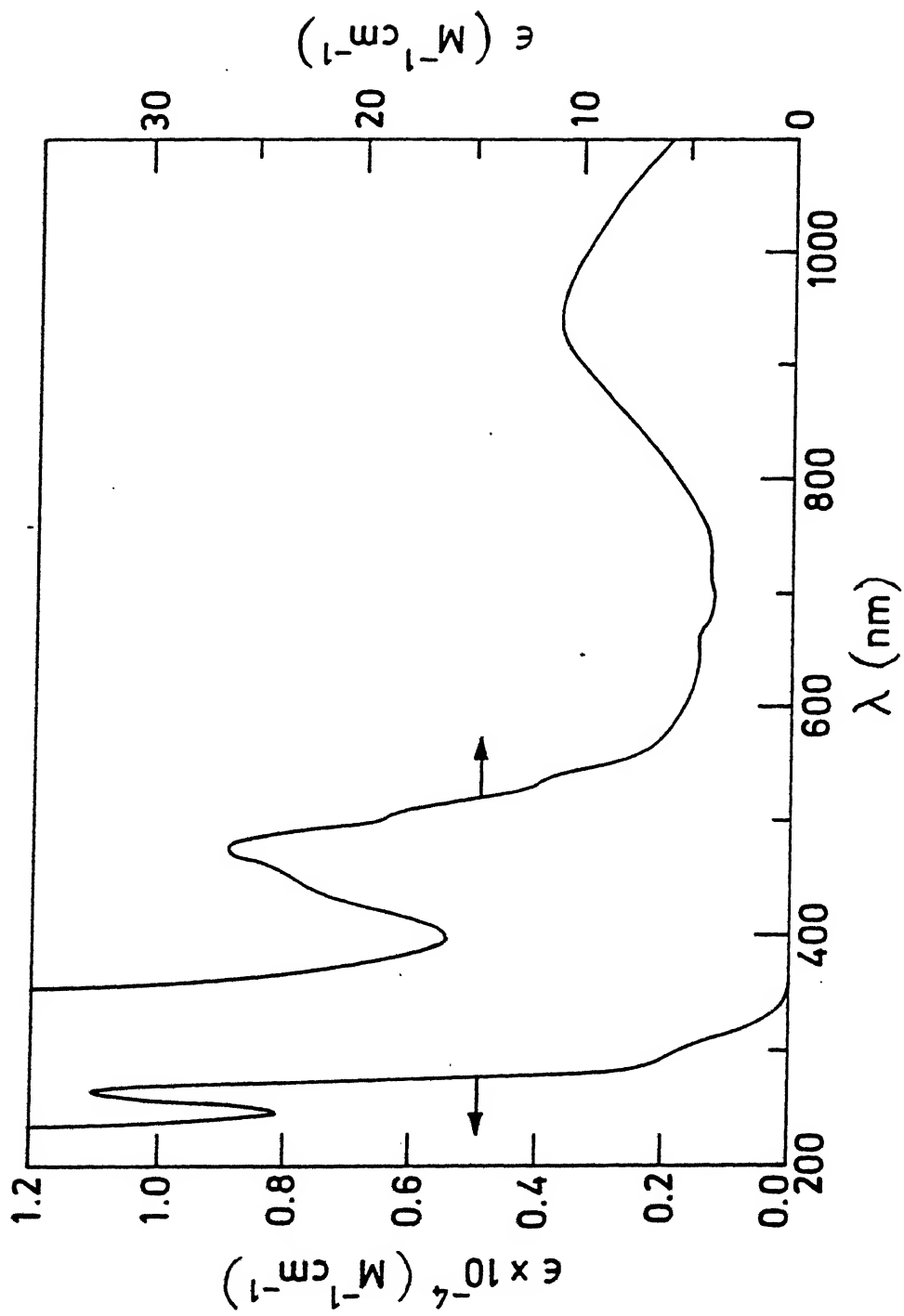


Figure 2.11 Electronic spectrum of  $[\text{Co}(\text{H}_4\text{bpp})_2](\text{ClO}_4)_2 \cdot 2\text{H}_2\text{O}$  in MeCN

spectral parameters can be calculated by using a Tanabe-Sugano<sup>152</sup> diagram. For a  $Dq/B$  ratio of 1.60,  $Dq$  and  $B$  were calculated as 1201 and 751  $\text{cm}^{-1}$  respectively. Similarly, for  $[\text{Co}(\text{H}_2\text{Me}_2\text{bpp})_2]^{2+}$  and  $[\text{Co}(\text{Me}_4\text{bpp})_2]^{2+}$  complexes  $Dq$  values were calculated as 1124 and 1076  $\text{cm}^{-1}$  respectively; and corresponding  $B$  values are 775 and 828  $\text{cm}^{-1}$  respectively (Table 2.13). From the above three complexes,  $B_{av}$  was calculated as 786  $\text{cm}^{-1}$ , which is approximately 70% of the free-ion value (1120  $\text{cm}^{-1}$ ).<sup>153</sup> This indicates ~30% covalent character in the metal-ligand bonds. A most interesting result emerging from the spectral analyses of  $[\text{Co}(\text{R}_4\text{bpp})_2]^{2+}$  is the gradual reduction in 10  $Dq$  values for  $\text{R}_4\text{bpp}$  ligands with cobalt(II) in the grossly octahedral coordination. We believe it is the increased steric crowding near donor site (3-methyl substituents) that progressively decreases the value of 10  $Dq$  due to interligand steric interactions. Similar effects were also observed in the iron(II) (Section 2.4.1) and nickel(II) (Section 2.4.2) complexes of these ligands.

#### 2.4.3.4 $^1\text{H}$ NMR Spectra

To extract structural information in these six-coordinated Co(II) ( $S=3/2$ ) complexes we have investigated the  $^1\text{H}$  NMR spectral properties of two representative bis complexes  $[\text{Co}(\text{H}_4\text{bpp})_2]^{2+}$  and  $[\text{Co}(\text{Me}_4\text{bpp})_2]^{2+}$ . Proton NMR spectra of  $[\text{Co}(\text{H}_4\text{bpp})_2]^{2+}$  and  $[\text{Co}(\text{Me}_4\text{bpp})_2]^{2+}$  in  $\text{CD}_3\text{CN}$  at 298 K are shown in Figure 2.12 and the chemical shifts are listed in Table 2.14. In the proton NMR spectra distinct peaks were observed in a wide range from +60 to -70 ppm and are also well separated. These two complexes are sufficient to establish the assignments given. The assignments

Table 2.13: Visible Spectral Data for the Cobalt(II) Complexes in MeCN at 298 K

Compound	${}^4T_{2g}(F) \leftarrow {}^4T_{1g}(F)$		${}^4T_{1g}(P) \leftarrow {}^4T_{1g}(F)$			
	$\lambda$ , nm	$\epsilon$ , $M^{-1}cm^{-1}$	$\lambda$ , nm	$\epsilon$ , $M^{-1}cm^{-1}$	$Dq$ , $cm^{-1}$	$B$ , $cm^{-1}$
$[Co(H_4bpp)_2](ClO_4)_2 \cdot H_2O$	934	11	479	26	1202	751
$[Co(H_2Me_2bpp)_2](ClO_4)_2 \cdot H_2O$	992	14	485(sh)	70	1124	775
$[Co(Me_4bpp)_2](ClO_4)_2 \cdot H_2O$	1050	11	486	31	1076	828

**Table 2.14:**  $^1\text{H}$  NMR Chemical Shifts Relative to TMS for High-spin Pseudooctahedral Cobalt(II) complexes

Compounds		Intensity	Assignments
$[\text{Co}(\text{H}_4\text{bpp})_2](\text{ClO}_4)_2 \cdot \text{H}_2\text{O}$	$[\text{Co}(\text{Me}_4\text{bpp})_2](\text{ClO}_4)_2 \cdot \text{H}_2\text{O}$		
62.2	63.8	4	$\text{H}^3, \text{H}^5$
60.4	82.0 <sup>a</sup>	4	$\text{CH}_2$
55.2	22.8	4, 12	$\text{H}$ or $\text{CH}_3$ ( $5'$ )
17.2	16.8	4	$\text{H}^{4'}$
-6.6	-28.8	4, 12	$\text{H}$ or $\text{CH}_3$ ( $3'$ )
-8.0	-3.2	4	$\text{CH}_2$
-10.2	-9.6	2	$\text{H}^4$

<sup>a</sup>Broad signal

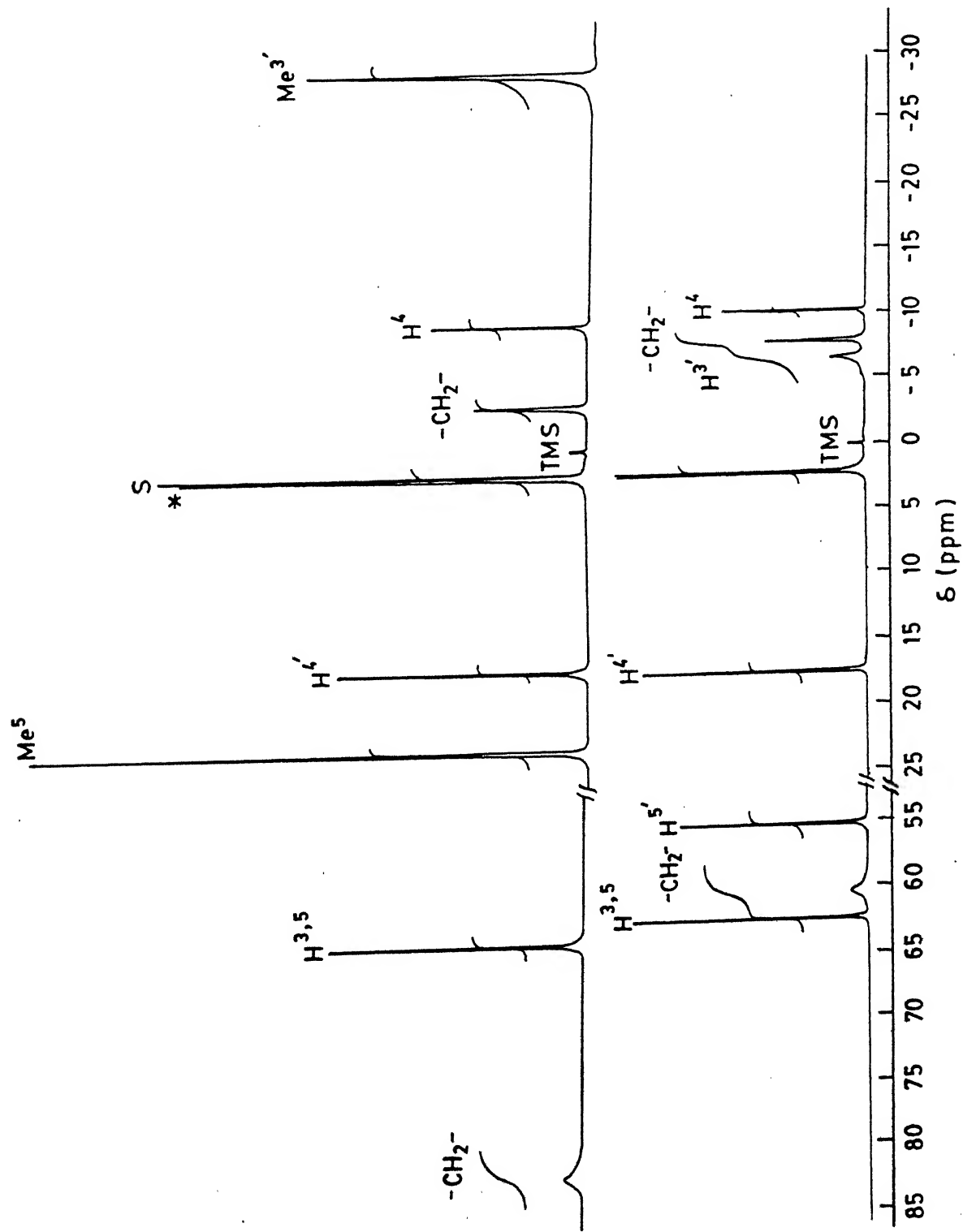


Figure 2.12 400 MHz  $^1\text{H}$  NMR spectra of (a)  $[\text{Co}(\text{H}_4\text{bpp})_2](\text{ClO}_4)_2 \cdot 2\text{H}_2\text{O}$  and (b)  $[\text{Co}(\text{Me}_4\text{bpp})_2](\text{ClO}_4)_2 \cdot 2\text{H}_2\text{O}$  in  $\text{CD}_3\text{CN}$  (solvent and water peaks marked by S and x respectively).

(Table 2.14) have been made on the basis of intensity, the effects of substitution of the methyl group for hydrogen, relative line widths and comparison with the spectra of related Fe(II) (Section 2.4.1.2) and Ni(II) (Section 2.4.2.2) complexes. Although the symmetry of the high-spin cobalt(II) complexes are found to be grossly octahedral in CD<sub>3</sub>CN solution, the occurrence of two methylene proton resonances is indicative of a nonplanar chelate ring conformations as observed for corresponding iron(II) and nickel(II) complexes. The <sup>1</sup>H NMR spectra as in Figure 2.12 have been reported very recently<sup>154</sup> utilizing cobalt(II) complexes of pyrazole-rich tridentate ligands.

#### 2.4.3.5 Redox Properties

Cyclic voltammetric studies using a Pt electrode gave an 1e<sup>-</sup> oxidative response in 0.2 M TBAP with  $i_{pc}/i_{pa} = 1.0$ . At a scan rate of 50 mV/s the peak differences were 80 mV, 100 mV, and 180 mV (Table 2.15) for [Co(H<sub>4</sub>bpp)<sub>2</sub>]<sup>2+</sup>, [Co(H<sub>2</sub>Me<sub>2</sub>bpp)<sub>2</sub>]<sup>2+</sup>, and [Co(Me<sub>4</sub>bpp)<sub>2</sub>]<sup>2+</sup> respectively. Thus the Co<sup>III</sup>/Co<sup>II</sup> couple is electrochemically reversible<sup>155</sup> for [Co(H<sub>4</sub>bpp)<sub>2</sub>]<sup>2+</sup> (Figure 2.13); however, the reversibility progressively decreases for [Co(H<sub>2</sub>Me<sub>2</sub>-bpp)<sub>2</sub>]<sup>2+</sup> and [Co(Me<sub>4</sub>bpp)<sub>2</sub>]<sup>2+</sup>. This is understandable given an incremental steric crowding at the Co<sup>II</sup>N<sub>6</sub> coordination unit on passing from [Co(H<sub>4</sub>bpp)<sub>2</sub>]<sup>2+</sup> to [Co(Me<sub>4</sub>bpp)<sub>2</sub>]<sup>2+</sup> which in turn causes a substantial structural change between the redox states Co<sup>II</sup> and Co<sup>III</sup> and hence the decrease in the reversibility. Interestingly, the  $E_f(E_{pa})$  values observed for the present complexes are at the highest end<sup>30,39,156-163</sup> amongst high-spin cobalt(II) complexes having CoN<sub>6</sub> coordination, known so far.



**Table 2.15:** Electrochemical Data<sup>a</sup> of Cobalt(II) Complexes in MeCN at 298 K

Compounds	$E_{pa}(V)$	$E_{pc}(V)$	$E_f(V)$	$\Delta E_p(mV)$
$[Co(H_4bpp)_2](ClO_4)_2 \cdot H_2O$	0.78	0.70	0.74	80
$[Co(H_2Me_2bpp)_2](ClO_4)_2 \cdot H_2O$	0.88	0.78	0.83	100
$[Co(Me_4bpp)_2](ClO_4)_2 \cdot H_2O$	1.06	0.97	- <sup>b</sup>	180

<sup>a</sup> Scan rate: 50 mV s<sup>-1</sup>; platinum working electrode; reference electrode SCE; supporting electrolyte, TBAP.

<sup>b</sup>  $\Delta E_p > 120$  mV.

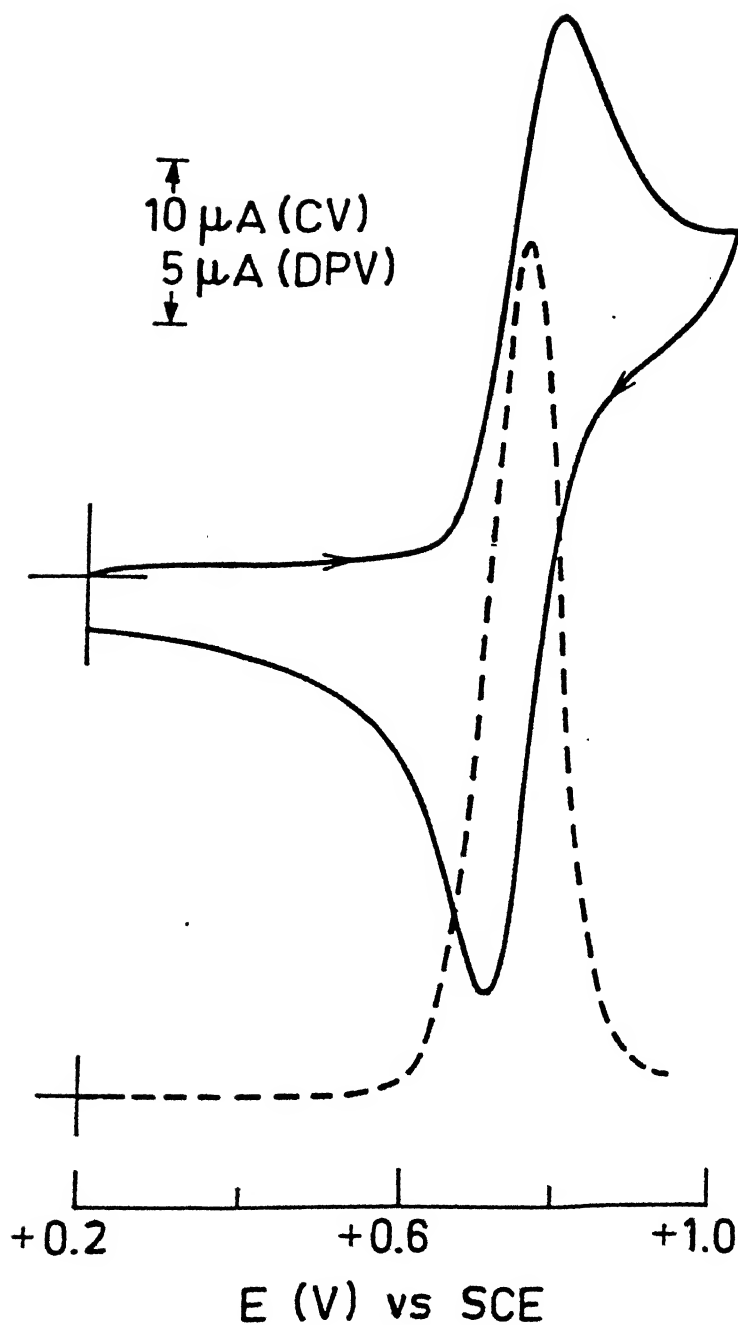


Figure 2.13;

Cyclic voltammogram (scan rate  $50 \text{ mV s}^{-1}$ ) and differential pulse voltammogram (scan rate  $5 \text{ mV s}^{-1}$ , modulation amplitude  $25 \text{ mV}$ , drop time  $0.5 \text{ s}$ ) of  $[\text{Co}(\text{H}_4\text{bpp})_2](\text{ClO}_4)_2 \cdot 2\text{H}_2\text{O}$  in MeCN at a platinum electrode; supporting electrolyte TBAP.

Since the observed oxidative responses are not reversible for all the three complexes, for the purpose of comparison the emphasis is given to the anodic peak potentials which are the potentials measured where the anodic peak current is at its maximum. The observed trend in the  $E_{pa}$  values of  $[\text{Co}(\text{H}_4\text{bpp})_2]^{2+}$  (0.78 V),  $[\text{Co}(\text{H}_2\text{Me}_2\text{bpp})_2]^{2+}$  (0.88 V), and  $[\text{Co}(\text{Me}_4\text{bpp})_2]^{2+}$  (1.06V) is similar to that encountered in the case of iron(II) bis chelates (Section 2.4.1.4). This unusual redox behavior further strengthens the argument of the predominance of steric effect caused by methyl substitution at the 3-position(s) over the electronic contribution at the 5-position(s) in the ligands  $\text{H}_2\text{Me}_2\text{bpp}$  and  $\text{Me}_4\text{bpp}$ .

#### 2.4.4 Mono and Bis Chelates of Manganese(II)

In order to generalize the observation of steric/electronic factors over the other in these systems we have also chosen manganese(II) complexes of  $\text{R}_4\text{bpp}$  ligands as an electrochemical probe.

##### 2.4.4.1 Syntheses and Characterization

Reactions of  $\text{Mn}(\text{ClO}_4)_2 \cdot 6\text{H}_2\text{O}$  with two equivalents of ligands  $\text{H}_4\text{bpp}$ ,  $\text{H}_2\text{Me}_2\text{bpp}$  or  $\text{Me}_4\text{bpp}$  produced the cations  $[\text{Mn}(\text{ClO}_4)_2]^{2+}$  which were isolated as the perchlorate salts. Reactions of equimolar ratios of  $\text{MnCl}_2 \cdot 4\text{H}_2\text{O}$  and the ligands  $\text{H}_4\text{bpp}$  and  $\text{Me}_4\text{bpp}$  afforded the five-coordinate complexes,  $[\text{Mn}(\text{H}_4\text{bpp})\text{Cl}_2]$  and  $[\text{Mn}(\text{Me}_4\text{bpp})\text{Cl}_2]$  respectively. The complexes in solid state are pale yellow, almost colorless, and stable in air at room temperature. The IR spectra between 4000 and 600  $\text{cm}^{-1}$  are not particularly informative, merely indicating that the ligands have coordinated to the metal. The manganese(II) bis complexes display

$\nu(\text{OH})$  absorptions at  $\sim 3400\text{ cm}^{-1}$  and  $\nu(\text{ClO}_4^-)$  absorptions at  $\sim 1100\text{ cm}^{-1}$  in their IR spectra. The dichloro complexes do not show  $\nu(\text{OH})$  absorption indicating the absence of coordinating water in the complexes. The structure of the dichloro complexes is presumably five-coordinate. This structural pattern has been authenticated in similar complexes using three-dimensional X-ray crystallography.<sup>164</sup>

The bis complexes are soluble in polar organic solvents but insoluble in water; however, the dichloro complexes are soluble in water, methanol and DMF. Conductivities of the dichloro complexes in water are suggestive of dissociation of the chlorides (Table 2.16). As expected, the bis-chelates behave as 1:2 electrolytes.<sup>138</sup> The room temperature magnetic moments in MeCN/DMF solution indicate the presence of high-spin  $d^5$  manganese(II) complexes (Table 2.16). All the complexes display in MeCN/H<sub>2</sub>O featureless electronic absorption spectra characteristic of only intraligand transitions. The X-band EPR spectra of all five manganese(II) complexes were recorded in MeCN/H<sub>2</sub>O at room temperature exhibiting well-resolved intense resonances centered at  $\sim 3300\text{ G}$  showing  $^{55}\text{Mn}$  hyperfine structure (Table 2.16). X-Band EPR spectrum of  $[\text{Mn}(\text{H}_4\text{bpp})_2]^{2+}$  in MeCN at room temperature is shown in Figure 2.14. The hyperfine coupling constant ( $A \sim 90\text{ G}$ ) and the hyperfine intensity patterns are typical of a monomeric manganese(II) complex.

#### 2.4.4.2 Electrochemistry. (a) Bis Chelate Complexes

To investigate the electronic/steric effect on  $\text{Mn}^{\text{III}}/\text{Mn}^{\text{II}}$  redox potentials due to the substituents present in  $\text{R}_4\text{bpp}$

Table 2.16: Molar Conductivity, Magnetic Moment and X-band EPR  
Spectral Data of Manganese(II) Complexes at 298 K

Compound	Solvent	$\Lambda_M(\Omega^{-1}\text{cm}^2\text{mol}^{-1})^a$	$\mu_{\text{eff}}(\text{B.M.})^b$	$g_{\text{av}}$	$A(\text{G})$
$[\text{Mn}(\text{H}_4\text{bpp})_2](\text{ClO}_4)_2 \cdot 2\text{H}_2\text{O}$	MeCN	271	6.01	1.92	93
$[\text{Mn}(\text{H}_2\text{Me}_2\text{bpp})_2](\text{ClO}_4)_2 \cdot 2\text{H}_2\text{O}$	MeCN	270	5.91	1.93	87
$[\text{Mn}(\text{Me}_4\text{bpp})_2](\text{ClO}_4)_2 \cdot 2\text{H}_2\text{O}$	MeCN	282	6.02	2.00	87
$[\text{Mn}(\text{H}_4\text{bpp})\text{Cl}_2]$	H <sub>2</sub> O	225	-	1.99	95.5
	DMF	52	5.82	2.00	95
$[\text{Mn}(\text{Me}_4\text{bpp})\text{Cl}_2]$	H <sub>2</sub> O	226	-	-	-
	DMF	48	5.97	1.98	94

<sup>a</sup>In MeCN, expected 1:2 electrolyte range, 220–300  $\Omega^{-1}\text{cm}^2\text{mol}^{-1}$ . For aqueous solution of  $\text{MnCl}_2 \cdot 4\text{H}_2\text{O}$ ,  $\Lambda_M = 225 \Omega^{-1}\text{cm}^2\text{mol}^{-1}$ . In DMF, expected 1:1 electrolyte range, 65–90  $\Omega^{-1}\text{cm}^2\text{mol}^{-1}$ .

<sup>b</sup>Measured in solution by Evans' method.

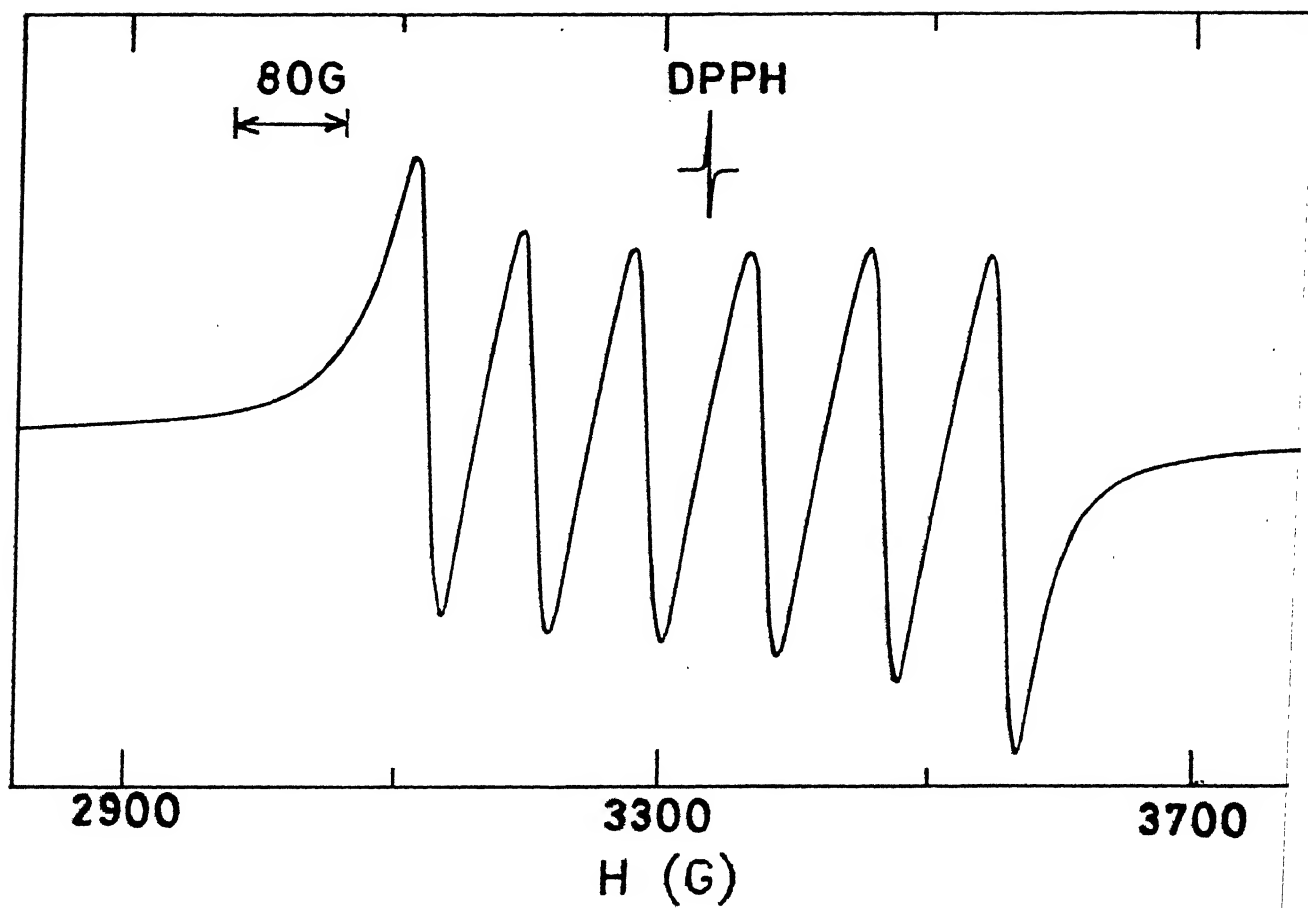


Figure 2.14 EPR spectrum of  $[\text{Mn}(\text{H}_4\text{bpp})_2](\text{ClO}_4)_2 \cdot 2\text{H}_2\text{O}$  in MeCN at room temperature

ligands, cyclic voltammetry was utilized. In MeCN solution all the three bis complexes undergo irreversible (however, the rereduction waves are seen) one-electron oxidative responses. Representative cyclic voltammograms are displayed in the Figure 2.15 and the data are compiled in the Table 2.17.

The strong resistance (very positive potential) of high-spin manganese(II) complexes to oxidation is attributed to the effect of the symmetrical  $d^5$  configuration.<sup>165</sup> It is worth mentioning here that the corresponding iron(II) and cobalt(II) complexes exhibit reversible/quasireversible cyclic voltammograms at a less positive potential (Section 2.4.1.4). Since the observed oxidative responses are irreversible, the emphasis is given to the anodic peak potentials ( $E_{pa}$ ). This should not be confused with thermodynamic reduction potentials, which are obtained from reversible cyclic voltammograms. We became interested in seeing how the  $E_{pa}$  values of this group of three manganese(II) bis-chelates are affected through systematic changes in ligand structure.

In the bis-chelate series the anodic peak potential values of  $[Mn(H_2Me_2bpp)_2]^{2+}$  and  $[Mn(Me_4bpp)_2]^{2+}$  are greater than the corresponding unsubstituted complex. The extent of steric predominance over electronic effect observed in these manganese(II) bis complexes as revealed by cyclic voltammetric experiments can be compared with a similar effect observed for  $Fe^{III}/Fe^{II}$  couple (Section 2.4.1.4) and  $Co^{III}/Co^{II}$  couple (Section 2.4.3.5) in corresponding iron(II) and cobalt(II) bis complexes respectively using the present ligands. Interestingly, the effect is more

**Table 2.17: Cyclic voltammetric<sup>a,b</sup> Data of Manganese(II) Complexes at 298 K**

Compound	Solvent	$E_{pa}$ (V)	$E_{pc}$ (V)	$\Delta E_p$ (mV)
$[Mn(H_4bpp)_2]^{2+}$	MeCN	1.52	1.25	270
$[Mn(H_2Me_2bpp)_2]^{2+}$	MeCN	1.72	1.29	430
$[Mn(Me_4bpp)_2]^{2+}$	MeCN	1.85	1.42	430
$[Mn(H_4bpp)(H_2O)_n]^{2+}$	H <sub>2</sub> O	0.92	0.72	200
$[Mn(Me_4bpp)(H_2O)_n]^{2+}$	H <sub>2</sub> O	0.89	0.67	220

<sup>a</sup>All potentials are referenced to SCE; scan rate 50 mV s<sup>-1</sup>.

<sup>b</sup>In MeCN, supporting electrolyte TBAP; platinum working electrode. In H<sub>2</sub>O solution, supporting electrolyte KNO<sub>3</sub>; glassy carbon working electrode.



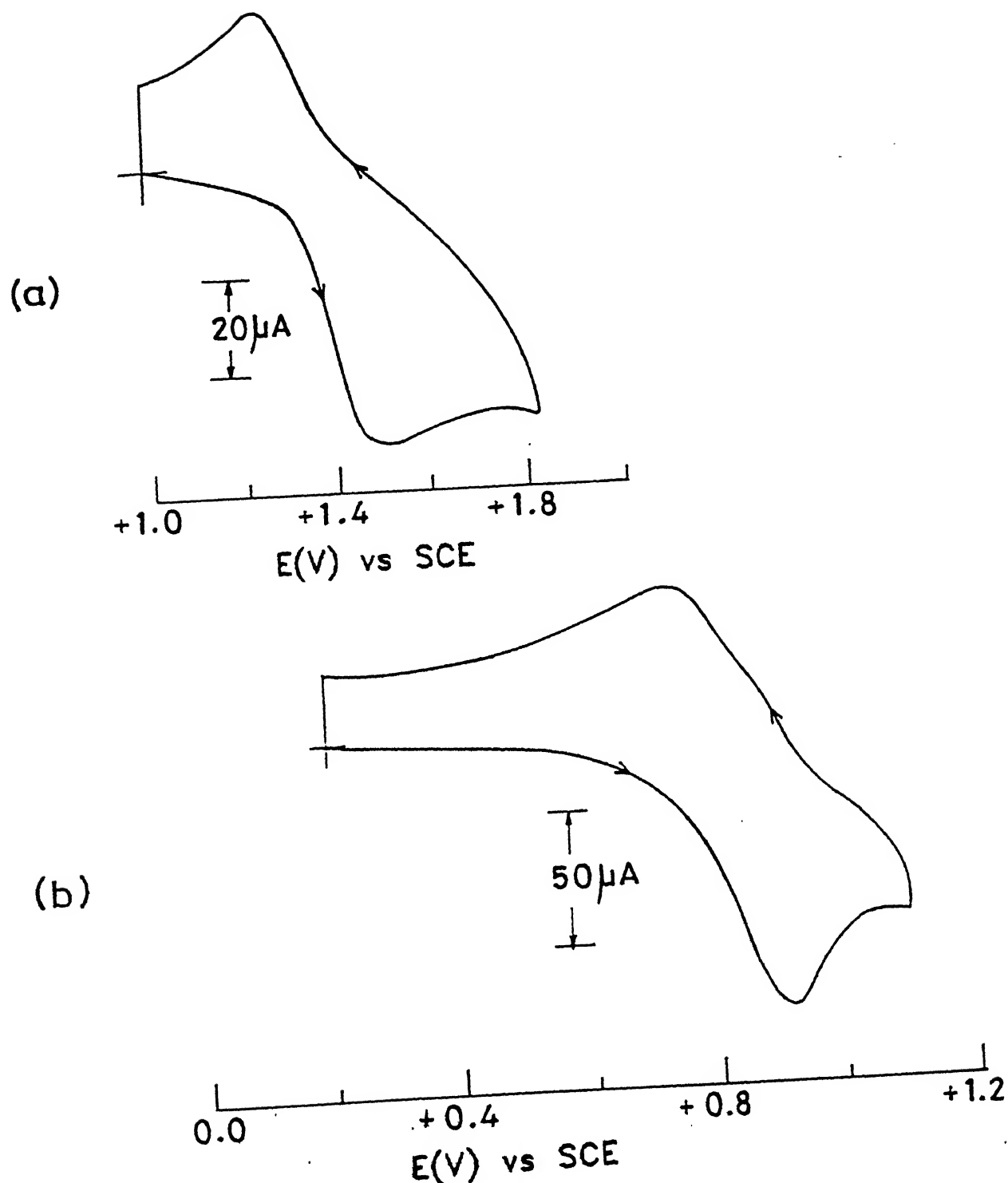


Figure 2.15 Cyclic voltammograms of (a)  $\text{Mn}(\text{H}_4\text{bpp})_2^{2+}$  in MeCN (1.01 mM) at a platinum electrode; (b)  $\text{Mn}(\text{H}_4\text{bpp})(\text{H}_2\text{O})_n^{2+}$  in water (1.2 mM) at a glassy carbon electrode. Scan rate  $50 \text{ mV s}^{-1}$

pronounced here compared to the iron and cobalt case.

(b) **Mono Chelate Complexes.** If our argument is correct then decreasing the number of ligands around the metal center should allow one to observe the usual electronic effect of the 3-methyl substituents since lesser number of ligand is expected to relax the steric strain in the metal coordination geometry. For this purpose we prepared two mono chelates of manganese(II).

As the two dichloro complexes studied here dissociate in aqueous solution we decided to exploit this information in a useful chemical sense. Thus we have generated in aqueous solution mono-chelate species of general composition,  $[\text{Mn}(\text{R}_4\text{bpp})(\text{H}_2\text{O})_n]^{2+}$  following nucleophilic halide displacement reactions on dichloro precursors. The aqua species thus generated were examined by cyclic voltammetry. The electrochemical data for these two aqua complexes are in Table 2.17 and the cyclic voltammogram of  $[\text{Mn}(\text{H}_4\text{bpp})(\text{H}_2\text{O})_n]^{2+}$  is shown in Figure 2.15. Now we see that the anodic peak potential of  $[\text{Mn}(\text{Me}_4\text{bpp})(\text{H}_2\text{O})_n]^{2+}$  is less positive than that of  $[\text{Mn}(\text{H}_4\text{bpp})(\text{H}_2\text{O})_n]^{2+}$ . Thus in the case of aqua complexes, compared to  $\text{H}_4\text{bpp}$  ligand  $\text{Me}_4\text{bpp}$  is a better stabilizer of the +3 state of manganese. This is understandable on the basis of its being a comparatively better  $\sigma$ -donor due to the presence of electron donating methyl groups as substituents.

The present electrochemical identification of predominance of electronic/steric effect over the other in the case of  $\text{Mn}^{2+}$  complexes is unique since in this case upon complexation the high-spin configuration of  $\text{Mn}^{2+}$  ion provides no crystal field stabilization energy.

### 2.4.5 Ruthenium(II) Complexes with RuN<sub>6</sub> Coordination

Anticipating that by changing the size of the metal ion in going from the first- to second- transition-series lead to the observation of a predominance of electronic effect over the steric effect, we extended our study with ruthenium.

#### 2.4.5.1 Syntheses and Selected Properties

The general synthetic approach that was employed for the preparation of the ruthenium(II) complexes with various combinations of the ligands reported in this work has involved the reactions of (R<sub>4</sub>bpp)RuCl<sub>3</sub> (R = H or Me) with the tridentate ligands(R<sub>4</sub>bpp) in the presence of sodium hypophosphite as reducing agent. The successful syntheses of these complexes demonstrate the generality of substitution reactions that the complexes (R<sub>4</sub>bpp)RuCl<sub>3</sub> can undergo. The synthesis and a very limited characterization data of the complex [Ru(H<sub>4</sub>bpp)<sub>2</sub>]<sup>2+</sup> are reported in the literature<sup>114</sup> following a direct reaction between the ligand and RuCl<sub>3</sub>.3H<sub>2</sub>O in the presence of NaH<sub>2</sub>PO<sub>2</sub> as reducing agent.

New monochelate ruthenium(III) starting complexes used in this work were prepared following direct reactions between the appropriate ligand and RuCl<sub>3</sub>.3H<sub>2</sub>O in ethanol. The molar conductance value of (H<sub>4</sub>bpp)RuCl<sub>3</sub>.3H<sub>2</sub>O in DMF solution reveals a partial dissociation of supposedly neutral complex. Measurement of the magnetic susceptibility of this complex in DMF solution gives  $\mu_{\text{eff}}$  value of 1.98 (Experimental section), consistent with the presence of monomeric octahedral d<sup>5</sup> low-spin ( $S = \frac{1}{2}$ ) ruthenium(III). The bis-chelates of ruthenium(II) were isolated as crystalline diperchlorate salts and are diamagnetic.

#### 2.4.5.2 Absorption Spectra

The absorption spectral data for all the ruthenium(II) complexes are presented in Table 2.18. The absorption spectrum of  $(H_4bpp)RuCl_3 \cdot 3H_2O$  in DMSO and a representative ruthenium(II) bis-complex in MeCN are shown in Figure 2.16. For  $(H_4bpp)RuCl_3$  the shoulders at 460 nm and 600 nm are assigned as ligand( $\pi$ )-to-metal( $t_2$ ) charge-transfer transitions. The band at 369 nm is due to  $Cl^- \rightarrow Ru(t_2)$  charge-transfer transition. The spectral feature observed for this mononuclear ruthenium(III) complex is well documented in the literature.<sup>166</sup>

All the ruthenium(II) bis complexes show three types of bands. Comparatively less intense shoulder at ~580 nm, absorptions of medium intensity in the region 350-430 nm and very strong bands due to intraligand transitions at further higher energies.

The occurrence of a less intense shoulder at ~580 nm demands a special attention since an absorption tail at 546 nm with molar extinction coefficient of  $\sim 700 \text{ M}^{-1}\text{cm}^{-1}$  for the most thoroughly studied ruthenium(II) complex,  $[Ru(bpy)_3]^{2+}$  ( $bpy=2,2'$ -bipyridine) is responsible for its luminescence and is assigned to spin forbidden metal-to-ligand charge-transfer,  $^3MLCT$  transition.<sup>167-169</sup> We believe that the weak-field nature of  $R_4bpp$  ligands has made low-lying metal-ligand antibonding orbital  $do^*$  thermally accessible and the shoulder at ~ 580 nm is due to  $(d\pi)^6 \rightarrow (d\pi)^5 (do^*)^1$  transition. We rule out the possibility of this being spin forbidden charge-transfer ( $^3MLCT$ ) transition since the ligands used in this work are very poor  $\pi$ -acceptors (see below).

The absorptions in the region 350 - 430 nm, are attributed

Table 2.18: Molar Conductance<sup>a</sup>, Electronic Spectra and Cyclic Voltammetric<sup>b</sup>  
Data of Ruthenium(II) Complexes in MeCN at 298 K

Compounds	$\Lambda_M (\Omega^{-1} \text{ cm}^2 \text{ mol}^{-1})$	$\lambda, \text{nm} (\epsilon, \text{M}^{-1} \text{ cm}^{-1})$	Ru <sup>III</sup> /Ru <sup>II</sup> couple	
			$E_f(\text{V})$	$\Delta E_p(\text{mV})$
[Ru(H <sub>4</sub> bpp) <sub>2</sub> ] (ClO <sub>4</sub> ) <sub>2</sub> ·H <sub>2</sub> O	274	256 (19 000), 285 (sh) (10 240), 395 (7 234), 586 (sh) (330)	1.06	80
[Ru(H <sub>2</sub> Me <sub>2</sub> bpp) <sub>2</sub> ] (ClO <sub>4</sub> ) <sub>2</sub> ·H <sub>2</sub> O	280	257 (18 020), 285 (sh) (9 690), 404 (5 910), 580 (sh) (787)	1.03	80
[Ru(Me <sub>4</sub> bpp) <sub>2</sub> ] (ClO <sub>4</sub> ) <sub>2</sub> ·H <sub>2</sub> O	281	257 (19 050), 285 (sh) (9 960), 350(sh)(3 070), 419 (8 420), 605 (sh) (920)	1.00	80
[Ru(H <sub>4</sub> bpp)(H <sub>2</sub> Me <sub>2</sub> - bpp)](ClO <sub>4</sub> ) <sub>2</sub> ·H <sub>2</sub> O	270	257 (17 750), 286 (sh) (9 880), 392 (6 060), 591 (sh) (635)	1.05	90
[Ru(H <sub>4</sub> bpp)(Me <sub>4</sub> - bpp)](ClO <sub>4</sub> ) <sub>2</sub> ·H <sub>2</sub> O	281	257 (18 800), 286 (sh) (7 990), 350(sh)(3 070), 409 (6 220), 580 (sh) (280)	1.04	90
[Ru(H <sub>2</sub> Me <sub>2</sub> bpp)(Me <sub>4</sub> - bpp)](ClO <sub>4</sub> ) <sub>2</sub> ·H <sub>2</sub> O	283	257 (18 090), 285 (sh) (9 590), 403 (5 820), 600 (sh) (730)	1.01	90

<sup>a</sup>Expected 1:2 electrolyte range: 220 - 300  $\Omega^{-1} \text{ cm}^2 \text{ mol}^{-1}$ .

<sup>b</sup>Beckman planar platinum inlay (M-39273) working electrode; supporting electrolyte, TBAP (0.2 M); scan rate, 50 mV s<sup>-1</sup>; potentials are vs. saturated calomel electrode (SCE).

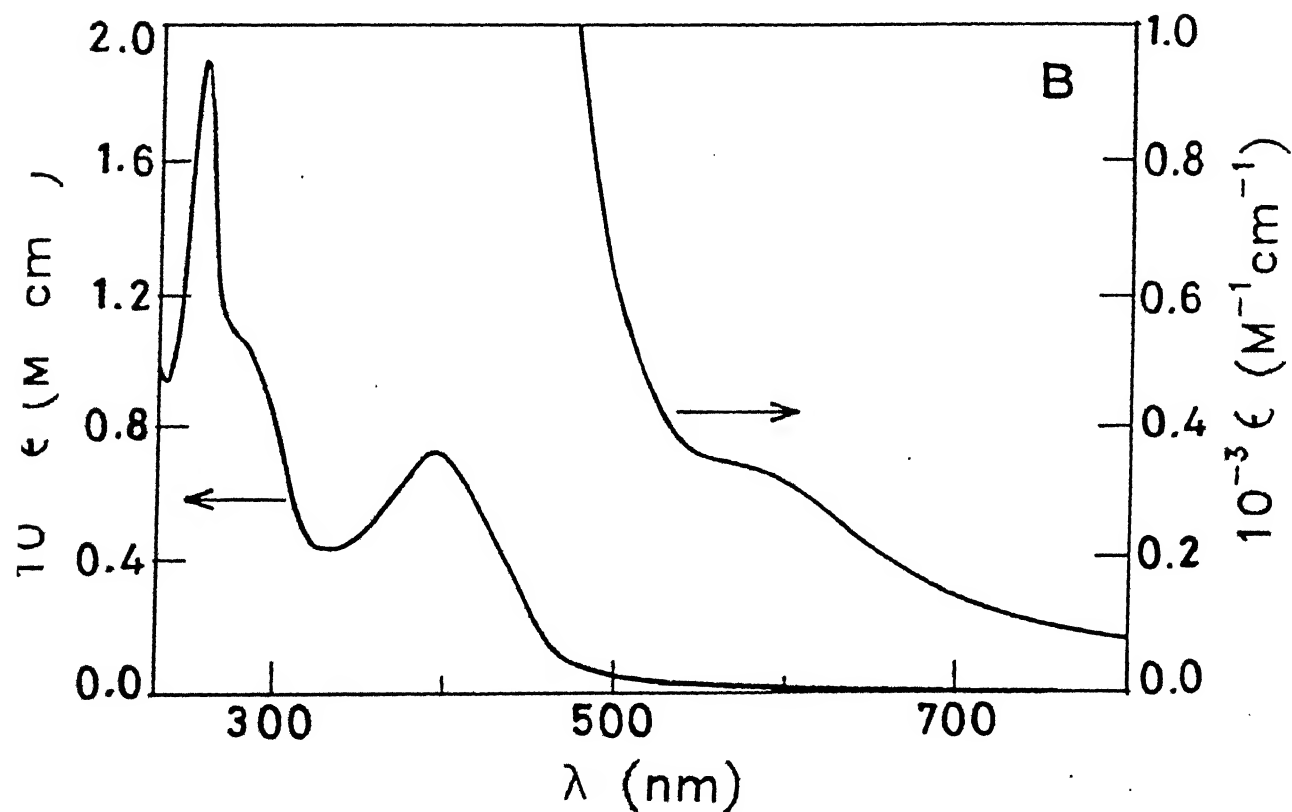
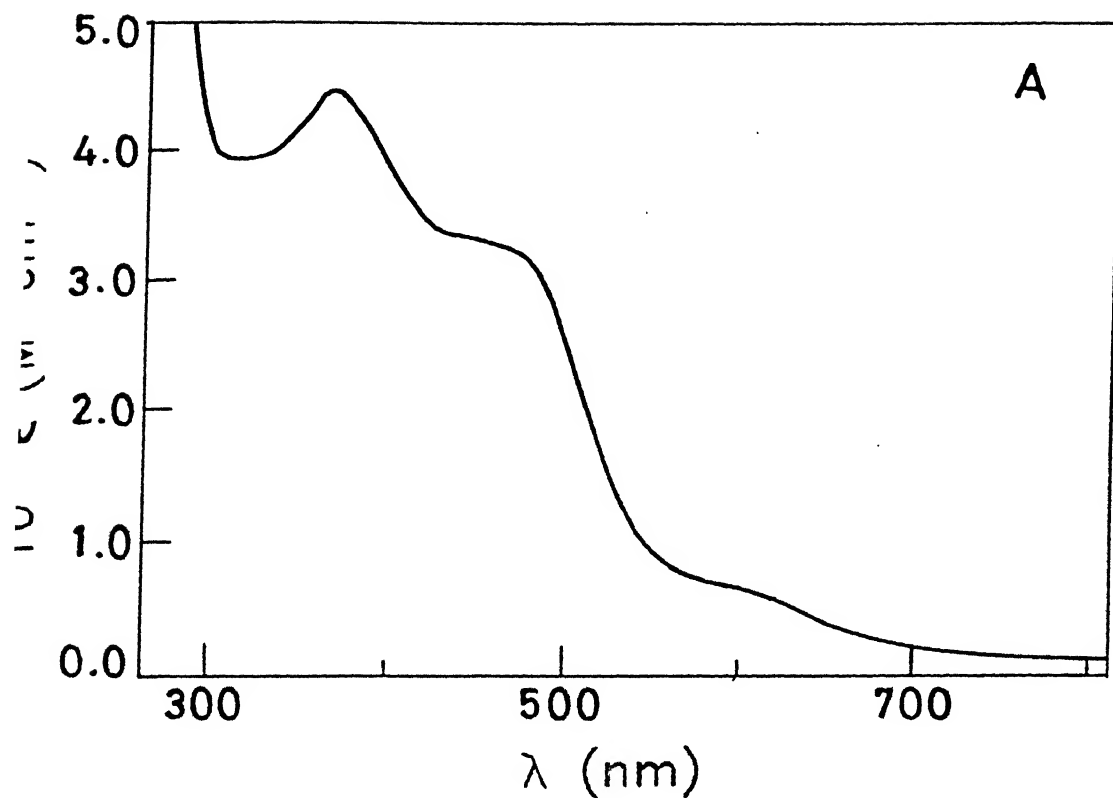


Figure 2.16 Electronic spectra of (A)  $(H_4bpp)RuCl_3 \cdot 3H_2O$  in DMSO and (B)  $[Ru(H_4bpp)(Me_4bpp)](ClO_4)_2 \cdot H_2O$  in MeCN

to the spin-allowed charge-transfer transitions from the metal  $d\pi$  orbitals to the ligand  $\pi^*$  orbitals (MLCT). Inspection of Table 2.18 shows that, in going from  $[\text{Ru}(\text{H}_4\text{bpp})_2]^{2+}$  to  $[\text{Ru}(\text{Me}_4\text{bpp})_2]^{2+}$  a significant red shift in the band maxima is observed as the number of methyl substituents near the donor site increases. A similar trend was observed in the cases with substituent in a sterically hindering position.<sup>170-172</sup>

The MLCT band positions of the present complexes are comparable to the related group of complexes of 2,6-bis(N-pyrazolyl)pyridine ligands.<sup>14</sup> It is worth noting here that the MLCT band energy for  $[\text{Ru}(\text{trpy})_2]^{2+}$  (trpy = 2,2':6',2''-terpyridine) is 476 nm.<sup>14</sup> This indicates an increase in separation of the energy levels of the metal  $d$  and ligand  $\pi^*$  orbitals in these complexes of pyrazole-rich ligands compared to pyridine-rich planar trpy ligand. Since the same orbitals are well known<sup>168,169</sup> to be involved in the redox processes this is also reflected in an increase in the potential gap between the  $\text{Ru}^{\text{III}}/\text{Ru}^{\text{II}}$  redox couple and the first ligand reduction process (see below). Furthermore, it appears that this increase results from both an increase in the energy of the metal  $d$  orbitals, as shown by the decrease in  $\text{Ru}^{\text{III}}/\text{Ru}^{\text{II}}$  reduction potentials (cathodically shifted), and a large raising of the level of the ligand  $\pi^*$  orbitals (see below). The band at ~250 nm and the shoulder at ~285 nm are assigned to ligand-localized transitions.

#### 2.4.5.3 $^1\text{H}$ NMR Spectra

To throw light on the bonding interactions between the metal and the chosen ligands in these diamagnetic complexes we

have examined the  $^1\text{H}$  NMR spectral properties of two representative bis complexes, viz.,  $[\text{Ru}(\text{H}_4\text{bpp})_2](\text{ClO}_4)_2 \cdot \text{H}_2\text{O}$  and  $[\text{Ru}(\text{Me}_4\text{bpp})_2](\text{ClO}_4)_2 \cdot \text{H}_2\text{O}$  in  $\text{CD}_3\text{CN}$ . Table 2.19 lists the  $^1\text{H}$  NMR chemical shifts for the complexes with coordination-induced shifts ( $\text{CIS} = \delta_{\text{complex}} - \delta_{\text{ligand}}$ ).<sup>15,108,173</sup> A typical spectrum is shown in Figure 2.17. Assignments were made by comparison with the spectra of the free ligands and of related complexes from the literature.<sup>15</sup> In both the complexes studied here it is expected that the six-membered chelate rings exist in boat conformations.<sup>114</sup> In the spectra of  $[\text{Ru}(\text{H}_4\text{bpp})_2]^{2+}$  and  $[\text{Ru}(\text{Me}_4\text{bpp})_2]^{2+}$ , the  $\text{CH}_2$  protons give rise to an AB quartet, which confirms the presence of two diastereotopic protons, axial and equatorial. Thus it is obvious that these two protons are not interconverting on the NMR time scale, otherwise a singlet would have resulted.

Inspection of the chemical shifts and CIS values in Table 2.19 allows a number of observations to be made. The CIS values are, in general, positive except for protons on carbon atoms adjacent to the coordinating nitrogens and the methylene protons. The former protons show significant negative (upfield) CIS values.

A large range of CIS values (+1.06 to -1.64 ppm) reflects some dramatic changes in the  $^1\text{H}$  NMR chemical shifts upon coordination of ligands to ruthenium. The sign and magnitude of CIS values depend on several factors<sup>15,108,173</sup> like, ligand-to-metal  $\sigma$  donation, metal-to-ligand  $\pi$  back-donation, chelation-imposed conformational changes, coordinative disruption of inter-ring conjugation and through-space ring-current anisotropy.

The large negative CIS values observed for protons



Table 2.19:  $^1\text{H}$  NMR Chemical Shifts<sup>a</sup> and Coordination Induced Shifts<sup>b</sup> of Ruthenium(II) Complexes

Compound	$^1\text{H}$ NMR					
	$\text{H}^4$	$\text{H}^3, \text{H}^5$	$\text{H}^{4'}$	$\text{CH}_2$	$\text{R}^{3'c}$	$\text{R}^{5'c}$
$\text{H}_4\text{bpp}$	7.43 (q, $J=8\text{Hz}$ )	6.80 (d, $J=8\text{Hz}$ )	6.23 (t, $J=2.5\text{Hz}$ )	5.33 (s)	7.33 (d, $J=2.5\text{Hz}$ )	7.60 (d, $J=2.5\text{Hz}$ )
$[\text{Ru}(\text{H}_4\text{bpp})_2]$ ( $\text{ClO}_4$ ) <sub>2</sub>	8.15 (t, $J=8\text{Hz}$ )	7.78 (d, $J=8\text{Hz}$ )	6.25 (m)	5.15 (AB, q, $J=16\text{Hz}$ )	6.25 (m)	7.80 (s, br)
CIS	+0.72	+0.98	+0.02	-0.18	-1.08	+0.20
$\text{Me}_4\text{bpp}$	7.50 (q, $J=8\text{Hz}$ )	6.73 (d, $J=9\text{Hz}$ )	5.80 (s)	5.16 (s)	2.06 (s)	2.13 (s)
$[\text{Ru}(\text{Me}_4\text{bpp})_2]$ ( $\text{ClO}_4$ ) <sub>2</sub>	8.08 (t, $J=8\text{Hz}$ )	7.79 (d, $J=8\text{Hz}$ )	5.95 (s)	5.06 (AB, q, $J=16\text{Hz}$ )	0.42 (s)	2.42 (s)
CIS	+0.58	+1.06	+0.15	-0.10	-1.64	+0.29

<sup>a</sup>For deuterated acetonitrile solutions.

<sup>b</sup> CIS=  $\delta_{\text{complex}} - \delta_{\text{ligand}}$ .

<sup>c</sup> H or  $\text{CH}_3$ .

adjacent to coordinating pyrazole nitrogens ( $R^3$  position) result from interligand through-space ring-current anisotropy effects since on complexation the protons involved all lie over the shielding plane of the central pyridine ring of the other coordinated ligand. It is clearly seen when 3'-position is methyl substituted.

The large positive CIS values for pyridine protons ( $H^{3,4,5}$ ) (downfield shifts) suggest that the ligand to metal  $\sigma$  donation is more important (as this will decrease the electron density at those sites and lead to positive CIS values) than metal-to-ligand  $\pi$  back donation in the ground state of these complexes (see below). Since ring-current-induced fields depend on the aromaticity and  $\pi$  polarisability of the heterocycle these effects will differ significantly for the different type of heterocycle.<sup>174</sup> Thus in contrast to pyridine ring protons pyrazole ring protons are shifted toward upfield. This is in accord with the well established fact that pyrazole-containing ligands are expected to be weaker<sup>14</sup> donors than the analogous pyridine-containing ligands, given the difference in ligand basicities for pyridine and pyrazole ring systems. The reduced donor ability of pyrazole ring systems relative to pyridine ring systems may also be a result of the geometric constraints on the chelate bite. In the case of  $[Ru(H_4bpp)_2]^{2+}$  the CIS values for the pyrazole ring protons ( $H^4$  and  $R^5$ ) are less positive than that of  $[Ru(Me_4bpp)_2]^{2+}$  suggesting that compared to  $H_4bpp$  the ligand  $Me_4bpp$  is a better donor to ruthenium (see below).

In the ligands  $H_4bpp$  and  $Me_4bpp$  the  $\pi$ -excessive (pyrazole)

heterocycle is not directly bound to a  $\pi$ -deficient (pyridine) heterocycle. Due to this disrupted conjugation the coordinated ruthenium can act as an alternative acceptor of  $\pi$ -electron density from the pyrazole and donor to the pyridine.<sup>174</sup>

#### 2.4.5.4 Electrochemistry

The electrochemical behavior of  $[(H_4bpp)RuCl_3]$  in DMF solution was investigated by cyclic voltammetry to examine the extent of stabilization of ruthenium(III) state by  $H_4bpp$  with respect to reduction. The cyclic voltammogram exhibits a quasi-reversible ( $\Delta E_p = 100$  mV at a scan rate of  $50 \text{ mV s}^{-1}$ ; with a tenfold increase in scan rate  $\Delta E_p$  increases by 70 mV) one-electron reductive wave at  $-0.24 \text{ V vs. SCE}$  with two additional oxidative responses during the anodic (reoxidative) scan (Figure 2.18). This behavior is a prototype of electron-transfer followed by chemical reaction.<sup>155</sup> When studied in DMSO, the  $Ru^{III}/Ru^{II}$  formal potential ( $E_f$ ) increases by 100 mV. The formal potential for couple 1 justifies the successful use of sodium hypophosphite ( $H_3PO_3 + 2 H^+ + 2e^- \rightleftharpoons H_3PO_2 + H_2O$ ,  $-0.75 \text{ V vs. SCE}$ )<sup>175</sup> as reducing agent in the syntheses of the ruthenium(II) complexes. Even though the syntheses were carried out in acidic aqueous medium and the electrochemical experiments were done in DMF/DMSO, an idea about the ease of reducibility of  $[(H_4bpp)RuCl_3]$  is of significance.

All the ruthenium(II) bis complexes exhibit a well-defined nearly reversible  $Ru^{III}/Ru^{II}$  oxidative responses (Figure 2.18 and Table 2.18) when examined by cyclic voltammetry. The  $Ru^{III}/Ru^{II}$  formal potentials for the present complexes are about 200 mV

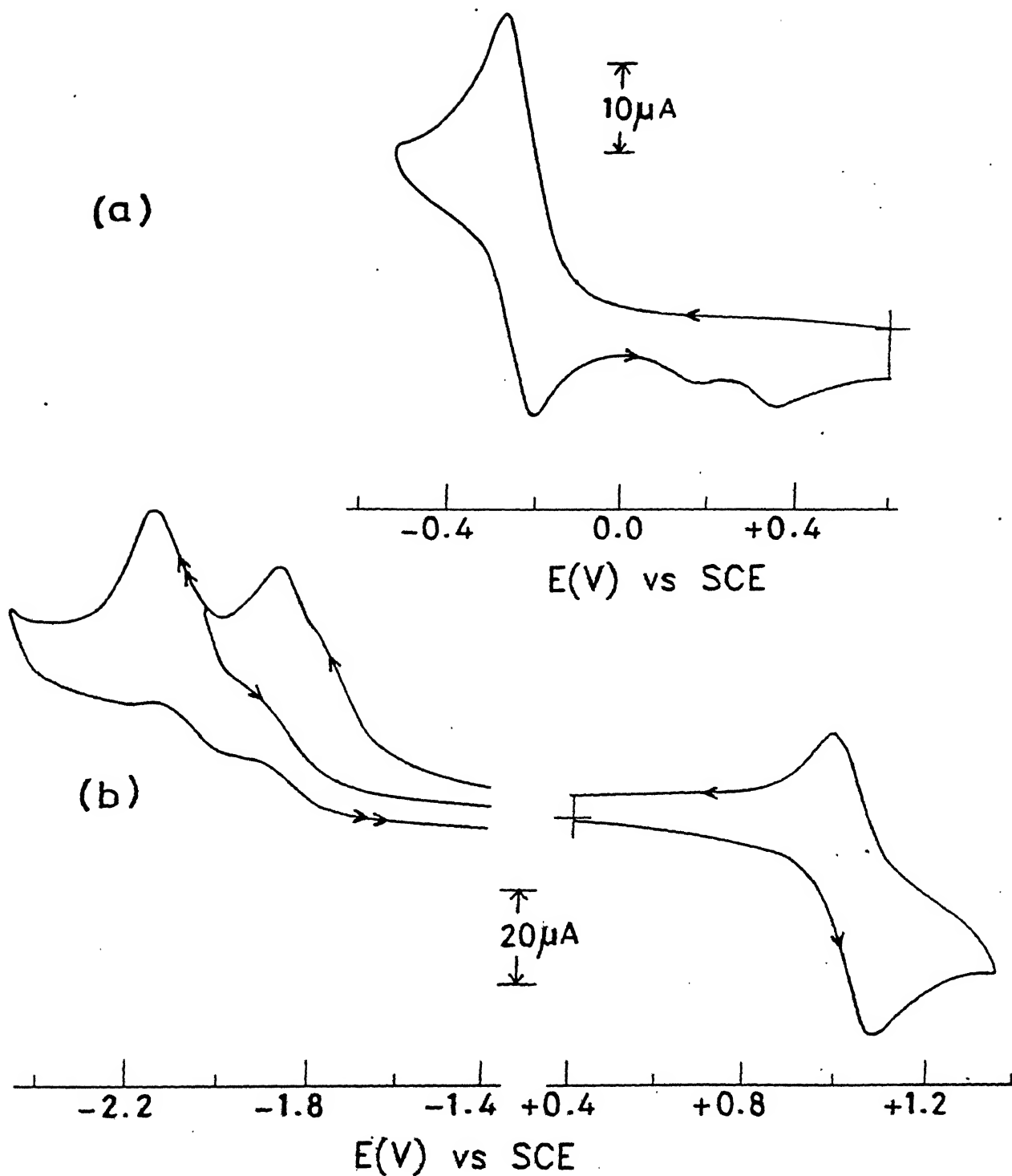


Figure 2.18 Cyclic voltammograms of (a)  $(H_4bpp)RuCl_3$  in DMF and (b)  $[Ru(H_4bpp)(Me_4bpp)]^{2+}$  in MeCN at a platinum electrode; scan rate  $50 \text{ mV s}^{-1}$ ; solute concentrations are  $10^{-3} \text{ M}$

cathodic than those of related complexes (1.06-1.25 V vs. SCE) of Jameson and coworkers<sup>14</sup>. This trend points toward a destabilization of filled  $t_2$  orbitals by the present ligands. Thus compared to Jameson's ligands<sup>14</sup> the present ligands are better donor towards ruthenium(II). It is worth mentioning here that the  $R_4bpy$  ligands are weak field ligands towards Mn(II), Fe(II), and Co(II) as a result of the increased metal-pyridine bond distance caused by steric requirements.

Two ill-defined irreversible ligand-based reductions were observed for all the complexes when scanned cathodically (Figure 2.18). The potentials are very negative ( $E_{pc}$  values lie in the range -1.90 to -2.20 V vs. SCE) revealing that the LUMO's (lowest unoccupied molecular orbitals) are relatively high in energy compared to  $trpy$ .<sup>14</sup> It is worth noting that for Jameson's ruthenium(II) complexes irreversible ligand reductions were observed at -1.66 V vs. SCE.<sup>14</sup> Thus these  $R_4bpy$  ligands are even weaker as  $\pi$ -acceptors. The poorer  $\pi$ -accepting property of pyrazole-containing ligands relative to polypyridine ligands has also been noted previously.<sup>14,108,174,176,177</sup>

A steady decrease in the  $Ru^{III}/Ru^{II}$  formal potentials from 1.06 to 1.00 V vs. SCE was observed (Table 2.18) with an increase in the total number of methyl groups from zero to eight. A plot of  $E_f$  ( $Ru^{III}/Ru^{II}$  couple) vs. the total number of methyl groups is shown in Figure 2.19. The trend is understandable given the electron-releasing nature of the methyl groups. An average potential step size of  $\sim 8$  mV / methyl group is obtained from the slope of the graph. Interestingly, when the pyrazole rings are attached directly to the pyridine ring this potential step

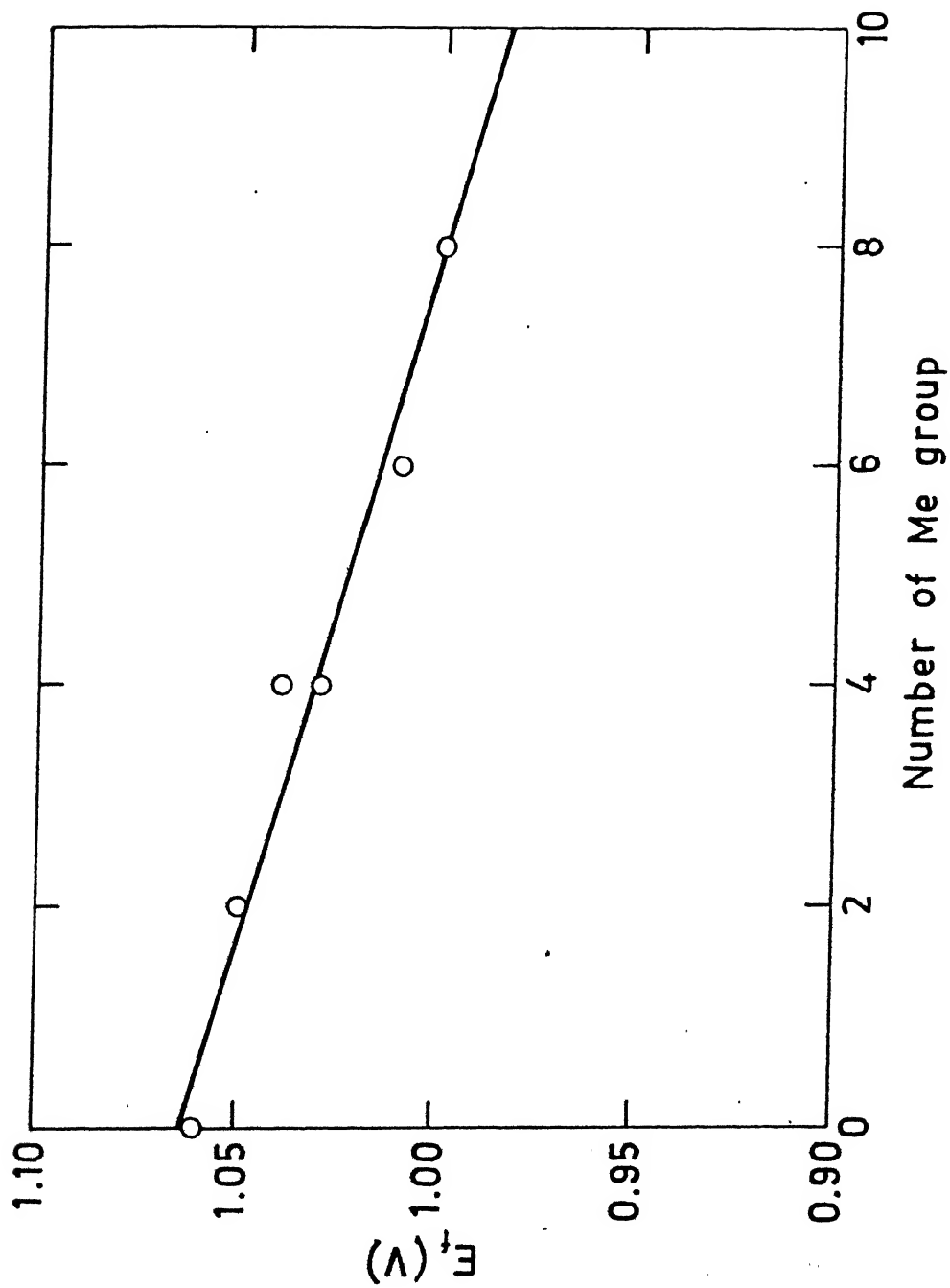


Figure 2.19 Plot of the  $\text{Ru}^{\text{III}}/\text{Ru}^{\text{II}}$  couple vs. total number of methyl groups in the complex.

size is much larger (24 mV / methyl group).<sup>14,15</sup> We believe that the reduced inductive effect of the methyl groups observed here is due to a partial contribution of the steric effect.

## 2.5 Concluding Remarks

Followings are the salient features of the work described in this chapter:

(i) The recognition and characterization of a new class of tridentate mixed heterocyclic ligands  $R_4bpp$  have been achieved.

(ii) To investigate the influence of methyl substituents near the donor site ( $R_4bpp$  ligands) the bis chelates of Mn(II), Fe(II), Co(II), Ni(II), and Ru(II) complexes have been synthesized. All the first-transition-series metal ions show high-spin behavior and +2 states are significantly stabilized in their bis chelates. Additionally, it is interesting to note that the high-spin cobalt(II) complexes belong to a rare family of species having  $CoN_6$  coordination.

(iii) Solution stereochemistry of high-spin Fe(II), Co(II), and Ni(II) complexes has been determined using  $^1H$  NMR spectroscopy. The proton NMR spectral results are summarized in Table 2.20. For low-spin ruthenium(II) complexes coordination induced shifts were calculated from their  $^1H$  NMR spectra.

(iv) The predominance of steric effect over electronic is manifested by the steric barrier to the close approach of the metal atom to the donor atoms which causes an effective reduction in the field strength experienced by the metal and in the distortions in the coordination octahedron. This has been nicely revealed from the absorption spectral studies. Table 2.21

Table 2.20: Paramagnetically Shifted  $^1\text{H}$  NMR Assignments for High-spin Iron(II), Cobalt(II), and Nickel(II) Bis Chelates

Compound	$\text{H}^3, \text{H}^5$	$\text{H}^4$	$\text{H}^{3'}$ (or Me)	$\text{H}^{5'}$ (or Me)	$\text{H}^{4'}$	$\text{CH}_2$	$\text{CH}_2$
$[\text{Fe}(\text{H}_4\text{bpp})_2](\text{ClO}_4)_2 \cdot \text{H}_2\text{O}$	44.0	10.0	27.0	22.0	39.0	-18.0	-48.0
$[\text{Fe}(\text{Me}_4\text{bpp})_2](\text{ClO}_4)_2 \cdot 2\text{H}_2\text{O}$	50.0	9.0	39.5	21.5	47.5	-25.0	-68.0
$[\text{Co}(\text{H}_4\text{bpp})_2](\text{ClO}_4)_2 \cdot 2\text{H}_2\text{O}$	62.2	-10.2	-6.6	55.2	17.2	60.4	-8.0
$[\text{Co}(\text{H}_4\text{bpp})_2](\text{ClO}_4)_2 \cdot 2\text{H}_2\text{O}$	63.8	-9.6	-28.8	22.8	16.8	82.0	-3.2
$[\text{Ni}(\text{H}_4\text{bpp})_2](\text{ClO}_4)_2$	55.0	17.6	32.0	44.5	47.0	-5.5	-10.5
$[\text{Ni}(\text{H}_4\text{bpp})_2](\text{ClO}_4)_2$	49.5	19.6	-7.0	-1.0	43.5	-4.5	-10.0



**Table 2.21:** Ligand Field Splitting Parameter ( $10Dq$ ) for Iron(II), Cobalt(II), and Nickel(II) Complexes

Compounds	$10Dq$ ( $\text{cm}^{-1}$ )		
	M = Fe	M = Co	M = Ni
$[\text{M}(\text{H}_4\text{bpp})_2]^{2+}$	11 870	12 020	11 520
$[\text{M}(\text{H}_2\text{Me}_2\text{bpp})_2]^{2+}$	11 310	11 240	11 070
$[\text{M}(\text{Me}_4\text{bpp})_2]^{2+}$	11 020	10 760	10 730

summarizes the ligand field splitting parameter  $10Dq$  for Fe(II), Co(II), and Ni(II) complexes.

(v) In the case of first-transition series selected bis-chelate complexes of  $R_4bpp$  we observe that the  $M^{III}/M^{II}$  redox potential ( $M = Mn, Fe, \text{ and } Co$ ) increases as the number of methyl groups near the donor site increases, demonstrating the predominance of steric effect over the electronic effect. Thus we believe that for a second-transition series metal ion like ruthenium(II), the larger size of the metal ion has caused a better metal-ligand orbital overlap and hence overrides the steric effect. The decreased potential step size observed in the case of Ru(II) relative to those observed for the Mn(II), Fe(II), and Co(II) complexes indicates that the steric factor is still operative in Ru(II) bis-chelate complexes, although it is outweighed by the electronic effect. A plot of the kind presented in Figure 2.20 neatly summarizes our experimental findings for  $M^{III}/M^{II}$  couple ( $M = Mn, Fe, Co, \text{ and } Ru$ ) in the bis complexes of the present ligands.

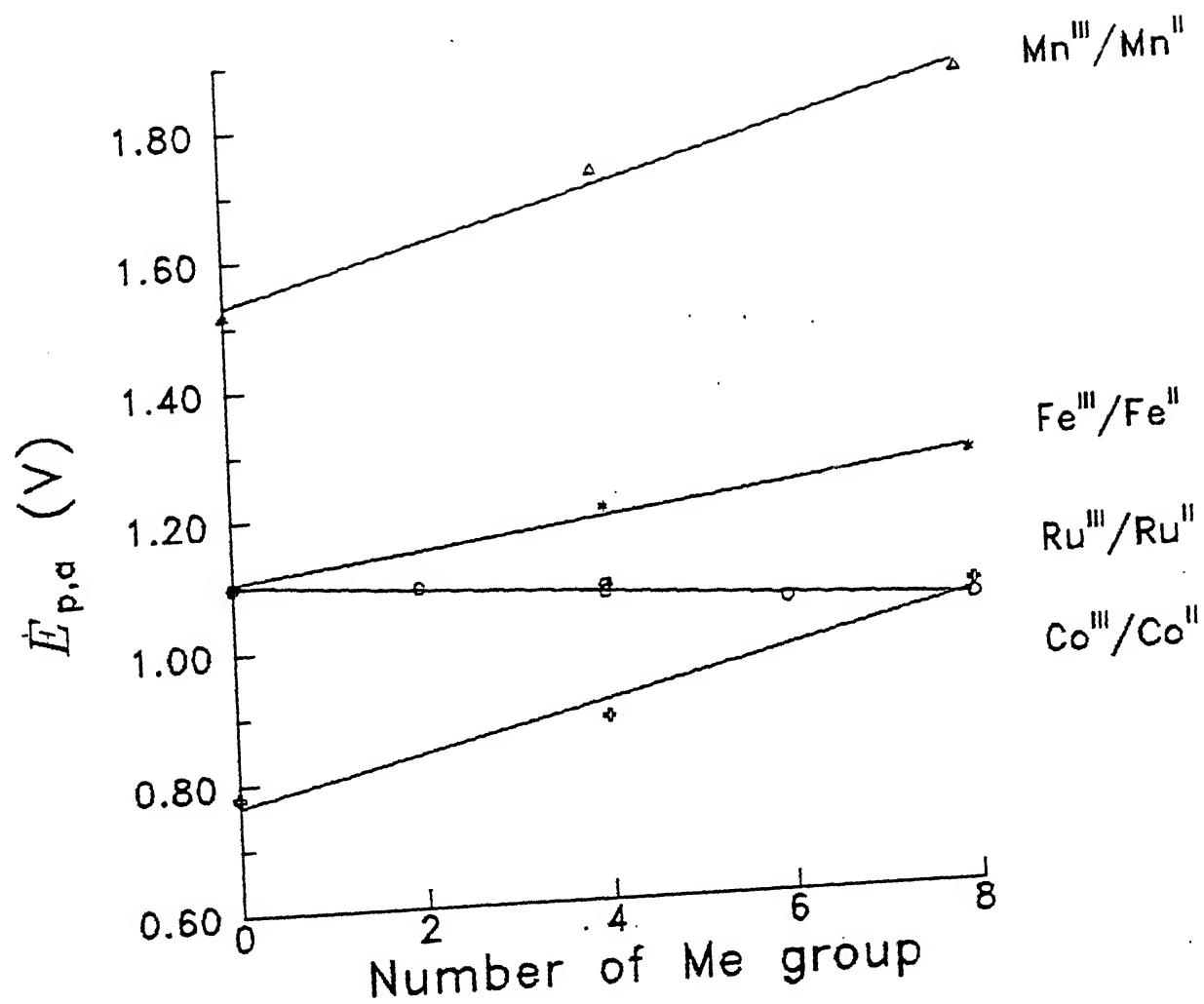


Figure 2.20 Variation of  $M^{III}/M^{II}$  redox potential with Me substitution in the ligand framework.

## CHAPTER 3

**Solution and Crystal Structure of Sterically Hindered Iron(II) Bis  
Chelate with Unsymmetrically Methyl Substituted Ligand  $H_2Me_2bpp$**

During the course of identification of steric effect over electronic or vice versa (Chapter 2), we have observed that in the bis chelates of first-row transition metals, increase in the steric crowding by methyl substituents near donor site results in decrease in strength of the ligand, which means effectively poorer metal-ligand orbital overlap. The consequence of this is expected to be reflected by longer M-N bond distance(s). For obvious reasons we became interested in identifying this phenomenon. Fortunately, we were able to grow X-ray quality single crystals for iron(II) bis complex with unsymmetrically methyl substituted ligand,  $\text{H}_2\text{Me}_2\text{bpp}$ . In this chapter we describe the crystal structure of  $[\text{Fe}(\text{H}_2\text{Me}_2\text{bpp})_2](\text{ClO}_4)_2$  and solution structure of the same compound as revealed from  $^1\text{H}$  NMR spectroscopy.

### 3.1 Experimental Section

#### 3.1.1 Measurements

##### X-ray Data Collection and Structure Solution and Refinement.

Crystals of  $[\text{Fe}(\text{H}_2\text{Me}_2\text{bpp})_2](\text{ClO}_4)_2$  suitable for diffraction work were obtained by slow evaporation from an aqueous-methanol solution of  $[\text{Fe}(\text{H}_2\text{Me}_2\text{bpp})_2](\text{ClO}_4)_2 \cdot 2\text{H}_2\text{O}$ . A single yellow crystal was mounted on a glass fiber and placed on a Rigaku AFC-6S diffractometer using graphite-monochromated  $\text{Mo K}_\alpha$  X-radiation ( $\lambda = 0.71073 \text{ \AA}$ ). Diffraction data at 296 K were collected at Keene State College, Keene, New Hampshire.

The unit cell dimensions were obtained from a least-squares refinement of 25 strong, machine-centered reflections in the range  $30.14 < 2\theta < 31.73^\circ$ . Crystal data, data collection and refinement parameters are summarized in Table 3.1. The scan technique was

Table 3.1: Summary of X-ray Diffraction Data for  $[\text{Fe}(\text{H}_2\text{Me}_2\text{bpp})_2](\text{ClO}_4)_2$ 

formula	$\text{C}_{30}\text{H}_{34}\text{NFeO}_8\text{N}_{10}\text{Cl}_2$
fw	789.41
a, Å	14.209 (2)
b, Å	13.666 (2)
c, Å	18.532 (2)
$\beta$ , deg	99.42 (1)
cryst system	monoclinic
Z	4
V, Å <sup>3</sup>	3550 (2)
$d_{\text{calcd}}$ , g/cm <sup>3</sup>	1.477
space group	$P2_1/n$ (No.14)
T, °C	23
radiation	Mo $K_\alpha$ ( $\lambda = 0.71069$ Å)
abs coeff ( $\mu$ ), cm <sup>-1</sup>	6.35
no. of obsd data	3298
no. of variables	589
$R(E_o)^a$	0.057
$R_w(E_o)^b$	0.060
quality-of-fit indicator <sup>c</sup>	1.86

$$^a R = \sum |E_o| - |E_c| / \sum |E_o|. \quad ^b R_w = [(\sum w(|E_o| - |E_c|)^2) / \sum w|E_o|^2)]^{1/2}$$

where  $w = 4 E_o^2 / \sigma^2 (E_o^2)$  and  $\sigma^2 (E_o^2) = [S^2(C + R^2 \times B) + (p E_o^2)^2] / L_p^2$ , where  $S$  = scan rate,  $C$  = total integrated peak count,  $R$  = ratio of scan time to background counting time,  $B$  = total background count,  $L_p$  = Lorentz polarization factor, and  $p$  = fudge factor (fixed at 0.03).

$$^c \text{quality of fit} = [w(|E_o| - |E_c|)^2 / (N_{\text{observns}} - N_{\text{parameters}})]^{1/2}.$$

employed for which  $6^\circ < 2\theta < 55^\circ$ . Omega scans of several intense reflections, made prior to data collection, had an average peak width at half-height of  $0.28^\circ$  with a take-off angle of  $6.0^\circ$ . Scans of  $(1.17 + 0.30 \tan\theta)^\circ$  were made at a speed of  $8.0^\circ/\text{min}$  (in omega). The weak reflections ( $I < 10.0\sigma(I)$ ) were rescanned (maximum of 2 rescans) and the counts were accumulated to assure good counting statistics. Stationary background counts were recorded on each side of the reflection. The ratio of peak counting time to background counting time was 2:1. Three check reflections were measured every 150 reflections: they exhibited no significant decay during the data collection. An empirical absorption correction, based on azimuthal scans of several reflections, was applied which resulted in transmission factors ranging from 0.90 to 1.00. Intensities were corrected for Lorentz and polarization effects. Considerations of molecular formula weight and volume calculation suggested  $Z = 4$ . Monoclinic space group  $P2_1/n$  (no.14) was uniquely established by systematic absences  $h0l$  ( $h + l \neq 2n$ ) and  $0k0$  ( $k \neq 2n$ ). Successive solution and refinement of the structure (Professor R. J. Butcher, Howard University, Washington, D.C. via Modem) confirmed this space group.

Neutral atom scattering factors were taken from the tabulation of Cromer and Waber.<sup>178</sup> Anomalous dispersion effects were included in  $F_{\text{calc}}$ ;<sup>179</sup> the values for  $f'$  and  $f''$  were those of Cromer.<sup>180</sup> All data with  $I > 3.0 \sigma(I)$  were retained as observed and used in all subsequent least-squares refinements. The structure was solved by the direct methods.<sup>181,182</sup> Subsequent Fourier syntheses revealed the positions of the remaining non-hydrogen atoms. The structure was refined by a full-matrix

least-squares method with anisotropic thermal parameters used for the non-hydrogen atoms. The function minimized was  $\sum w(|E_o| - |E_c|)^2$  where  $E_o$  and  $E_c$  are the observed and calculated structure amplitudes, and the weight,  $w$ , is  $4E_o^2 / \sigma^2(E_o^2)$ . The maximum and minimum peaks on the final difference Fourier map corresponded to 0.63 and -0.41 e- /Å<sup>3</sup>, respectively. All calculations were performed using the TEXSAN<sup>183</sup> crystallographic software package of Molecular Structure Corporation for the structural calculations and the programs PLUTO<sup>184</sup> and ORTEP<sup>185</sup> for the molecular and structural drawings. The final weighted R factor (on F) was 0.060 and the unweighted R factor was 0.057.

Details of <sup>1</sup>H NMR measurements are given in Chapter 2 (Section 2.1.2).

### 3.2 Synthesis of Compound

The synthesis of [Fe(H<sub>2</sub>Me<sub>2</sub>bpp)<sub>2</sub>](ClO<sub>4</sub>)<sub>2</sub>·2H<sub>2</sub>O has been given in chapter 2 (Section 2.1.3). <sup>1</sup>H NMR spectrum of [Fe(H<sub>2</sub>Me<sub>2</sub>bpp)<sub>2</sub>](ClO<sub>4</sub>)<sub>2</sub>·2H<sub>2</sub>O (CD<sub>3</sub>CN at 298 K, δ in ppm): 54.0 (2H, H<sup>3,5</sup>), 51.8 (1H, H<sup>4'</sup> or H<sup>4''</sup>), 48.8 (1H, H<sup>4'</sup> or H<sup>4''</sup>), 47.0 (2H, H<sup>3,5</sup>), 46.4 (1H, H<sup>4'</sup> or H<sup>4''</sup>), 45.8 (1H, H<sup>4'</sup> or H<sup>4''</sup>), 44.0 (6H, Me<sup>3'</sup>), 30.5 (1H, H<sup>5'</sup>), 29.5 (3H, Me<sup>5'</sup>), 28.8 (2H, H<sup>3'</sup>), 26.2 (3H, Me<sup>5'</sup>), 25.2 (1H, H<sup>5'</sup>), 11.8 (1H, H<sup>4</sup>), 9.8 (1H, H<sup>4</sup>), -16.5 (1H, CH<sub>2</sub>), -18.8 (1H, CH<sub>2</sub>), -25.0 (1H, CH<sub>2</sub>), -31.0 (1H, CH<sub>2</sub>), -47.0 (1H, CH<sub>2</sub>), -56.8 (1H, CH<sub>2</sub>), -65.0 (1H, CH<sub>2</sub>), -76.0 (1H, CH<sub>2</sub>).



### 3.3 Results and Discussion

#### 3.3.1 Description of Structure

##### 3.3.1.1 Solid State by X-ray

A perspective view of the discrete complex cation and the atom-labeling scheme are shown in Figure 3.1. Figure 3.2 presents a view of the unit cell contents. Table 3.2 and Table 3.3 contain the essential bond distances and the bond angles respectively. Positional and isotropic thermal parameters are listed in Table 3.4. The two perchlorate counterions exhibit some disorder, as is evident from the large anisotropic thermal parameters for the oxygen atoms listed in Table I (appendix).

The six nitrogen atoms of the two  $\text{H}_2\text{Me}_2\text{bpp}$  ligands coordinate to the iron atom and form a distorted octahedron about it. The ligands adopt the *mer* configuration about the metal atom so that the complex cation has no overall symmetry. This kind of configuration, similar to many other related systems,<sup>125</sup> arise presumably because it leads to reduced interligand interactions. Gross distortions from octahedral symmetry are evident in the  $\text{FeN}_6$  core geometry with Fe-N distances varying from 2.166(4) to 2.277(4) Å (Table 3.2) and angular deviations (Table 3.3). There are two types of heterocyclic nitrogen donor atoms: four pyrazole nitrogens and two pyridine nitrogens. The two types of nitrogen atoms are associated with two different Fe-N bond distances: the pyrazole nitrogens are more closely bound, while the pyridine nitrogens are about 4% more distant. The Fe-N(pyridine) and Fe-N(pyrazole) bond distances are reasonable for iron(II) in the high-spin electronic configuration and agrees well with earlier

**Table 3.2:** Selected Intramolecular Bond Lengths (Å) for  
 $[\text{Fe}(\text{H}_2\text{Me}_2\text{bpp})_2](\text{ClO}_4)_2$

---

Fe - N(1A) 2.277 (4)	Fe - N(1B) 2.264 (4)
Fe - N(1C) 2.176 (4)	Fe - N(1E) 2.166 (4)
Fe - N(1D) 2.207 (4)	Fe - N(1F) 2.169 (4)
N(1B) - C(2B) 1.345 (6)	N(1E) - N(2E) 1.351 (6)
N(1B) - C(6B) 1.335 (6)	N(2E) - C(3E) 1.335 (7)
C(2B) - C(3B) 1.387 (7)	N(1E) - C(5E) 1.339 (7)
C(3B) - C(4B) 1.357 (8)	C(3E) - C(4E) 1.339 (9)
C(4B) - C(5B) 1.391 (8)	C(4E) - C(5E) 1.379 (8)
C(5B) - C(6B) 1.385 (7)	C(4F) - C(5F) 1.367 (7)
C(3) - C(6B) 1.492 (7)	N(1F) - N(2F) 1.364 (5)
C(4) - C(2B) 1.496 (7)	N(1F) - C(5F) 1.327 (6)
C(3) - N(2E) 1.443 (7)	N(2F) - C(3F) 1.331 (6)
C(4) - N(2F) 1.443 (7)	

---

**Table 3.3:** Selected Intramolecular Angles (deg) for  
 $[\text{Fe}(\text{H}_2\text{Me}_2\text{bpp})_2](\text{ClO}_4)_2$

N(1A) - Fe - N(1C) 84.1 (1)	N(1B) - Fe - N(1E) 83.7 (2)
N(1A) - Fe - N(1D) 85.8 (1)	N(1B) - Fe - N(1F) 85.1 (1)
N(1A) - Fe - N(1B) 174.4 (1)	N(1E) - Fe - N(1F) 168.7 (2)
Fe - N(1A) - C(2A) 121.8 (3)	Fe - N(1B) - C(2B) 119.7 (3)
Fe - N(1A) - C(6A) 121.0 (3)	Fe - N(1B) - C(6B) 121.4 (3)
Fe - N(1E) - N(2E) 121.1 (3)	Fe - N(1F) - N(2F) 119.6 (3)
Fe - N(1E) - C(5E) 131.8 (4)	Fe - N(1F) - C(5F) 134.4 (3)
N(1A) - C(2A) - C(3A) 122.6 (5)	N(1B) - C(6B) - C(5B) 122.4 (5)
N(1A) - C(6A) - C(5A) 123.5 (5)	N(1B) - C(2B) - C(3B) 121.2 (5)
C(3A) - C(4A) - C(5A) 118.7 (6)	C(3B) - C(4B) - C(5B) 118.0 (6)
C(2A) - C(3A) - C(4A) 119.2 (6)	C(2B) - C(3B) - C(4B) 120.8 (6)
C(2A) - N(1A) - C(6A) 116.9 (4)	C(2B) - N(1B) - C(6B) 118.5 (4)
C(4A) - C(5A) - C(6A) 119.0 (6)	C(4B) - C(5B) - C(6B) 119.1 (6)
N(1E) - N(2E) - C(3E) 110.0 (5)	N(1F) - N(2F) - C(3F) 111.0 (4)
N(1E) - C(5E) - C(4E) 109.6 (6)	N(1F) - C(5F) - C(4F) 108.8 (5)
N(2E) - C(3E) - C(4E) 108.5 (6)	N(2F) - C(3F) - C(4F) 106.1 (5)
N(2E) - N(1E) - C(5E) 105.8 (5)	N(2F) - N(1F) - C(5F) 105.6 (4)
C(3E) - C(4E) - C(5E) 106.1 (6)	C(3F) - C(4F) - C(5F) 108.5 (5)
C(2A) - C(1) - N(2C) 113.2 (5)	C(2B) - C(4) - N(2F) 115.1 (4)
C(6A) - C(2) - N(2D) 113.2 (4)	C(6B) - C(3) - N(2E) 114.0 (5)

Table 3.4: Positional parameters and B(eq) for  
 $[\text{Fe}(\text{H}_2\text{Me}_2\text{bpp})_2](\text{ClO}_4)_2$

atom	x	y	z	B(eq)
Fe	0.20542(5)	0.24540(5)	0.43460(4)	2.87(2)
Cl(1)	-0.2268(1)	0.7418(2)	0.2090(1)	7.4(1)
Cl(2)	-0.7158(1)	0.7685(1)	0.3965(1)	6.39(8)
O(11)	-0.272(1)	0.645(1)	0.222(1)	10.1(4)
O(12)	-0.212(1)	0.785(1)	0.149(1)	9.8(5)
O(13)	-0.291(1)	0.711(1)	0.2490(8)	6.4(4)
O(14)	-0.252(1)	0.802(1)	0.2649(8)	12.0(4)
O(15)	-0.2867(8)	0.7350(9)	0.1341(6)	9.2(3)
O(16)	-0.179(1)	0.837(1)	0.219(1)	10.0(5)
O(17)	-0.1462(8)	0.6884(8)	0.2152(6)	9.3(3)
O(18)	-0.290(2)	0.799(2)	0.163(1)	6.9(6)
O(19)	-0.176(2)	0.827(2)	0.183(1)	2.4(4)
O(21)	-0.769(2)	0.867(2)	0.406(1)	8.7(6)
O(22)	-0.6512(8)	0.6801(8)	0.4219(6)	5.6(3)
O(23)	-0.8005(4)	0.7256(4)	0.3620(3)	7.8(1)
O(24)	-0.6964(7)	0.8408(8)	0.4487(6)	8.4(3)
O(25)	-0.6625(4)	0.7961(4)	0.3379(3)	7.6(1)
O(26)	-0.6719(7)	0.7073(7)	0.4537(5)	9.3(3)
O(27)	-0.746(1)	0.855(1)	0.4348(8)	3.9(3)
O(28)	-0.636(2)	0.761(2)	0.373(2)	4.8(7)
O(110)	-0.133(1)	0.712(1)	0.262(1)	7.2(5)
O(111)	-0.2797(9)	0.766(1)	0.2686(7)	3.0(3)
O(112)	-0.301(2)	0.674(2)	0.152(2)	11(1)
O(113)	-0.174(2)	0.648(2)	0.213(1)	9.0(7)
N(1A)	0.3040(3)	0.1438(3)	0.5096(2)	3.2(2)
N(1B)	0.1179(3)	0.3583(3)	0.3635(2)	3.1(2)
N(1C)	0.3329(3)	0.2778(3)	0.3880(2)	3.6(2)
N(1D)	0.0920(3)	0.1931(3)	0.4934(2)	3.7(2)
N(1E)	0.2272(3)	0.3634(3)	0.5136(2)	3.8(2)
N(1F)	0.1662(3)	0.1479(3)	0.3422(2)	3.2(2)
N(2C)	0.4210(3)	0.2713(3)	0.4270(2)	4.2(2)
N(2D)	0.1069(3)	0.1061(3)	0.5293(2)	3.9(2)
N(2E)	0.2325(3)	0.4579(3)	0.4932(2)	3.9(2)
N(2F)	0.0804(3)	0.1596(3)	0.2977(2)	3.4(2)
C(1)	0.4328(4)	0.2595(5)	0.5057(3)	4.6(3)
C(2)	0.1700(4)	0.0343(4)	0.5060(3)	3.9(3)
C(2A)	0.3983(4)	0.1628(4)	0.5286(3)	3.7(2)
C(2B)	0.0366(4)	0.3313(4)	0.3203(3)	3.6(2)
C(3)	0.2298(4)	0.4826(4)	0.4172(3)	4.3(3)
C(3A)	0.4604(4)	0.0986(5)	0.5692(3)	5.1(3)
C(3B)	-0.0243(4)	0.4001(4)	0.2828(3)	4.7(3)
C(3C)	0.4866(4)	0.2772(5)	0.3835(4)	5.5(3)
C(3D)	0.0536(4)	0.1004(5)	0.5824(3)	5.0(3)
C(3E)	0.2375(4)	0.5162(5)	0.5516(4)	5.2(3)
C(3F)	0.0733(4)	0.1007(4)	0.2399(3)	4.1(3)
C(4)	0.0100(4)	0.2253(4)	0.3185(3)	3.9(2)
C(4A)	0.4263(5)	0.0104(5)	0.5906(4)	5.9(3)
C(4B)	-0.0039(4)	0.4970(4)	0.2890(3)	5.2(3)
C(4C)	0.4415(5)	0.2873(5)	0.3139(4)	6.0(3)

Table 3.4 (contd.)

atom	x	y	z	B(eq)
C(4D)	0.0025(4)	0.1826(5)	0.5797(4)	5.8(3)
C(4E)	0.2359(5)	0.4603(5)	0.6107(3)	5.5(3)
C(4F)	0.1551(5)	0.0500(4)	0.2476(3)	5.0(3)
C(5A)	0.3309(4)	-0.0098(4)	0.5715(3)	4.9(3)
C(5B)	0.0803(5)	0.5249(4)	0.3334(3)	4.8(3)
C(5C)	0.3454(4)	0.2880(4)	0.3181(3)	4.4(3)
C(5D)	0.0274(4)	0.2394(4)	0.5249(3)	4.4(2)
C(5E)	0.2294(4)	0.3649(5)	0.5861(3)	4.7(3)
C(5F)	0.2118(4)	0.0796(4)	0.3105(3)	3.5(2)
C(6A)	0.2730(4)	0.0573(4)	0.5303(3)	3.6(2)
C(6B)	0.1397(4)	0.4533(4)	0.3689(3)	3.4(2)
C(6D)	0.0592(6)	0.0149(6)	0.6333(5)	8.6(4)
C(6F)	-0.0134(6)	0.0974(7)	0.1826(4)	7.5(4)
C(7D)	-0.0103(5)	0.3380(6)	0.5016(5)	7.2(4)
C(7F)	0.3099(5)	0.0470(5)	0.3402(4)	5.8(3)
H(3A)	0.525(4)	0.115(4)	0.582(3)	8(2)
H(3B)	-0.081(3)	0.384(3)	0.255(2)	4(1)
H(3C)	0.549(3)	0.277(3)	0.406(2)	4(1)
H(3E)	0.247(3)	0.581(3)	0.546(2)	3(1)
H(4A)	0.461(4)	-0.031(4)	0.623(3)	6(1)
H(4B)	-0.045(3)	0.548(3)	0.270(2)	4(1)
H(4C)	0.465(3)	0.292(4)	0.272(2)	5(1)
H(4D)	-0.034(4)	0.197(4)	0.609(3)	6(1)
H(4E)	0.238(3)	0.470(3)	0.657(3)	5(1)
H(4F)	0.165(3)	0.009(3)	0.224(2)	2(1)
H(5A)	0.305(3)	-0.076(4)	0.582(3)	6(1)
H(5B)	0.101(3)	0.586(4)	0.336(3)	5(1)
H(5C)	0.294(3)	0.285(3)	0.280(3)	5(1)
H(5E)	0.227(3)	0.299(3)	0.610(2)	4(1)
H(6DA)	0.013(4)	0.020(4)	0.660(3)	8(2)
H(6DB)	0.0428	-0.0453	0.6054	9.8
H(6FA)	-0.025(4)	0.152(4)	0.169(3)	7(2)
H(6DC)	0.1224	0.0014	0.6634	8.5
H(6FB)	0.005(4)	0.057(4)	0.151(3)	8(2)
H(6FC)	-0.067(4)	0.072(5)	0.204(3)	9(2)
H(7DA)	0.0322	0.3890	0.5099	8.6
H(7DB)	-0.040(4)	0.340(4)	0.459(3)	9(2)
H(7FA)	0.3195	0.0294	0.3854	7.1
H(7DC)	-0.057(4)	0.358(4)	0.522(3)	6(2)
H(7FB)	0.330(3)	0.001(3)	0.319(2)	4(1)
H(7FC)	0.3614	0.0972	0.3418	9.9
H(11)	0.495(3)	0.266(3)	0.523(2)	4(1)
H(12)	0.406(3)	0.310(3)	0.531(2)	5(1)
H(21)	0.153(3)	-0.032(3)	0.523(2)	4(1)
H(22)	0.158(3)	0.024(3)	0.453(3)	4(1)
H(31)	0.233(3)	0.547(3)	0.419(2)	4(1)
H(32)	0.282(3)	0.459(3)	0.401(2)	4(1)
H(41)	-0.048(3)	0.214(4)	0.291(3)	5(1)
H(42)	-0.002(3)	0.206(4)	0.369(3)	5(1)

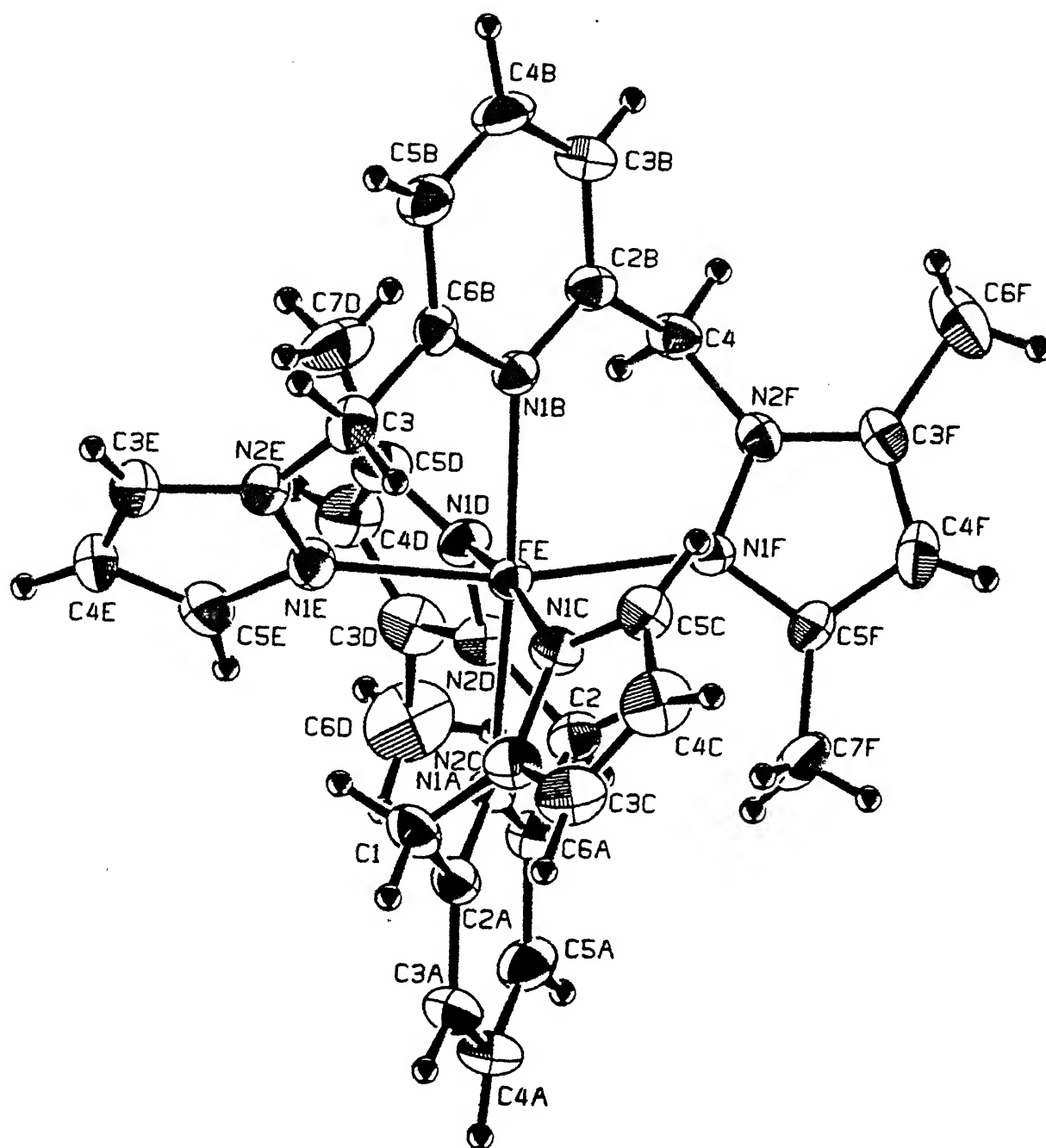


Figure 3.1 Crystal structure of  $[\text{Fe}(\text{H}_2\text{Me}_2\text{bpp})_2](\text{ClO}_4)_2$  showing the atom-labeling scheme

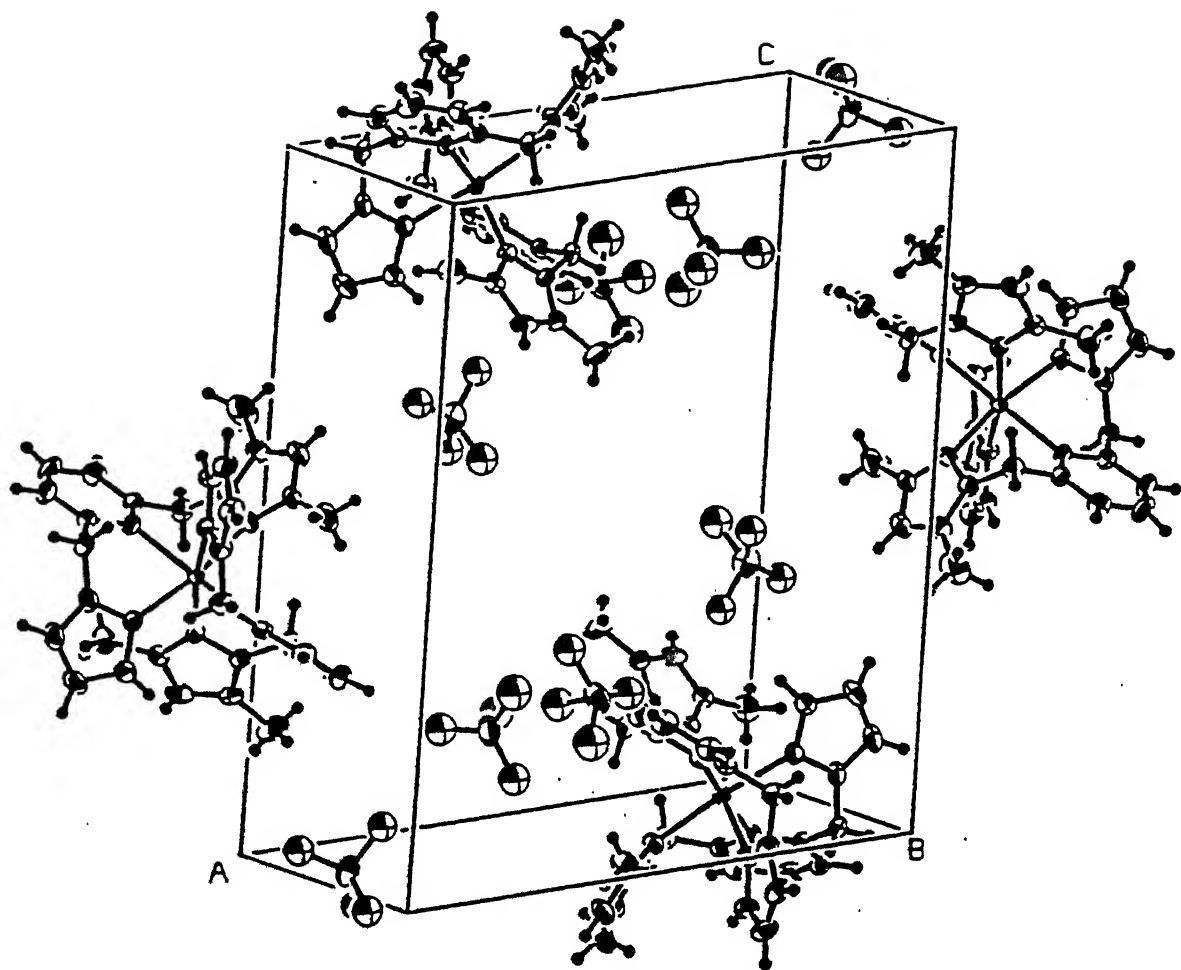


Figure 3.2 Molecular packing in the unit cell of  $[\text{Fe}(\text{H}_2\text{Me}_2\text{bpp})_2](\text{ClO}_4)_2$

results for six-coordinate iron(II) complexes with heteroaromatic nitrogen atoms (see below). It has previously been observed that the donor atom of the five-membered heterocycle is closer to the metal atom than that of the six-membered in a mixed chelate ligand.<sup>186,187</sup> Comparison with the complexes of  $N^1$ -(pyridin-2-yl)-3,5-dimethylpyrazole<sup>186</sup> is particularly relevant since in these and in  $[Fe(H_2Me_2bpp)_2](ClO_4)_2 \cdot 2H_2O$  there is a methyl group adjacent to the donor atom of the five-membered heterocycle. Despite the barrier to coordination expected from this group, the metal-donor atom distance is relatively short and the effect is most marked in the present complex where the average difference  $(Fe-N_{pyridine}) - (Fe-N_{pyrazole})$  is 0.091 Å. The shortness of the  $Fe-N_{pyrazole}$  bond is consistent with the fact that the metal atom is out of the plane of the pyridinyl ring (Table 3.3). Of particular interest are the iron-pyridine bond lengths, which range from 2.264(4) to 2.277(4) Å. The average  $Fe-N_{pyridine}$  bond distance encountered here is the longest observed for high-spin six-coordinate heteroaromatic nitrogen donors (Table 3.5).

The pyridine and pyrazole rings are each planar to within 0.006 Å and 0.002 Å respectively. The two pyridine ring meanplanes are tilted to each other at an angle of 26.98°. The two pyrazole meanplanes of each ligand make an angle of 60.40° and 68.45° to each other. The pyridine meanplane is tilted to adjacent pyrazole rings within a ligand at angles of 59.60° and 49.27° and 59.20° and 58.70°. Thus the six-membered chelate rings exist in boat conformations. A similar chelate ring conformation was observed in the X-ray structure of  $[Ni(H_4bpp)_2](ClO_4)_2$ .<sup>114</sup>



Table 3.5: Comparison of Fe-N<sub>pyridine</sub> and Fe-N<sub>pyrazole</sub> Distances  
in Mononuclear High-Spin Fe<sup>II</sup>N<sub>6</sub> Complexes

Complexes	av Fe-N dist, Å		ref
	Fe-N <sub>pyridine</sub>	Fe-N <sub>pyrazole</sub>	
Fe(H <sub>2</sub> Me <sub>2</sub> bpp) <sub>2</sub> <sup>2+</sup> (2)	2.271	2.180	this work
Fe(pyridine) <sub>6</sub> <sup>2+</sup>	2.258		188
Fe(pyridine) <sub>4</sub> (NCS) <sub>2</sub>	2.255		189
Fe[HB(3-Phpz) <sub>3</sub> ] <sub>2</sub>		2.246	127
Fe[HB(3,5-Me <sub>2</sub> pz) <sub>3</sub> ] <sub>2</sub>		2.172	190
Fe(2-Mephen) <sub>3</sub> <sup>2+</sup>	2.237 (2.208)		191
Fe(α-picolylamine) <sub>3</sub> <sup>2+</sup> (bromide salt; 215 K)	2.223		192
Fe(6-Mebpy) <sub>3</sub> <sup>2+</sup>	2.209		125
Fe(α-picolylamine) <sub>3</sub> <sup>2+</sup> (methanol solvate)	2.210		193
Fe(4mpt) <sub>3</sub> <sup>2+</sup> [4mpt = 4-methyl-2-(pyridin-2-yl)thiazole]	2.199		187
FeL <sub>3</sub> <sup>2+</sup> [L = N <sup>1</sup> -(pyridin-2-yl)-3,5-dimethylpyrazole]	2.064	1.984	186

### 3.3.1.2 Solution State by $^1\text{H}$ NMR

Solution structure of  $[\text{Fe}(\text{H}_2\text{Me}_2\text{bpp})_2]^{2+}$  has been examined using  $^1\text{H}$  NMR spectroscopy. An immediate question is whether or not the solid-state structure in Figure 3.1 is retained in solution.

Analysis of the spectra of  $[\text{Fe}(\text{H}_4\text{bpp})_2]^{2+}$  and  $[\text{Fe}(\text{Me}_4\text{bpp})_2]^{2+}$  in  $\text{CD}_3\text{CN}$  has been given earlier (Chapter 2, Section 2.4.1.2). The spectrum of  $[\text{Fe}(\text{H}_2\text{Me}_2\text{bpp})_2](\text{ClO}_4)_2$  in  $\text{CD}_3\text{CN}$  is shown in Figure 3.3. Assignments of the resonances are made by a combination of the expected behavior for paramagnetically shifted resonances,<sup>140,141</sup> integrated area ratios and comparison with the spectra of  $[\text{Fe}(\text{R}_4\text{bpp})_2]^{2+}$  ( $\text{R} = \text{H}, \text{Me}$ ). As the symmetry of the complex,  $[\text{Fe}(\text{H}_2\text{Me}_2\text{bpp})_2]^{2+}$  is very low (vide X-ray structure) due to the presence of unsymmetrical nature of  $\text{H}_2\text{Me}_2\text{bpp}$ , almost all the protons are expected to be magnetically non-equivalent. A large number of peaks are observed (Figure 3.3) justifying our expectation. The eight upfield resonances out of which four are very broad are assigned to axial and equatorial protons of the four methylene groups. Thus these two protons present in both arms of each ligand are not interconverting on the NMR time scale, otherwise a singlet would have resulted for each methylene group.

### 3.4 Concluding Remarks

(i) A fairly distorted octahedral coordination is observed for  $[\text{Fe}(\text{H}_2\text{Me}_2\text{bpp})_2](\text{ClO}_4)_2$  from single crystal X-ray analysis. This is arising out of the steric crowding of the methyl group substituents near the donor site. The average  $\text{Fe}-\text{N}(\text{pyridine})$  bond length for this complex is the longest among the known iron(II) complexes with  $\text{FeN}_6$  coordination.

(ii) The solid-state structure is retained in solution as is

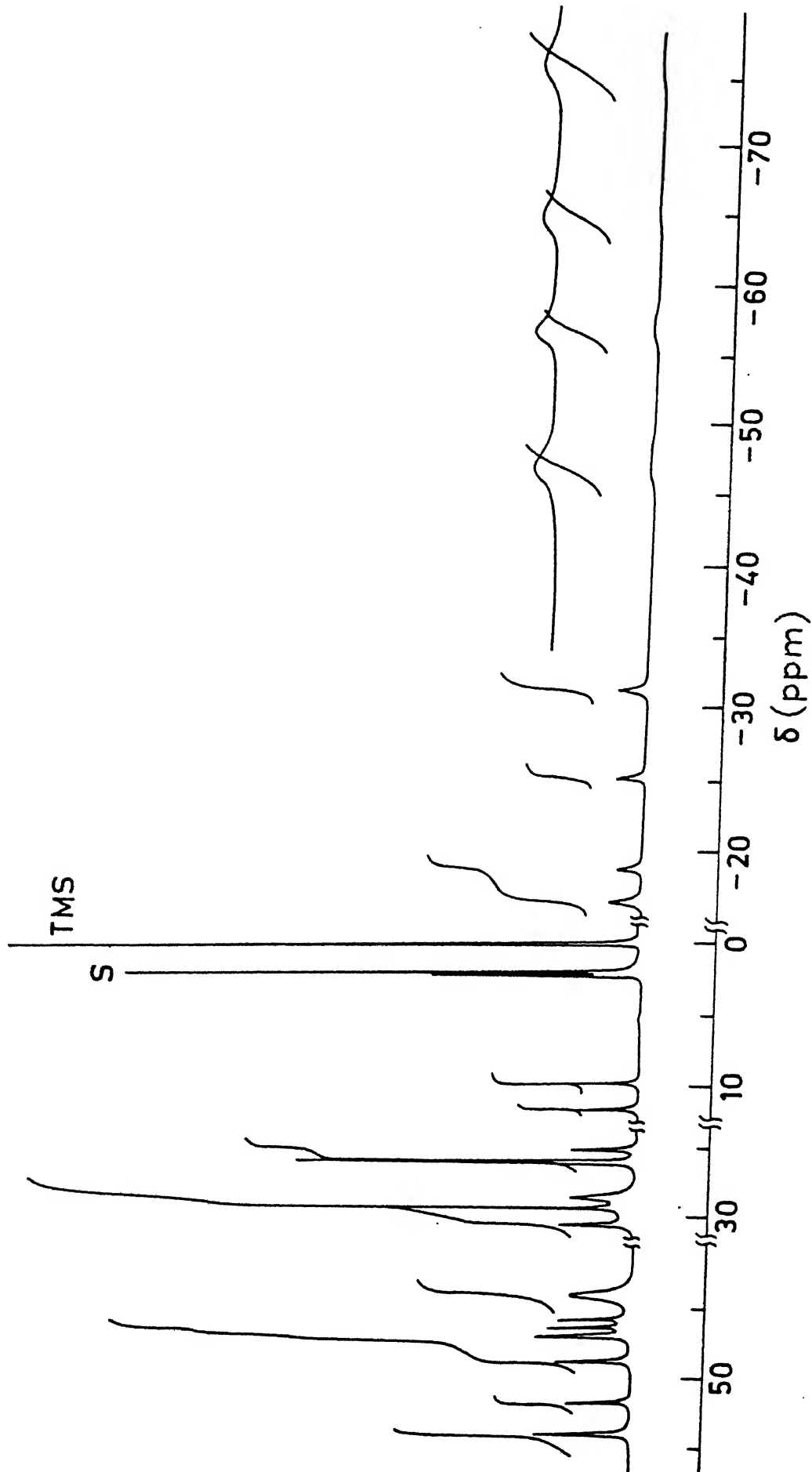


Figure 3.3 400 MHz  $^1\text{H}$  NMR spectrum of  $[\text{Fe}(\text{H}_2\text{Me}_2\text{bpp})_2](\text{ClO}_4)_2$  in  $\text{CD}_3\text{CN}$  at 300 K (solvent peak marked by S)

## CHAPTER 4

Magnetic and Mössbauer Spectroscopic Characterization of  
Singlet  $\rightleftharpoons$  Quintet Transition in a Six-Coordinate Iron(II)  
Complex of a Tridentate Pyridylpyrazole Ligand.

In Chapter 2 it has been shown that 2,6-bis(pyrazol-1-yl-methyl)pyridine,  $H_4bpp$ , and its methyl substituted derivatives,  $H_2Me_2bpp$  and  $Me_4bpp$ , form bis chelates with iron(II) ( $S = 2$ ) and nickel(II) ( $S = 1$ ) producing ligand fields in the range expected<sup>43</sup> to exhibit spin-transition in the iron(II) complexes. The profound changes in the absorption spectral and electrochemical properties of the iron(II) ion,  $[Fe(H_4bpp)_2]^{2+}$ , on the introduction of methyl groups in the other two ligands are associated with the steric effects of these methyl groups which are adjacent to donor atoms. These effects are manifested by the steric barrier to the close approach of the metal atom to the donor atoms which causes an effective reduction in the field strength experienced by the metal and distortions in the coordination octahedron.

In this chapter we describe the characterization of a novel iron(II) system  $[Fe(H_4bpp)_2](ClO_4)_2 \cdot H_2O$  exhibiting spin transition in the solid-state from variable temperature (8-300 K) magnetic susceptibility and  $^{57}Fe$  Mössbauer spectral measurements.

A relatively large variety of systems exhibiting spin-transition have been found in the class of six-coordinate iron(II) complexes<sup>40,144-146,192-203</sup> with heterocyclic nitrogen donor atoms and  $\alpha$ -diimine ligands. It is worth noting that the first example of an iron(II) spin crossover system was discovered by Madeja and König<sup>204</sup> in 1963. A selected listing of iron(II) complexes having  $Fe^{II}N_6$  coordination sphere which exhibit spin equilibria is compiled in Table 4.1.

Table 4.1: Selected Six Coordinate Iron(II) Complexes Exhibiting Spin Equilibra

Compounds	Comments	References
[Fe(phen) <sub>2</sub> (NCX) <sub>2</sub> ] (X = S or Se) (phen = phenanthroline)	Both the compounds are high spin at room temperature and low spin at 77 K, with $T_c$ of 174 K (for X=S) and 232 K (for X=Se)	205
[Fe(HBPz <sub>3</sub> ) <sub>2</sub> ] {HBPz <sub>3</sub> = hydrotris(1-pyrazolyl)borate}	Complexes with high spin, low spin and intermediate spin produced by appropriate substitution; characterization in solution by optical spectra, susceptibility data and NMR experiments	206
[Fe(6Mepy)(py) <sub>2</sub> -tren](PF <sub>6</sub> ) <sub>2</sub> {(6Mepy)(py) <sub>2</sub> tren = 4-(6-methylpyridyl)bis(2-pyridyl)-3-aza-3-butenylamine}	Tunning of ligand field strength by substitution near donor site; spin equilibrium in the solid state as well as in solution	118
[Fe(papth) <sub>2</sub> ] <sub>2</sub> X <sub>2</sub> (X = NO <sub>3</sub> <sup>-</sup> , ClO <sub>4</sub> <sup>-</sup> ) {papth = 2-(2-pyridylamino)-4-(2-pyridyl)thiazole}	A detail study of Mössbauer spectroscopy with $T_c$ = 34 K	207
[Fe{(py)imH} <sub>3</sub> ] (BPh <sub>4</sub> ) <sub>2</sub> {(py)imH = 2-(2-pyridyl)imidazole}	Spin equilibrium in solution by variable temperature magnetic and electronic spectral studies; determination of forward and reverse rate constants by Laser Raman temperature-jump kinetics	208
[Fe(tpen)](ClO <sub>4</sub> ) <sub>2</sub> {tpen = N,N,N',N'-tetra(2-pyridylmethyl)-1,2-ethane diamine}	Correlation of molecular and electronic structure of iron(II) complex to their nickel(II) and cobalt(II) analogs in solution; characterization in solution by <sup>13</sup> C NMR; magnetic measurement and electronic spectra	120

Table 4.1 (contd.)

Compounds	Comments	References
[Fe(bpen)(NCS) <sub>2</sub> ] {bpen = N,N'-bis-(2-pyridylmethyl)-1,2-ethanediamine}	Dependence of ligand field strength with chelate ring size; magnetic and infrared measurements for characterization	122
[Fe(tpa)(NCS) <sub>2</sub> ] {tpa = tris(2-pyridylmethyl)amine}	Variable temperature magnetic susceptibility measurements and infrared spectra characterize $^5T_{2g} \rightleftharpoons ^1A_1$ equilibrium	121
[Fe(bi) <sub>3</sub> ](ClO <sub>4</sub> ) <sub>2</sub> {bi = 2,2'-bi-2-imidazoline}	Variable temperature Mössbauer and X-ray powder diffraction measurements; an order-disorder transition of ClO <sub>4</sub> anion	209
[Fe(AMP) <sub>3</sub> ](ClO <sub>4</sub> ) <sub>2</sub> {AMP = 2-(amino-methyl)pyridine}	Temperature dependence of magnetic moment, EPR and absorption spectra in solution describe spin equilibrium; calculations of thermodynamic parameters, $\Delta H$ and $\Delta S$	210, 211
[Fe(2-pea) <sub>3</sub> ](ClO <sub>4</sub> ) <sub>2</sub> {2-pea = 2-(2-pyridylmethyl)ethylamine}	Transition temperature ( $T_C$ ) at 90 K	210
[Fe(bztpy) <sub>2</sub> ](ClO <sub>4</sub> ) <sub>2</sub> ·CHCl <sub>3</sub> {bztpy = 2,6-bis-(benzothiazol-2'-yl)pyridine}	Variable temperature magnetism and electronic spectral characterization; calculation of $\Delta H$ and $\Delta S$	203
[Fe(sar)] <sup>2+</sup> {sar = 3,6,10,13,16,19-hexaazabicyclo[6,6,6]icosane}	Spin-equilibrium in solution; characterized by magnetism, visible and <sup>1</sup> H NMR spectra	212

Table 4.1 (contd.)

Compounds	Comments	References
[Fe(ppz) <sub>3</sub> ](BF <sub>4</sub> ) <sub>2</sub> ·H <sub>2</sub> O {ppz = (pyridine-2-yl)-3,5-dimethylpyrazole}	Single crystal X-ray diffraction at two temperatures, variable temperature Mössbauer and magnetism determine spin equilibrium	187
[Fe(2bt) <sub>3</sub> ](BF <sub>4</sub> ) <sub>2</sub> {2bt = 2,2'-bi-thiazole}	Characterization by magnetic and Mössbauer measurements; single crystal X-ray diffraction of nickel analog	213
[Fe(pyq) <sub>3</sub> ](BF <sub>4</sub> ) <sub>2</sub> {pyq = 2-(pyridine-2-yl)quinoline}	Steric crowding near donor site; characterization of spin equilibrium both in solid and solution	196
[Fe(btr) <sub>2</sub> (NCX) <sub>2</sub> ] (X = S or Se) {btr = 4,4'-bi-1,2,4-triazole}	Variable temperature EPR and NMR studies; single crystal X-ray of NCSe complex	195



## 4.1 Experimental Section

### 4.1.1 Solvents and reagents

Details of solvent purification are already discussed in Chapter 2 (Section 2.1.1).

### 4.1.2 Measurements

Variable-temperature magnetic susceptibility measurements were made on powdered samples over the temperature range  $8.0 < T < 300$  K by the Faraday method. Details are given in Chapter 2 (Section 2.1.2). Effective magnetic moments were calculated from  $\mu_{\text{eff}} = 2.828 [\chi_M T]^{1/2}$ , where  $\chi_M$  is the corrected molar susceptibility. The diamagnetic contributions were calculated by using values<sup>134</sup> of  $-239 \times 10^{-6} \text{ cm}^3 \text{ mol}^{-1}$  for  $[\text{Fe}(\text{H}_4\text{bpp})_2](\text{ClO}_4)_2 \cdot \text{H}_2\text{O}$  and  $-400 \times 10^{-6} \text{ cm}^3 \text{ mol}^{-1}$  for  $[\text{Fe}(\text{Me}_4\text{bpp})_2](\text{ClO}_4)_2 \cdot 2\text{H}_2\text{O}$ . All measurements were made at a fixed field strength and field dependence of the magnetic susceptibility was not studied. The magnetic susceptibility data, corrected for diamagnetism, are listed in Tables 4.2 and 4.3.

For  $^{57}\text{Fe}$  Mössbauer spectroscopy,  $\gamma$ -ray resonance spectra were obtained in the laboratory of Dr. A. K. Nigam, Low-Temperature Physics Group, TIFR, India by using a standard, constant-acceleration spectrometer calibrated with metallic iron at room temperature. All isomer shifts are reported with respect to the room-temperature  $\text{Fe}(0)$  transmission spectrum. The observed spectra were computer-fitted to Lorentzian lines employing a least-squares minimization technique.

## 4.2 Syntheses of Compounds

Details of preparation of compounds are given in Chapter 2 (Section 2.3).

## 4.3 Results and Discussion

### 4.3.1 Evidence for Spin-State Transition

#### 4.3.1.1 Magnetic Susceptibility and Thermodynamic Considerations

Our interest in the examination of the behavior of the spin-state of these complexes as a function of temperature stems from two experimental facts: (i) The room-temperature magnetic moments of these bis(ligand) complexes with  $\text{Fe}^{\text{II}}\text{N}_6$  coordination sphere correspond to high-spin configuration (Chapter 2) which is not very common for this coordination sphere. (ii) The ligand  $\text{H}_4\text{bpp}$  provides a field about iron(II) close to the critical value at the singlet/quintet crossover, as is suggested by the spectral data for this complex as well as from the data on related nickel(II) complex (Chapter 2). Hence the magnetic susceptibility studies on two extreme members  $[\text{Fe}(\text{H}_4\text{bpp})_2](\text{ClO}_4)_2 \cdot \text{H}_2\text{O}$  and  $[\text{Fe}(\text{Me}_4\text{bpp})_2](\text{ClO}_4)_2 \cdot 2\text{H}_2\text{O}$  were investigated in the temperature range 8-300 K (Table 4.2 and Table 4.3). The magnetic properties are shown in Figures 4.1 and 4.2 in the form of  $\mu_{\text{eff}}$  vs.  $T$  and  $1/\chi_M$  vs.  $T$  respectively.

The magnetic properties of  $[\text{Fe}(\text{H}_4\text{bpp})_2](\text{ClO}_4)_2 \cdot \text{H}_2\text{O}$  are indicative of the occurrence of a temperature-induced singlet  $\rightleftharpoons$  quintet transition in the cation. The moments at high temperature are normal for iron(II) in the quintet  $^5\text{T}_2$  state (for convenience, the designation of overall octahedral symmetry is used throughout, although the actual symmetry of the coordination polyhedron is lower than that). At low temperatures  $[\text{Fe}(\text{H}_4\text{bpp})_2](\text{ClO}_4)_2 \cdot \text{H}_2\text{O}$

**Table 4.2:** Variable Temperature Magnetic Susceptibility Data for  
 $[\text{Fe}(\text{H}_4\text{bpp})_2](\text{ClO}_4)_2 \cdot \text{H}_2\text{O}$

T(K)	$\chi_M$	$\mu_{\text{eff}}$	T(K)	$\chi_M$	$\mu_{\text{eff}}$
8.8	$5.087 \times 10^{-3}$	0.60	90.0	$7.654 \times 10^{-4}$	0.74
11.8	$3.734 \times 10^{-3}$	0.59	110.0	$7.467 \times 10^{-4}$	0.81
15.0	$2.870 \times 10^{-3}$	0.59	130.0	$5.963 \times 10^{-4}$	0.79
20.0	$2.419 \times 10^{-3}$	0.62	140.0	$3.521 \times 10^{-4}$	0.63
25.0	$1.883 \times 10^{-3}$	0.61	150.0	$6.715 \times 10^{-4}$	0.90
30.0	$1.273 \times 10^{-3}$	0.55	170.0	$1.912 \times 10^{-3}$	1.61
35.0	$7.467 \times 10^{-4}$	0.46	180.0	$3.020 \times 10^{-3}$	2.09
45.0	$7.091 \times 10^{-4}$	0.51	200.0	$4.899 \times 10^{-3}$	2.80
50.0	$8.782 \times 10^{-4}$	0.59	220.0	$6.440 \times 10^{-3}$	3.37
60.0	$8.406 \times 10^{-4}$	0.64	240.0	$7.680 \times 10^{-3}$	3.84
65.0	$8.030 \times 10^{-4}$	0.65	260.0	$8.657 \times 10^{-3}$	4.26
70.0	$8.030 \times 10^{-4}$	0.67	280.0	$9.296 \times 10^{-3}$	4.57
75.0	$7.654 \times 10^{-4}$	0.68	300.0	$9.620 \times 10^{-3}$	4.87
80.0	$7.654 \times 10^{-4}$	0.70			

**Table 4.3:** Variable Temperature Magnetic Susceptibility Data for  
 $[\text{Fe}(\text{Me}_4\text{bpp})_2](\text{ClO}_4)_2 \cdot 2\text{H}_2\text{O}$

T(K)	$\chi_M$	$\mu_{\text{eff}}$	T(K)	$\chi_M$	$\mu_{\text{eff}}$
8.8	0.3929	5.26	100.0	0.0346	5.27
11.8	0.3015	5.34	120.0	0.0292	5.30
15.0	0.2284	5.24	140.0	0.0250	5.29
20.0	0.1806	5.38	160.0	0.0217	5.27
30.0	0.1235	5.45	180.0	0.0192	5.26
40.0	0.0928	5.45	220.0	0.0157	5.26
50.0	0.0651	5.11	240.0	0.0144	5.25
70.0	0.0502	5.30	280.0	0.0123	5.24
90.0	0.0388	5.29	300.0	0.0112	5.19

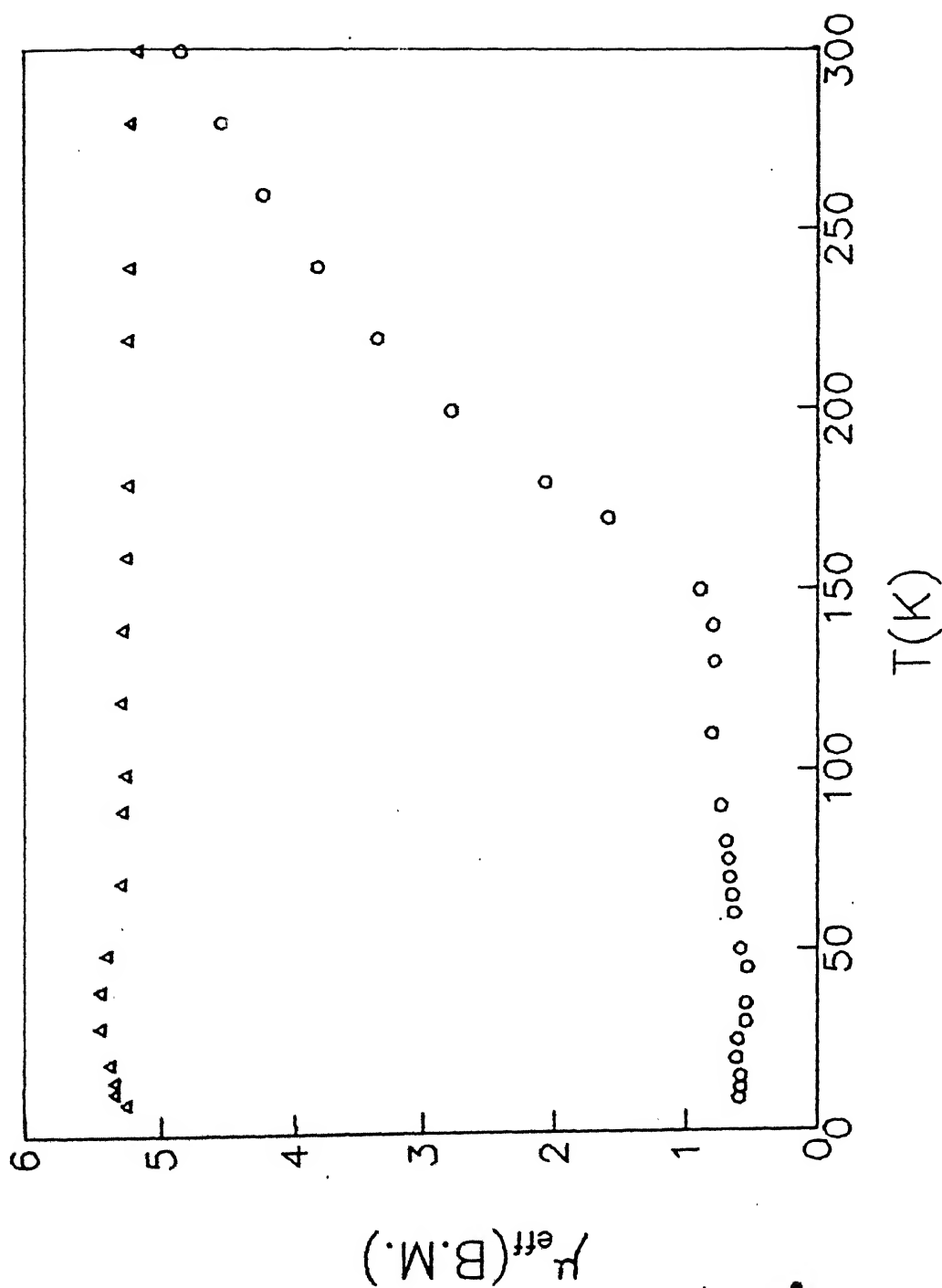


Figure 4.1 Effective magnetic moment of  $[\text{Fe}(\text{H}_4\text{bpp})_2](\text{ClO}_4)_2 \cdot \text{H}_2\text{O}$  (o) and  $[\text{Fe}(\text{Me}_4\text{bpp})_2](\text{ClO}_4)_2 \cdot 2\text{H}_2\text{O}$  ( $\Delta$ ) as a function of temperature

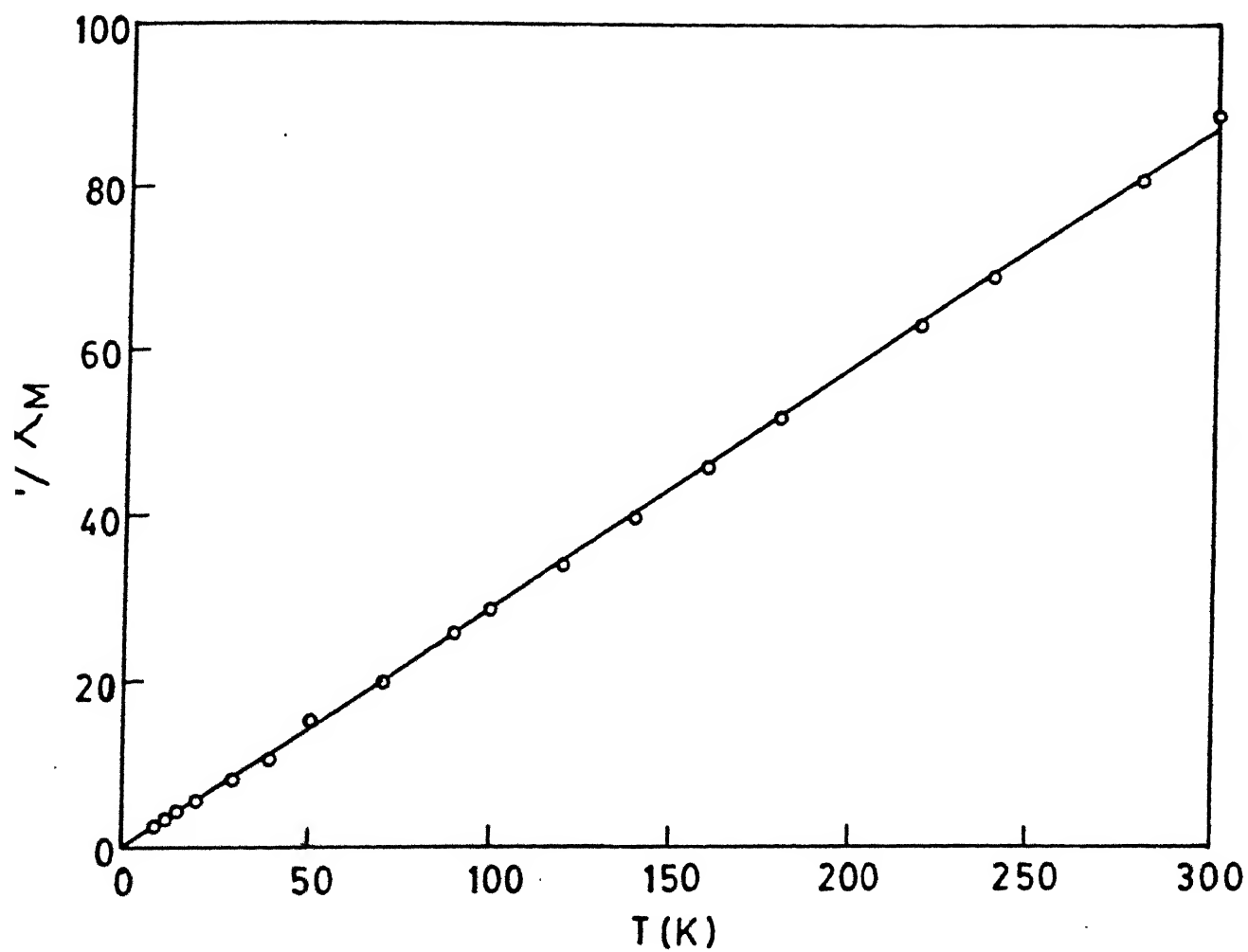
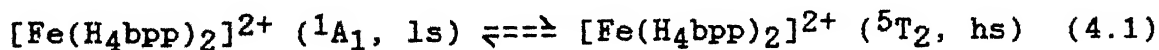


Figure 4.2 Reciprocal of molar susceptibility of  $[\text{Fe}(\text{Me}_4\text{bpp})_2](\text{ClO}_4)_2 \cdot 2\text{H}_2\text{O}$  as a function of temperature

has very low magnetic moments which are typical for the metal ion in the singlet  $^1A_1$  state. As the temperature is increased the moment gradually increases and this is indicative of an increased population of quintet state species. The behavior of this complex is more or less normal for a system displaying a continuous transition over a fairly broad range of temperature. Within the experimental temperature range the transition is almost complete.

As is apparent from Figure 4.2,  $[\text{Fe}(\text{Me}_4\text{bpp})_2](\text{ClO}_4)_2 \cdot 2\text{H}_2\text{O}$  follows the Curie-Weiss behavior from room temperature to 8.8 K. The Curie constant is in good agreement with that for a  $S = 2$  ground state ( $C = 3$  when  $g = 2$ )<sup>214</sup> with a Curie-Weiss temperature of -1.45 K. Thus no spin pairing was observed in  $[\text{Fe}(\text{Me}_4\text{bpp})_2](\text{ClO}_4)_2 \cdot 2\text{H}_2\text{O}$  even at the lowest limit of the experimental temperature range. The methyl group adjacent to the pyrazole nitrogen atom apparently interferes with the close approach to the metal atom necessary for spin pairing.

An attempt to evaluate enthalpy and entropy changes for the spin transition of  $[\text{Fe}(\text{H}_4\text{bpp})_2](\text{ClO}_4)_2 \cdot \text{H}_2\text{O}$  (Equation 4.1) was



made using the following equations<sup>118,120</sup> whereby equilibrium

$$m(\text{hs}) = (\chi_M - \chi_{\text{ls}}) / (\chi_{\text{hs}} - \chi_{\text{ls}}) \quad (4.2)$$

$$m(\text{ls}) = (\chi_{\text{hs}} - \chi_M) / (\chi_{\text{hs}} - \chi_{\text{ls}}) \quad (4.3)$$

constants,  $K_{\text{eq}} = m(\text{hs})/m(\text{ls})$  are calculated from the relative concentrations of the high- and low-spin forms present at any temperature. Here  $m$  is the mole fraction of the spin isomer,  $\chi_M$

is the experimental molar susceptibility at a given temperature, while  $\chi_{hs}$  and  $\chi_{ls}$  are the corrected molar susceptibilities of the pure high-spin and pure low-spin components, respectively. The pure high-spin data was evaluated from the data for  $[\text{Fe}(\text{Me}_4\text{bpp})_2](\text{ClO}_4)_2 \cdot 2\text{H}_2\text{O}$  at the corresponding temperatures and the pure low-spin data was determined for  $[\text{Fe}(\text{H}_4\text{bpp})_2](\text{ClO}_4)_2 \cdot \text{H}_2\text{O}$  from the low temperature data (Table 4.4). Figure 4.3 gives a linear plot of  $\ln K_{eq}$  vs  $1/T$  in the temperature range 170-300 K. The plot reveals a marked curvature below 170 K. It is well known that this spin transition is a cooperative one in most Fe(II) systems and cannot be fitted solely by the kind of simple thermodynamic model we have chosen here. Nevertheless, it is possible to extract some information of the thermodynamic parameters. The derived  $\Delta H$  and  $\Delta S$  values are  $3.10 \text{ kcal mol}^{-1}$  and  $13.38 \text{ eu}$  respectively. These thermodynamic parameters are similar to those found for other spin equilibria systems of iron(II).<sup>118,120,211,215-217</sup> The source of the  $\Delta H$  is the Fe-N bond length increase,<sup>40</sup> of the order of 0.15-0.20 Å, which accompanies the transition from low- to high-spin, i.e., reorganization of the inner coordination sphere. The entropy term for a simple spin equilibrium between singlet and quintet levels would be only 3.2 eu due to the spin multiplicity change ( $R \ln 5 = 3.2$ ).<sup>116,206,211</sup> The value of  $\Delta S$  in excess of that predicted for a change in spin only is a feature of most of the examples of spin equilibria in octahedral iron(II) systems so far described.<sup>40,41</sup> This could be accounted for in terms of a temperature dependence of the effective crystal field and on the different vibrational frequencies in the high-spin and



Table 4.4: Mole fractions of High-spin and Low-spin part, and Equilibrium Constant for  $[\text{Fe}(\text{H}_4\text{bfp})_2](\text{ClO}_4)_2 \cdot \text{H}_2\text{O}$

T(K)	$10^3/T$	$10^3 \times \chi_M$	$\chi_{\text{hs}}$	m(hs)	m(ls)	$K_{\text{eq}}$	$\ln K_{\text{eq}}$
300	3.33	9.62	0.0112	0.8543	0.1457	5.8634	1.769
280	3.57	9.30	0.0123	0.7486	0.2514	2.9777	1.091
260	3.85	8.66	0.0134	0.6389	0.3611	1.7693	0.571
240	4.17	7.68	0.0144	0.5216	0.4784	1.0903	0.086
220	4.55	6.44	0.0157	0.3967	0.6033	0.6576	-0.419
200	5.00	4.90	0.0175	0.2659	0.7341	0.3622	-1.016
180	5.55	3.02	0.0192	0.1415	0.8584	0.1648	-1.803
170	5.88	1.91	0.0205	0.0776	0.9224	0.0841	-2.475
150	6.67	0.67	0.0234	0.0139	0.9861	0.0141	-4.262

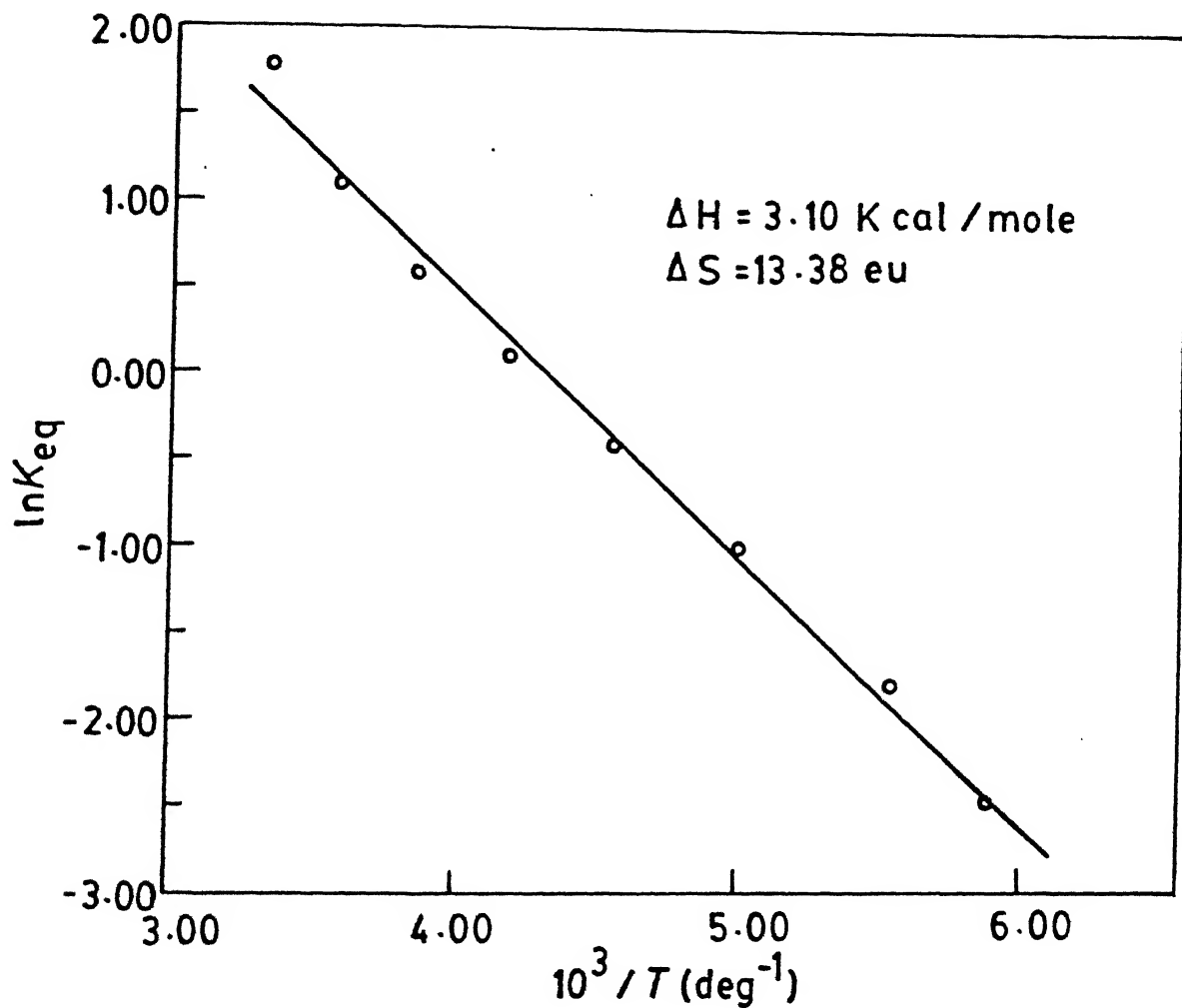


Figure 4.3 Plot of the variation of  $\ln K_{eq}$  against  $T$  for the spin-state equilibrium of  $[\text{Fe}(\text{H}_4\text{bpp})_2](\text{ClO}_4)_2 \cdot \text{H}_2\text{O}$

low-spin states.

#### 4.3.1.2 Mössbauer Spectral Effect

The origin of the temperature dependence of the magnetism of  $[\text{Fe}(\text{H}_4\text{bpp})_2](\text{ClO}_4)_2 \cdot \text{H}_2\text{O}$  is clearly revealed by Mössbauer spectral data. The Mössbauer spectral data (Table 4.5), like the magnetic, show the temperature-induced change in ground state for  $[\text{Fe}(\text{H}_4\text{bpp})_2](\text{ClO}_4)_2 \cdot \text{H}_2\text{O}$ . Figure 4.4 shows three typical spectra, i.e. those collected at 80, 200, and 300 K. With increasing temperature, the  $^5\text{T}_2$  state gains intensity, while the intensity of the  $^1\text{A}_1$  state simultaneously decreases. At 300 K, the contribution of the  $^5\text{T}_2$  state is clearly predominant. At 80 K, the contribution of quintet state species has disappeared and the spectrum shows a doublet with small quadrupole splitting characteristic of the  $^1\text{A}_1$  state. The spectrum at 200 K reveals a superposition of separate spectra due to singlet and quintet state species.

The complex  $[\text{Fe}(\text{Me}_4\text{bpp})_2](\text{ClO}_4)_2 \cdot 2\text{H}_2\text{O}$  has Mössbauer spectral behavior at 300 K (Figure 4.5) characteristic of a purely high-spin state. The isomer shift and quadrupole splitting observed for the singlet and quintet state species in the spectra of  $[\text{Fe}(\text{H}_4\text{bpp})_2](\text{ClO}_4)_2 \cdot \text{H}_2\text{O}$  and  $[\text{Fe}(\text{Me}_4\text{bpp})_2](\text{ClO}_4)_2 \cdot 2\text{H}_2\text{O}$  are comparable with that of the high-spin and low-spin complexes of related systems.<sup>43</sup>

#### 4.3.1.3 d-d Transitions

The ligand field strengths of  $\text{H}_4\text{bpp}$ ,  $\text{H}_2\text{Me}_2\text{bpp}$ , and  $\text{Me}_4\text{bpp}$  ligands toward six-coordinate iron(II) were determined from their  $^5\text{T}_2 \rightarrow ^5\text{E}$  transitions (Chapter 2). Interestingly,

Table 4.5: Mössbauer Data for Iron(II) Systems

Complexes	Temperature	Spin-state	$\delta$ , mm s <sup>-1</sup>	$\Delta E_Q$ , mm s <sup>-1</sup>
[Fe(H <sub>4</sub> bpp) <sub>2</sub> ] (ClO <sub>4</sub> ) <sub>2</sub> ·H <sub>2</sub> O	300 K	<sup>5</sup> T <sub>2</sub>	0.98	1.92
	200 K	<sup>5</sup> T <sub>2</sub>	0.71	2.42
		<sup>1</sup> A <sub>1</sub>	0.50	0.37
	80 K	<sup>1</sup> A <sub>1</sub>	0.53	0.39
[Fe(Me <sub>4</sub> bpp) <sub>2</sub> ] (ClO <sub>4</sub> ) <sub>2</sub> ·2H <sub>2</sub> O	300 K	<sup>5</sup> T <sub>2</sub>	1.07	2.85

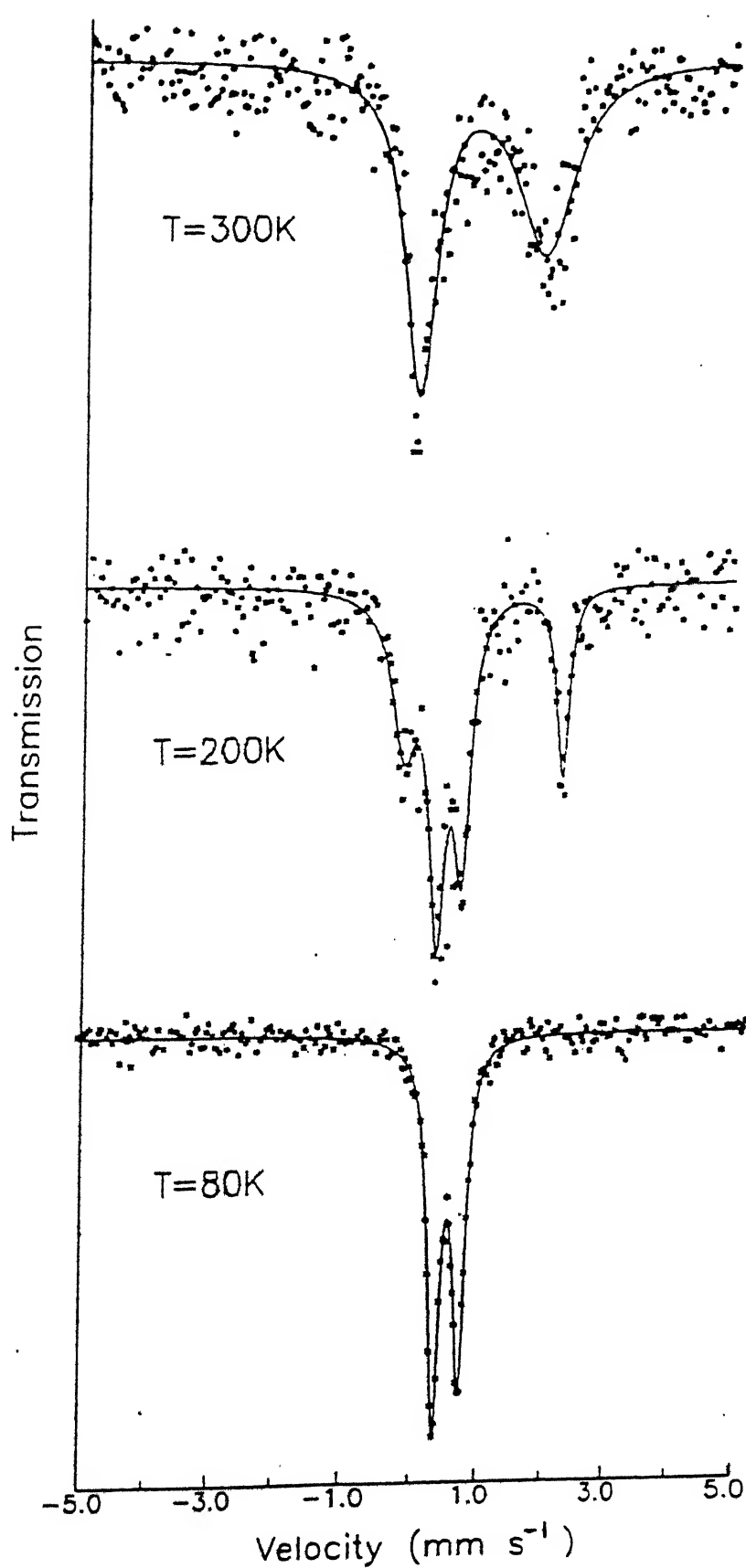


Figure 4.4  $^{57}\text{Fe}$  Mössbauer spectra of  $[\text{Fe}(\text{H}_4\text{bpp})_2](\text{ClO}_4)_2 \cdot \text{H}_2\text{O}$  at 80, 200, and 300 K.

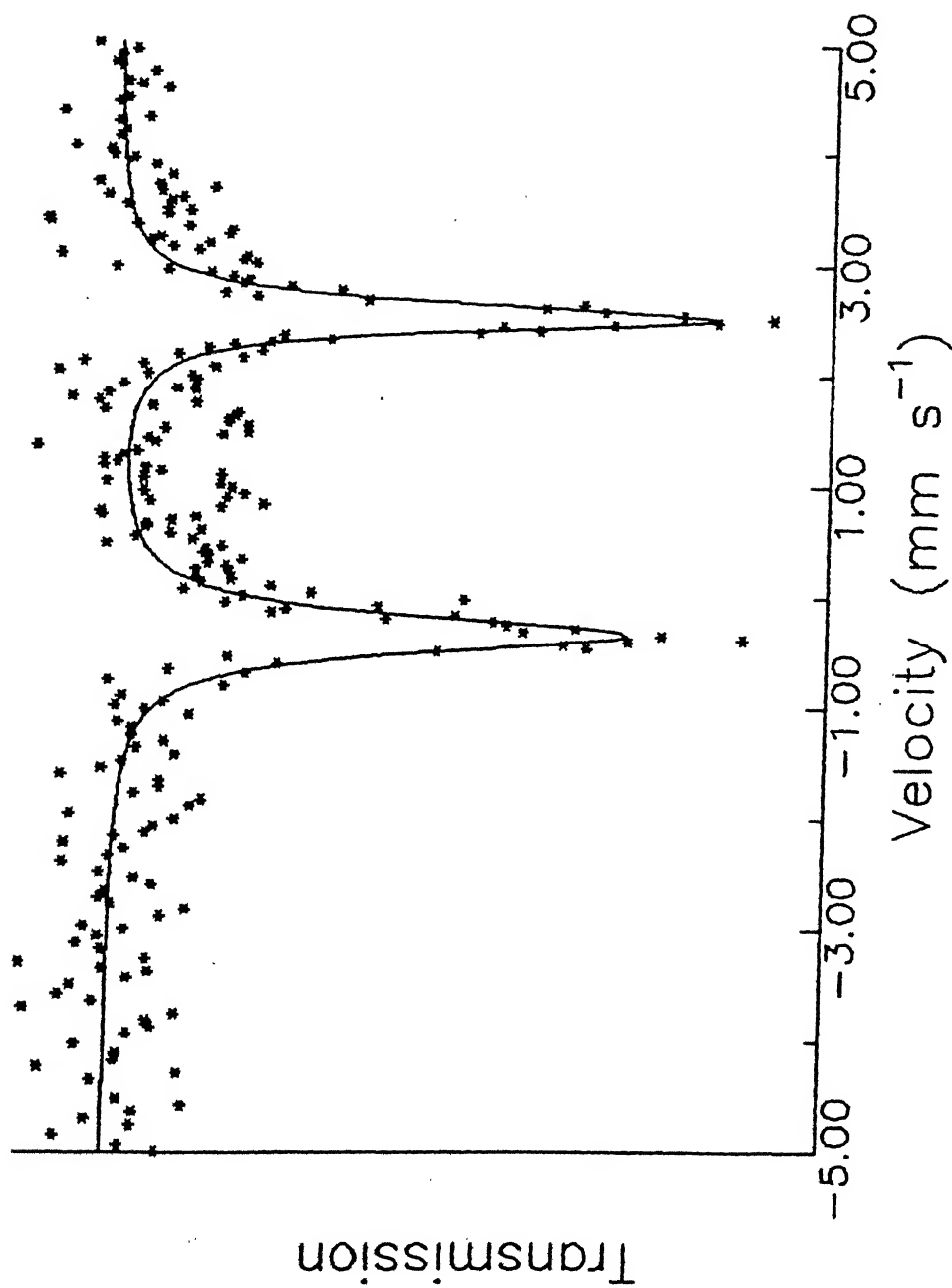


Figure 4.5 <sup>57</sup>Fe Mössbauer spectrum of [Fe(Me<sub>4</sub>bpp)<sub>2</sub>](ClO<sub>4</sub>)<sub>2</sub>·2H<sub>2</sub>O at 300K

$[\text{Fe}(\text{H}_4\text{bpp})_2]^{2+}$  exhibits an additional absorption at 543 nm of low intensity and a band at 415 nm with a shoulder at 368 nm. The shoulder is due to the metal-to-ligand charge-transfer (MLCT) transition (Chapter 2, Section 2.4.1.3). Due to the high energy and the intensity of the band at 543 nm, we tentatively assign this band to the spin-allowed  $^1\text{A}_1 \rightarrow ^1\text{T}_1$  transition.<sup>43</sup> The band at 415 nm is probably due to<sup>43</sup> the transition  $^1\text{A}_1 \rightarrow ^1\text{T}_2$ . The observed high intensity of this band could arise due to intensity stealing from the MLCT band at 368 nm. The feature observed at ~400 nm is closely similar to a related spin equilibrium system.<sup>211</sup>

#### 4.4 Concluding Remarks

It follows from the temperature dependence of the magnetic susceptibility for  $[\text{Fe}(\text{H}_4\text{bpp})_2](\text{ClO}_4)_2 \cdot \text{H}_2\text{O}$  that the ligand field arising from the two tridentate ligands is such that the difference between the two spin states of the iron(II) ion is of the order of  $kT$  and that the population of the states in question can be altered by changes in temperature. This has been substantiated by the Mössbauer results.

The present investigation provides a clear indication of the existence of a spin-state transition for the complex  $[\text{Fe}(\text{H}_4\text{bpp})_2](\text{ClO}_4)_2 \cdot \text{H}_2\text{O}$ . In contrast, methyl group substituents in the 3-positions of the pyrazole rings in the  $\text{Me}_4\text{bpp}$  ligand give rise to a much weaker ligand field to exhibit a high-spin configuration over the accessible temperature range. Thus the field strength of this ligand towards Fe(II) is such that it is unable to cause spin pairing even at the lowest temperature attained in this study.

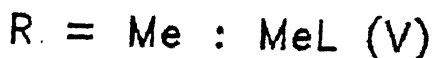
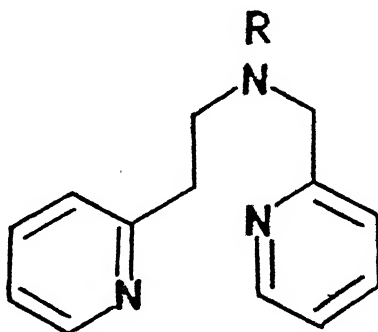
## CHAPTER 5

New Triply Bridged Diiron(III) Complexes with  $[\text{Fe}_2(\mu\text{-O})(\mu\text{-X})_2]^{2+}$   
Cores {X =  $\text{MeCO}_2$ ,  $\text{PhCO}_2$  or  $(\text{PhO})_2\text{PO}_2$ }\*

\*A part of this work has been accepted for publication in  
J. Chem. Soc. Dalton Trans. 1992, in press.



We have seen in the last three chapters the use of a group of three tridentate pyridylpyrazole ligands to address the problem of steric/electronic effects on the metal-ligand orbital interactions. In the present chapter we explore a very different use of two tridentate pyridine-rich ligands IV-V.



Hemerythrin,<sup>45,46</sup> a marine invertebrate respiratory protein is a prototypical of an emerging class of oxo-bridged non-heme iron proteins and enzymes,<sup>45,46,71,103,218-222</sup> including ribonucleotide reductase, purple acid phosphatases, methane monooxygenase and rubrerythrin. To understand the chemistry of the assembly and function of these metalloproteins a large number of tribridged<sup>223-238</sup> models have been synthesized by using a variety of tridentate N-based ligands. Selected triply-bridged diiron(III) complexes having  $[Fe_2(\mu-O)(\mu-O_2CR)_2]^{2+}$  core with various terminal capping ligands have been compiled in Table 5.1.

Herein we describe the syntheses of a group of three triply

**Table 5.1: Selected Oxo-Bridged Diiron(III) Complexes having  
[Fe<sub>2</sub>(μ-O)(μ-O<sub>2</sub>CR)<sub>2</sub>]<sup>2+</sup> Core**

Terminal Ligands	Comments	References
Hydrotris(1-pyrazolyl) borate(-) (HBpz <sub>3</sub> )	Syntheses and X-ray structures of (μ-oxo/hydroxo)bis(μ-acetato), (μ-oxo)bis(μ-formato), (μ-oxo)bis(μ-benzoato), (μ-oxo)bis(μ-diphenylphosphato) bridged dimers; electronic spectra, Resonance Raman and FTIR spectra, EXAFS, NMR and Mössbauer spectra, magnetic susceptibility (antiferromagnetism), cyclic voltammetry; acetate bridge exchange reactions	223-226, 251
1,4,7 triazacyclononane (TACN) and N,N',N''-trimethyl-1,4,7 triazacyclononane (MTACN)	Syntheses and X-ray structures of oxo-bridged diiron(III) core with additional acetate, carbonate, chromate, phosphate bridges; EXAFS, IR and Resonance Raman spectra, electronic spectra, magnetic susceptibility (antiferromagnetism), Mössbauer spectra, electrochemistry	229-232
Tris(imidazol-2-yl)phosphine (TIP) and its N-methyl analogue (TMIP)	Syntheses and X-ray structures of (μ-oxo/hydroxo)bis(μ-acetato)diiron(III) core; detailed NMR studies, IR and electronic spectra, magnetic susceptibility (antiferromagnetism), Mössbauer spectra	25,26
Bis(benzimidazolylmethyl)amine (BBA) and its methyl derivative	<sup>1</sup> H NMR, IR, and electronic spectra, variable temperature magnetic susceptibility, X-ray structures	22,23

Table 5.1 (contd.)

Terminal ligands	Comments	References
Tris(2-pyridyl-methyl)amine (TPA) and Bis(2-pyridyl-methyl)amine (BPA)	Syntheses and structures of di- and tribridged core with $\mu$ -oxo and additional $\mu$ -acetato, $\mu$ -carbonato, $\mu$ -maleato, $\mu$ -phthalato and $\mu$ -phosphato bridges; electronic spectra, Resonance Raman, $^1\text{H}$ NMR and Mössbauer spectra, magnetic susceptibility; distinct iron sites	239-241
N,N,N',N'-tetra-kis(2-pyridylmethyl)-1,2-butane-diamine (TPBN)	Dimer of dimer; X-ray structure, IR, Mössbauer, and electronic spectra, variable temperature magnetic susceptibility	234
1,4-Bis(1,4,7-triaza-1-cyclo-nonyl)butane (BTCB)	X-ray structure; dimer of dimer; IR and electronic spectra	237,238
2,2'-Bipyridine (BPY) and $\text{Cl}^-$	X-ray structure of ( $\mu$ -oxo) bis( $\mu$ -acetato)diiron core; labile sites; magnetic susceptibility, Mössbauer spectra; hydroxylation of hydrocarbon using this core	242
Bis(1-methyl-imidazol-2-yl)-phenylmethoxy-methane (BIPhMe)	X-ray structure; open coordination sites; electronic IR, Resonance Raman, NMR and Mössbauer spectra; synthesis and spectroscopic characterization of diferrus core	243,244

bridged diiron(III) complexes with  $[\text{Fe}_2(\mu\text{-O})(\mu\text{-X})_2]^{2+}$  cores {X =  $\text{MeCO}_2$ ,  $\text{PhCO}_2$  or  $(\text{PhO})_2\text{PO}_2$ } using facially capping tridentate amine ligands HL (IV) and MeL (V). The reasons for choosing these two ligands are as follows. A very interesting point to note is that the majority of tridentate nitrogenous capping ligands thus far used<sup>26,27,103</sup> for tribridged core formation give rise to Fe(III)/Fe(II) mononuclear complexes either of low-spin type or of spin-equilibria variety. Size of chelate rings in the resulting complex offers a possibility for variation in the ligand field strength. Specifically, expansion of one chelate ring from five- to six-membered has been shown to result<sup>121,122</sup> in a decrease in the ligand field strength. Nelson and coworkers<sup>25</sup> reported that iron(II) bis-ligand complex of bis(2-pyridylmethyl)-amine (BPA) is low-spin, while the corresponding iron(II) complex with N-methyl derivative of BPA is high-spin. Thus our ligands (HL and MeL) are expected to behave as weak field ligands. In this background we became interested to examine the properties of tribridged core using HL and MeL as capping ligands capable of providing unsymmetrical chelate rings..

These new diiron(III) complexes have been characterized by elemental analyses, solution electrical conductivity, spectral (IR, UV/VIS, Mössbauer, and  $^1\text{H}$  NMR) and magnetic susceptibility measurements. The results of our investigation on acetate bridge-exchange reactions of  $[\text{Fe}_2(\mu\text{-O})(\mu\text{-CH}_3\text{CO}_2)_2(\text{MeL})_2]^{2+}$  (i) with  $\text{CD}_3\text{CO}_2\text{D}$  producing  $[\text{Fe}_2(\mu\text{-O})(\mu\text{-CD}_3\text{CO}_2)_2(\text{MeL})_2]^{2+}$  and (ii) with  $(\text{PhO})_2\text{PO}_2\text{H}$  producing  $[\text{Fe}_2(\mu\text{-O})\{\mu\text{-(PhO)}_2\text{PO}_2\}_2(\text{MeL})_2]^{2+}$  have also been described in this chapter.

## 5.1 Experimental Section

### 5.1.1 Solvents and Reagents

Solvents and reagents were obtained from commercial sources and used without further purification unless otherwise stated. Details of solvent purification are already discussed in Chapter 2 (Section 2.1.1).

### 5.1.2 Measurements

Details of spectroscopic measurements are given in Chapter 2 (Section 2.1.2).

Variable-temperature magnetic susceptibility measurements were made on powdered samples over the temperature range  $8.0 < T < 300$  K by the Faraday method. Details of measurements are given in Chapter 2 (Section 2.1.2). The diamagnetic contributions were calculated by using values<sup>134</sup> of  $-435 \times 10^{-6} \text{ cm}^3 \text{ mol}^{-1}$  for  $[\text{Fe}_2(\mu\text{-O})(\mu\text{-PhCO}_2)_2(\text{MeL})_2](\text{ClO}_4)_2 \cdot 2\text{H}_2\text{O}$ ,  $-387 \times 10^{-6} \text{ cm}^3 \text{ mol}^{-1}$  for  $[\text{Fe}_2(\mu\text{-O})(\mu\text{-MeCO}_2)_2(\text{MeL})_2](\text{ClO}_4)_2 \cdot 2\text{H}_2\text{O}$ , and  $-588 \times 10^{-6} \text{ cm}^3 \text{ mol}^{-1}$  for  $[\text{Fe}_2(\mu\text{-O})\{\mu\text{-(PhO)}_2\text{PO}_2\}_2(\text{MeL})_2](\text{ClO}_4)_2 \cdot \text{H}_2\text{O}$ . All measurements were made at a fixed field strength and field dependence of the magnetic susceptibility was not studied. The data were fitted to the appropriate theoretical expression for two interacting high-spin iron(III) ions developed under the usual isotropic spin Hamiltonian  $H_0 = -2JS_1S_2$ .<sup>134</sup> Inclusion of terms for the temperature-independent paramagnetic susceptibility (t.i.p.) and for possible sample contamination by a paramagnetic iron(III) impurity exhibiting Curie behavior yields the relationship (Equation 5.1)

$$\chi_{\text{calc.}} = \frac{N g^2 \beta^2}{k T} \left[ \frac{2e^{2x} + 10e^{6x} + 28e^{12x} + 60e^{20x} + 110e^{30x}}{1 + 3e^{2x} + 5e^{6x} + 7e^{12x} + 9e^{20x} + 11e^{30x}} \right] + \frac{N g^2 \beta^2 S(S+1)}{3k T} \chi_{\text{para}} + \text{t.i.p.} \quad (5.1)$$

where  $x = J/kT$  and  $N$ ,  $g$ , and  $k$  have their usual meaning and  $\chi_{\text{para}}$  is the mole fraction of iron(III) contaminant. A multiplicative term of  $(1-\chi_{\text{para}})$  for the first two terms was omitted owing to the very small value of  $\chi_{\text{para}}$  in these experiments. A nonlinear least-squares fitting computer program was used to fit the observed data to equation 5.1. In these calculations  $g$  was fixed at 2.00. With all data  $J$ ,  $\chi_{\text{para}}$  and t.i.p. were allowed to vary to obtain a best fit as determined by the best  $R$  index. The function minimized was  $R = (\chi_{\text{expl.}} - \chi_{\text{calc.}})^2 / (\chi_{\text{expl.}})^2$ .

## 5.2 Syntheses of Ligands

### 5.2.1 2-pyridylethyl-(2-pyridylmethyl)amine (HL)

This was prepared following a slightly modified procedure as described in literature.<sup>245</sup> A mixture of 2,2'-aminoethylpyridine (3.10 g, 25.0 mmol) and pyridine-2-carbaldehyde (2.70 g, 25.0 mmol) in 15 mL of absolute ethanol was refluxed for 10 min. The solvent was stripped off in a rotary evaporator. To this residue a suspension of sodium tetrahydridoborate (0.13 g) in 35 mL of absolute ethanol was added in small portions over a period of 2h. The solution was left overnight, warmed to boiling for 1 h and cooled to room temperature. The pH of the solution was brought to 5.5-7.0 by dropwise addition of 6M HCl. The solvent was stripped off under reduced pressure and the slurry obtained was extracted

with chloroform. The chloroform layer was dried over anhydrous  $\text{Na}_2\text{SO}_4$  and after removal of solvent the desired product was obtained as a yellowish brown liquid (yield 2.70 g, 50%).  $^1\text{H}$  NMR: 8.87-6.87 (8H, m, aromatic), 3.83 (2H, s,  $\text{NCH}_2$ ), 2.95 (4H, s,  $\text{NCH}_2\text{CH}_2$ ), 1.93 (1H, s, NH).

### 5.2.2 2-pyridylethyl-(2-pyridylmethyl)methylamine (MeL)

To a solution of 2-(2-methylaminoethyl)pyridine (3.34 g, 24.40 mmol) and  $\text{Et}_3\text{N}$  (2.50 g, 24.70 mmol) in 90 mL of ethylacetate was added 10 mL of an ethanolic solution of 2-chloromethylpyridine (obtained by neutralization of the monohydrochloride (4.00 g, 24.40 mmol) with a 10% excess of a 2 mL saturated aqueous  $\text{K}_2\text{CO}_3$  solution with vigorous shaking). The mixture was allowed to stir at room temperature for 5 days. After filtration, the solvent was removed under reduced pressure to give a yellowish oil. To this, 20 mL of ethylacetate was added, filtered, and the volume of the filtrate was reduced down to ~5 mL by rotary evaporation. The remaining solution was extracted with chloroform and dried over anhydrous  $\text{Na}_2\text{SO}_4$ . After complete removal of the solvent the desired product was obtained as a yellowish brown liquid (yield 4.50 g, 81%).  $^1\text{H}$  NMR (in  $\text{CDCl}_3$ ): 8.57-6.83 (8H, m, aromatic), 3.85 (2H, s,  $\text{NCH}_2$ ), 2.95 (4H, s,  $\text{NCH}_2\text{CH}_2$ ), 2.40 (3H, s,  $\text{NCH}_3$ ). The  $^1\text{H}$  NMR spectrum of MeL is shown in Figure 5.1.

## 5.3 Syntheses of Complexes

### 5.3.1 $(\text{Et}_4\text{N})_2[\text{Fe}_2\text{OCl}_6]$

This was prepared according to literature procedure.<sup>246</sup> Metallic sodium (1.20 g, 52.2 mmol) was allowed to react with

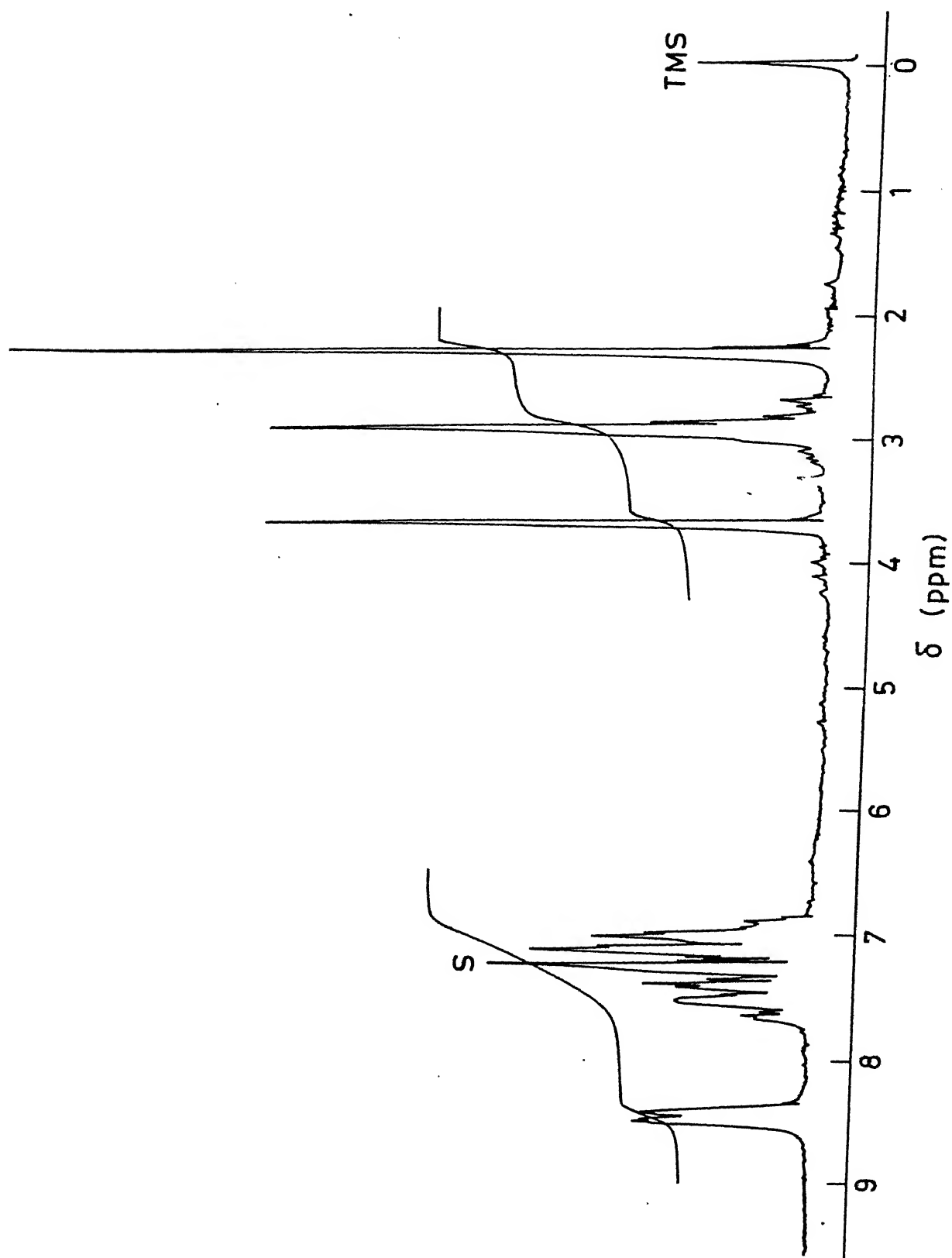


Figure 5.1  $^1\text{H}$  NMR spectrum of 2-pyridylethyl (2-pyridylmethyl)methylamine (MeL) in  $\text{CDCl}_3$



250 mL of  $\text{CH}_3\text{OH}$  to give  $\text{NaOCH}_3$ . A solution of  $\text{NaOCH}_3$  (250 mL) was added dropwise over a period of 2.5 h to a solution of 8.52 g (52.5 mmol) of anhydrous  $\text{FeCl}_3$  in 350 mL of  $\text{CH}_3\text{OH}$  with rapid stirring. After the addition was complete, the deep brown reaction mixture stirred for 1 h and then 9.50 g (57.3 mmol) of solid  $\text{Et}_4\text{NCl}$  was added. After ~10 min  $\text{CH}_3\text{OH}$  was stripped off by a rotary evaporator (maintaining temperature below  $35^\circ\text{C}$ ) until a thick slurry was obtained. To the slurry was added 200 mL  $\text{CH}_3\text{CN}$  and the resulting cloudy brown suspension was stirred for 15 min and filtered through a pad of Celite to remove  $\text{NaCl}$ . After washing the Celite cake with ~50 mL  $\text{CH}_3\text{CN}$ , the combine filtrates were concentrated to a thick brown oil. This material was dissolved in 20 mL  $\text{CH}_3\text{CN}$ , and 300 mL of  $\text{CHCl}_3$  was added over several minutes. The product was separated as brown oily layer, leaving unreacted  $\text{Et}_4\text{NCl}$  to remain in solution. The oily product was separated from  $\text{CHCl}_3$  layer and diluted to 50 mL with  $\text{CH}_3\text{CN}$ . After the addition of ~100 mL THF to this deep red-brown solution it was filtered. To the filtrate another ~150 mL THF was added and the solution was cooled to  $-20^\circ\text{C}$ . After 24 h the first crop of brown crystals were filtered and washed with THF. More THF was added to the filtrate until it becomes cloudy and the mixture was again kept at  $-20^\circ\text{C}$  for one more day. The second crop obtained was washed with THF and both the crops were dried in vacuo to give a combined yield of 13.50 g (86%).

### 5.3.2 $[\text{Fe}_2(\mu\text{-O})(\mu\text{-PhCO}_2)_2(\text{HL})_2](\text{ClO}_4)_2 \cdot 2\text{H}_2\text{O}$

A mixture of  $(\text{Et}_4\text{N})_2[\text{Fe}_2\text{OCl}_6]$  (0.82 g, 1.36 mmol) and  $\text{PhCO}_2\text{Na}$  (0.42 g, 2.92 mmol) in MeCN (20 mL) was stirred for 20 min. The ligand HL (0.60 g, 2.8 mmol) in MeCN (10 mL) was then

added slowly over a period of 10 min. The mixture was stirred at 298 K for 4 h. Then solid  $\text{NaClO}_4 \cdot \text{H}_2\text{O}$  (0.60 g, 4.3 mmol) was added and stirred for 15 min, filtered and removed the solvent using a rotary evaporator at 30-40°C. The residue was then dissolved in MeCN (10 mL) and filtered through a G-4 frit. The resulting brown crystals obtained after cooling (273 K) the filtrate were collected and recrystallized from (1:1) MeCN-Et<sub>2</sub>O (yield ~ 40%).

### 5.3.3 $[\text{Fe}_2(\mu\text{-O})(\mu\text{-MeCO}_2)_2(\text{MeL})_2](\text{ClO}_4)_2 \cdot 2\text{H}_2\text{O}$

This complex was synthesized using the ligand MeL following a similar procedure as described above, except that  $\text{MeCO}_2\text{Na}$  was used instead of  $\text{PhCO}_2\text{Na}$ . (yield ~ 55%).

### 5.3.4 $[\text{Fe}_2(\mu\text{-O})\{\mu\text{-(PhO)}_2\text{PO}_2\}_2(\text{MeL})_2](\text{ClO}_4)_2 \cdot \text{H}_2\text{O}$

A mixture of  $(\text{PhO})_2\text{PO}_2\text{H}$  (0.17 g, 0.66 mmol) and Et<sub>3</sub>N (0.67 g, 0.66 mmol) in MeCN (10 mL) were added to a stirred MeCN (10 mL) solution of  $(\text{Et}_4\text{N})_2[\text{Fe}_2\text{OCl}_6]$  (0.20 g, 0.33 mmol). After stirring the mixture for 15 min, the ligand MeL (0.15 g, 0.66 mmol) in MeCN (10 mL) was added slowly over a period of 10 min. The mixture was stirred at 298 K for 4 h. Then solid  $\text{NaClO}_4 \cdot \text{H}_2\text{O}$  (0.30 g, 2.1 mmol) was added and stirred for 15 min, filtered and removed the solvent using rotary evaporator. The residue was then dissolved in MeCN (10 mL) and filtered through a G-4 frit and Et<sub>2</sub>O (10 mL) was added slowly. Storage of this solution at ~273 K for 24 h resulted green microcrystalline solid. The compound was recrystallized from (1:1) MeCN-Et<sub>2</sub>O and dried in vacuo (yield ~50%).

The microanalytical data for these oxo-bridged complexes are given in Table 5.2.

Table 5.2: Microanalytical Data of Oxo-Bridged Diiron(III) Complexes

Compounds	Empirical Formula	Analysis <sup>a</sup>		
		% C	% H	% N
$[\text{Fe}_2(\mu\text{-O})(\mu\text{-OBz})_2(\text{HL})_2](\text{ClO}_4)_2 \cdot 2\text{H}_2\text{O}$	$\text{C}_{40}\text{H}_{44}\text{N}_6\text{O}_{15}\text{Cl}_2\text{Fe}_2$	46.30 (46.60)	4.30 (4.30)	8.10 (8.20)
$[\text{Fe}_2(\mu\text{-O})(\mu\text{-OAc})_2(\text{MeL})_2](\text{ClO}_4)_2 \cdot 2\text{H}_2\text{O}$	$\text{C}_{32}\text{H}_{44}\text{N}_6\text{O}_{15}\text{Cl}_2\text{Fe}_2$	40.95 (41.10)	4.70 (4.75)	9.00 (9.00)
$[\text{Fe}_2(\mu\text{-O})\{\mu\text{-(OPh)}_2\text{PO}_2\}_2(\text{HL})_2](\text{ClO}_4)_2 \cdot \text{H}_2\text{O}$	$\text{C}_{52}\text{H}_{56}\text{N}_6\text{P}_2\text{O}_{18}\text{Cl}_2\text{Fe}_2$	48.30 (48.10)	4.40 (4.35)	6.45 (6.50)

<sup>a</sup>Calculated values are in parentheses

## 5.4 Results and Discussion

### 5.4.1 Synthetic Aspects

Since 1983 there has been a growing interest in the syntheses of triply bridged ( $\mu$ -oxo)bis( $\mu$ -carboxylato)diiron(III) complexes using a variety of tridentate nitrogen-containing capping ligands to model the oxo-bridged dinuclear iron protein hemerythrin. The synthetic strategy adopted has mainly been the "self-assembly" method of Holm and Ibers.<sup>247</sup> However, our approach resembles that of Lippard and coworkers<sup>223,228</sup> using preformed  $[\text{Fe}_2\text{OCl}_6]^{2-}$  ion.

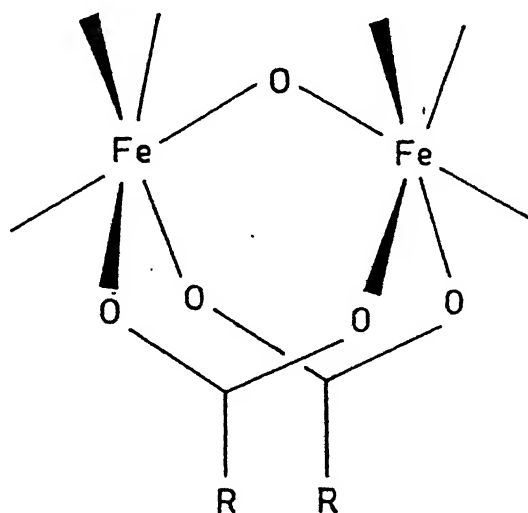
Treatment of  $(\text{Et}_4\text{N})_2[\text{Fe}_2\text{OCl}_6]$  with sodium acetate or sodium benzoate and the triamine ligands HL and MeL in MeCN at room temperature gave orangish brown solutions which after workup and addition of sodium perchlorate, afforded  $[\text{Fe}_2(\mu\text{-O})(\mu\text{-PhCO}_2)_2(\text{HL})_2](\text{ClO}_4)_2 \cdot 2\text{H}_2\text{O}$  and  $[\text{Fe}_2(\mu\text{-O})(\mu\text{-MeCO}_2)_2(\text{MeL})_2](\text{ClO}_4)_2 \cdot 2\text{H}_2\text{O}$  as orange brown microcrystals in ~ 50% yield. The synthesis of  $[\text{Fe}_2(\mu\text{-O})\{\mu\text{-(PhO)}_2\text{PO}_2\}_2(\text{MeL})_2]^{2+}$  was achieved by two different routes, one being similar to that used for the syntheses of acetate and benzoate bridged complexes, to afford in this case  $[\text{Fe}_2(\mu\text{-O})\{\mu\text{-(PhO)}_2\text{PO}_2\}_2(\text{MeL})_2](\text{ClO}_4)_2 \cdot \text{H}_2\text{O}$  in ~ 50% yield and the other involving an acetate bridge-exchange reaction (see below).

### 5.4.2 Characterization of the Triply Bridged Core

The orange brown solids  $[\text{Fe}_2(\mu\text{-O})(\mu\text{-PhCO}_2)_2(\text{MeL})_2](\text{ClO}_4)_2 \cdot 2\text{H}_2\text{O}$  and  $[\text{Fe}_2(\mu\text{-O})(\mu\text{-MeCO}_2)_2(\text{MeL})_2](\text{ClO}_4)_2 \cdot 2\text{H}_2\text{O}$  showed the characteristic IR bands typical of bridging acetate and benzoate groups, asymmetric  $\nu(\text{FeOFe})$  vibration mode,<sup>103,220</sup> water of crystallization, and  $\text{ClO}_4^-$ . The presence of N-H in the co-

ordinated ligand is clearly seen in the IR spectrum of  $[\text{Fe}_2(\mu\text{-O})(\mu\text{-PhCO}_2)_2(\text{MeL})_2](\text{ClO}_4)_2 \cdot 2\text{H}_2\text{O}$  (Figure 5.2). For  $[\text{Fe}_2(\mu\text{-O})\{\mu\text{-(PhO)}_2\text{PO}_2\}_2(\text{MeL})_2](\text{ClO}_4)_2 \cdot \text{H}_2\text{O}$  the IR bands characteristic of bridging phosphate groups<sup>248</sup> could not be assigned with certainty due to overlapping of  $\text{ClO}_4^-$  vibration in the same region. Selected characterization IR data of the complexes are set out in Table 5.3.

Solution electrical conductivity measurements in MeCN reveal that all three compounds are 1:2 electrolytes<sup>138</sup> (Table 5.3). Magnetic susceptibility measurements at 300 K in MeCN solutions using Evans' NMR method<sup>131</sup> gave effective magnetic moments of  $\sim 1.70$  / Fe (carboxylate bridge) and  $1.86/\text{Fe}$  (phosphate bridge), which are typical<sup>103,220</sup> for triply bridged cores (see below) and which confirm the integrity of these cores in solution.



The  $(\mu\text{-oxo})\text{bis}(\mu\text{-carboxylato})\text{diiron(III)}$  core formulation seems reasonable, given the similarities in the absorption spectra of these complexes in MeCN solution when compared to the spectra of all the structurally characterized dimers of the

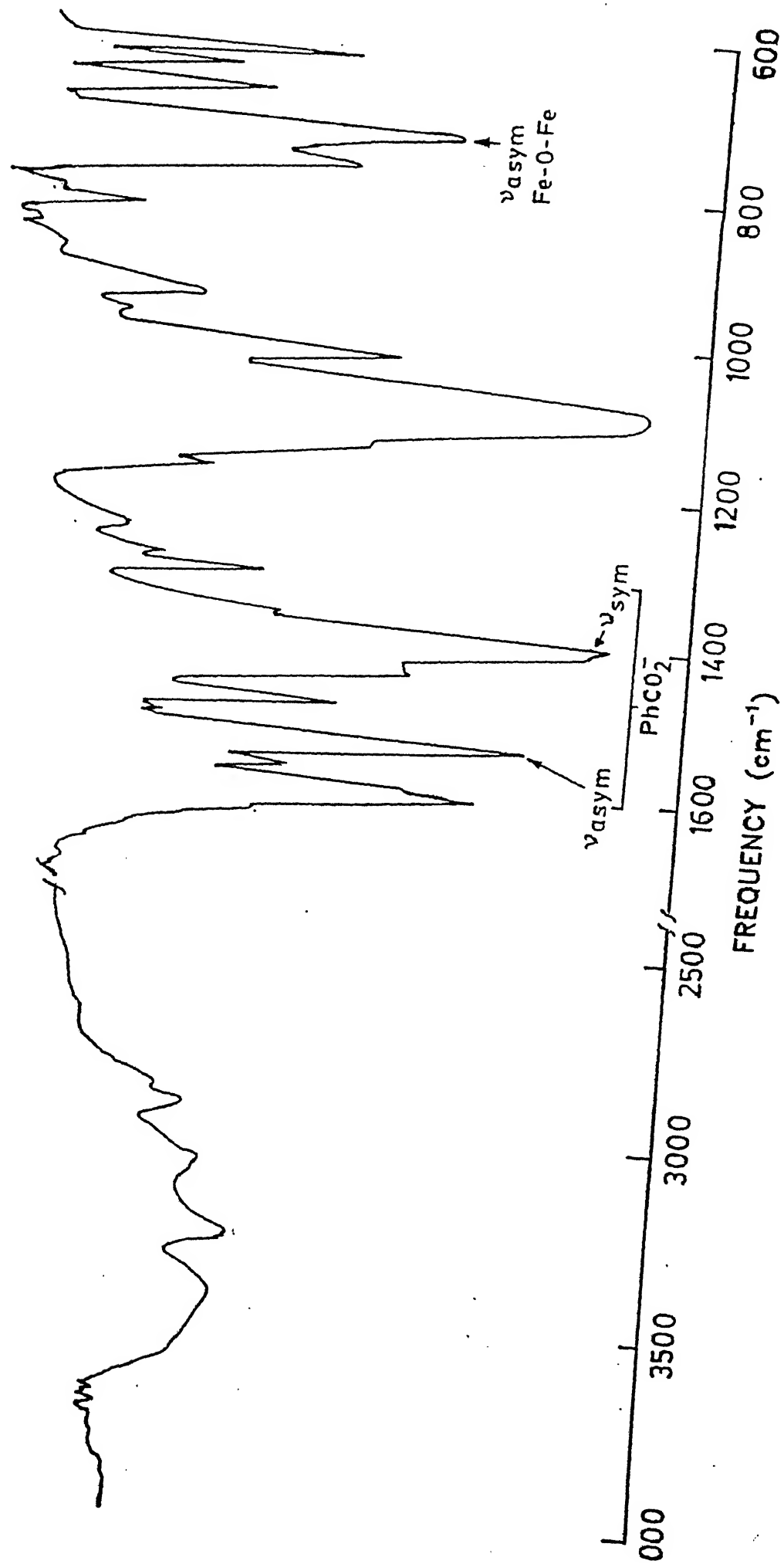


Figure 5.2 IR spectrum of  $[\text{Fe}_2(\mu\text{-O})(\mu\text{-OBz})_2(\text{MeL})_2](\text{ClO}_4)_2 \cdot 2\text{H}_2\text{O}$

Table 5.3: Infrared Spectral Data<sup>a</sup> of Oxo-Bridged Diiron(III) Complexes

Compounds	$\nu_{as}(\text{FeOFe})$	$\nu_{as}(\text{RCO}_2)$	$\nu_s(\text{RCO}_2)$	$\nu(\text{PO})$	$\nu(\text{ClO}_4)$
$[\text{Fe}_2(\mu\text{-O})(\mu\text{-OBz})_2(\text{HL})_2](\text{ClO}_4)_2 \cdot 2\text{H}_2\text{O}$	725(m)	1540(s)	1400(s)	-	1090(vs)
$[\text{Fe}_2(\mu\text{-O})(\mu\text{-OAc})_2(\text{MeL})_2](\text{ClO}_4)_2 \cdot 2\text{H}_2\text{O}$	730(m)	1550(s)	1440(s)	-	1090(vs)
$[\text{Fe}_2(\mu\text{-O})\{\mu\text{-(OPh)}_2\text{PO}_2\}_2(\text{HL})_2](\text{ClO}_4)_2 \cdot \text{H}_2\text{O}$	735(m)	-	-	1195(s) <sup>b</sup> 1060(m), 1025(m)	1180(vs) <sup>b</sup>

<sup>a</sup>KBr disc; values are in  $\text{cm}^{-1}$ ; symbols: vs = very strong, s = strong,

m = medium.

<sup>b</sup> $\nu(\text{PO}) + \nu(\text{ClO}_4)$ .

( $\mu$ -oxo)bis( $\mu$ -carboxylato)diiron(III) family<sup>71,103,220</sup> and of met-azidohemerythrin itself.<sup>103,249,250</sup> Figure 5.3 shows the electronic spectrum of  $[\text{Fe}_2(\mu\text{-O})(\mu\text{-PhCO}_2)_2(\text{HL})_2](\text{ClO}_4)_2 \cdot 2\text{H}_2\text{O}$  in MeCN. The spectrum consists of two absorptions in the UV region ( $\sim 340$  and  $\sim 380$  nm), four features in the visible region ( $\sim 420$ ,  $\sim 470$ ,  $\sim 500$ , and  $\sim 550$  nm), a broad band at  $\sim 730$  nm and a shoulder in the near-IR region (1050 nm). The peaks between 300 and 400 nm are characteristic of the oxo-bridge.<sup>219,222</sup> The series of bands between 400 and 600 nm with extinction coefficients of  $\epsilon_{\text{Fe}} = 100\text{-}600 \text{ M}^{-1}\text{cm}^{-1}$  are very specific for oxo-bridged compounds containing additional bridging carboxylate ligands. The region, 550 to 1100 nm, contains only Fe (III) ligand field transitions. The band at  $\sim 730$  nm is assigned as  ${}^6\text{A}_1 \rightarrow {}^4\text{T}_2 ({}^4\text{G})$  d-d transition and a very weak and broad shoulder at  $\sim 1050$  nm which is not shown in Figure 5.3 is assigned as  ${}^6\text{A}_1 \rightarrow {}^4\text{T}_1 ({}^4\text{G})$  origin. Many features characteristic of such a core are also present in the phosphate-bridged complex  $[\text{Fe}_2(\mu\text{-O})\{\mu\text{-(PhO)}_2\text{PO}_2\}_2(\text{MeL})_2](\text{ClO}_4)_2 \cdot \text{H}_2\text{O}$ , since absorption energies and intensities compare well for the two classes of compounds.<sup>248,251,252</sup> The absorption spectral results for all three triply bridged complexes are summarized in Table 5.4. The shifts in the d-d transitions on going from  $[\text{Fe}_2(\mu\text{-O})(\mu\text{-O}_2\text{CMe})_2(\text{MeL})_2](\text{ClO}_4)_2 \cdot 2\text{H}_2\text{O}$  to  $[\text{Fe}_2(\mu\text{-O})\{\mu\text{-(PhO)}_2\text{PO}_2\}_2(\text{MeL})_2](\text{ClO}_4)_2 \cdot \text{H}_2\text{O}$  imply that diphenyl phosphates are weaker field ligands than carboxylates. Interestingly, the band position of  ${}^6\text{A}_1 \rightarrow {}^4\text{T}_2 ({}^4\text{G})$  for  $[\text{Fe}_2(\mu\text{-O})(\mu\text{-O}_2\text{CPh})_2(\text{HL})_2](\text{ClO}_4)_2 \cdot 2\text{H}_2\text{O}$  is 733 nm while that of a closely related complex  $[\text{Fe}_2(\mu\text{-O})(\mu\text{-PhCO}_2)_2(\text{BPA})_2](\text{ClO}_4)_2 \cdot \text{H}_2\text{O}$  is 704 nm {BPA = bis(2-pyridylmethyl)-



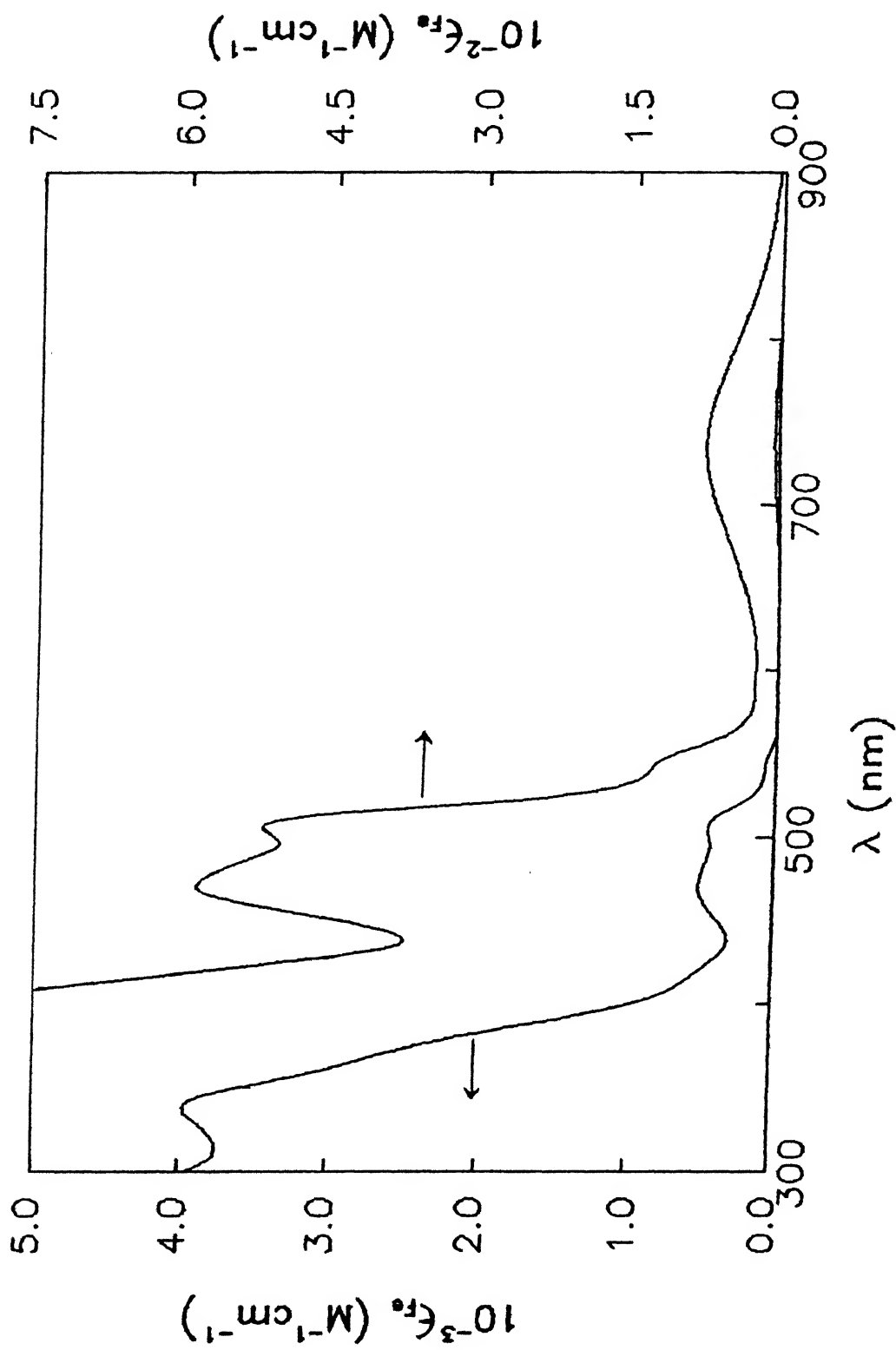


Figure 5.3 Electronic spectrum of  $[\text{Fe}_2(\mu\text{-O})(\mu\text{-O}_2\text{CPh})_2(\text{HL})_2](\text{ClO}_4)_2 \cdot 2\text{H}_2\text{O}$  in MeCN

Table 5.4: Characterization Data of Oxo-Bridged Diiron(III) Complexes  
in MeCN at 298 K

Compounds	Molar conductance <sup>a</sup>	Magnetic moment <sup>b</sup>	Electronic spectra
	$\Lambda_M, \Omega^{-1}\text{cm}^2\text{mol}^{-1}$	$\mu_{\text{eff}}, \mu_B$	$\lambda, \text{nm} (\epsilon_{\text{Fe}}, \text{M}^{-1}\text{cm}^{-1})$
$[\text{Fe}_2(\mu\text{-O})(\mu\text{-OBz})_2(\text{HL})_2](\text{ClO}_4)_2 \cdot 2\text{H}_2\text{O}$	286	1.75	733 (75), 546 (sh) (120), 505 (520), 470 (580), 420 (sh)(520), 372(sh)(2 550), 337 (3 950), 238 (21 350)
$[\text{Fe}_2(\mu\text{-O})(\mu\text{-OAc})_2(\text{MeL})_2](\text{ClO}_4)_2 \cdot 2\text{H}_2\text{O}$	292	1.77	727 (76), 551 (sh) (125), 506 (525), 472 (590), 420 (sh)(810), 380(sh)(3 000), 339 (4 000), 238 (11 200)
$[\text{Fe}_2(\mu\text{-O})\{\mu\text{-(OPh)}_2\text{PO}_2\}_2(\text{HL})_2](\text{ClO}_4)_2 \cdot \text{H}_2\text{O}$	280	1.86	661(65), 527(sh)(90), 490 (sh) (290), 453(sh) (390), 416(sh)(670), 365(sh)(2990), 329 (4 000), 254 (9 600)

<sup>a</sup>In MeCN 1:2 electrolyte:  $220\text{--}300 \Omega^{-1} \text{cm}^2 \text{mol}^{-1}$ .

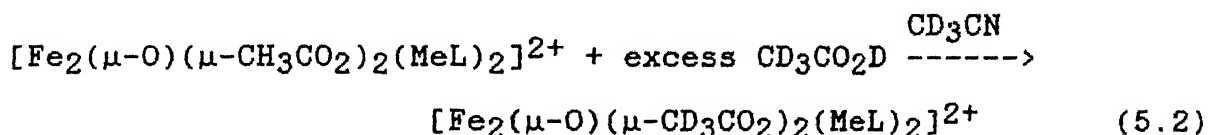
<sup>b</sup>Measured by Evans' method.

amine}.<sup>252</sup> This observation underscores the weaker ligand field strength of HL compared to BPA. This is understandable given the fact that expansion of one chelate ring from five- to six-membered results in a decrease in its ligand field strength.<sup>43</sup>

#### 5.4.3 Carboxylate Bridge Exchange Reactions

To investigate the lability of the carboxylate bridges the following experiments have been done on  $[\text{Fe}_2(\mu\text{-O})(\mu\text{-O}_2\text{CMe})_2(\text{MeL})_2]^{2+}$ , viz., (i) acetate bridge exchange reaction by deuterioacetic acid and (ii) exchange of acetate bridge by phosphate bridge.

In  $[\text{Fe}_2(\mu\text{-O})(\mu\text{-O}_2\text{CMe})_2(\text{MeL})_2]^{2+}$  the bridging acetate groups exchange readily with  $\text{CD}_3\text{CO}_2\text{D}$  in  $\text{CD}_3\text{CN}$  solution with addition of 10 equivalents of  $\text{CD}_3\text{CO}_2\text{D}$  as revealed by  $^1\text{H}$  NMR spectroscopy (Equation 5.2, Figure 5.4).



The spectrum recorded within 10 min of mixing reveals that the bridged diiron(III) structure remains intact and that resonances associated with  $\text{CH}_3$  of the co-ordinated acetate groups ( $\delta = 10.5$  ppm) vanish as the deuterioacetate analogue is formed. Moreover, the entire spectra of  $[\text{Fe}_2(\mu\text{-O})(\mu\text{-O}_2\text{CMe})_2(\text{MeL})_2](\text{ClO}_4)_2 \cdot 2\text{H}_2\text{O}$  and its deuterio analogue are seen in the range  $\delta -10$  to  $+30$  ppm. This is understandable given the strong antiferromagnetic exchange coupling between the diiron(III) sites (see below).

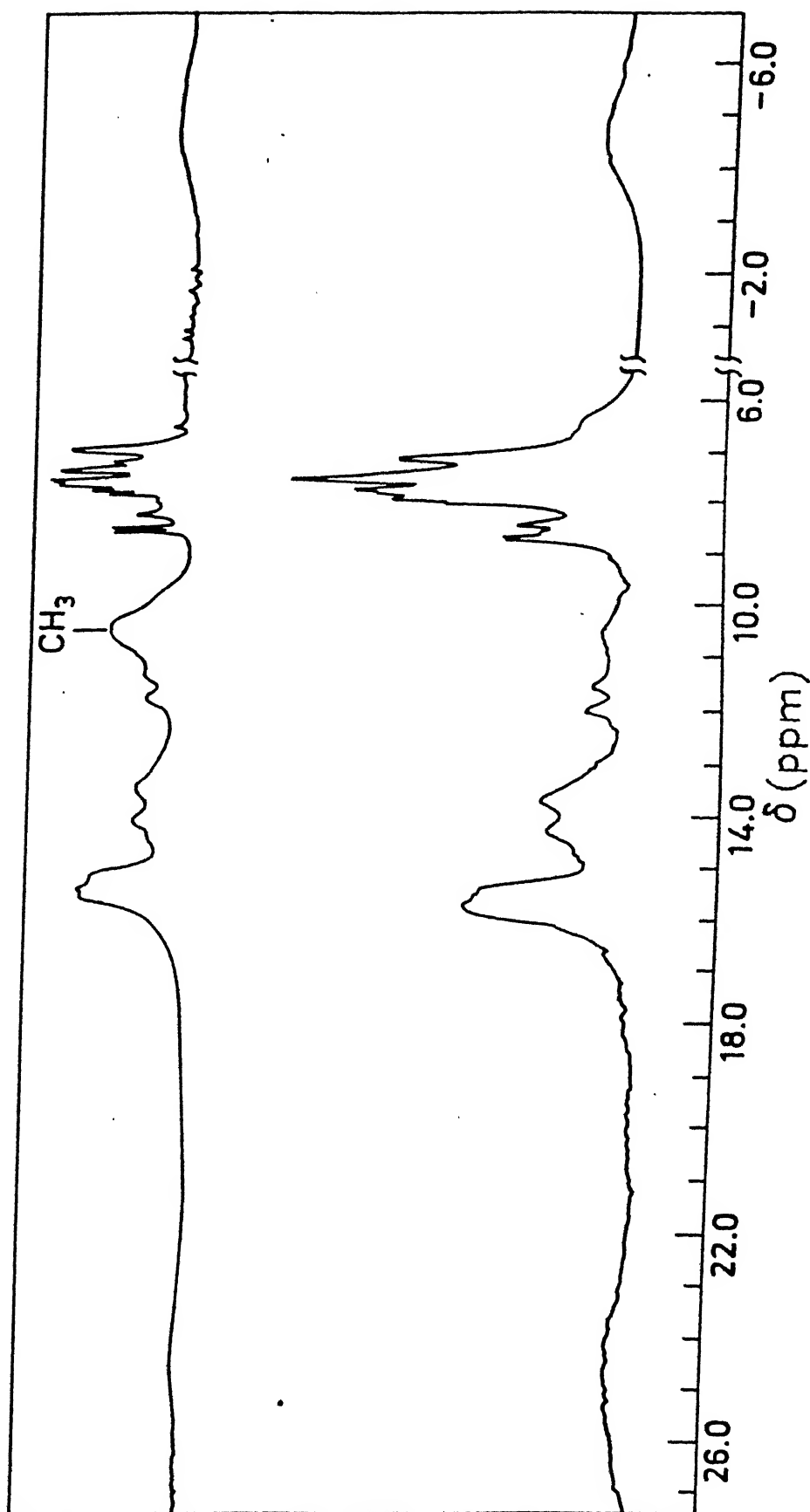
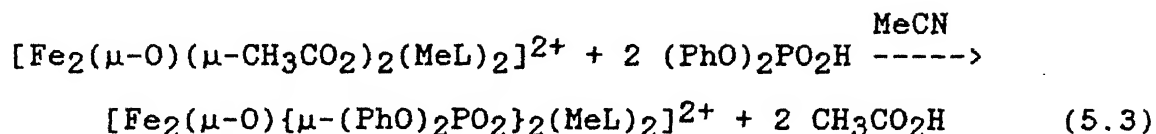


Figure 5.4 Carboxylate exchange reaction  $[\text{Fe}_2(\mu\text{-O})(\mu\text{-O}_2\text{CMe})_2(\text{MeL})_2](\text{ClO}_4)_2$  as monitored by 400 MHz  $^1\text{H}$  NMR spectroscopy in  $\text{CD}_3\text{CN}$ . Assignment of the methyl resonance of the bridging acetate is indicated.

The phosphate-bridged complex  $[\text{Fe}_2(\mu\text{-O})\{\mu\text{-(PhO)}_2\text{PO}_2\}_2\text{-(MeL)}_2]^{2+}$  could be readily generated at 298 K as described in (Equation 5.3).



The electronic spectrum of the resulting solution was recorded (Figure 5.5) within 5 min of mixing. The absorption spectrum of phosphate-bridged dimer generated following (Equation 5.3) is identical to that obtained for the isolated species. Thus the acetate bridge exchange reaction for phosphate proceeds instantaneously. Similar reactions were investigated by Lippard and co-workers.<sup>251</sup>

#### 5.4.4 $^{57}\text{Fe}$ Mössbauer Spectra

$^{57}\text{Fe}$  Mössbauer spectroscopy was utilized to provide a direct probe of the electronic and chemical environment of the dinuclear iron(III) sites in these complexes. Zero field Mössbauer spectra of  $[\text{Fe}_2(\mu\text{-O})(\mu\text{-O}_2\text{CMe})_2(\text{MeL})_2](\text{ClO}_4)_2 \cdot 2\text{H}_2\text{O}$  at 77 K and  $[\text{Fe}_2(\mu\text{-O})\{\mu\text{-(PhO)}_2\text{PO}_2\}_2(\text{MeL})_2](\text{ClO}_4)_2 \cdot \text{H}_2\text{O}$  at 300 K are shown in Figures 5.6 and 5.7, and the results are in Table 5.5. Each spectrum consists of a single quadrupole-split doublet. The two lines of the quadrupole-doublet are of unequal intensity for the room-temperature spectrum and the cause of the asymmetric line broadening is attributed to slow spin-lattice relaxation rates.<sup>253</sup> This is justifiable given the fact that as the absorber temperature is lowered the components of the quadrupole pair become more equal in intensity. The 77 K spectrum appears almost symmetric (Figure 5.5). The values of the isomer shift ( $\delta$ ) and

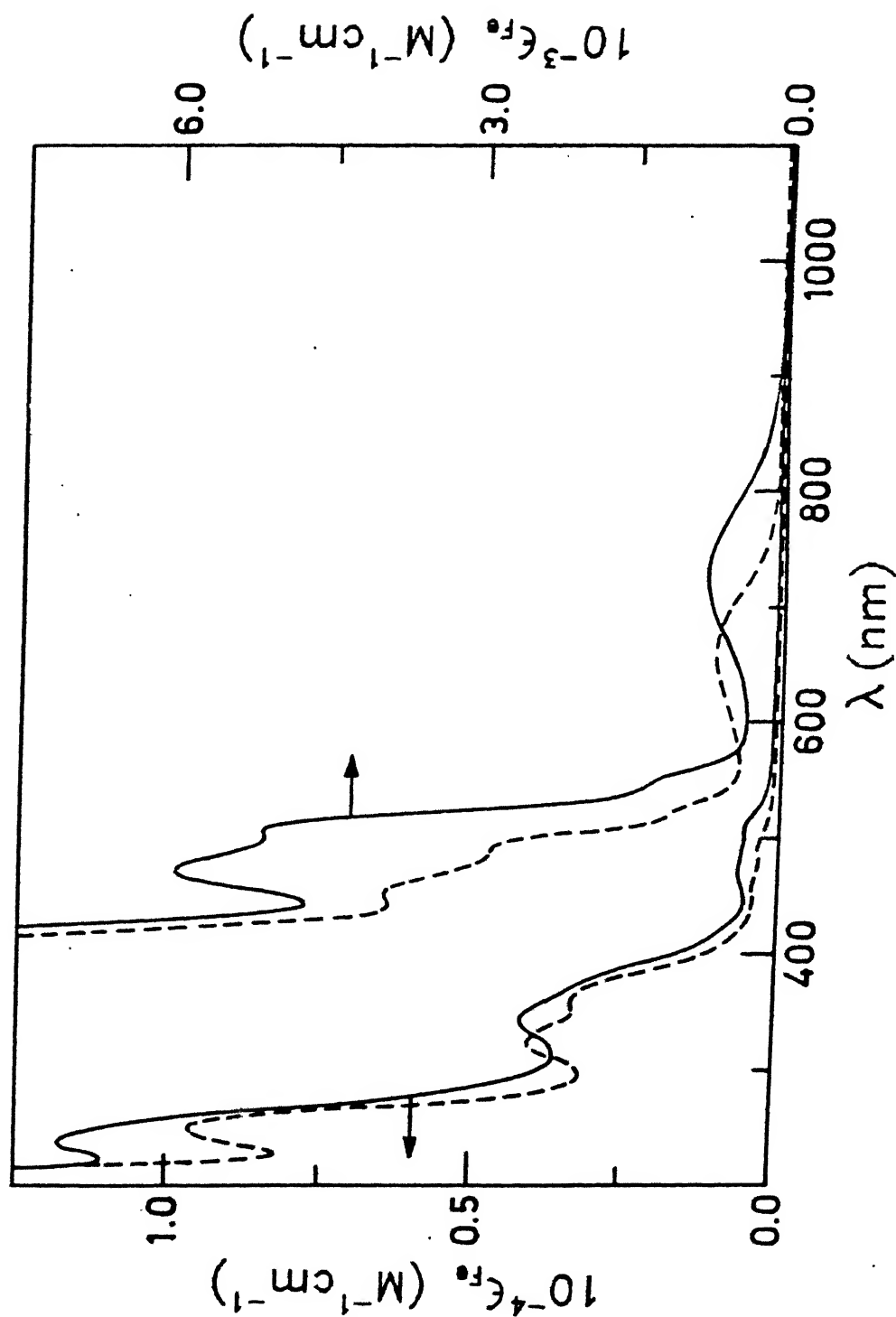


Figure 5.5 Carboxylate exchange reaction of  $[\text{Fe}_2(\mu\text{-O})(\mu\text{-O}_2\text{CMe})_2(\text{MeL})_2](\text{ClO}_4)_2 \cdot 2\text{H}_2\text{O}$  with diphenyl phosphate as monitored by absorption spectroscopy in MeCN solution (—) before and (---) after addition of 2 equivalents of  $(\text{PhO})_2\text{PO}_2\text{H}$

**Table 5.5:** Magnetic and Mössbauer Properties of Some Selected ( $\mu$ -oxo)di-iron(III) Complexes of Relevance to this work

Complexes	$-J(\text{cm}^{-1})$	$\mu_{\text{eff}}/\text{Fe}^{\text{a}}$	T (K)	$\delta(\text{mm s}^{-1})$	$\Delta E_{\text{Q}}(\text{mm s}^{-1})$
[Fe <sub>2</sub> ( $\mu$ -O)( $\mu$ -PhCO <sub>2</sub> ) <sub>2</sub> -(HL) <sub>2</sub> ](ClO <sub>4</sub> ) <sub>2</sub> ·2H <sub>2</sub> O	127 <sup>b</sup>	1.58	300	0.38	1.68
		(1.68) <sup>c</sup>	77	0.52	1.59
[Fe <sub>2</sub> ( $\mu$ -O)( $\mu$ -MeCO <sub>2</sub> ) <sub>2</sub> -(MeL) <sub>2</sub> ](ClO <sub>4</sub> ) <sub>2</sub> ·2H <sub>2</sub> O	125 <sup>d</sup>	1.64	300	0.37	1.29
		(1.70) <sup>c</sup>	77	0.50	1.48
[Fe <sub>2</sub> ( $\mu$ -O){ $\mu$ -(PhO) <sub>2</sub> -PO <sub>2</sub> } <sub>2</sub> (MeL) <sub>2</sub> ](ClO <sub>4</sub> ) <sub>2</sub> ·H <sub>2</sub> O	108 <sup>e</sup>	1.82 (1.86) <sup>c</sup>	300	0.39	1.49
[Fe <sub>2</sub> ( $\mu$ -O)( $\mu$ -MeCO <sub>2</sub> ) <sub>2</sub> -(MTACN) <sub>2</sub> ](ClO <sub>4</sub> ) <sub>2</sub> <sup>f</sup>	115	-	4.2	0.47	1.50
[Fe <sub>2</sub> ( $\mu$ -O)( $\mu$ -MeCO <sub>2</sub> ) <sub>2</sub> -(TMIP) <sub>2</sub> ](ClO <sub>4</sub> ) <sub>2</sub> <sup>g</sup>	120	1.66	100	0.51	1.64
[Fe <sub>2</sub> ( $\mu$ -O)( $\mu$ -MeCO <sub>2</sub> ) <sub>2</sub> -(HBpz <sub>3</sub> ) <sub>2</sub> ] <sup>h</sup>	121	1.71	4.2	0.52	1.60
[Fe <sub>2</sub> ( $\mu$ -O)( $\mu$ -Me <sub>3</sub> CCO <sub>2</sub> ) <sub>2</sub> -(L) <sub>2</sub> ](ClO <sub>4</sub> ) <sub>2</sub> <sup>i</sup>	116	-	293	0.44	1.37
			70	0.55	1.30
[Fe <sub>2</sub> ( $\mu$ -O){ $\mu$ -(PhO) <sub>2</sub> -PO <sub>2</sub> } <sub>2</sub> (HBpz <sub>3</sub> ) <sub>2</sub> ] <sup>j</sup>	97.5	1.82	4.2	0.53	1.60

<sup>a</sup>Solid state values at 300 K. <sup>b</sup> $\chi_{\text{para}}$ :  $3.947 \times 10^{-3}$ , t.i.p.:  $2.909 \times 10^{-6}$ .

<sup>c</sup>Measured in MeCN solution by Evans' method<sup>131</sup> at 300 K. <sup>d</sup> $\chi_{\text{para}}$ :  $7.598 \times 10^{-3}$ , t.i.p.:  $-1.819 \times 10^{-4}$ . <sup>e</sup> $\chi_{\text{para}}$ :  $6.397 \times 10^{-3}$ , t.i.p.:  $5.415 \times 10^{-5}$ .

<sup>f</sup> MTACN = 1,4,7-trimethyl-1,4,7-triazacyclononane: Ref. 229. <sup>g</sup> TMIP = tris-(N-methylimidazol-2-yl)phosphine: Ref 25,26. <sup>h</sup> HBpz<sub>3</sub> = hydrotris(1-pyrazol-yl)borate(1-): Ref. 224. <sup>i</sup> L = bis-(benzimidazol-2-ylmethyl)amine: Ref. 23.

<sup>j</sup> Ref. 251.

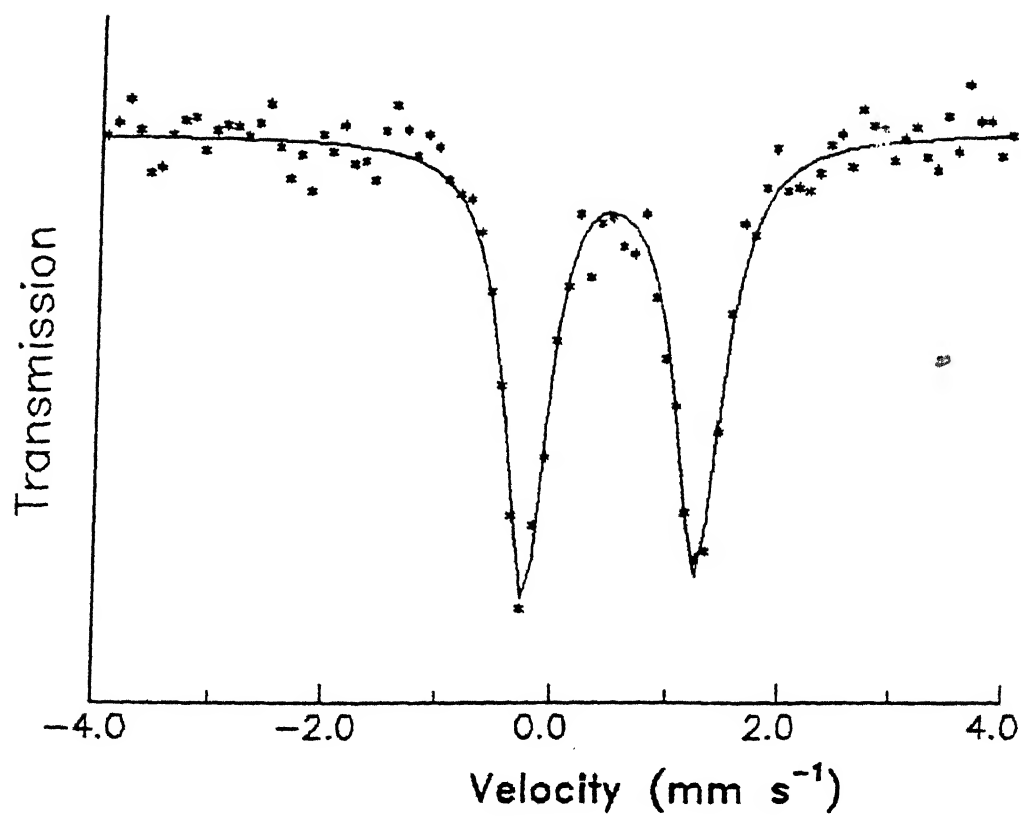


Figure 5.6  $^{57}\text{Fe}$  Mössbauer spectrum of  $[\text{Fe}_2(\mu\text{-O})(\mu\text{-OAc})_2(\text{MeL})_2](\text{ClO}_4)_2 \cdot 2\text{H}_2\text{O}$  at 77 K.



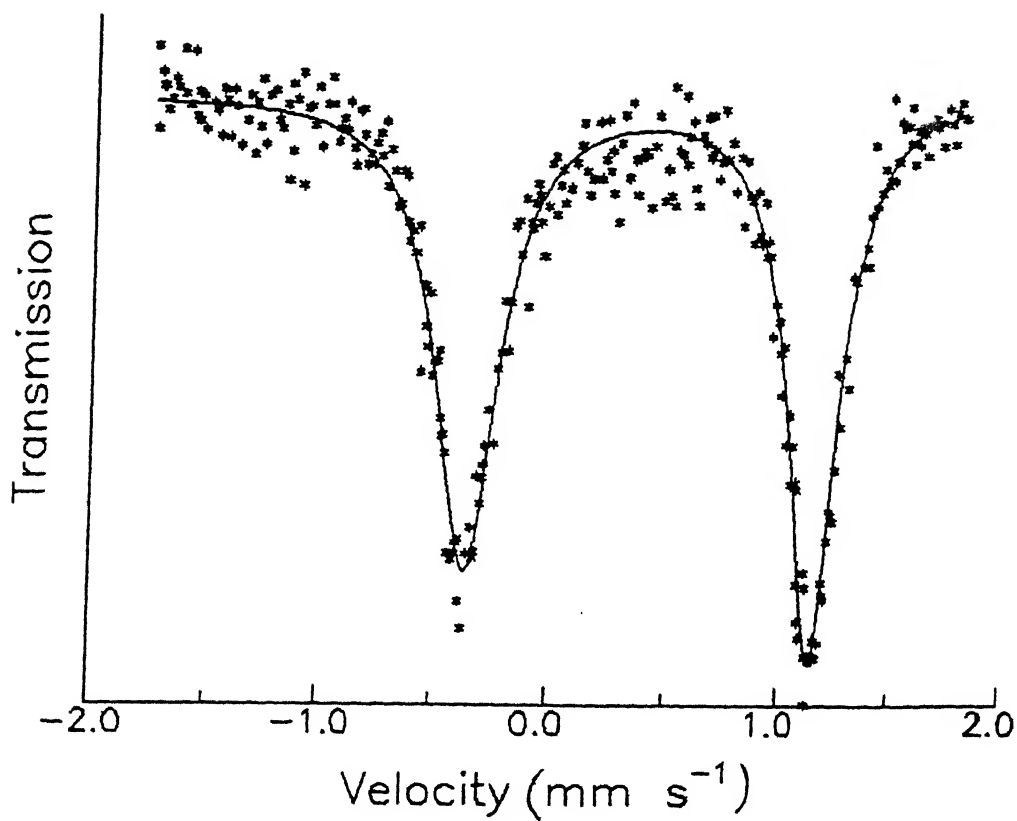


Figure 5.7 <sup>57</sup>Fe Mössbauer spectrum of  $[\text{Fe}_2(\mu\text{-O})\{\mu\text{-O}_2\text{P(OPh)}_2\}_2(\text{MeL})_2](\text{ClO}_4)_2 \cdot \text{H}_2\text{O}$  at 300 K.

quadrupole splitting ( $\Delta E_Q$ ) relative to metallic iron at room temperature were obtained from least-squares computer fitting (solid line) of the experimental points assuming Lorentzian line shapes. The parameters obtained from these complexes are characteristic of  $\mu$ -oxo-bridged dinuclear high-spin iron(III) complexes and proteins in general.<sup>71,220</sup> For the present complexes the isomer shift values at 300 K lie at the lower end<sup>254-256</sup> of the range usually observed.<sup>220</sup> The difference in isomer shift values at 77 K and at 300 K may be accounted for by the second-order Doppler shift (s.o.d.s.) arising from the different source and absorber temperatures.

#### 5.4.5 Magnetism

We have so far been unsuccessful in determining three-dimensional X-ray structure of these compounds because the single crystals grown from many solvents, quite readily lose solvent of crystallization at room temperature. Therefore, we have undertaken a detailed variable-temperature (8-300 K) magnetic susceptibility analyses on all the three complexes to throw light from the standpoint of magneto-structural correlation.<sup>257</sup> Measurements were carried out on solid samples and the magnetic susceptibility data are listed in Tables 5.6, 5.7, and 5.8.

The temperature dependence of the magnetic susceptibilities of acetate and diphenylphosphate bridged complexes are shown in Figures 5.8 and 5.9. The plots are as expected for strongly coupled  $S = 5/2$  dimers.<sup>258-260</sup> The rapid increase in  $\chi_{Fe}$  at low temperatures is due to the presence of traces of monomeric high-spin impurity. This is quite a common feature in the susceptibi-

**Table 5.6:** Variable Temperature Magnetic Susceptibility Data for  
 $[\text{Fe}_2(\mu\text{-O})(\mu\text{-O}_2\text{CPh})_2(\text{HL})_2](\text{ClO}_4)_2 \cdot 2\text{H}_2\text{O}$

T (K)	$10^3 \chi_M/\text{dimer}$ ( $\text{cm}^3 \text{mol}^{-1}$ )	$\mu_{\text{eff}}/\text{Fe}$ (BM)	T (K)	$10^3 \chi_M/\text{dimer}$ ( $\text{cm}^3 \text{mol}^{-1}$ )	$\mu_{\text{eff}}/\text{Fe}$ (BM)
300	2.081	1.58	90	0.873	0.56
289	2.062	1.52	80	0.727	0.53
260	1.998	1.44	70	0.629	0.42
240	1.951	1.37	60	0.629	0.39
220	1.865	1.28	50	0.523	0.33
200	1.797	1.20	40	0.727	0.34
180	1.699	1.11	30	0.751	0.30
160	1.602	1.01	25	1.006	0.32
140	1.456	0.90	20	1.602	0.36
130	1.286	0.82	11.8	2.380	0.34
115	1.177	0.74			
100	0.970	0.62			

**Table 5.7:** Variable Temperature Magnetic Susceptibility Data for  
 $[\text{Fe}_2(\mu\text{-O})(\mu\text{-O}_2\text{CMe})_2(\text{MeL})_2](\text{ClO}_4)_2 \cdot 2\text{H}_2\text{O}$

T (K)	$10^3 \chi_{\text{M}}/\text{dimer}$ ( $\text{cm}^3 \text{mol}^{-1}$ )	$\mu_{\text{eff}}/\text{Fe}$ (BM)	T (K)	$10^3 \chi_{\text{M}}/\text{dimer}$ ( $\text{cm}^3 \text{mol}^{-1}$ )	$\mu_{\text{eff}}/\text{Fe}$ (BM)
300	2.244	1.64	90	0.838	0.55
280	2.208	1.57	80	0.669	0.46
260	2.147	1.50	70	0.500	0.37
240	2.136	1.43	60	0.387	0.31
220	1.967	1.32	50	0.443	0.30
200	1.910	1.24	40	0.443	0.27
180	1.854	1.16	30	0.472	0.24
160	1.685	1.04	20	1.008	0.28
140	1.172	0.94	11.8	1.346	0.25
120	1.290	0.79	8.8	2.023	0.27
100	1.008	0.64			

Table 5.6 Variable Temperature Magnetic Susceptibility Data for  
 $[\text{Fe}_2(\mu\text{-O})\{(\mu\text{-O}_2\text{P(OPh)}_2)_2(\text{MeL})_2\}(\text{ClO}_4)_2\cdot\text{H}_2\text{O}]$

T (K)	$10^3\chi_{\text{M}}/\text{dimer}$ ( $\text{cm}^3 \text{mol}^{-1}$ )	$\mu_{\text{eff}}/\text{Fe}$ (BM)	T (K)	$10^3\chi_{\text{M}}/\text{dimer}$ ( $\text{cm}^3 \text{mol}^{-1}$ )	$\mu_{\text{eff}}/\text{Fe}$ (BM)
300	2.750	1.82	80	1.234	0.60
270	2.680	1.70	70	0.994	0.53
240	2.616	1.59	60	0.858	0.45
200	2.481	1.41	50	0.656	0.36
180	1.346	1.30	40	0.791	0.36
160	1.278	1.21	20	1.399	0.34
140	2.210	1.11	11.8	2.548	0.35
120	1.940	0.97	8.8	3.157	0.33
100	1.602	0.80			

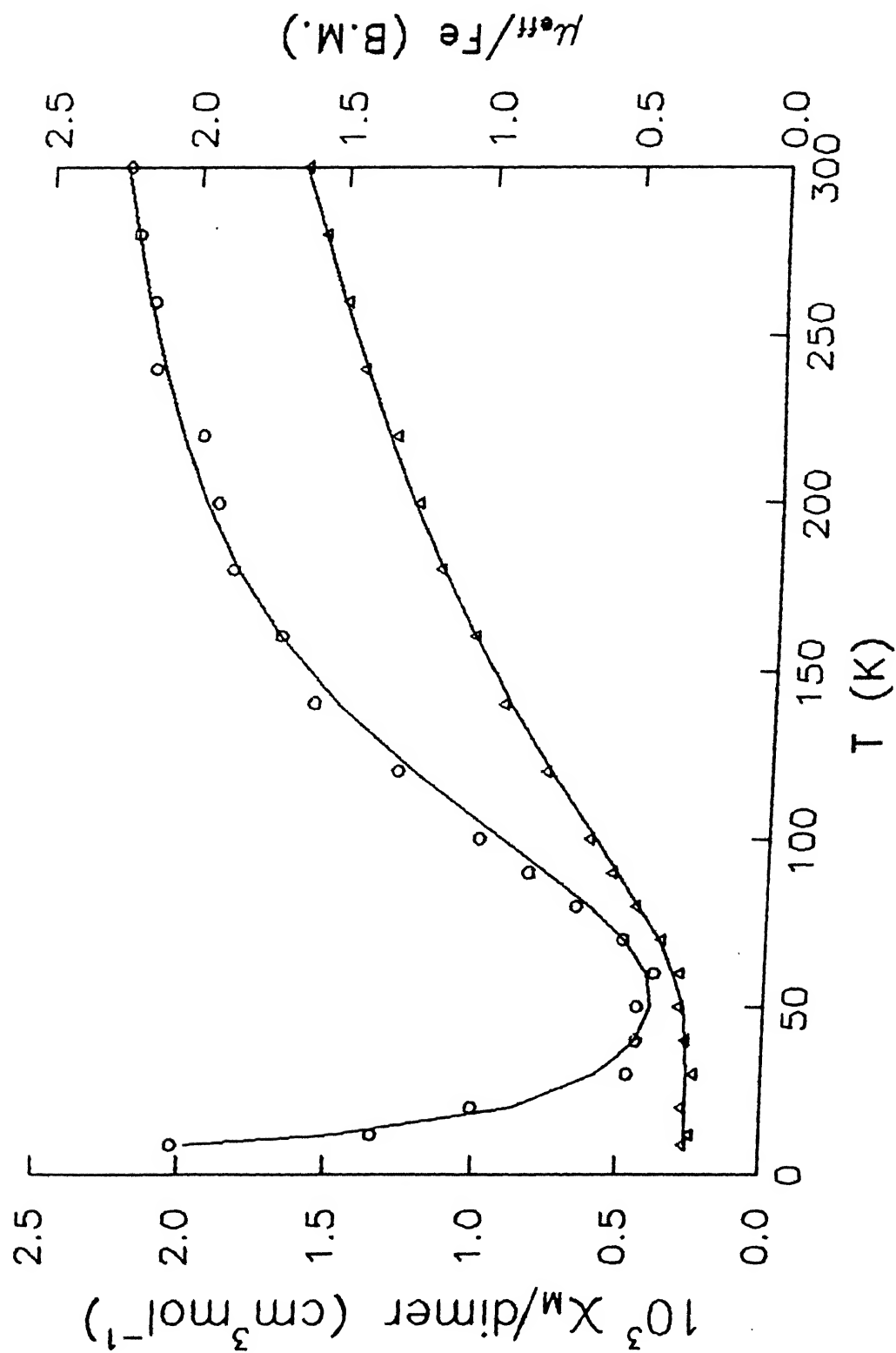


Figure 5.8 Molar susceptibility (o) and effective magnetic moment per iron ( $\Delta$ ) of  $[\text{Fe}_2(\mu\text{-O})(\mu\text{-O}_2\text{CMe})_2(\text{MeL})_2](\text{ClO}_4)_2 \cdot 2\text{H}_2\text{O}$  as a function of temperature. The solid lines are theoretical curves calculated as indicated in the text.

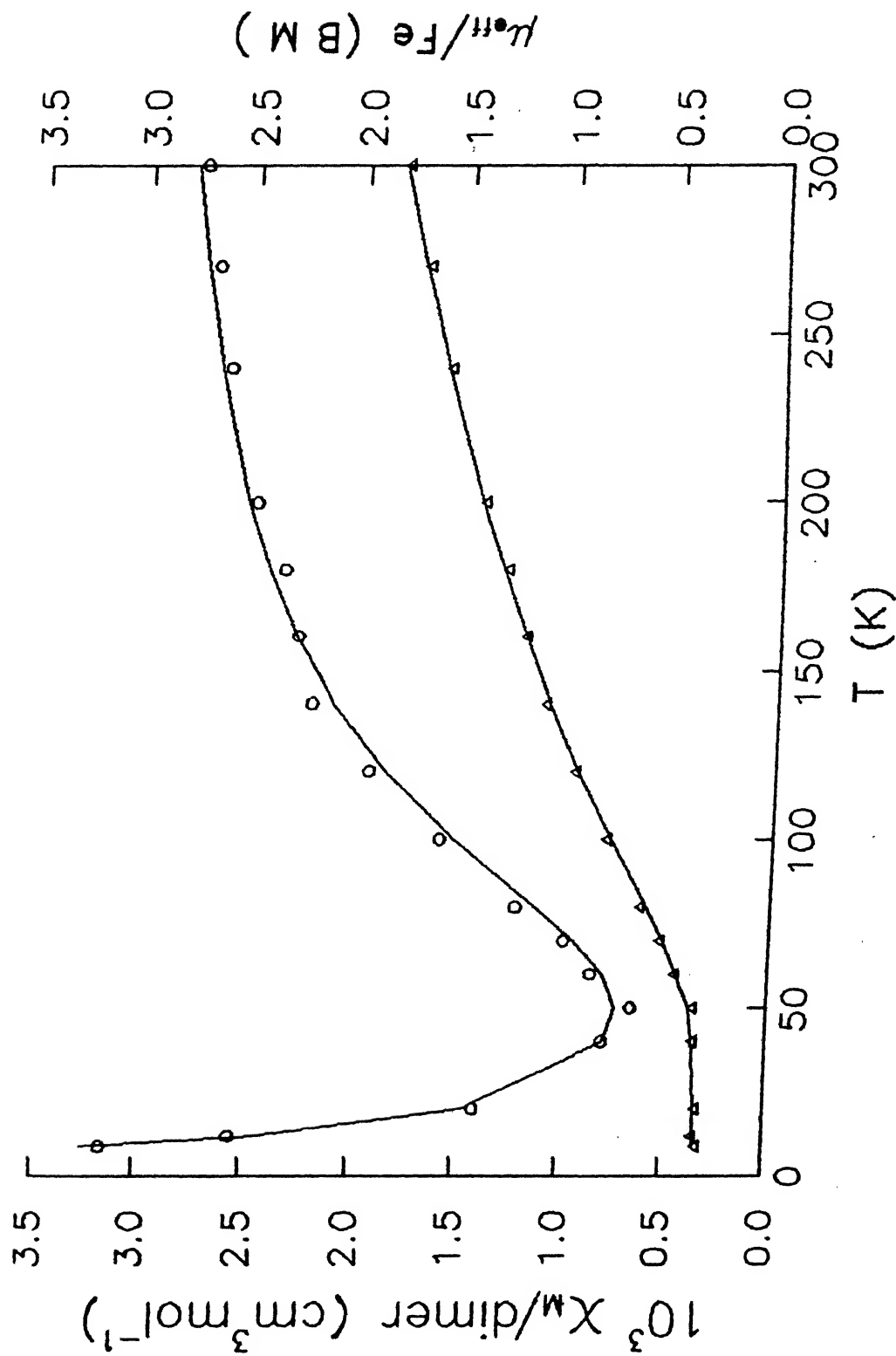


Figure 5.9 Molar susceptibility ( $\circ$ ) and effective magnetic moment per iron ( $\Delta$ ) of  $[\text{Fe}_2(\mu\text{-O})(\mu\text{-O}_2\text{CMe})_2(\text{MeL})_2](\text{ClO}_4)_2 \cdot 2\text{H}_2\text{O}$  as a function of temperature. The solid lines are theoretical curves calculated as indicated in the text.

lities of ( $\mu$ -oxo)iron(III) complexes. The best-fit  $J$  values for these complexes are in Table 5.5. Given the presence of high-spin Fe(III), we constrained  $g$  to the free electron value. It is interesting to note that the  $J$  values are somewhat more negative than found for related complexes (Table 5.5), implying a better spin exchange in the present systems. In the absence of solid-state structural data it would not be appropriate to attempt a definitive explanation. However the following statement is in order. The presence of unsymmetrical chelate rings in HL and MeL might have increased the asymmetry<sup>252,255,256</sup> in these compounds which has contributed to stronger magnetic coupling pathway. By unsymmetrical we mean that no symmetry or pseudo-symmetry operation, other than the identity operation  $C_1$ , relates the coordination environment around one iron to that around a second.

#### 5.4.6 Redox Properties

Figure 5.10 displays the cyclic voltammogram of a representative complex  $[\text{Fe}_2(\mu\text{-O})(\mu\text{-O}_2\text{CMe})_2(\text{MeL})_2]^{2+}$  in MeCN. Measurements over the range +1.70 to -1.70 V at a platinum electrode revealed only an irreversible reductive wave at -0.40 V vs SCE followed by during the anodic scan, two ill-defined waves at +0.26 V and +0.40 V, respectively. It is worth mentioning here that usually the electrochemical properties of this class of complexes behave the same way<sup>224</sup> as we have observed in this work.



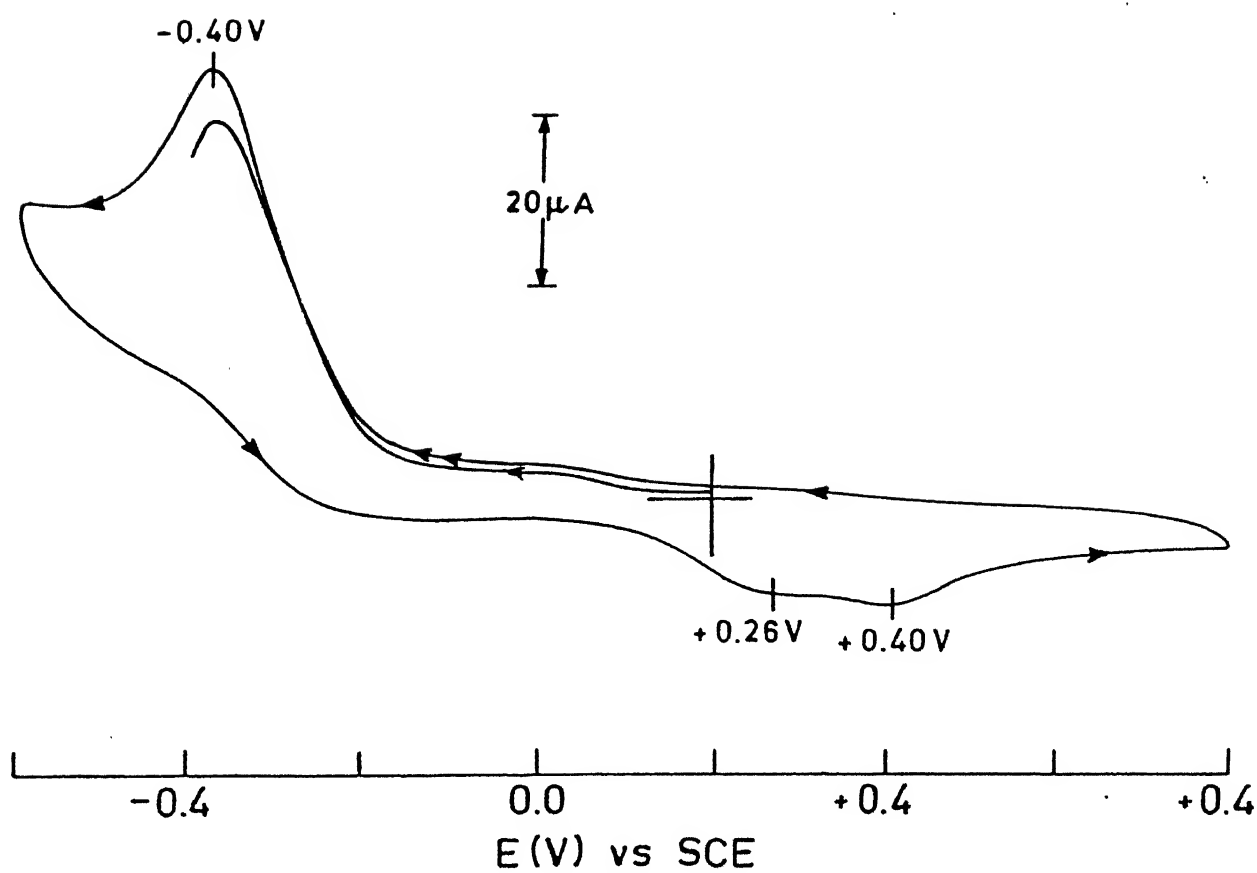


Figure 5.10 Cyclic voltammograms of  $\text{Fe}_2(\mu\text{-O})(\mu\text{-OAc})_2(\text{MeL})_2$   
 $(\text{ClO}_4)_2 \cdot 2\text{H}_2\text{O}$  in MeCN at a platinum electrode;  
 scan rate  $50 \text{ mV s}^{-1}$ .

### 5.5 Concluding Remarks

(i) Successful syntheses of diiron(III) complexes containing the triply bridged  $[\text{Fe}_2(\mu\text{-O})(\mu\text{-X})_2]^{2+}$  core  $\{\text{X} = \text{MeCO}_2, \text{PhCO}_2 \text{ or } (\text{PhO})_2\text{PO}_2\}$  have been achieved by using HL and MeL as terminal capping ligands.

(ii) Using  $^1\text{H}$  NMR and absorption spectroscopy, it has been nicely demonstrated that the acetate bridges present in  $[\text{Fe}_2(\mu\text{-O})(\mu\text{-O}_2\text{CMe})_2(\text{MeL})_2]^{2+}$  are quite labile.

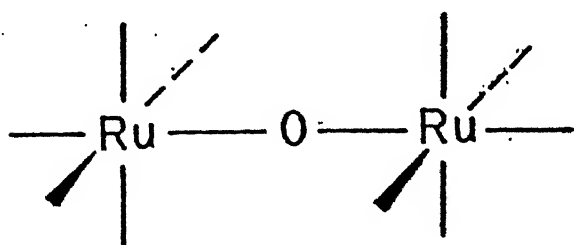
(iii) Mössbauer spectral parameters and the temperature dependence of magnetic susceptibilities point toward the presence of two antiferromagnetically coupled diiron(III) centers in these complexes. The extent of exchange coupling observed here is somewhat larger compared to many related complexes. We believe that the unsymmetric ligand chelate rings in HL and MeL have caused unfavorable interligand steric interactions and hence introduced asymmetry in the core structure.

## CHAPTER 6

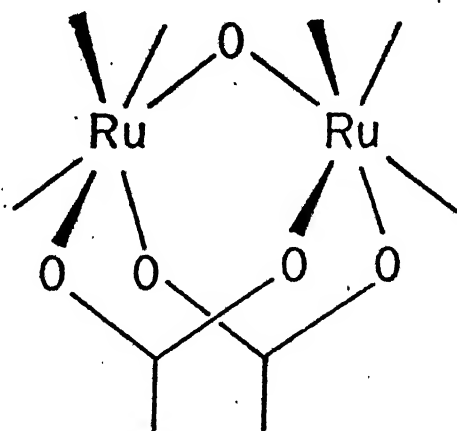
Triply Bridged Diruthenium Complexes with  $\{\text{Ru}_2^{\text{III}}(\mu\text{-O})(\mu\text{-O}_2\text{CMe})_2\}^{2+}$  and  $\{\text{Ru}^{\text{IV}}\text{Ru}^{\text{III}}(\mu\text{-O})(\mu\text{-O}_2\text{CMe})_2\}^{3+}$  Cores: Synthesis, Spectra, and Electrochemistry\*

\*A part of this work has been published in  
Inorg. Chem. 1992, 31, 139.

Modeling the diiron core,  $[\text{Fe}_2(\mu\text{-O})(\mu\text{-O}_2\text{CR})_2]^{2+}$  (Chapter 5), present in iron-containing nonheme protein, hemerythrin, has stimulated an interest in the syntheses of many transition metal compounds with an analogous core structure.<sup>3,73,75,261,262</sup> The studies made on several systems suggest the possibility of developing a parallel chemistry of diruthenium compounds.  $[\text{Ru}_2\text{OCl}_{10}]^{4-}$  and related compounds,<sup>263-270</sup> and various ruthenium red analogues<sup>271</sup> are familiar examples of unsupported  $\mu$ -oxo bridge, 1(a), of ruthenium. Examples are also found<sup>272-279</sup> in which two additional bridging groups support the oxo bridge, 1(b).



Monobridged 1(a)



Tribridged 1(b)

The species hydrogen phosphate and carbonate in place of carboxylate bridges are a subset of this bridge unit. Table 6.1 presents a listing of diruthenium compounds with  $[\text{Ru}_2(\mu\text{-O})(\mu\text{-O}_2\text{CR})_2]^{2+}$  core.

The chemistry of the oxo-carboxylato-bridged diruthenium complexes is expected to be different from those of its diiron

**Table 6.1:** Listing of Triply Bridged Diruthenium(III) Complexes  
with  $[\text{Ru}_2(\mu\text{-O})(\mu\text{-O}_2\text{CR})_2]^{2+}$  Core

Terminal Ligands	Comments	Reference
Pyridine	X-ray structure, absorption spectra, cyclic voltammetry	272, 273
2,2'-bipyridine (BPY), pyridine	Absorption spectra, $^1\text{H}$ NMR spectra, cyclic voltammetry	273
N,N',N''-trime-thyl-1,4,7 tri-azacyclononane (MTACN)	Syntheses and X-ray structures of oxo/hydroxo bridged diruthenium core with additional carb-oxylate bridges; absorption spectra, variable temperature magnetism, $^1\text{H}$ NMR spectra, electrochemistry	274, 275
Tris(1-pyrazol-yl)methane (TPM)	X-ray structure of phosphate bridged dimer, absorption spectra, $^1\text{H}$ NMR spectra, electrochemistry	276
MeCN, $\text{PPh}_3$	X-ray structure, absorption spectra, $^1\text{H}$ NMR spectra; substitutionally labile terminal ligands	277-279

congener. As for example, the oxo-bridged complexes of first-row transition metal elements exhibit comparatively weak antiferromagnetic interactions of electron spins of the metal centers; however, these interactions seem to be much stronger<sup>264</sup> for the second-row transition metals.

Understandably, the electron-transfer properties of ( $\mu$ -oxo)-bis( $\mu$ -acetato)diruthenium(III) complexes are of considerable interest. It is worth mentioning here that among all known complexes with above-mentioned core, the occurrence of both  $[\text{Ru}^{\text{IV}}_2(\mu\text{-O})(\mu\text{-O}_2\text{CMe})_2]^{4+}$  and  $[\text{Ru}^{\text{III}}\text{Ru}^{\text{IV}}(\mu\text{-O})(\mu\text{-O}_2\text{CMe})_2]^{3+}$  species at least on the time scale of cyclic voltammetry, is thus far known<sup>272</sup> in only Sasaki's complex.

In Chapter 5 we have demonstrated the use of the ligand MeL to develop the chemistry of ( $\mu$ -oxo)bis( $\mu$ -acetato)diiron(III) core. In the present chapter using the same ligand we describe the synthesis, spectroscopy, and a comprehensive electrochemistry of diruthenium analogue of the same core structure,  $[\text{Ru}_2(\mu\text{-O})(\mu\text{-O}_2\text{CMe})_2(\text{MeL})_2]^{2+}$ .

## 6.1 Experimental Section

### 6.1.1 Solvents and reagents

Details of solvent purification are already discussed in Chapter 2 (Section 2.1.1).

### 5.1.2 Measurements

Spectroscopic data were obtained by using the following instruments: infrared spectra, Perkin Elmer M-580 spectrophotometer; electronic spectra, Perkin Elmer Lambda 2 spectrophotometer; solution electrical conductivity, Elico (Hyderabad, India)

Type CM-82 T conductivity bridge. The pH measurements were made with a Systronics (Ahmedabad, India) Type 335 digital pH meter. All electrochemical experiments were performed under dinitrogen atmosphere by using a Princeton Applied Research (PAR) Model 370-4 electrochemistry system. Details of electrochemical measurements are given in Chapter 2 (Section 2.1.2). Coulometric experiments were carried out using the Model 173 Potentiostat/Galvanostat and a platinum-wire-gauze electrode was used as a working electrode. Number of electron ( $n$ ) passed through the complex was determined from the ratio of  $Q/Q'$ , where  $Q$  is the coulomb count at the end of electrolysis and  $Q'$  is the calculated coulomb count for one-electron transfer. The solutions were  $\sim 1.0$  mM in complex and 0.2 M in supporting electrolyte, TBAP.

## 6.2 Synthesis of ligand

Synthesis of 2-pyridylethyl-(2-pyridylmethyl)methylamine (MeL) has been described in Chapter 5 (Section 5.2).

## 6.3 Syntheses of Compounds

### 6.3.1 (MeL) $\text{RuCl}_3 \cdot 3\text{H}_2\text{O}$

To a solution of  $\text{RuCl}_3 \cdot 3\text{H}_2\text{O}$  (1.0 g, 3.82 mmol) in 50 mL of ethanol was added 2-pyridylethyl-(2-pyridylmethyl)methylamine (0.87 g, 3.83 mmol). The mixture was stirred for 1 h at room-temperature. The greenish brown solid thus formed was collected, washed with small amounts of ethanol and acetone, and air dried; (yield 1.25 g, 67%). Anal. Calcd for  $\text{C}_{14}\text{H}_{23}\text{N}_3\text{O}_3\text{Cl}_3\text{Ru}$ : C, 34.38; H, 4.71; N, 8.60. Found: C, 34.18; H, 4.31; N, 8.40.

### 6.3.2 $[\text{Ru}_2\text{O}(\text{O}_2\text{CMe})_2(\text{MeL})_2](\text{ClO}_4)_2 \cdot 4\text{H}_2\text{O}$

To a suspension of  $(\text{MeL})\text{RuCl}_3 \cdot 3\text{H}_2\text{O}$  (0.22g, 0.47 mmol) in 15 mL of water was added 9.0 g of sodium acetate to adjust the pH of the solution to ~7.1-7.2. The mixture was then refluxed for 30 min whereupon the color of the resulting solution changed from green to dark purplish blue. The solution was filtered while hot and to the filtrate ~ 5 mL of a saturated aqueous solution of sodium perchlorate was added. Immediately blue solid product started separating out. The microcrystalline solid was collected, washed with a small amount of cold water, and dried under vacuum (yield 0.15 g, 31%). Anal. Calcd for  $\text{C}_{32}\text{H}_{48}\text{N}_6\text{O}_{17}\text{Cl}_2\text{Ru}_2$ : C, 36.19; H, 4.52; N, 7.92. Found: C, 35.83; H, 4.42; N, 7.77. IR (KBr,  $\text{cm}^{-1}$ , selected peaks): 3420 (m) ( $\nu(\text{OH})$ ), 1545 (m) ( $\nu_{\text{as}}(\text{CO})$ ), 1440 (s) ( $\nu_{\text{s}}(\text{CO})$ ), 1100 (s) ( $\nu(\text{ClO}_4^-)$ ), 775 (s) ( $\nu_{\text{as}}(\text{RuORu})$ ). Absorption spectrum (in MeCN),  $\lambda$ , nm ( $\epsilon_{\text{Ru}}$ ,  $\text{M}^{-1}\text{cm}^{-1}$ ): 247 (12 450), 345 (7 350), 564 (4 980). Conductivity (MeCN,  $10^{-3}$  M solution at 298 K):  $\Lambda_{\text{M}} = 292 \text{ } \Omega^{-1}\text{cm}^2\text{mol}^{-1}$ .

## 6.4 Results and Discussion

### 6.4.1 Synthesis of the Tribridged Core

The key intermediate in the formation of  $[\text{Ru}_2(\mu\text{-O})(\mu\text{-O}_2\text{CMe})_2(\text{MeL})_2]^{2+}$  core using tridentate facially coordinating ligand **MeL** is the trichloride,  $[(\text{MeL})\text{RuCl}_3]$ . On boiling the aqueous suspension with sodium acetate an intense purplish blue coloration was observed. When pH of the solution was adjusted to ~7.0 using sodium acetate the tribridged cation,  $[\text{Ru}_2(\mu\text{-O})(\mu\text{-O}_2\text{CMe})_2(\text{MeL})_2]^{2+}$  was readily formed. Isolation in the crystalline state was achieved by the addition of an aqueous sodium perchlorate solution.



#### 6.4.2 Characterization of the Core

The blue solid,  $[\text{Ru}_2(\mu\text{-O})(\mu\text{-O}_2\text{CMe})_2(\text{MeL})_2](\text{ClO}_4)_2 \cdot 4\text{H}_2\text{O}$  exhibited the characteristic IR bands assignable to bridging acetates, the presence of RuORu moiety, water of crystallization, and  $\text{ClO}_4^-$  as anion. Figure 6.1 presents the IR spectrum of the present complex. Solution electrical conductivity measurement in MeCN solution reveals that the compound behaves as a 1:2 electrolyte.<sup>138</sup> The electronic spectrum (in MeCN) of the cation,  $[\text{Ru}_2(\mu\text{-O})(\mu\text{-O}_2\text{CMe})_2(\text{MeL})_2]^{2+}$  in the range 200-800 nm is displayed in Figure 6.2. The  $(\mu\text{-oxo})\text{bis}(\mu\text{-acetato})\text{diruthenium(III)}$  core formulation seems reasonable given similarities in the optical spectrum (Figure 6.2) of the present complex when compared to the spectrum<sup>272</sup> of the related structurally characterized dimer,  $[\text{Ru}_2(\mu\text{-O})(\mu\text{-O}_2\text{CMe})_2(\text{py})_6](\text{ClO}_4)_2 \cdot 4\text{H}_2\text{O}$ . The electronic spectra of all  $(\mu\text{-oxo})\text{bis}(\mu\text{-carboxylato})\text{diruthenium(III)}$  complexes are very similar regardless of the nature of the capping ligands. The band at 564 nm in the present complex is assigned to the ligand-to-metal charge-transfer (LMCT) transition of  $\pi(\text{O}^{2-}) \rightarrow d\pi(\text{Ru}^{\text{III}})$  origin.

The effective magnetic moment of this new tribridged compound in acetonitrile was determined by using the NMR method<sup>131</sup> and was found to be diamagnetic at room temperature. The diamagnetism can be explained as follows based on the model given by Dunitz and Orgel<sup>280</sup> for the linear ion,  $[\text{Cl}_5\text{RuORuCl}_5]^{4-}$ . A basis for rationalizing the bending along RuORu axis for our Ru(III)-Ru(III) case is available from simple MO arguments. If the Ru-O bond is taken as the z-axis for each Ru site, mixing can occur between each set

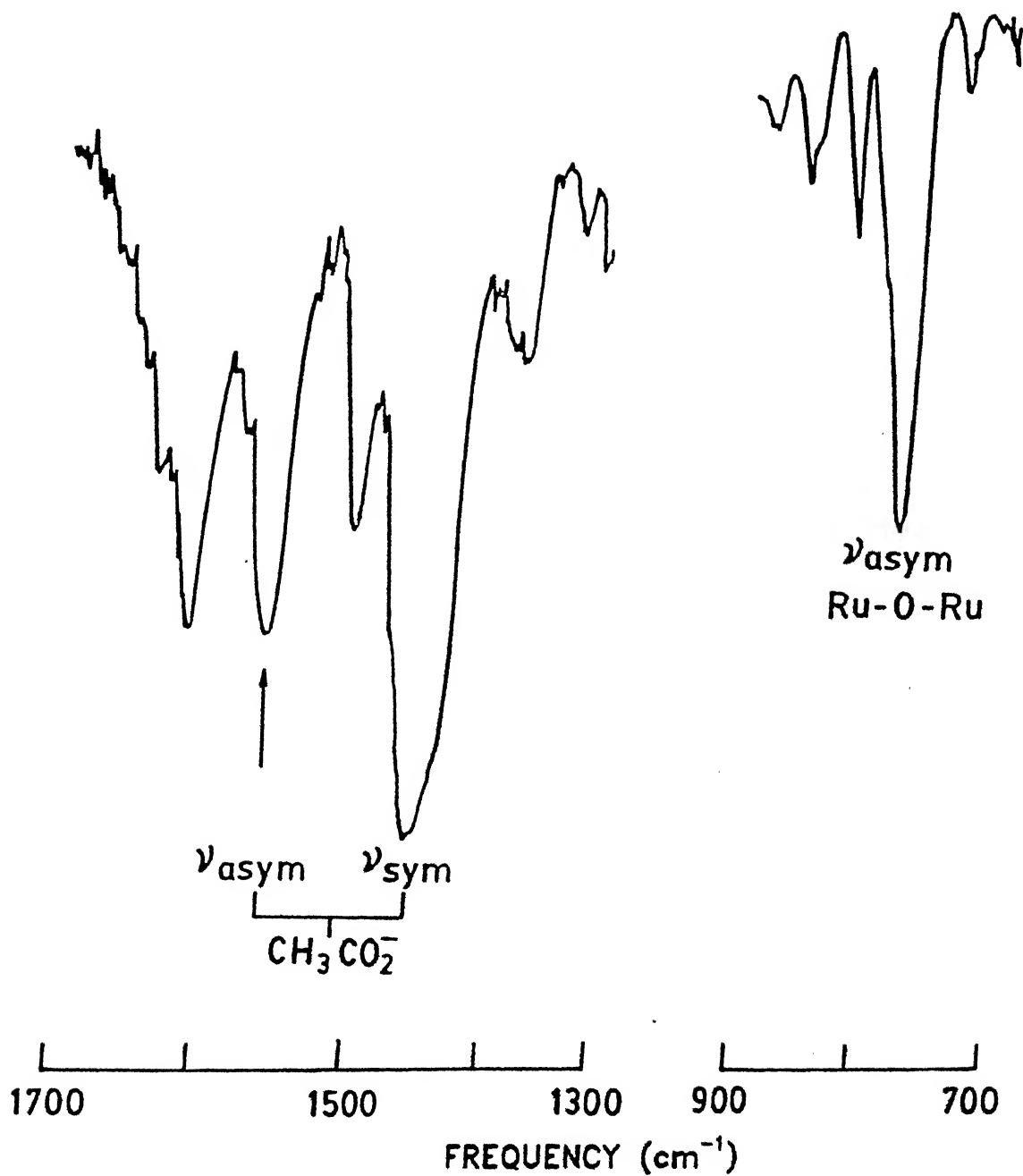


Figure 6.1 Selected portions of the infrared spectrum of  $[\text{Ru}^{\text{III}}_2(\mu\text{-O})(\mu\text{-OAc})_2(\text{MeL})_2](\text{ClO}_4)_2 \cdot 4\text{H}_2\text{O}$

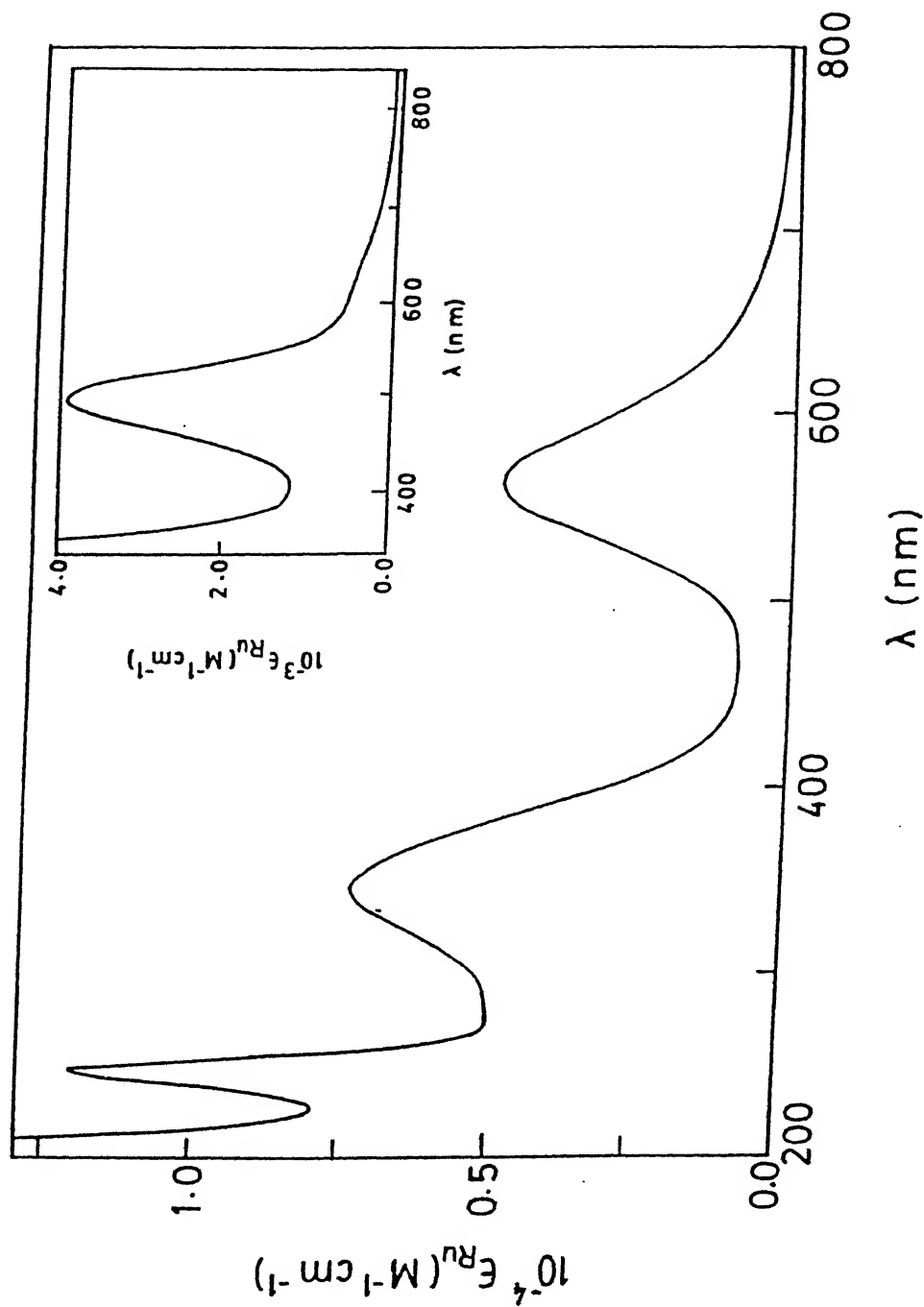


Figure 6.2 Electronic spectrum of  $[\text{Ru}^{\text{III}}_2(\mu\text{-O})(\mu\text{-OAc})_2(\text{MeL})_2](\text{ClO}_4)_2 \cdot 4\text{H}_2\text{O}$  in MeCN. The visible spectrum of coulometrically generated  $[\text{Ru}^{\text{IV,III}}_2(\mu\text{-O})(\mu\text{-OAc})_2(\text{MeL})_2]^{3+}$  in MeCN is shown as an inset.

of  $d_{xz}$ ,  $d_{yz}$  orbitals with two  $\pi$ -type p orbitals on the bridging O atom. The result is three sets of bridge-based orbitals. Two are bonding orbitals that are largely pO in character ( $\pi_1^b$ ,  $\pi_2^b$ ). Two are non-bonding or slightly antibonding orbitals that are largely  $d\pi_{Ru}$  in character ( $\pi_1^{nb}$ ,  $\pi_2^{nb}$ ). Two are antibonding orbitals that are also largely  $d\pi_{Ru}$  in character ( $\pi_1^*$ ,  $\pi_2^*$ ).

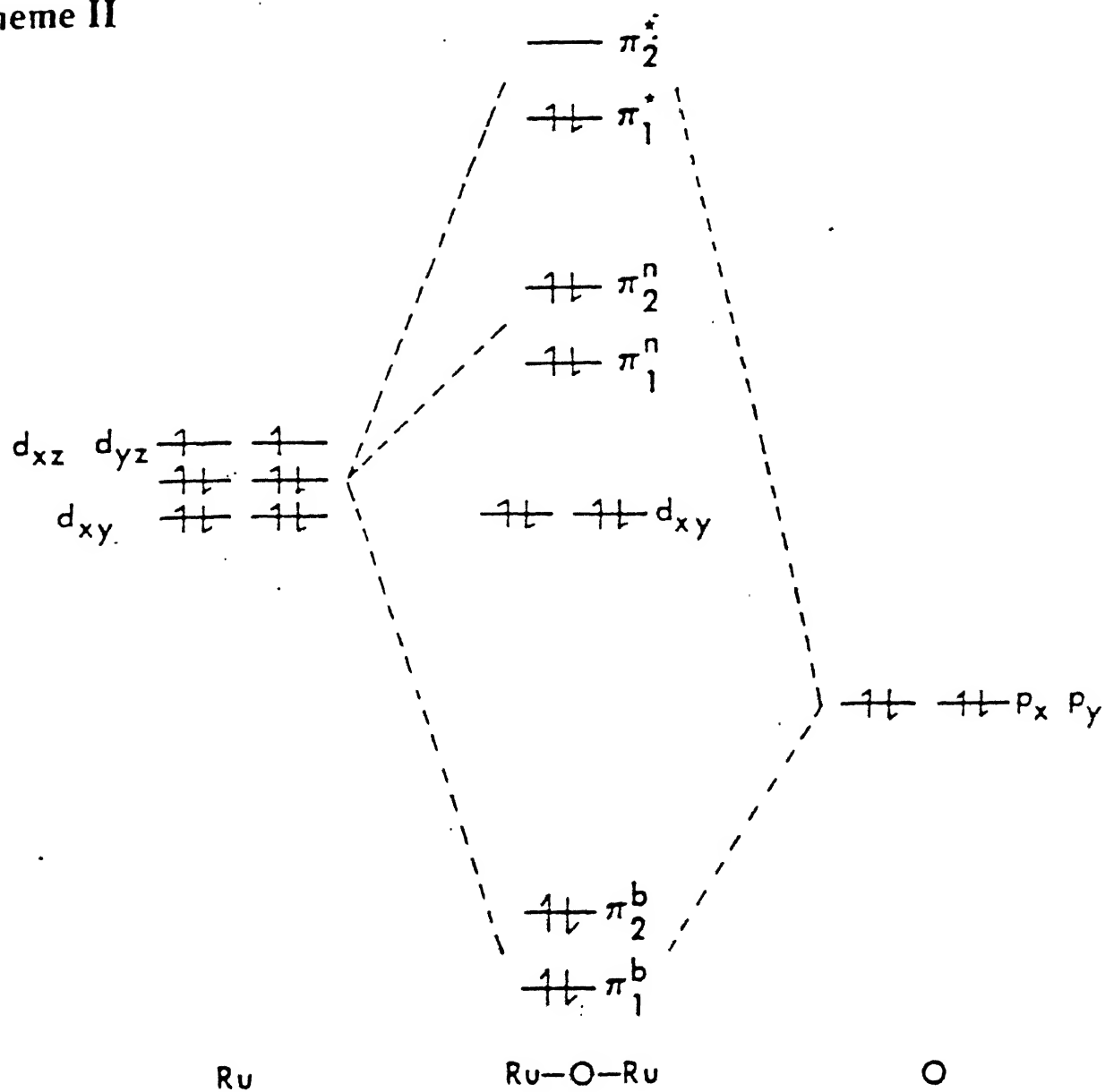
In terms of electron count for a  $\mu$ -oxo  $d^5$  Ru(III) complex, the occupancy of the bridging orbitals is  $(\pi_1^b)^2(\pi_2^b)^2(\pi_1^{nb})^2(\pi_2^{nb})^2(\pi_1^*, \pi_2^*)^2$ . A bending along Ru-O-Ru bonding axis results in a further increase in the energy separation between  $\pi_1^*$ ,  $\pi_2^*$  and a further electronic stabilization arising from the double occupation of  $\pi_1^*$ . A qualitative molecular orbital picture is given in Scheme I.

#### 6.4.3 Electrochemistry

Cyclic voltammetry in acetonitrile (0.1 M TBAP) was utilized to identify the core structure and to study the electrochemical properties of this tribridged complex using a platinum working electrode. Typical cyclic voltammograms for  $[Ru_2(\mu-O)(\mu-O_2CMe)_2-(MeL)_2]^{2+}$  are shown in Figure 6.3.

There are two well-defined oxidative responses in the potential region 0.0-2.4 V, the formal potentials ( $E_f$ ) being 0.86 V and 2.03 V vs SCE. The peak-to-peak separations ( $\Delta E_p$ ) at a scan rate of 50 mVs<sup>-1</sup> are 90 mV and 100 mV, respectively. Under our experimental conditions, the reversible couple  $Fc^+/Fc$  has  $\Delta E_p$  of 80 mV (Chapter 2; Section 2.1.2), which is used as the criterion for electrochemical reversibility. Also, the ratio of anodic to cathodic peak currents ( $i_{pa}/i_{pc}$ ) is  $\sim 1.0$  for each of

## Scheme II



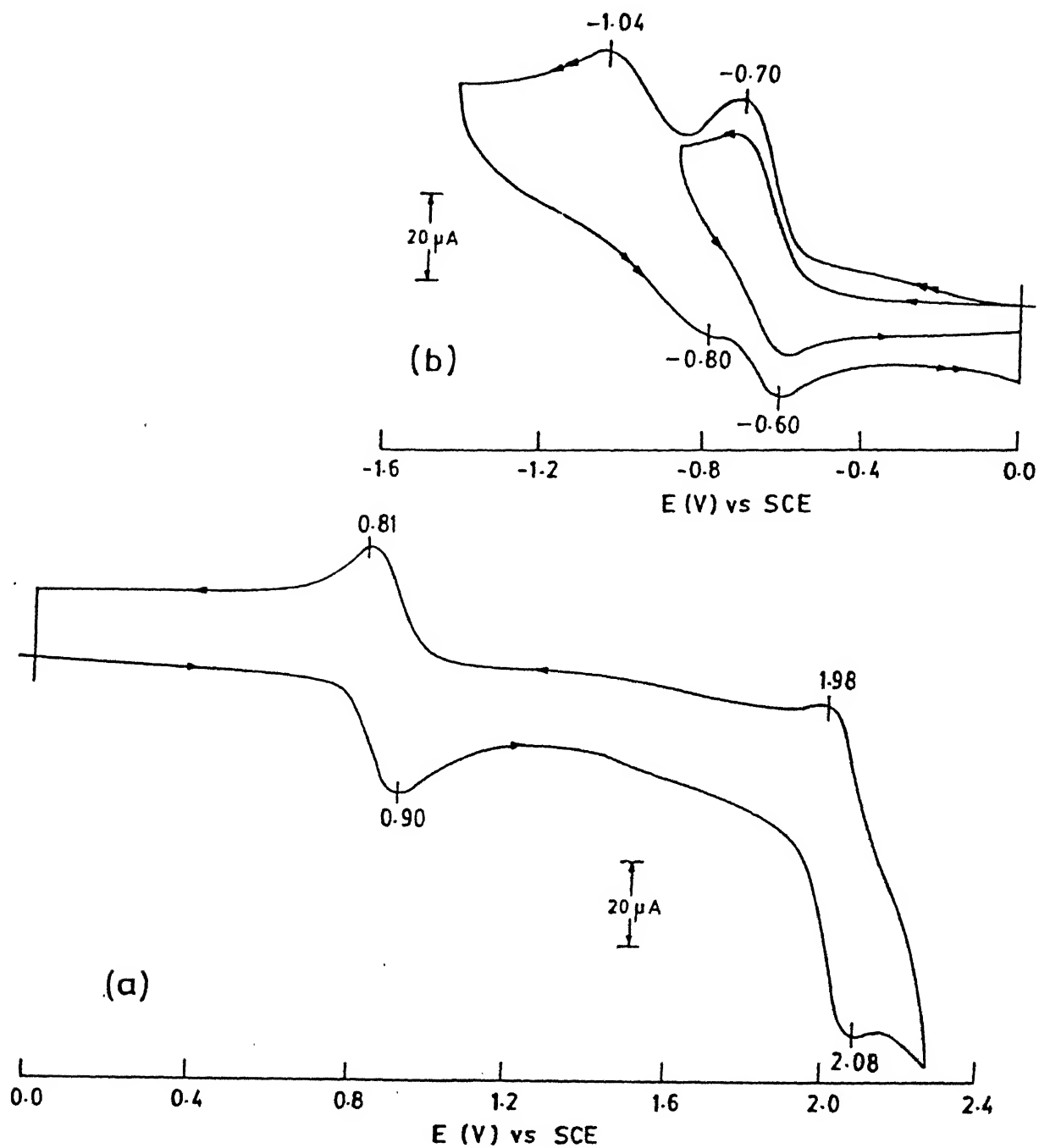
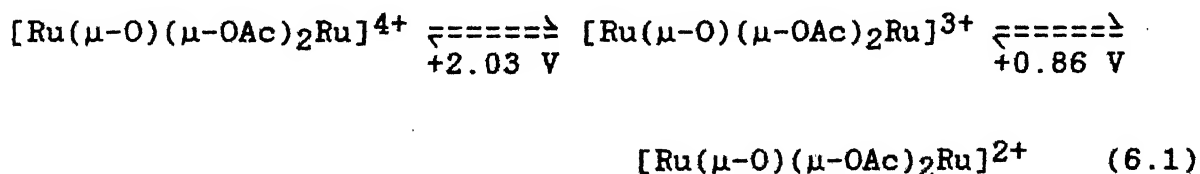


Figure 6.3 Cyclic voltammograms (scan rate  $50 \text{ mV s}^{-1}$ ) of  $[\text{Ru}^{\text{III}}_2(\mu\text{-O})(\mu\text{-OAc})_2(\text{MeL})_2]^{2+}$  in MeCN at a platinum electrode ( $[\text{Ru}]$ ,  $1.88 \text{ mM}$ ;  $0.2 \text{ M}$  TBAP) (a) anodic and (b) cathodic scan.

the processes. Coulometric oxidation at 1.06 V gave  $n = 1.01$  for the net electrochemical oxidation of  $[\text{Ru}_2(\mu\text{-O})(\mu\text{-O}_2\text{CMe})_2(\text{MeL})_2]^{2+}$ . Coulometric data are averages of at least three independent experiments and  $n$  is the number of electron passed per dimer. The above facts suggest that the  $[\text{Ru}_2(\mu\text{-O})(\mu\text{-O}_2\text{CMe})_2(\text{MeL})_2]^{2+}$  ion undergoes chemically and electrochemically reversible one-electron oxidation process generating the mixed-valence species  $[\text{Ru}_2^{\text{III,IV}}(\mu\text{-O})(\mu\text{-O}_2\text{CMe})_2(\text{MeL})_2]^{3+}$ . The cyclic voltammogram of the one-electron oxidized solution (Figure 6.4) is identical with the voltammogram of  $[\text{Ru}_2^{\text{III}}(\mu\text{-O})(\mu\text{-O}_2\text{CMe})_2(\text{MeL})_2]^{2+}$  but, as expected, this time the response at 0.86 V becomes reductive. The oxidized solution can be quantitatively reduced (applied potential, 0.66 V,  $n=0.88$ ) giving back  $[\text{Ru}_2^{\text{III}}(\mu\text{-O})(\mu\text{-O}_2\text{CMe})_2(\text{MeL})_2]^{2+}$ . Attempted electrolysis at 2.10 V to generate the two-electron oxidized dimer causes decomposition of the tri-bridged core. Thus the species  $[\text{Ru}_2^{\text{IV}}(\mu\text{-O})(\mu\text{-O}_2\text{CMe})_2(\text{MeL})_2]^{4+}$  is stable only on the time scale of cyclic voltammetry. The occurrence of the second oxidation process at such a high positive potential vitiates meaningful coulometric experiments. These observations are understandable from equation 6.1.



The tribridged complex also exhibits two reductive responses (Figure 6.3). The less negative wave with  $E_f$  of -0.65 V is quasi-reversible ( $\Delta E_p = 100 \text{ mV}$  at a scan rate of  $50 \text{ mVs}^{-1}$ ). This is

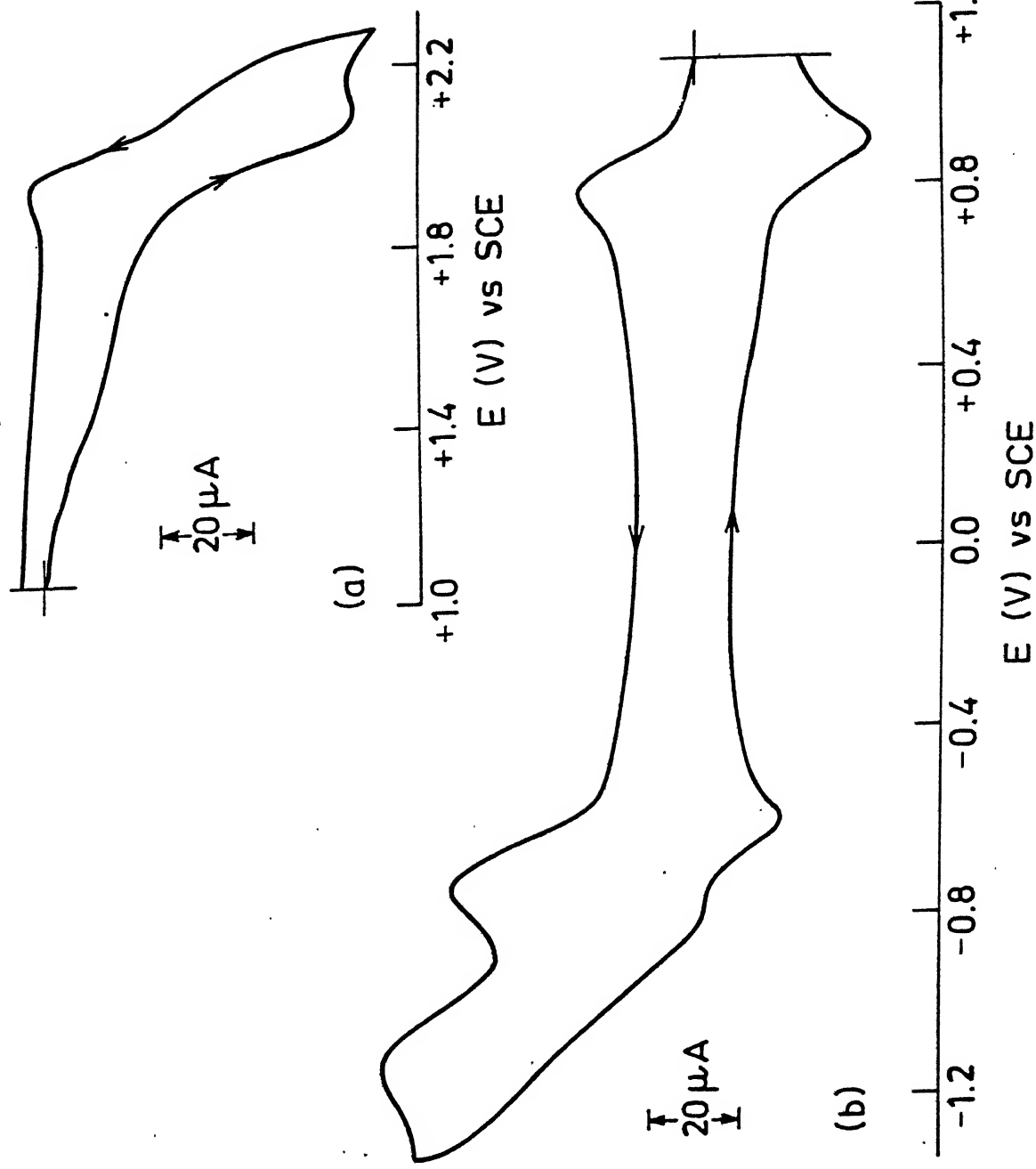


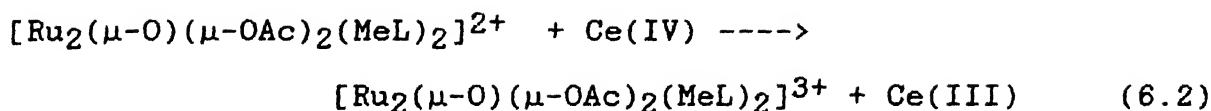
Figure 6.4 Cyclic voltammograms of Coulometrically generated  $[\text{Ru}_2(\mu\text{-O})(\mu\text{-OAc})_2(\text{MeL})_2]^{3+}$  in MeCN at a platinum electrode; scan rate  $50 \text{ mV s}^{-1}$ ; (a) anodic, (b) cathodic scan



assigned to the reduction to the  $\text{Ru}_2(\text{II},\text{III})$  state. At this level of reduction a  $\mu$ -hydroxo bridge formation is definitely<sup>220,268</sup> a possibility given the fact that the diruthenium(III) complex as isolated contained sufficient water of crystallization. An additional irreversible reductive response is seen with  $E_{pc} = -1.04$  V and  $\Delta E_p = 240$  mV. No attempt was made to examine the chemical and electrochemical properties of the coulometrically reduced solutions since it is expected that it would lead to decomposition of the tribridged structure yielding mononuclear ruthenium(II) compounds.<sup>281</sup>

#### 6.4.4 Stability and Optical Spectrum of $[\text{Ru}_2(\mu\text{-O})(\mu\text{-O}_2\text{CMe})_2(\text{MeL})_2]^{3+}$

Though stable under dry anaerobic conditions, electrochemically and/or chemically (see below) generated MeCN solutions of  $[\text{Ru}_2(\mu\text{-O})(\mu\text{-O}_2\text{CMe})_2(\text{MeL})_2]^{3+}$  are very sensitive to air. Under aerobic conditions such red solutions slowly turn purplish blue, the color of the diruthenium(III) precursor. Figure 6.2 exhibits the visible spectrum of the coulometrically oxidized  $3+$  ion in deoxygenated MeCN solution. The molar extinction coefficient ( $\epsilon_{\text{Ru}}$ ) for the intense peak at 494 nm is estimated to be  $3890 \text{ M}^{-1}\text{cm}^{-1}$ . The spectral feature is very similar to<sup>274</sup> that observed with a related species,  $[\text{Ru}^{\text{IV}}\text{Ru}^{\text{III}}(\mu\text{-O})(\mu\text{-O}_2\text{CMe})_2(\text{Me}_3\text{tacn})_2]^{3+}$ . The strong band at 564 nm of LMCT origin for  $[\text{Ru}_2(\mu\text{-O})(\mu\text{-O}_2\text{CMe})_2(\text{MeL})_2]^{2+}$  is considerably blue shifted ( $\lambda = 494$  nm) for  $[\text{Ru}_2(\mu\text{-O})(\mu\text{-O}_2\text{CMe})_2(\text{MeL})_2]^{3+}$ . The oxidation of  $[\text{Ru}_2(\mu\text{-O})(\mu\text{-O}_2\text{CMe})_2(\text{MeL})_2]^{2+}$  in deoxygenated MeCN could also be achieved chemically (Equation 6.2) by 1.06 equiv of ammoniumcerium(IV) nitrate.



We have done the following controlled experiments to identify the actual component of air responsible for the quantitative reduction of the 3+ ion to the 2+ ion. Incremental amounts of deoxygenated water (0.05 to 0.30 mL) were added to the deoxygenated MeCN solutions (0.29 mM in 2+ species) of chemically generated 3+ ion. We observe that the greater the amount of added water the faster the progress of reduction. These experiments confirm that under aerobic conditions the moisture of air acts as the reducing agent. Clean isosbestic points at 417 nm and 525 nm are observed when followed spectrophotometrically (Figure 6.5). Thermodynamically, the 3+ ion is capable of oxidizing water. The  $E_f$  value of  $\text{Ru}^{\text{IV}}\text{Ru}^{\text{III}}/\text{Ru}_2^{\text{III}}$  couple is ~200 mV more positive than that of the  $\text{O}_2/\text{H}_2\text{O}$  couple (pH ~ 7). The high moisture sensitivity of the oxidized species has made its isolation as a pure salt in the solid state unachievable.

The above-mentioned novel reactivity property of the 3+ ion towards water (moisture) can be summarized in Scheme II. It is to be noted that the catalytic oxidations of water by higher valent mononuclear ruthenium(IV) and/or oxo-bridged diruthenium complexes are well documented in literature.<sup>268,270,282,283</sup> The oxidation chemistry of the 3+ ion presented in this chapter is noteworthy in the sense that this is the first example among all known ( $\mu$ -oxo)bis( $\mu$ -carboxylato)diruthenium complexes to exhibit such a reactivity towards water.

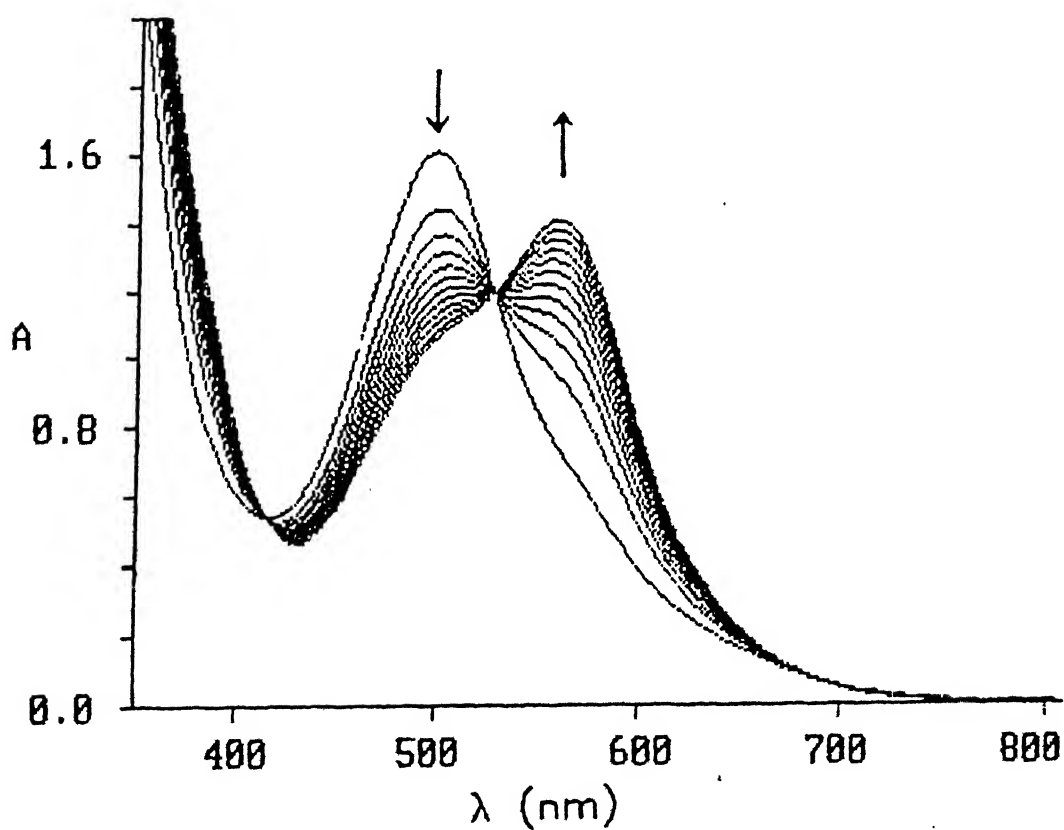
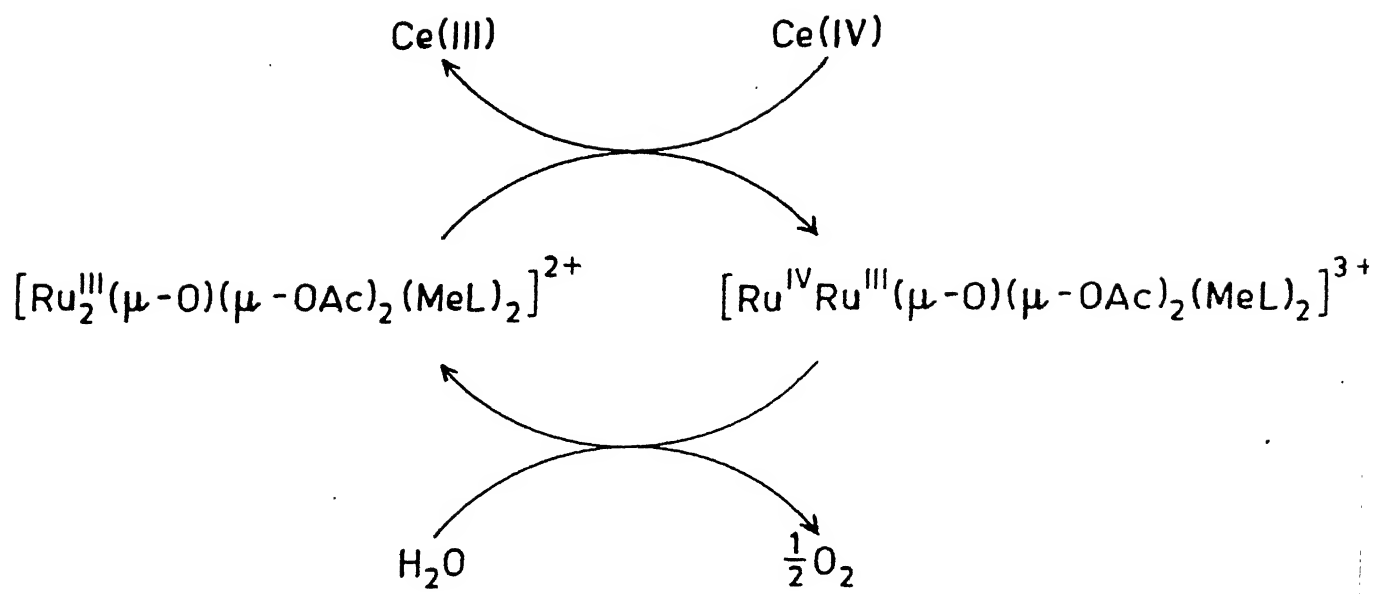


Figure 6.5 Conversion of  $[\text{Ru}_2^{\text{IV,III}}(\mu\text{-O})(\mu\text{-OAc})_2(\text{MeL})_2]^{3+}$  to  $[\text{Ru}_2^{\text{III}}(\mu\text{-O})(\mu\text{-OAc})_2(\text{MeL})_2]^{2+}$  in presence of water

## 6.5 Concluding Remarks

(i) Synthesis of a tribridged diruthenium(III) complex with  $[\text{Ru}_2(\mu\text{-O})(\mu\text{-O}_2\text{CMe})_2]^{2+}$  core using a tridentate  $\text{N}_3$  facially capping ligand MeL has been achieved. This work corroborates the generality and versatility of the existence of tribridge core structure.

(ii) The purplish blue diamagnetic complex,  $[\text{Ru}_2(\mu\text{-O})(\mu\text{-O}_2\text{CMe})_2(\text{MeL})_2]^{2+}$  displays in acetonitrile solution a chemically and electrochemically reversible oxidative redox response at 0.86 V vs. SCE.

(iii) The one-electron oxidized complex,  $[\text{Ru}_2(\mu\text{-O})(\mu\text{-O}_2\text{CMe})_2(\text{MeL})_2]^{3+}$  exhibits a strong LMCT transition at a comparatively higher energy than its diruthenium(III) analogue.

(iv) The red oxidised species,  $[\text{Ru}_2(\mu\text{-O})(\mu\text{-O}_2\text{CMe})_2(\text{MeL})_2]^{3+}$ , generated chemically (by  $\text{Ce}^{4+}$  oxidation) and/or electrochemically (coulometric oxidation) is very sensitive towards moisture giving back to the diruthenium(III) complex, and thus is capable of oxidizing water stoichiometrically.

## CHAPTER 7

New Mixed Valence Binuclear Complex Containing the  $\{\text{Mn}^{\text{IV}}(\mu\text{-O})_2(\mu\text{-OAc})\text{Mn}^{\text{III}}\}_2^{2+}$  Core: A Synthetic Model for the Active Site of Photosystem II.

Interest in  $\{\text{Mn}^{\text{IV}}(\mu\text{-O})_2\text{Mn}^{\text{III}}\}^{3+}$  species<sup>284-287</sup> has grown enormously in recent years<sup>288-300</sup> largely from the involvement of such species in the water oxidation photosystem II (PS II) of the photosynthetic apparatus.<sup>73,82,301</sup> For the  $\text{S}_2$  state in PS II, the multiline signal at  $g \sim 2$  in the EPR spectrum and the short Mn--Mn separation (2.70 Å, as indicated by extended X-ray absorption fine structure analysis) are both consistent<sup>302</sup> with, minimally, a binuclear formulation for the manganese centre. These characteristic physical properties are modeled remarkably well by a group of synthetic complexes having  $\{\text{Mn}^{\text{IV}}(\mu\text{-O})_2\text{Mn}^{\text{III}}\}^{3+}$  core structure. The di- $\mu$ -oxo complexes with an additional carboxylato bridge  $\{\text{Mn}^{\text{IV}}(\mu\text{-O})_2(\mu\text{-OAc})\text{Mn}^{\text{III}}\}^{2+}$  have also been devised as model complexes for the  $\text{S}_2$  state.<sup>303-305</sup> Although so far three bis( $\mu$ -oxo)( $\mu$ -carboxylato)dimanganese(IV,III) complexes have been reported, there has been no report on the existence of bis( $\mu$ -oxo)( $\mu$ -carboxylato)dimanganese(IV,IV) species. Tables 7.1 and 7.2 summarize bis( $\mu$ -oxo)dimanganese(IV,III) complexes with various terminal ligands.

In the last two chapters we have demonstrated the use of MeL as a facially capping ligand in the synthesis of transition metal complexes containing the  $\{\text{M}(\mu\text{-O})(\mu\text{-OAc})_2\text{M}\}^{2+,3+}$  ( $\text{M}=\text{Fe}, \text{Ru}$ ) cores. Having achieved that we decided to explore the dimanganese core formation using MeL as terminal ligands. The outcome of that endeavor is presented here. In this chapter we describe a new mixed valence binuclear Mn complex and its one-electron oxidation product containing  $\{\text{Mn}_2(\mu\text{-O})_2(\mu\text{-OAc})\}^{2+/3+}$  unit with interesting magnetic, EPR, and redox properties.

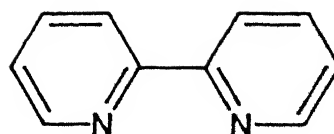
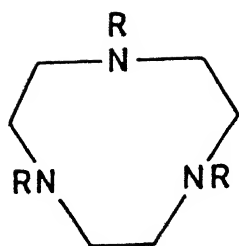
Table 7.1: Triply Bridged Dimanganese Complexes Having  
 $\{\text{Mn}^{\text{IV}}, \text{III}\}_2(\mu\text{-O})_2(\mu\text{-OAc})\}^{2+}$  Core

Terminal Ligands	Comments	References
1,4,7 triaza- cyclononane (TACN)	X-ray structure, variable temperature magnetic suscep- tibility (antiferromagnetism), EPR and absorption spectra	303
2,2'-bipyridine (BPY), and $\text{Cl}^-$	X-ray structure, variable temperature magnetic suscep- tibility (antiferromagnetism), EPR and absorption spectra	304
N,N,N',N'-tetra- kis(2-pyridylme- thyl)-1,2-ethane- diamine (TPEN)	X-ray structure, variable temperature magnetic suscep- tibility (antiferromagnetism), EPR and absorption spectra, cyclic voltammetry	305

**Table 7.2: A Selected Listing of Dibridged Dimanganese Complexes  
Having  $\{\text{Mn}^{\text{IV}}, \text{III}_2(\mu\text{-O})_2\}^{3+}$  Core**

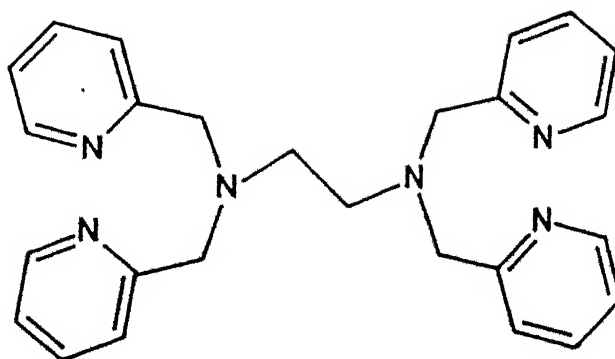
Terminal Ligands	Comments	References
2,2'-bipyridine (BPY)	X-ray structure, infrared, EPR, and absorption spectra, variable temperature magnetic susceptibility, electrochemistry	286
1,10-phenanthroline (PHEN)	X-ray structure, Variable temperature magnetic susceptibi- lity, EPR and absorption spectra, electrochemistry	288
1,4,8,11-tetra- azacyclotetra- decane (CYCLAM)	IR, absorption, and EPR spectra, electrochemistry	297
N,N'-bis(2-pyr- idylmethyl)-1,2- ethanediamine (BISPICEN)	Antiferromagnetism, EPR, and absorption spectra, cyclic voltammetry; X-ray structure and magnetic susceptibility of IV/IV dimer	289
Tris(2-pyridyl- methyl)amine (TMPA)	Absorption and EPR spectra, antiferromagnetism, cyclic voltammetry; X-ray structure of IV/IV dimer	290



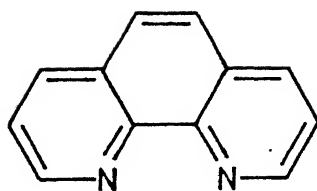


BPY

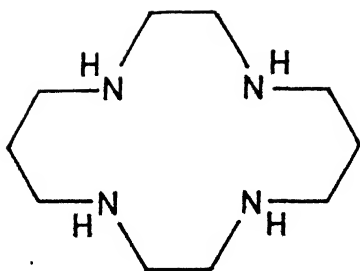
R = H : TACN



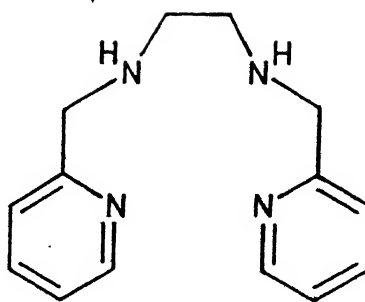
TPEN



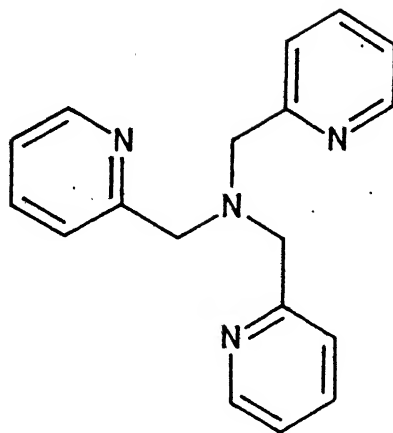
PHEN



CYCLAM



BISPICEN



TMPA

## 7.1 Experimental Section

### 7.1.1 Solvents and reagents

Solvents and reagents were obtained from commercial sources and used without further purification unless otherwise stated. Details of solvent purification are discussed in Chapter 2 (Section 2.1.1).

### 7.1.2 Measurements

Details of spectroscopic measurements are given in Chapter 2 (Section 2.1.2). Variable-temperature magnetic susceptibility measurements were made on powdered samples over the temperature range  $19.8 < T < 300$  K by the Faraday method. The diamagnetic contribution was calculated by using values<sup>134</sup> of  $-351 \times 10^{-6} \text{ cm}^3 \text{ mol}^{-1}$  for  $[\text{Mn}_2(\mu\text{-O})_2(\mu\text{-MeCO}_2)(\text{MeL})_2](\text{ClO}_4)_2 \cdot \text{H}_2\text{O}$ . Details of magnetic susceptibility measurements are in Chapters 2 and 5. The data were fitted to the appropriate theoretical expression for two interacting high-spin manganese(III) and manganese(IV) ions developed under the usual isotropic spin Hamiltonian  $H_0 = -2JS_1S_2$ .<sup>134</sup> Inclusion of terms for the temperature-independent paramagnetic susceptibility (t.i.p.) and for possible sample contamination by paramagnetic manganese(III) impurity exhibiting Curie behavior yields the relationship (Equation 7.1)

$$\chi_{\text{calc.}} = \frac{N g^2 \beta^2}{kT} \left[ \frac{1 + 10e^{3x} + 35e^{8x} + 84e^{15x}}{4 + 8e^{3x} + 12e^{8x} + 16e^{15x}} \right] + \frac{N g^2 \beta^2 S(S+1)}{3kT} \chi_{\text{para}} + \text{t.i.p.} \quad (7.1)$$

where  $x = J/kT$  and  $N$ ,  $g$ , and  $k$  have their usual meaning and  $\chi_{\text{para}}$  is the mole fraction of manganese(III) contaminant. A nonlinear least-squares fitting computer program was used to fit the observed data to equation 7.1. Details are in Chapter 5.

Cyclic voltammetry, differential pulse voltammetry, and coulometric measurements were performed by using the PAR Model 370-4 electrochemistry system. Details of electrochemical measurements are in Chapters 2 and 6.

## 7.2 Synthesis of ligand

Synthesis of 2-pyridylethyl-(2-pyridylmethyl)methylamine (MeL) has already been described in Chapter 5 (Section 5.2).

## 7.3 Syntheses of Compound

### 7.3.1 $[\text{Mn}_2(\mu\text{-O})_2(\mu\text{-MeCO}_2)(\text{MeL})_2](\text{ClO}_4)_2 \cdot \text{H}_2\text{O}$

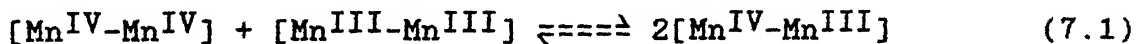
A suspension of 'Mn(OAc) $_3$ ·2H $_2$ O' (0.40 g, 1.49 mmol) and NaClO $_4$ ·H $_2$ O (0.21 g, 1.49 mmol) in 5 mL of degassed MeCN was stirred for 1 h. The ligand 2-pyridylethyl-(2-pyridylmethyl)methylamine (MeL) (0.34 g, 1.49 mmol) in 5 mL of degassed MeCN was then added slowly over a period of 5 min and the mixture was stirred at room temperature for 2 h. The brownish-green solution mixture was filtered through a G-4 frit. Layering of Et $_2$ O (5 mL) initiated the precipitation of a green microcrystalline complex of  $[\text{Mn}_2(\mu\text{-O})_2(\mu\text{-OAc})(\text{MeL})_2](\text{ClO}_4)_2 \cdot \text{H}_2\text{O}$  in 42% yield. For getting pure compound strict exclusion of air was found to be critical at all stages of reaction and workup. Anal. Calcd. for C $_{30}$ H $_{39}$ N $_6$ O $_{13}$ Cl $_2$ Mn $_2$ : C, 41.28; H, 4.51; N, 9.63%. Found: C, 41.20; H, 4.60; N, 9.70%. IR (KBr, cm $^{-1}$ , selected peaks): 3420 br ( $\nu$ (OH)), 1550 ( $\nu_{\text{as}}$ (OCO)), 1440 ( $\nu_{\text{s}}$ (OCO)), 1100 vs, br and 620 m ( $\nu$ (ClO $_4$ )),

670 ( $\chi(\text{Mn}_2\text{O}_2)$ ). Conductivity (MeCN,  $10^{-3}\text{M}$  solution at 298 K)  $\Lambda_{\text{M}} = 295 \text{ mho cm}^2\text{mol}^{-1}$ .

## 7.4 Results and Discussion

### 7.4.1 Synthesis of the Tribridged Core

Two different synthetic routes are known to make bis( $\mu$ -oxo)-dimanganese complexes; (i) oxidation of readily available  $\text{Mn}^{\text{II}}$  starting materials ( $\text{Mn}(\text{OAc})_2$ ,  $\text{MnCO}_3$ ) with reagents like  $\text{K}_2\text{S}_2\text{O}_8$  or  $\text{KMnO}_4$ , and (ii) addition of bidentate or tridentate capping ligand to a stirred solution of 'manganese(III) acetate' having  $\{\text{Mn}_3\text{O}\}^{7+}$  moiety. In the present work, the spontaneous self-assembly method<sup>247</sup> has been adopted to synthesize novel  $\{\text{Mn}^{\text{IV}}(\mu\text{-O})_2(\mu\text{-OAc})\text{Mn}^{\text{III}}\}^{2+}$  core utilizing MeL as terminal blocking agents. This is the second example where the terminal ends of the bis( $\mu$ -oxo)( $\mu$ -carboxylato)dimanganese(III,IV) unit have been blocked by this kind of tridentate ligands and is the fourth example of this type of core structure. The low yield of product is primarily a consequence of the disproportionation reaction as shown in equation 7.1:



### 7.4.2 Characterization of the Core

The  $\{\text{Mn}^{\text{IV}}(\mu\text{-O})_2(\mu\text{-OAc})\text{Mn}^{\text{III}}\}^{2+}$  core formulation results in a dipositively charged complex, which is consistent with the conductivity data.<sup>138</sup> The green solid  $[\text{Mn}_2(\mu\text{-O})_2(\mu\text{-OAc})(\text{MeL})_2](\text{ClO}_4)_2 \cdot \text{H}_2\text{O}$  exhibited the characteristic IR bands assignable to bridging acetate, the  $\text{Mn}_2(\mu\text{-O})_2$ , the water of crystallization and  $\text{ClO}_4^-$ . Figure 7.1 illustrates the IR spectrum of the complex.

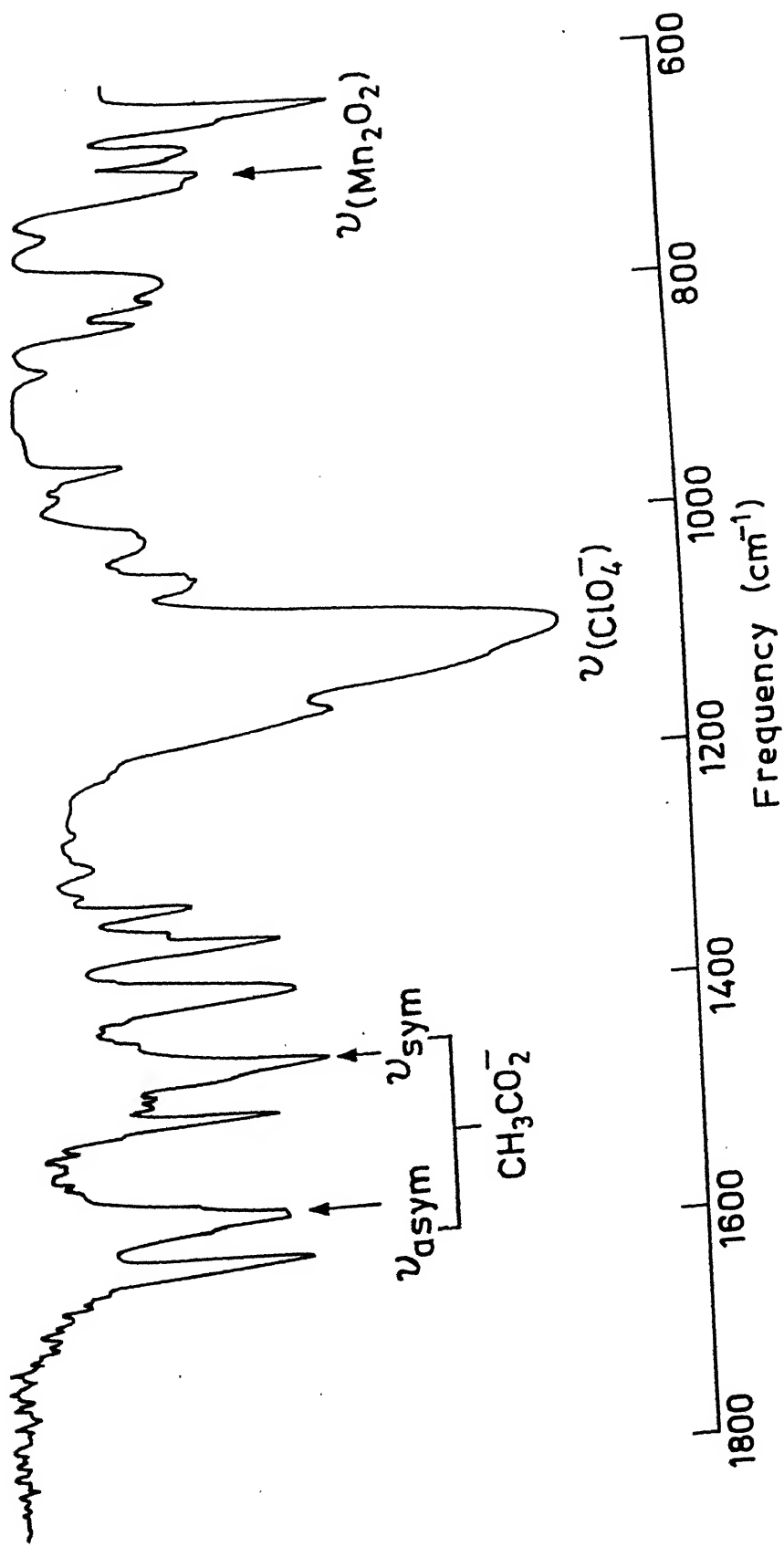
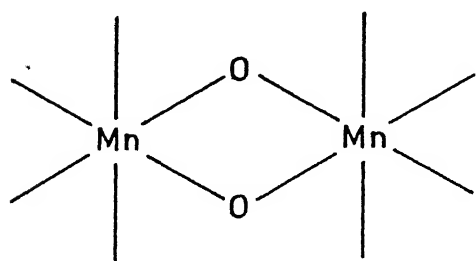
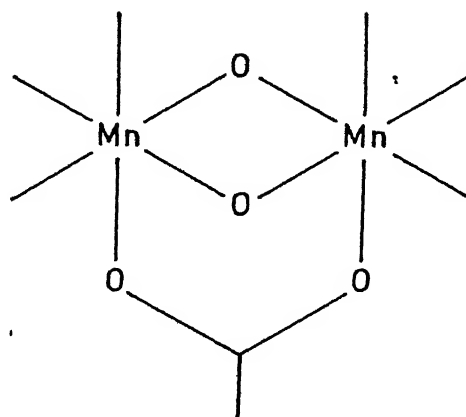


Figure 7.1 IR spectrum of  $[\text{Mn}^{\text{IV}}]_2(\mu\text{-O})_2(\mu\text{-OAc})(\text{MeL})_2(\text{ClO}_4)_2 \cdot \text{H}_2\text{O}$

The electronic spectrum of  $[\text{Mn}_2(\mu\text{-O})_2(\mu\text{-OAc})(\text{MeL})_2](\text{ClO}_4)_2 \cdot \text{H}_2\text{O}$  in acetonitrile is shown in Figure 7.2. A tentative assignment of the bands has been made (see below) from the spectra of structurally authenticated compounds having (a) bis( $\mu$ -oxo)dimanganese(IV,III) and (b) bis( $\mu$ -oxo)( $\mu$ -acetate)dimanganese(IV,III)



(a)



(b)

cores. Table 7.3 summarizes the absorption spectral data for compounds having these two core structures. From this it can be concluded that one cannot differentiate between these two cores on the basis of electronic structure alone. But given the similarities<sup>286-300,305</sup> between the absorption spectrum of the present complex and structurally characterized these two cores, one can definitely say about the presence of bis( $\mu$ -oxo)dimanganese(IV,III) core in our complex. The distinct peak at 540 nm is probably due to d-d transition<sup>286</sup> centered on Mn(III).

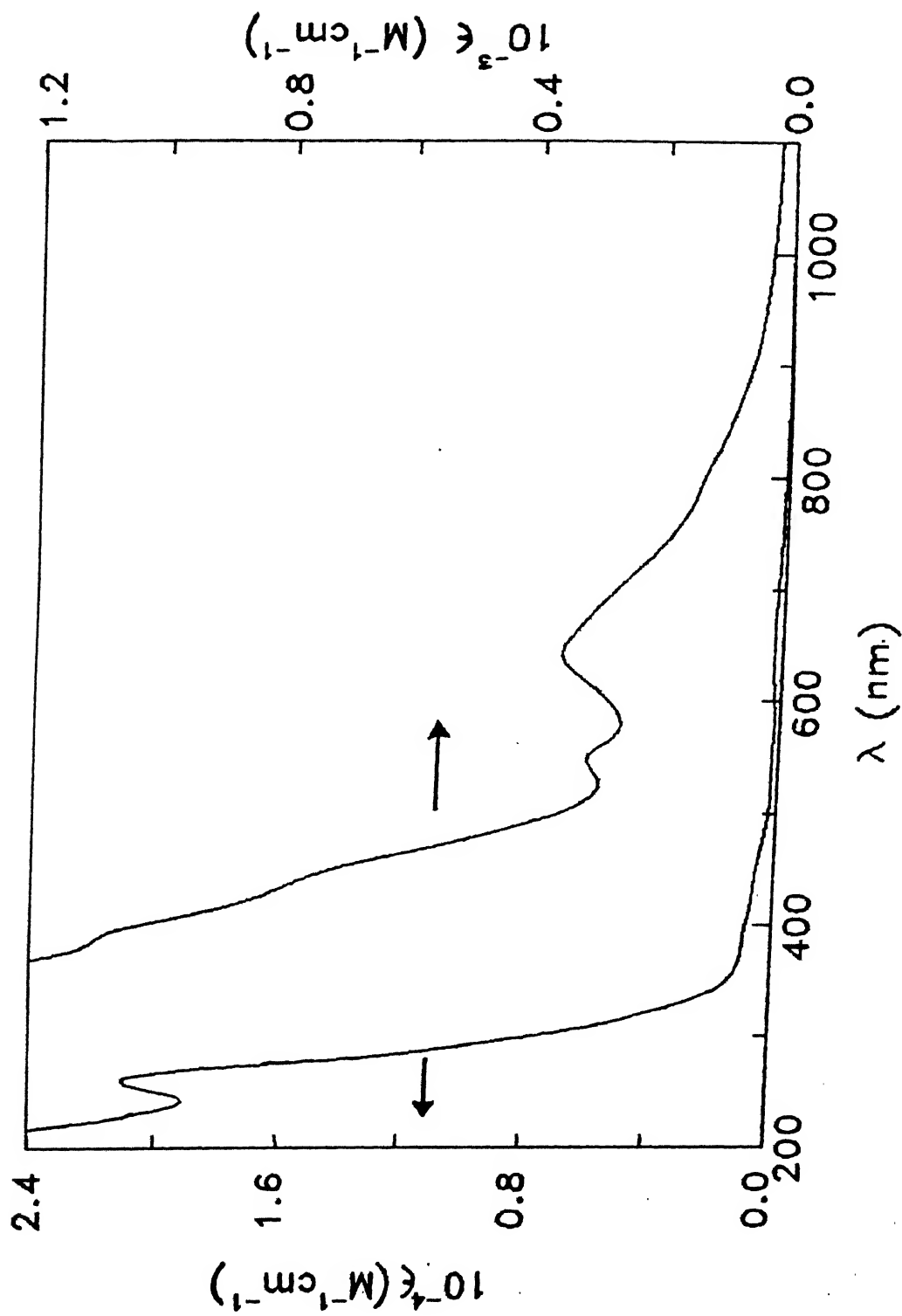


Figure 7.2 Electronic spectrum of  $[\text{Mn}^{\text{IV,III}}_2(\mu\text{-O})_2(\mu\text{-OAc})(\text{MeL})_2](\text{ClO}_4)_2 \cdot \text{H}_2\text{O}$



The peak at 640 nm is in the same energy region as has been observed for monomeric Mn(IV) complexes with oxygen donor ligands and may be assigned as an oxide-to-manganese(IV) charge transfer transition.<sup>298</sup> The broad low energy features centered near 800 nm has been attributed due to Mn(III)-Mn(IV) intervalence charge transfer.

#### 7.4.3 Magnetism

Solution magnetic susceptibility measurements using the Evans' method<sup>131</sup> (MeCN, 300 K) gave magnetic moment of 2.34  $\mu_B$  per Mn. This is well below the spin-only values expected for magnetically isolated Mn<sup>IV</sup> ( $d^3$ ) ion 3.87  $\mu_B$  or Mn<sup>III</sup> (high-spin  $d^4$ ) ion 4.90  $\mu_B$ . The present result agrees well with values expected<sup>287,295,296</sup> for antiferromagnetically coupled Mn<sup>IV</sup>( $S=3/2$ )-Mn<sup>III</sup>( $S=2$ ) pair. This behavior of the present complex is confirmed by the temperature dependent magnetic susceptibility measurements (Faraday method) in the range 19.8-300 K on solid samples (Figure 7.3). The effective magnetic moment decreases gradually from a value of 3.05  $\mu_B$  per dimer at room temperature to 1.98  $\mu_B$  at 19.8 K. The experimental data were fitted to the expression as stated in Section 7.1.2 for an isotropic exchange interaction between an Mn<sup>IV</sup> ( $S=3/2$ ) and Mn<sup>III</sup> ( $S=2$ ) ion. The spin exchange coupling constant  $J$  was found to be  $-144 \text{ cm}^{-1}$  (fixed  $g = 2.0$ ; t.i.p. =  $1.11 \times 10^{-3} \text{ emu mol}^{-1}$ ; paramagnetic impurity as monomeric Mn<sup>III</sup> = 1%). The  $J$  value for the present complex is comparable to that of Armstrong and coworkers.<sup>305</sup>

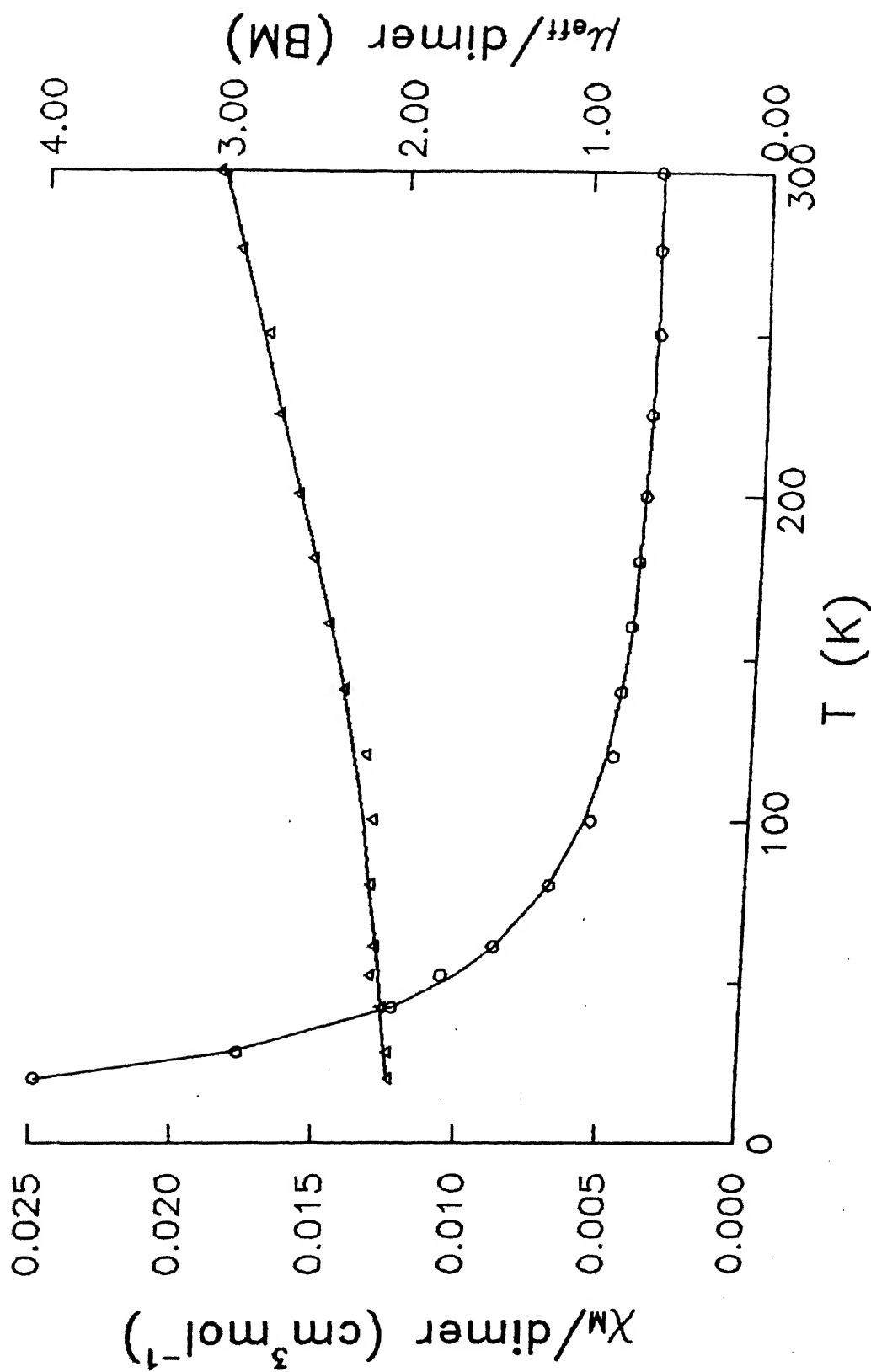


Figure 7.3 Molar susceptibility ( $\circ$ ) and effective magnetic moment per dimer ( $\Delta$ ) of  $[\text{Mn}^{\text{IV}}_2(\mu\text{-O})_2(\mu\text{-OAc})(\text{MeL})_2](\text{ClO}_4)_2 \cdot \text{H}_2\text{O}$  as a function of temperature. The solid lines are the theoretical values as indicated in the text.

#### 7.4.4 EPR Spectra

The frozen solution EPR spectrum of  $[\text{Mn}_2(\mu\text{-O})_2(\mu\text{-OAc})(\text{MeL})_2]^{2+}$  at 77 K exhibiting sixteen  $^{55}\text{Mn}$  hyperfine pattern (Figure 7.4) centered near  $g \approx 2.0$  is representative of binuclear  $\text{Mn}(\text{IV},\text{III})$  systems<sup>302</sup> including the  $S_2$  state of the Mn center of the PS II. Such a sixteen hyperfine pattern at  $g \approx 2$  is expected for an antiferromagnetically coupled  $\text{Mn}(\text{IV},\text{III})$  dimer with doublet ground state where two manganese ions are inequivalent. The observed spectral pattern is indicative of a situation, where one of the Mn nucleus has about twice the hyperfine coupling constant of the other.

#### 7.4.5 Redox Behavior

An important test for the merit of any PS II model system is the thermodynamics of its redox reaction. The cyclic voltammogram of a  $10^{-3}$  M MeCN solution of the present complex in 0.15 M TBAP shows (Figure 7.5) a well-behaved quasireversible ( $\Delta E_p = 100$  mV, scan rate =  $0.05 \text{ V s}^{-1}$ ) oxidative response at 1.00 V and an irreversible reduction wave at -0.01 V vs. SCE. The  $E_f$  value of 1.00 V corresponds to the one-electron  $\text{Mn}_2^{\text{IV}}/\text{Mn}^{\text{IV}}\text{Mn}^{\text{III}}$  couple (see below) and the reduction wave is assigned to  $\text{Mn}^{\text{IV}}\text{Mn}^{\text{III}}/\text{Mn}_2^{\text{III}}$  couple. Interestingly, the  $E_f$  value of the oxidative couple for  $[\text{Mn}_2(\mu\text{-O})_2(\mu\text{-OAc})(\text{MeL})_2]^{2+}$  is identical to that of the  $\{\text{Mn}^{\text{IV}}(\mu\text{-O})_2\text{Mn}^{\text{III}}\}^{3+}$  species with cyclam<sup>297</sup> as the terminal ligand. From the separation of  $E_f$  (oxidative response) and  $E_f$  [reductive response; as this is not a reversible response we have added 0.05 V to  $E_{pc}$  (cathodic peak potential)] values for  $[\text{Mn}_2(\mu\text{-O})_2(\mu\text{-OAc})(\text{MeL})_2]^{2+}$ , comproportionation constant ( $K_c$  at 25 °C) of the

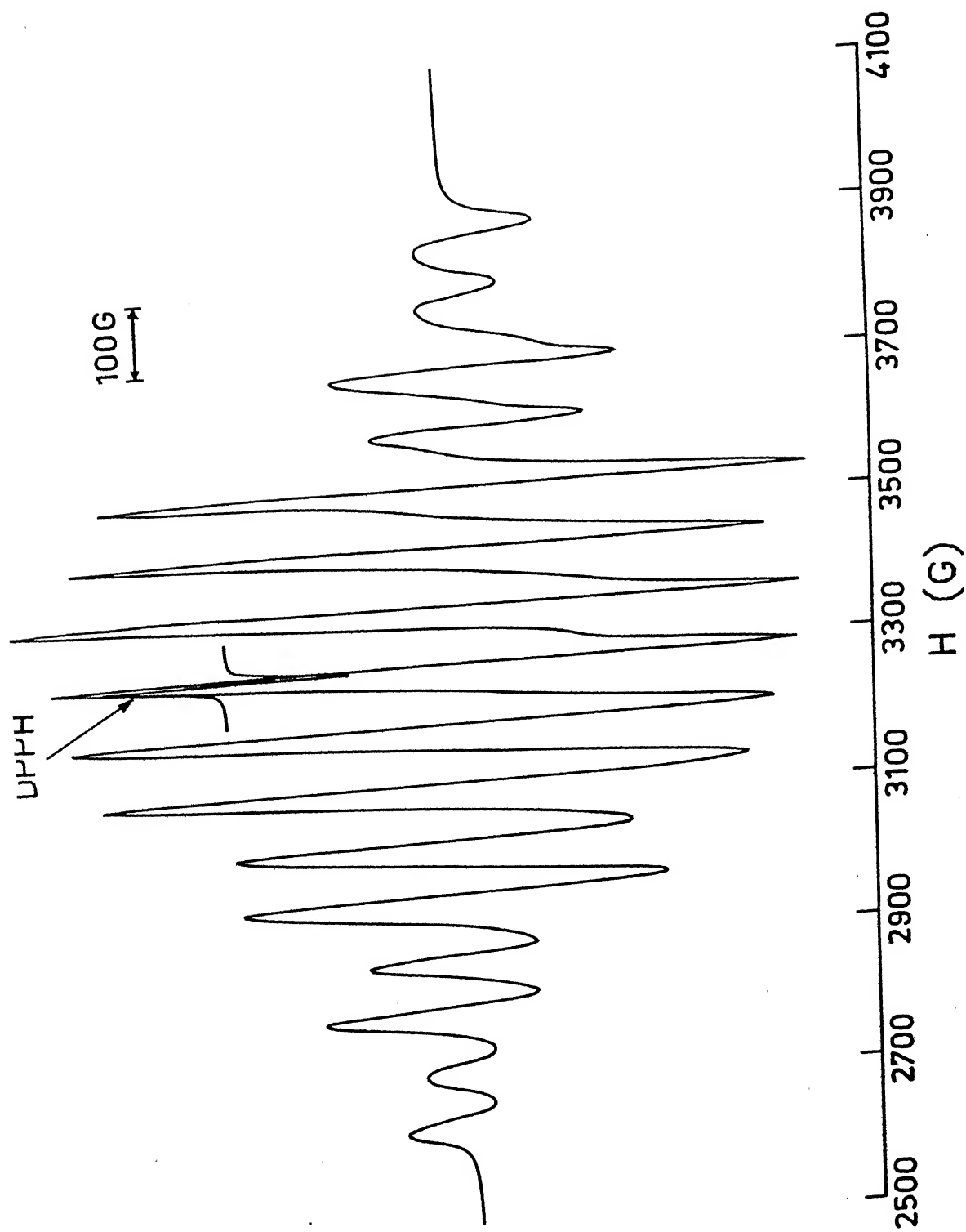


Figure 7.4 X-Band ESR spectrum of  $[\text{Mn}^{\text{IV,III}}_2(\mu\text{-O})_2(\mu\text{-OAc})(\text{MeL})_2](\text{ClO}_4)_2 \cdot \text{H}_2\text{O}$  in dichloromethane at 77 K.

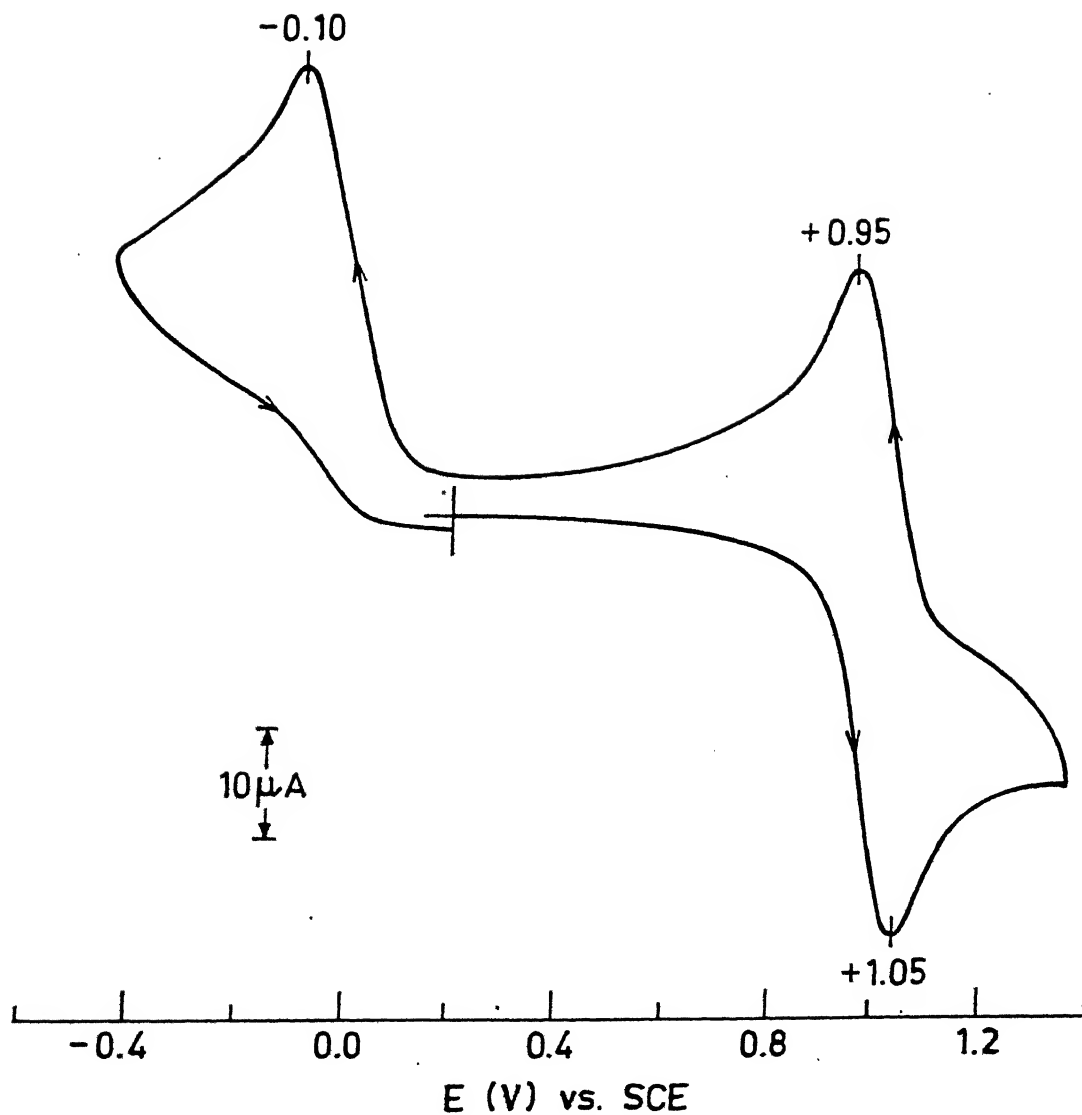


Figure 7.5 Cyclic voltammogram (scan rate 50 mV/s) of  $[\text{Mn}^{\text{IV,III}}_2(\mu\text{-O})_2(\mu\text{-OAc})(\text{MeL})_2](\text{ClO}_4)_2 \cdot \text{H}_2\text{O}$  in MeCN at a platinum electrode ( $C=1.0$  mM); supporting electrolyte, TBAP.

reaction (Equation 7.1) is calculated to be  $6.26 \times 10^{17}$ , indicating that the mixed valence complex is considerably stabilized. In fact, our compound is the most stable species among all mixed valence dimanganese(IV,III) complexes reported so far.<sup>293,295,305</sup> The three other compounds containing the  $\{\text{Mn}^{\text{IV}}(\mu\text{-O})_2(\mu\text{-OAc})\text{-Mn}^{\text{III}}\}_2^{2+}$  core which have been synthesized so far the redox behavior of only one complex has been reported.<sup>305</sup>

#### 7.4.6 Synthesis and Properties of $\{\text{Mn}^{\text{IV}}_2(\mu\text{-O})_2(\mu\text{-OAc})(\text{MeL})_2\}_2^{3+}$

Controlled potential electrolysis at 1.24 V gave  $n = 0.92$  for the net electrochemical oxidation of  $\{\text{Mn}^{\text{IV}}_2(\mu\text{-O})_2(\mu\text{-OAc})(\text{MeL})_2\}_2^{2+}$  generating the dimanganese(IV,IV) complex which is stable in MeCN solution. The orange-brown solution of  $\{\text{Mn}^{\text{IV}}_2(\mu\text{-O})_2(\mu\text{-OAc})(\text{MeL})_2\}_2^{3+}$  can also be generated chemically by oxidation of  $\{\text{Mn}^{\text{IV}}_2(\mu\text{-O})_2(\mu\text{-OAc})(\text{MeL})_2\}_2^{2+}$  with perchloric acid. The one-electron oxidized species displays identical cyclic voltammogram (this time, as expected, both the responses are reductive in nature). The nature of the absorption spectrum of the  $\text{Mn}_2(\text{IV,IV})$  species is less complex than that of  $\text{Mn}_2(\text{IV,III})$  dimer, containing only one peak at 620 nm ( $\epsilon \approx 400 \text{ M}^{-1}\text{cm}^{-1}$ ) in the visible region. Absorption spectra of  $[\text{Mn}_2^{\text{IV}}(\mu\text{-O})_2(\mu\text{-OAc})(\text{MeL})_2]^{3+}$ , generated chemically (perchloric acid oxidation) and electrochemically are displayed in Figure 7.6. Unlike  $\text{Mn}_2(\text{IV,III})$  complex the oxidized product did not give any EPR spectrum at 77 K. This is for the first time that a stable  $\text{Mn}_2(\text{IV,IV})$  species having  $\{\text{Mn}^{\text{IV}}_2(\mu\text{-O})_2(\mu\text{-OAc})\}_2^{3+}$  core has been generated and the redox stability and spectral properties have been examined.

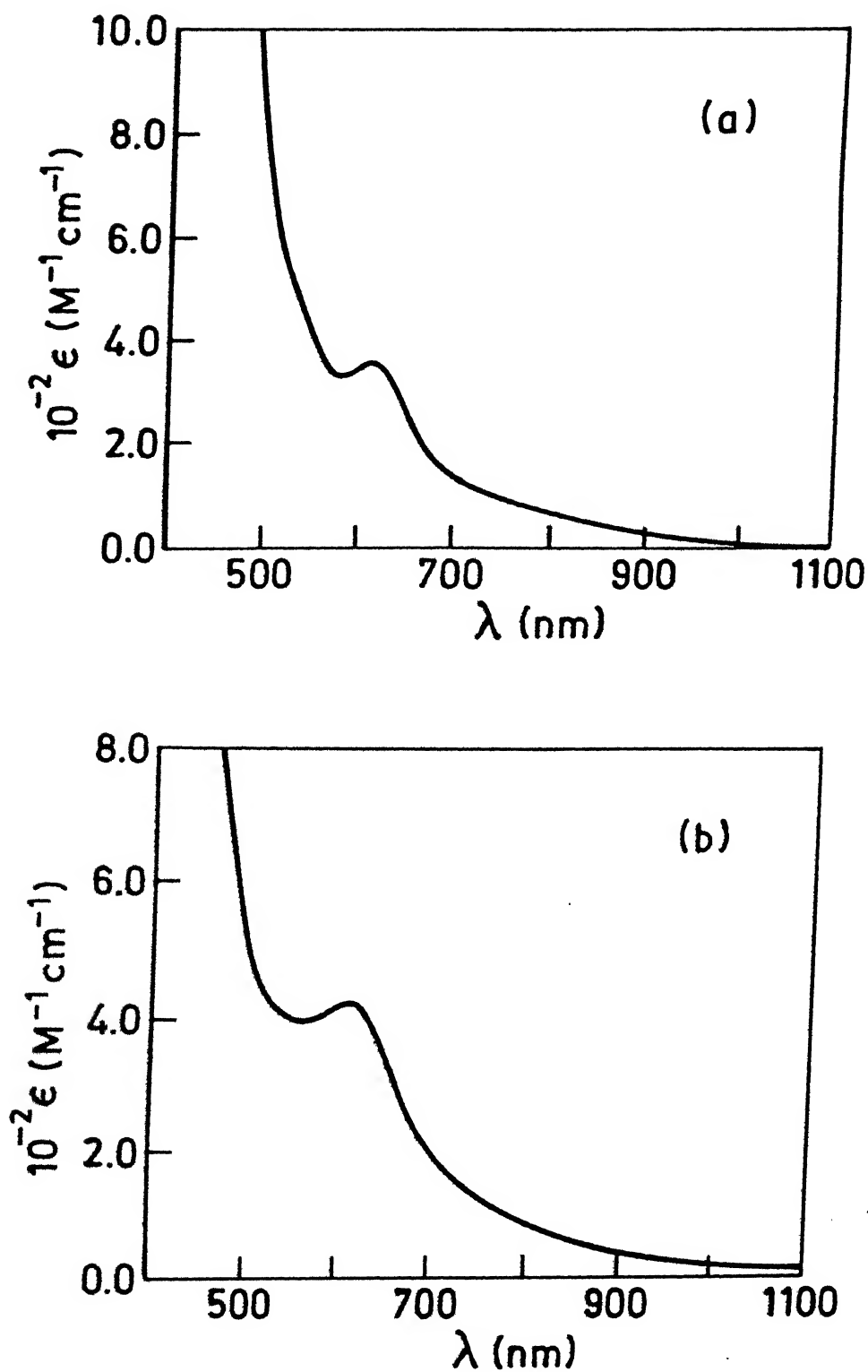


Figure 7.6:

Electronic spectrum of  $[\text{Mn}^{\text{IV}}_2(\mu\text{-O})_2(\mu\text{-OAc})(\text{MeL})_2](\text{ClO}_4)_3$  in MeCN

(a) Coulometrically generated

(b) Chemically generated by oxidation with perchloric acid

### 7.5 Concluding Remarks

The salient features of the results presented in Chapter 7 are as follows:

(i) The fourth example of a complex containing a  $\{\text{Mn}^{\text{IV}}(\mu\text{-O})_2(\mu\text{-OAc})\text{Mn}^{\text{III}}\}_2^{2+}$  core has been provided in this chapter.

(ii) Variable-temperature solid-state magnetic susceptibility data are consistent with a doublet ground state, with antiferromagnetic coupling constant,  $J = -144 \text{ cm}^{-1}$ .

(iii) The X-band EPR experiments at 77 K exhibit a 16-line spectrum centered at  $g = 2$ . This 16-line spectrum is attributed to the overlap of hyperfine splitting with two chemically different Mn nuclei ( $I = 5/2$ ) with one hyperfine coupling constant being roughly twice the magnitude of the other.

(iv) The complex  $\{\text{Mn}^{\text{IV}}_2(\mu\text{-O})_2(\mu\text{-OAc})(\text{MeL})_2\}^{3+}$  appears especially attractive for use as a reagent for one-electron oxidation in nonaqueous media. Interestingly, the  $E_f$  value for the oxidative couple is above the water oxidation threshold. Since four electrons are required for the formation of an  $\text{O}_2$ -molecule, a water oxidation<sup>306,307</sup> cannot be achieved if the oxidative process is not efficiently coupled.

(v) The redox stability and the absorption spectral properties of this IV,IV species have also been investigated for the first time.



## REFERENCES

- 1 Atkins, T. J.; Richman, J. E. J. Am. Chem. Soc. 1974, 96, 2268.
- 2 Atkins, T. J.; Richman, J. E.; Oettle, W. F. Org. Synth. 1978, 58, 86.
- 3 Choudhury, P.; Wieghardt, K Prog. Inorg. Chem. 1987, 35, 329 and references therein.
- 4 Taylor, L.T.; Vergez, S. C.; Busch, D. H. J. Am. Chem. Soc. 1966, 88, 3170.
- 5 Trofimenko, S. Prog. Inorg. Chem. 1986, 34, 115 and references therein.
- 6 Trofimenko, S J. Am. Chem. Soc. 1966, 88, 1842.
- 7 Trofimenko, S. J. Am. Chem. Soc. 1967, 89, 3170.
- 8 Trofimenko, S. J. Am. Chem. Soc. 1967, 89, 6208.
- 9 Trofimenko, S.; Calabrese, J. C.; Thompson, J. S. Inorg. Chem. 1987, 26, 1507.
- 10 Trofimenko, S. J. Am. Chem. Soc. 1966, 88, 1842.
- 11 Sorrell, T. N. Tetrahedron 1989, 45, 3.
- 12 (a) Brown, R. S.; Huguet, J. Can. J. Chem. 1980, 58, 889.  
(b) Canty, A. J.; George, E. E.; Lee, C. V. Aust. J. Chem. 1983, 36, 413.
- 13 Barqawi, K.; Llobet, A.; Meyer, T.J. J. Am. Chem. Soc. 1988, 110, 7751.
- 14 Jameson, D. L.; Blaho, J. K.; Kruger, K. T.; Goldsby, K. A. Inorg. Chem. 1989, 28, 4312.
- 15 Downard, A. J.; Honey, G. E.; Steel, P. J. Inorg. Chem. 1991, 30, 3733.

- 16 Sorrell, T. N.; Borovik, A. S. J. Am. Chem. Soc. 1987, 109, 4225.
- 17 Byers, P. K.; Canty, A. J.; Skekton, B. W.; White, A. W. Aust. J. Chem. 1985, 38, 1251.
- 18 Byers, P. K.; Canty, A. J.; Minchin, N. J.; Patrick, B. W.; Skekton, B. W.; White, A. W. J. Chem. Soc., Dalton Trans. 1985, 1183.
- 19 Addition, A.W.; Burman, S.; Wahlgren, C.G.; Rajan, O.A.; Rowe, T.M.; Sinn, E. J. Chem. Soc., Dalton Trans. 1987, 2621.
- 20 Bamidele sannu, S.; Behm, H. J.; Beurskens, P. T.; van Albada, G. A.; Reedijk, J.; Lenstra, A. T. H.; Addition, A. W.; Palaniandavar, M. J. Chem. Soc., Dalton Trans. 1988, 1429.
- 21 Piguet, C.; Bocquet, B.; Muller, E.; Willium, A. F. Helv. Chim. Acta 1989, 72, 323.
- 22 Gomez-Romero, P.; Casan-pastor, N.; Ben-Hussain, A.; Jameson, G. B. J. Am Chem. Soc. 1988, 110, 1988.
- 23 Adams, H.; Bailey, N. A.; Crane, J. D.; Fenton, D. E.; Latour, J.-M.; Williams, J. M. J. Chem. Soc., Dalton Trans. 1990, 1727.
- 24 Curtis, N. J.; Brown, R. S. J. Org. Chem. 1980, 45, 4038.
- 25 Wu, F.-J.; Kurtz, D. M., Jr., J. Am. Chem. Soc. 1989, 111, 6563.
- 26 Wu, F.-J.; Kurtz, D. M., Jr., Hagen, K. S.; Nyman, P. D.; Debrunner, P. G.; Vankai, V. A. Inorg. Chem. 1990, 29, 5174.
- 27 Nelson, S. M.; Rodgers, J. J. Chem. Soc. (A) 1968, 272.
- 28 Constable, E. C. Adv. in Inorg. Chem. and Radiochem. 1986, 30, 69.

- 29 Constable, E. C.; Lewish, J.; Liport, M. C.; Raithby, P. R. Inorg. Chim. Acta 1990, 178, 47.
- 30 Rao, J. M.; Macero, D. J.; Hughes, M. C. Inorg. Chim. Acta 1980, 41, 221.
- 31 Hughes, M. C.; Macero, D. J.; Rao, J. M.; Inorg. Chim. Acta 1981, 49, 241.
- 32 Mukherjee, R. N.; Rajan, O.A.; Chakravorty, A. Inorg. Chem. 1982, 21, 785.
- 33 Goswami, S.; Mukherjee, R. N.; Chakravorty, A. Inorg. Chem. 1983, 22, 2825.
- 34 Mukherjee, R. N.; Chakravorty, A. J. Chem. Soc., Dalton Trans. 1983, 955.
- 35 Bhattacharya, S.; Chakravorty, A.; Cotton, F. A.; Mukherjee, R. N.; Schwotzer, W. Inorg. Chem. 1984, 23, 1709.
- 36 Senoff, C. V. Coord. Chem. Rev. 1980, 32, 111.
- 37 Tsiamis, C.; Hadjikostas, C.C.; Karageorgiou, S.; Manoussakis, G. Inorg. Chim. Acta 1988, 143, 17.
- 38 Sorrell, T. N.; Jameson, D. L. Inorg. Chem. 1982, 21, 1014.
- 39 Boggess, R. K.; Hughes, Z. W.; Coleman, W. M.; Taylor, L. T. Inorg. Chim. Acta 1980, 38, 183.
- 40 König, K. Prog. Inorg. Chem. 1987, 35, 527.
- 41 Martin, R. L.; White, A. H. Transition Met. Chem. 1968, 4, 113.
- 42 Sacconi, L. Pure Appl. Chem. 1971, 27, 161.
- 43 Toftlund, H. Coord. Chem. Rev. 1989, 94, 67.
- 44 Wilkins, R. G.; Harrington, P. C. Adv. Inorg. Biochem. 1983, 5, 51.

- 45 Wilkins, P. C.; Wilkins, R. G. Coord. Chem. Rev. 1987, 79, 195.
- 46 Klotz, I. M.; Kurtz, D. M., Jr. Acc. Chem. Res. 1984, 17, 16.
- 47 Stenkamp, R. E.; Sieker, L. C.; Jensen, L. H.; McCallum, J. D.; Sanders-Loehr, J. Proc. Natl. Acad. Sci. (U.S.A.) 1985, 82, 713.
- 48 Stenkamp, R. E.; Sieker, L. C.; Jensen, L. H. J. Am. Chem. Soc. 1984, 106, 618.
- 49 Bunker, G.; Peterson, L.; Sjöberg, B.-M.; Sahlin, M.; Chance, M.; Chance, B.; Ehrenberg, A. Biochem. 1987, 26, 4708.
- 50 Sjöberg, B.-M.; Sanders-Loehr, J.; Loehr, T. M. Biochem. 1987, 26, 4242.
- 51 Scarrow, R. C.; Meroney, M. J.; Palmer, S. M.; Que, L. Jr.; Roe, A. L.; Salowe, S. P.; Stubbe, J. J. Am. Chem. Soc. 1987, 109, 7857.
- 52 Lammers, M.; Follmann, H. Struc. Bond. 1983, 54, 27.
- 53 Norlund, P.; Sjöberg, B.-M.; Eklund, H. Nature 1990, 345, 593.
- 54 Averill, B. A.; Davis, J. C.; Burman, S.; Zirino, T.; Sanders-Loehr, J.; Loehr, T. M.; Sage, J. T.; Deburnner, P. G. J. Am. Chem. Soc. 1987, 109, 3760 and references therein.
- 55 Woodland, M. P.; Patil, D. S.; Canmack, R.; Dalton, H. Biochim. Biophys. Acta. 1986, 873, 237.
- 56 Woodland, M. P.; Dalton, H. J. Biol. Chem. 1984, 259, 53.
- 57 Legall, J.; Prickril, B. C.; Moura, I.; Xavier, A. V.; Moura, J. J. G.; Huynh, B.-H. Biochem. 1988, 27, 1636.

- 58 Moura, I.; Moura, J. J. G.; LeGall, J.; Huynh, B.-H. J. Inorg. Biochem. 1989, 436, 228.
- 59 Chasteen, N. D.; Antanaitis, B. C.; Aissen, P. J. Biol. Chem. 1985, 260, 2926.
- 60 Hendrickson, W. A.; Klippenstein, G. L.; Ward, K. B. Proc. Natl. Acad. Sci. (U.S.A.) 1975, 72, 2160.
- 61 Seiker, L. C.; Bolts, L.; Stenkamp, R. E.; Jensen, L. H.; Appleby, C. A. J. Mol. Biol. 1981, 148, 493.
- 62 Stenkamp, R. E.; Seiker, L. C.; Jensen, L. H.; J. Inorg. Biochem. 1983, 19, 247.
- 63 Smith, J. L.; Hendrickson, W. A.; Addition, A. W. Nature 1983, 303, 86.
- 64 Stenkamp, R. E.; Seiker, L. C.; Jensen, L. H.; Sanders-Loehr, J. Nature 1981, 148, 493.
- 65 Stenkamp, R. E.; Seiker, L. C.; Jensen, L. H.; J. Am. Chem. Soc. 1984, 106, 618.
- 66 Sheriff, B.; Hendrickson, W. A.; Smith, J. L. J. Mol. Biol. 1987, 197, 273.
- 67 Stenkamp, R. E.; Seiker, L. C.; Jensen, L. H. Acta Crystallogr. 1983, B39, 697.
- 68 Shiemke, A. K.; Loehr, T. M.; Sanders-Loehr, J. J. Am. Chem. Soc. 1986, 108, 2437 and references therein.
- 69 Babcock, L. M.; Bradic, Z.; Harrington, P. C.; Wilkinson, R. G.; Yoneda, G. S. J. Am. Chem. Soc. 1980, 102, 2849.
- 70 Muhoberac, B. B.; Wharton, D. C.; Babcock, L. M.; Harrington, P. C.; Wilkins, R. G. Biochim. Biophys. Acta. 1980, 626, 337.

- 71 Vincent, V. B.; Olivier-Lilley, G. L.; Averill, B. A. Chem. Rev. 1990, 90, 1447.
- 72 George, G. N. ; Prince, R. C; Cramer, S. P. Science 1989, 243, 789.
- 73 Weighardt, K. Angew. Chem. Int. Ed. Engl. 1989, 28, 1153.
- 74 Brudvig, G. W. ; Crabtree, R. H. Prog. Inorg. Chem. 1989, 37, 99.
- 75 Christou, G. Acc. Chem. Res. 1989, 22, 328.
- 76 Renger, G. Angew. Chem. Int. Ed. Engl. 1987, 26, 643.
- 77 Oki, A. R.; Hodgson, D. J. Inorg. Chim. Acta 1990, 170, 65.
- 78 Dixit, P. S.; Srinivasan, K. Inorg. Chem. 1988, 27, 4507.
- 79 Srinivasan, K.; Michand, P.; Kochi, J. K. J. Am. Chem. Soc. 1986, 108, 2309.
- 80 Pirson, A. Z. Bot. 1937, 31, 193.
- 81 Kok, B.; Forbush, B.; McGloin, M. Photochem. Photobiol., 1970, 11, 457.
- 82 Vincent, J. B.; Christou, G. Adv. in Inorg. Chem., Eds., Sykes, A. G.; Academic Press, Inc. New York, San Diego; 1989, 33, 196.
- 83 Elguero, J. in 'Comprehensive Heterocyclic Chemistry', Eds., Potts, K. T. Pergamon press: New York, 1984, pp. 223.
- 84 Bhula, R.; Osvath, P.; Weatherburn, D. C. Coord. Chem. Rev. 1988, 91, 89.
- 85 Hancock, R. D.; Martell, A.E. Chem. Rev. 1989, 89, 1875.
- 86 Gruenwedel, D. W. Inorg. Chem. 1968, 7, 495.
- 87 Newkome, G. R.; Gupta, V. K.; Fronczek, F. R.; Pappalardo, S. Inorg. Chem. 1984, 23, 2400.

- 88 Newkome, G. R.; Frere, Y. A.; Fronczek, F. R.; Gupta, V. K. Inorg. Chem. 1985, 24, 1001.
- 89 Szalda, D. J.; Keene, F. R. Inorg. Chem. 1986, 25, 2795.
- 90 Karlin, K. D.; Haka, M. S.; Cruse, R. W.; Meyer, G. J.; Farooq, A.; Gultneh, Y.; Hayes, J. C.; Zubieta, J. J. Am. Chem. Soc. 1988, 110, 1196.
- 91 Mandel, J. B.; Maricondi, C.; Douglas, B. E. Inorg. Chem. 1988, 27, 2990.
- 92 Brown, R. S.; Huguet, J. Can. J. Chem. 1980, 58, 889.
- 93 Goodwin, J. A.; Stanbury, D. M.; Wilson, L. J.; Eigenbrot, C. W.; Scheidt, W. R. J. Am. Chem. Soc. 1987, 109, 2979.
- 94 Brown, S. J.; Hudson, S. E.; Stephan, D. W.; Mascharak, P. K. Inorg. Chem. 1989, 28, 468.
- 95 Lomis, T. J.; Elliott, M. G.; Siddiqui, S.; Moyer, M.; Koepsel, R. R.; Shepherd, R. E. Inorg. Chem. 1989, 28, 2369.
- 96 Oka, H.; Nakao, Y.; Suzuki, S.; Mori, W.; Kinoshita, I.; Ooi, S.; Ichimura, A. Inorg. Chim. Acta, 1989, 165, 111.
- 97 Piguet, C.; Bernardinelli, G.; Williams, A. F. Inorg. Chem. 1989, 28, 2920.
- 98 Patch, M. G.; Choi, H.-K.; Chapman, D. R.; Bau, R.; McKee, V.; Reed, C. A. Inorg. Chem. 1990, 29, 110.
- 99 Fenton, D. E. Pure Appl. Chem. 1986, 58, 1437.
- 100 Menif, R.; Chen, D.; Martell, A. E. Inorg. Chem. 1989, 28, 4633.
- 101 Cox, D. D.; Benkovic, S. J.; Bloom, L. M.; Bradley, F. C.; Nelson, M. J.; Que, L., Jr.; Wallick, D. E. J. Am. Chem. Soc. 1988, 110, 2026.

- 102 Cox, D. D.; Que, L., Jr., J. Am. Chem. Soc. 1988, 110, 8085.
- 103 Sanders-Loehr, J.; Wheeler, W. D.; Shiemke, A. K.; Averill, B. A.; Loehr, T. M. J. Am. Chem. Soc. 1989, 111, 8084.
- 104 Kamiyusuki, T.; Okawa, H.; Kitaura, E.; Koikawa, M.; Matsumoto, N.; Kida, S.; Oshio, H. J. Chem. Soc., Dalton Trans. 1989, 2077.
- 105 Malachowski M. R.; Davidson, M. G. Inorg. Chim. Acta 1989, 162, 199.
- 106 Driessen, W. L.; Wiesmeijer, W. G. R.; Schipper -Zablotskaja, M.; De Graff, R. A. G.; Reedijk, J. Inorg. Chim. Acta 1989, 162, 233.
- 107 Sorrell, T. N.; Vankai, V. A. Inorg. Chem. 1990, 29, 1687.
- 108 Steel, P. J.; Lahousse, F.; Lerner, D.; Merzin, C. Inorg. Chem. 1983, 22, 1488.
- 109 Campagna, S.; Denti, G.; DeRosa, G.; Sabatino, L.; Ciano, M.; Balzani, V. Inorg. Chem. 1989, 28, 2565.
- 110 Kawanishi, Y.; Kitamura, N.; Tazuke, S. Inorg. Chem. 1989, 28, 2968.
- 111 Tang, C. C.; Davalian, D.; Huang, P.; Breslow, R. J. J. Am. Chem. Soc. 1978, 100, 3918.
- 112 Breslow, R.; Hunt, J. T.; Smiley, R.; Tarnowski, T. J. Am. Chem. Soc. 1983, 105, 5337.
- 113 Gorun, S. M.; Papaefthymiou, G. C.; Frankel, R. B.; Lippard, S. J. J. Am. Chem. Soc. 1987, 109, 4244.
- 114 Watson, A. A.; House, D. A.; Steel, P. J. Inorg. Chim. Acta 1987, 130 167.
- 115 Nelson, S. M.; Rodgers, J. J. Chem. Soc. (A) 1968, 272;



- 116 Boylan, M.J.; Nelson, S. M.; Deeney, F. A. J. Chem. Soc.(A) 1971, 976.
- 117 Goodwin, H. A.; Mather, D. W. Aust. J. Chem. 1972, 25, 715;
- 118 Hoselton, M. A.; Wilson, L. J.; Drago, R. S. J. Am. Chem. Soc. 1975, 97, 1722.
- 119 Wilson, L. J.; Georges, D.; Hoselton, M. A. Inorg. Chem. 1975, 14, 2968.
- 120 Toftlund, H.; Yde-Andersen, S. Acta Chem. Scand. 1981, A35, 575.
- 121 Hojland, F.; Toftlund, H.; Yde-Andersen, S. Acta Chem. Scand. 1983, A37, 251.
- 122 Toftlund, H.; Pedersen, E.; Yde-Andersen, S. Acta Chem. Scand. 1984, A38, 693.
- 123 Christiansen, L.; Hendrickson, D. N.; Toftlund, H.; Wilson, S. R.; Xie, C.-L. Inorg. Chem. 1986, 25, 2813.
- 124 Mani, F.; Inorg. Chim. Acta 1986, 117, L1.
- 125 Onggo, D.; Hook, J. M.; Roe, A. D.; Goodwin, H.-A. Inorg. Chim. Acta 1990, 173, 19.
- 126 Oliver, J. D.; Mullica, D. F.; Hutchinson, B. B.; Mulligan, W. O. Inorg. Chem. 1980, 19, 165.
- 127 Eichhorn, D. M.; Armstrong, W. H. Inorg. Chem. 1990, 29, 3607.
- 128 Lever, A. B. P. Inorg. Chem., 1990, 29, 1271.
- 129 Sawyer, D. T.; Roberts, J. L., Jr., 'Experimental Electrochemistry for Chemists', Wiley: New York, 1974.
- 130 Ray, M.; Mukerjee, S.; Mukherjee, R. N. J. Chem. Soc., Dalton Trans. 1990, 3635.
- 131 Evans, D. F. J. Chem. Soc. 1959, 2003.

- 132 van Geet, A. L. Anal. Chem. 1968, 40, 2227.
- 133 Gerger, W.; Mayer, U.; Gutmann, V. Monatsh. Chem. 1977, 108, 417.
- 134 O'Connor, C. J. Prog. Inorg. Chem. 1982, 29, 203.
- 135 Ramesh, K.; Mukherjee, R. N. J. Chem. Soc., Dalton Trans. 1992, 83.
- 136 Newcomb, M.; Timko, J. M.; Walba, D. M.; Cram, D. J. J. Am. Chem. Soc. 1977, 99, 6392.
- 137 Baker, W.; Buggle nee Gallagher, K. M.; McOmie, J. F. W.; Watkins, D. A. M. J. Chem. Soc. 1958, 3594.
- 138 Geary, W. J. Coord. Chem. Rev. 1971, 7, 81.
- 139 Earnshaw, A. 'Introduction to Magneto-Chemistry', Academic Press: London and New York, 1968.
- 140 (a) DeW. Horrocks, W., Jr., in 'N.M.R. of Paramagnetic Molecules', Eds., La Mar, G. N.; DeW. Horrocks, W.; Holm, R. H. Academic Press: New York, 1973, pp. 127-177; (b) La Mar, G. N. ibid. p. 85-126.
- 141 Bertini, I.; Luchinat, C.; Messori, L. in 'Metal Ions in Biological Systems. Applications of N.M.R. to Paramagnetic Species', Vol. 21, Marcel Dekker: New York and Basel, 1987, p. 47-86.
- 142 Cotton, F. A.; Meyers, M.D. J. Am. Chem. Soc. 1960, 82, 5023.
- 143 Cotton, F. A.; Wilkinson, G. 'Advanced Inorganic Chemistry', 5th ed., Wiley: New York. Chichester. Brisbane. Toronto. Singapore, 1988, p. 716.
- 144 König, E.; Ritter, G.; Kulshreshtha, S. K. Chem. Rev. 1985, 85, 219.

- 145 Gutlich, P. Struct. Bonding (Berlin) 1981, 44, 83.
- 146 Goodwin, H. A. Coord. Chem. Rev. 1976, 18, 293.
- 147 Patterson, G. S.; Holm, R. H. Bioinorg. Chem. 1975, 4, 257.
- 148 Liver, A. B. P. J. Chem. Educ. 1968, 45, 711.
- 149 Wicholas, M. Inorg. Chem. 1971, 10, 1086.
- 150 Wandiga, S. O.; Sarneski, J. E.; Urbach, F. L. Inorg. Chem. 1972, 11, 1349.
- 151 Larsen, E.; La Mar, G. N.; Wagner, B. E.; Parks, J. E.; Holm, R. H. Inorg. Chem. 1972, 11, 2652.
- 152 Figgis, B. N. 'Introduction to Ligand Fields', Wiley Eastern Limited: New Delhi, 1976, p. 168.
- 153 Reference 152, p. 223-225.
- 154 Calabrese, J. C.; Domaille, P. J.; Trofimenko, S.; Long, G. J. Inorg. Chem. 1991, 30, 2795.
- 155 Nicholson, R. S.; Shain, I. Anal. Chem. 1964, 36, 706.
- 156 (a) Larsen, E.; La Mar, G. N.; Wagner, B. E.; Parks, J. E.; Holm, R. H. Inorg. Chem. 1972, 11, 2652.
- (b) Saji, T.; Aoyagui, S. J. Electroanal. Chem. 1975, 60, 1.
- 157 Rao, J. M.; Hughes, M. C.; Macero, D. J. Inorg. Chim. Acta 1976, 16, 231.
- 158 Creaser, I. I.; Geue, R. J.; Harrowfield, J. MacB.; Herlt, A. J.; Sargeson, A. M.; Snow, M. R.; Springborg, J. J. Am. Chem. Soc. 1982, 104, 6016.
- 159 Wieghardt, K.; Schmidt, W.; Herrmann, W.; Kuppers, H.-J. Inorg. Chem. 1983, 22, 2953.
- 160 Koval, C. A.; Pravata, R. L. A.; Reidsema, C. M. Inorg. Chem. 1984, 23, 545.

- 161 Ruminski, R. R.; Petersen, J. D. Inorg. Chim. Acta 1985, 97, 129.
- 162 Ventur, D.; Wieghardt, K.; Nuber, B.; Weiss, J. Z. Anorg. Allg. Chem. 1987, 551, 33.
- 163 Hunter, J.; Nelson, J.; Harding, C.; McCann, M.; McKee, V. J. Chem. Soc., Chem. Commun. 1990, 1148.
- 164 Edwards, D. A.; Mahon, M. F.; Martin, W. R.; Molloy, K. C.; Fanwick, P. E.; J. Chem. Soc., Dalton Trans. 1990, 3161 and references therein.
- 165 Greenwood, N. N.; Earnshaw, A. 'Chemistry of the Elements', Pergamon Press: Oxford, 1986, p. 1231.
- 166 Bryant, G. M.; Fergusson, J.E. Aust. J. Chem. 1971, 24, 275.
- 167 Kalyanasundaram, K. Coord. Chem. Rev. 1982, 46, 159.
- 168 Juris, A.; Balzani, V.; Barigelletti, F.; Campagna, S.; Belser, P.; von Zelewsky, A. Coord. Chem. Rev. 1988, 84, 85.
- 169 Meyer, T. J. Pure & Appl. Chem. 1986, 58, 1193.
- 170 Klassen, D. M. Inorg. Chem. 1976, 15, 3166.
- 171 Fabian, R. H.; Klassen, D. M.; Sonntag, R. W. Inorg. Chem. 1980, 19, 1977.
- 172 Nakamaru, K. Bull. Chem. Soc. Jpn. 1982, 55, 2697.
- 173 Orellana, G.; Ibrira, C. A.; Santoro, J. Inorg. Chem. 1988, 27, 1025.
- 174 Steel, P. J.; Constable, E. C. J. Chem. Soc., Dalton Trans. 1990, 1389.
- 175 'CRC Handbook of Chemistry and Physics', 64th Ed., CRC Press Inc., Boca Raton, Florida, 1983-1984, D-163.
- 176 Sullivan, B. P.; Salmon, D. J.; Meyer, T. J. Inorg. Chem. 1979, 18, 3369.

- 177 Hage, R.; Prins, R.; Haasnoot, J. G.; Reedijk, J.; Vos, J. G. J. Chem. Soc., Dalton Trans. 1987, 1389.
- 178 Cromer, D.T. 'International Tables for X-ray Crystallography'; Kynoch: Birmingham, England, Table 2.2 A, 1974; Vol.IV.
- 179 Ibers, J.A.; Hamilton, W.C. Acta Crystallogr. 1964, 17, 781.
- 180 Reference 178, Table 2.3.1, 1974; Vol.IV.
- 181 Gilmore, C. J. MITHRIL- An Integrated Direct Methods Computer Program; J. Appl. Cryst. 1984, 17, 42; University of Glasgow, Scotland.
- 182 Beurskens, P. T. DIRDIF - Direct Methods for Difference Structures - An Automatic Procedure Phase Extension and Refinement of Difference Structure Factors; Technical Report 1984/1 Crystallography Laboratory, Toernooiveld, 6255 Ed, Nijmegen, Netherlands.
- 183 TEXSAN - TEXRAY Structure Analysis Package, Molecular Structure Corp., College Station, TX, 1985.
- 184 Motherwell, S.; Clegg, W. PLUTO. Program for plotting molecular and crystal structures, University of Cambridge, England, 1978.
- 185 Johnson, C. K. OrtepII. Report ONRL-5138. Oak Ridge National Laboratory, Oak Ridge, Tennessee, 1976.
- 186 Baker, A. T.; Ferguson, N. J.; Goodwin, H. A.; Rae, A. D. Aust. J. Chem. 1989, 42, 623.
- 187 Baker, A. T.; Goodwin, H. A.; Rae, A. D. Inorg. Chem. 1987, 26, 3513.
- 188 Doedens, R. J.; Dahl, L. F. J. Am. Chem. Soc. 1966, 88, 4847.
- 189 Sotofte, I.; Rasmussen, S. V. Acta Chem. Scand. 1967, 21,

2028.

- 190 Oliver, J. D.; Mullica, D. F.; Hutchinson, B. B.; Milligan, W. O. Inorg. Chem. 1980, 19, 165.
- 191 Goodwin, H. A.; Kucharski, E.S.; White, A. H. Aust. J. Chem. 1983, 36, 1115.
- 192 Wiehl, L.; Kiel, G.; Kohler, C. P.; Spiering, H.; Gutlich, P. Inorg. Chem. 1986, 25, 1565.
- 193 Greenaway, A. M.; Sinn, E. J. Am. Chem. Soc. 1978, 100, 8080.
- 194 Figg, D. C.; Herber, R. H.; Felner, I. Inorg. Chem. 1991, 30, 2535.
- 195 Ozarowski, A.; Shunzhong, Y.; McGarvey, B. R.; Mislankar, A.; Drake, J. E. Inorg. Chem. 1991, 30, 3167 and references therein.
- 196 Onggo, D.; Hook, J. M.; Rae, A. D.; Goodwin, H. A. Inorg. Chim. Acta 1990, 173, 19.
- 197 Craig, D. C.; Goodwin, H. A.; Onggo, D. Aust. J. Chem. 1988, 41, 1157.
- 198 Grandjean, F.; Long, G. J.; Hutchinson, B. B.; Ohlhausen, L.; Neill, P.; Holcomb, J. D. Inorg. Chem. 1989, 28, 4406.
- 99 Martin, L. L.; Hagen, K. S.; Hauser, A.; Martin, R. L.; Sargeson, A. M. J. Chem. Soc., Chem. Commun. 1988, 1313.
- 00 Abushamleh, A. S.; Goodwin, H. A. Aust. J. Chem. 1988, 41, 873.
- 01 Sugiyarto, K. H.; Goodwin, H. A. Aust. J. Chem. 1988, 41, 1645.
- 02 Real, A.; Zarembowitch, J.; Kahn, O.; Solans, X. Inorg.

Chem. 1987, 26, 2939.

- 203 Addison, A. W.; Burman, S.; Wahlgren, C. G.; Rajan, O. A.; Rowe, T. M.; Sinn, E. J. Chem. Soc., Dalton Trans. 1987, 2621.
- 204 Madeja, K.; Konig, E. J. Inorg. Nucl. Chem. 1963, 25, 377.
- 205 Konig, E.; Madeja, K. Inorg. Chem. 1967, 6, 48.
- 206 Jesson, J. P.; Trofimenko, S.; Eaton, D. R. J. Am. Chem. Soc. 1967, 89, 3158.
- 207 Ritter, G.; Konig, E.; Erler, W.; Goodwin, H. A. Inorg. Chem. 1978, 17, 224.
- 208 Reeder, K. A.; Dose, E. V.; Wilson, L. J. Inorg. Chem. 1978, 17, 1071.
- 209 Konig, E.; Ritter, G.; Kulshreshtha, S. K.; Goodwin, H. A. Inorg. Chem. 1982, 21, 3022.
- 210 Christiansen, L.; Toftlund, H. 'Understanding Molecular Properties', Reidel, Dordrecht, 1987, p. 177.
- 211 Chum, H. L.; Vanin, J. A.; Holanda, M. I. D. Inorg. Chem. 1982, 21, 1146.
- 212 Martin, L. L.; Hagen, K. S.; Hauser, A.; Martin, R. L.; Sargeson, A. M. J. Chem. Soc. Dalton Trans. 1987, 2621.
- 213 Craig, D. C.; Goodwin, H. A.; Onggo, D.; Rae, A. D. Aust. J. Chem. 1988, 41, 1625.
- 214 Mukherjee, R. N.; Abrahamson, A. J.; Patterson, G. S.; Stack, T.D.P.; Holm, R. H. Inorg. Chem. 1988, 27, 2137.
- 215 Goodgame, D. M. L.; Machado, A. A. S. Inorg. Chem. 1969, 8, 2031.
- 216 Goedken, V. L.; Merrell, P. H.; Busch, D. H. J. Am. Chem. Soc. 1972, 94, 3397.

- 217 Dabrowiak, J. C.; Merrell, P. H.; Busch, D. H. Inorg. Chem. 1972, 11, 1979.
- 218 Sanders-Loehr, J. in 'Physical Bioinorganic Chemistry 5: Iron Carriers and Iron Proteins', Eds., Loehr, T. M.; VCH Publishers: New York, Weinheim, Cambridge, 1989, pp 373.
- 219 McCormick, J. M.; Solomon, E. I. J. Am. Chem. Soc. 1990, 11, 2005.
- 220 Kurtz, D. M., Jr., Chem. Rev. 1990, 90, 585.
- 221 Que, L, Jr.; Scarrow, R. C. in 'Metal Clusters in Proteins', Ed. L. Que, Jr., ACS Symp. Ser. No. 372, American Chemical Society, Washington, D.C., 1988, pp. 152.
- 222 Lippard, S. J. Angew. Chem. Int. Ed. Engl. 1988, 27, 344.
- 223 Armstrong, W. H.; Lippard, S. J. J. Am. Chem. Soc. 1983, 105, 4837.
- 224 Armstrong, W. H.; Spool, A.; Papaefthymiou, G. C.; Frankel, R. B.; Lippard, S. J. J. Am. Chem. Soc. 1984, 106, 3653.
- 225 Armstrong, W. H.; Lippard, S. J. J. Am. Chem. Soc. 1984, 106, 4633.
- 226 Armstrong, W. H.; Lippard, S. J. J. Am. Chem. Soc. 1985, 107, 3730.
- 227 Cho, S.-H.; Whang, D.; Han, K.-N.; Kim, K. Inorg. Chem. 1992, 31, 519.
- 228 Beer, R. H.; Tolman, W. B.; Bott, S. G.; Lippard, S. J. Inorg Chem. 1991, 30, 2082.
- 229 Hartman, J. R.; Rardin, R. L.; Chaudhuri, P.; Pohl, K.; Wieghardt, K; Nuber, B.; Weiss, J.; Papefthymiou, G. C.;



- Frankel, R. B.; Lippard, S. J. J. Am. Chem. Soc. 1987, 109, 7387.
- 230 Wieghardt, K.; Pohl, K.; Gebert, W. Angew. Chem. Int. Ed. Engl. 1983, 22, 727.
- 231 Chaudhuri, P.; Wieghardt, K.; Nuber, B.; Weiss, J. Angew. Chem. Int. Ed. Engl. 1985, 24, 778.
- 232 Drueke, S.; Wieghardt, K.; Nuber, B.; Weiss, J. Inorg. Chem. 1989, 28, 1414.
- 233 Wieghardt, K.; Tolksdorf, I.; Herrmann, W. Inorg. Chem. 1985, 24, 1230.
- 234 Toftlund, H.; Murray, K. S.; Zwack, P. R.; Taylor, L. F.; Anderson, O. P. J. Chem. Soc., Chem. Commun. 1986, 191.
- 235 Nishida, Y.; Haga, S.; Tokii, T. Chem. Lett. 1989, 109.
- 236 Crane, J. D.; Fenton, D. E. J. Chem. Soc., Dalton Trans. 1990, 3647.
- 237 Sessler, J. L.; Sibert, J. W.; Lynch, V. Inorg. Chem. 1990, 29, 4143.
- 238 Sessler, J. L.; Hugdahl, J. D.; Lynch, V.; Davis, B. Inorg. Chem. 1991, 30, 334.
- 239 Norman, R. E.; Yan, S.; Que, L., Jr.; Backes, G.; Ling, J.; Sanders-Loehr, J.; Zhang, J. H.; O'Connor, C. J. J. Am. Chem. Soc. 1990, 112, 1554.
- 240 Yan, S.; Cox, D. D.; Pearce, L. L.; Juarez-Garcia, C.; Que, L., Jr.; Zhang, J. H.; O'Connor, C. J. Inorg. Chem. 1989, 28, 2507.
- 241 Norman, R. E.; Holz, R. C.; Menage, S.; O'Connor, C. J.; Zhang, J. H.; Que, L., Jr. Inorg. Chem. 1990, 29, 4629.

- 242 Vincent, J. B.; Huffman, J. C.; Christou, G.; Li, Q.; Nanny, M. A.; Hendrickson, D. N.; Fong, R. H.; Fish, H. J. Am. Chem. Soc. 1988, 110, 6898.
- 243 Tolman, W. B.; Bino, A.; Lippard, S. J. J. Am. Chem. Soc. 1989, 111, 8522.
- 244 Tolman, W. B.; Liu, S.; Bentsen, J. G.; Lippard, S. J. J. Am. Chem. Soc. 1989, 111, 8522.
- 245 Romary, J. K.; Zachariasen, R. D.; Barger, J. D.; Schiesser, H. J. Chem. Soc. (C) 1968, 2884.
- 246 Armstrong, W. H.; Lippard, S. J. Inorg. Chem. 1985, 24, 981.
- 247 Holm, R. H.; Ibers, J. A. Science 1980, 209, 223.
- 248 Drueke, S.; Wieghardt, K.; Nuber, B.; Weiss, J.; Fleischhauer, H.-P.; Gehring, S.; Haase, W. J. Am. Chem. Soc. 1989, 111, 8622.
- 249 Sanders-Loehr, J.; Loehr, T. M.; Mauk, A. G.; Gray, H. B. J. Am. Chem. Soc. 1980, 102, 6992.
- 250 Reem, R. C.; McCormick, J. M.; Richardson, D. E.; Devlin, F. J.; Stephens, P. J.; Musselman, R. L.; Solomon, E. I. J. Am. Chem. Soc. 1989, 111, 4688.
- 251 Turowski, P. N.; Armstrong, W. H.; Roth, M. E.; Lippard, S. J. J. Am. Chem. Soc. 1990, 112, 681.
- 252 Norman, R. E.; Yan, S.; Que, L., Jr.; Backes, G.; Ling, J.; Sanders-Loehr, J.; Zhang, J. H.; O'Connor, C. J. J. Am. Chem. Soc. 1990, 112, 1554.
- 253 Medhi, O. K.; Silver, J. J. Chem. Soc. Dalton Trans. 1990, 263.
- 254 Reiff, W. M.; Baker, W. A.; Erickson, N. E. J. Am. Chem. Soc. 1968, 90, 4794.

- 255 Gomez-Romero, P.; Witten, E. H.; Reiff, W. M.; Backes, G.; Sanders-Loehr, J.; Jameson, G. B. J. Am. Chem. Soc. 1989, 111, 9039.
- 256 Gomez-Romero, P.; Witten, E. H.; Reiff, W. M.; Jameson, G. B. Inorg. Chem. 1990, 29, 5211.
- 257 Gorun, S. M.; Lippard, S. J. Inorg. Chem. 1991, 30, 1625.
- 258 Murray, K. S. Coord. Chem. Rev. 1974, 12, 1.
- 259 West, B. O. Polyhedron 1989, 8, 219.
- 260 Mukherjee, R. N.; Stack, T.D.P.; Holm, R. H. J. Am. Chem. Soc. 1988, 110, 1850.
- 261 Koppen, M.; Fiesen, G.; Weighardt, K.; Llausar, K. M.; Nuber, B.; Weiss, J. Inorg. Chem. 1988, 27, 721.
- 262 Bonder, A.; Drueke, S.; Weighardt, K. Angew. Chem. Int. Ed. Engl. 1990, 29, 68.
- 263 West, B. O. Polyhedron 1984, 3, 219.
- 264 Griffith, W. P. Coord. Chem. Rev. 1970, 5, 459.
- 265 Phelps, D. W.; Kahn, E. M.; Hodgson, D. J. Inorg. Chem. 1975, 14, 2486.
- 266 Weaver, T. R.; Meyer, T. J.; Adeyemi, S. A.; Brown, G. M.; Eckberg, R. P.; Hatfield, W. E.; Johnson, E. C.; Murray, R. W.; Untereker, D. J. Am. Chem. Soc. 1975, 97, 3039.
- 267 Baumann, J.; Meyer, T. J.; Inorg. Chem. 1980, 19, 345.
- 268 Gersten, S. W.; Samuels, G. J.; Meyer, T. J. J. Am. Chem. Soc. 1982, 104, 4029.
- 269 Honda, K.; Frank, A. J.; J. Chem. Soc., Chem. Commun. 1984, 1635.

- 270 Gilbert, J. A.; Eggleston, D. S.; Murphy, W. R., Jr.; Geselowitz, D. A.; Gersten, S. W.; Hodgson, D. J.; Meyer, T. J. J. Am. Chem. Soc. 1985, 107, 3855.
- 271 Geselowitz, D. A.; Kutner, W.; Meyer, T. J. Inorg. Chem. 1986, 25, 2015.
- 272 Sasaki, Y.; Suzuki, M.; Tokiwa, A.; Ebihara, M.; Yamaguchi, T.; Kabuto, C.; Ito, T. J. Am. Chem. Soc. 1988, 110, 6251.
- 273 Sasaki, Y.; Suzuki, M.; Nagasawa, A.; Tokiwa, A.; Ebihara, M.; Yamaguchi, T.; Kabuto, C.; Ochi, T.; Ito, T. Inorg. Chem. 1991, 30, 4903.
- 274 Neubold, P.; Wieghardt, K.; Nuber, B.; Weiss, J. Inorg. Chem. 1989, 28, 459.
- 275 Neubold, P.; Wieghardt, K.; Nuber, B.; Weiss, J. Angew. Chem. Int. Ed. Engl. 1988, 27, 933.
- 276 Llobet, A.; Curry, M. E.; Evans, H. T.; Meyer, T. J. Inorg. Chem. 1989, 28, 3131.
- 277 Das, B. K.; Chakravarty, A. R. Inorg. Chem. 1990, 29, 2078.
- 278 Syamala, A.; Chakravarty, A. R. Inorg. Chem. 1991, 30, 4699.
- 279 Das, B. K.; Chakravarty, A. R. Inorg. Chem. 1990, 29, 1783.
- 280 Dunitz, J. D.; Orgel, L. E. J. Chem. Soc. 1953, 2593.
- 281 Llobet, A.; Hodgson, D. J.; Meyer, T. J. Inorg. Chem. 1990, 29, 3760.
- 282 Goswami, S.; Chakravarty, A. R.; Chakravorty, A. J. Chem. Soc., Dalton Trans. 1982, 1288.
- 283 Ramaraj, R.; Kira, A.; Kanelo, M. J. Chem. Soc., Faraday Trans. 1986, 82, 3515.
- 284 Nyholm, R. S.; Turco, A. Chem. Ind. (London) 1960, 74.

- 285 Plaksin, P. M.; Stoufer, R. C.; Mathew, M.; Palenik, J. G. J. Am. Chem. Soc. 1972, 94, 2121.
- 286 Cooper, S. R.; Calvin, M. J. Am. Chem. Soc. 1977, 99, 6623.
- 287 Cooper, S. R.; Dismukes, G. C.; Klein, M. P.; Calvin, M. J. Am. Chem. Soc. 1978, 100, 7248.
- 288 Stebler, M.; Ludi, A.; Burgi, H.-B. Inorg. Chem. 1986, 25, 4743.
- 289 Collins, M. A.; Hodgson, D. J.; Michelsen, K.; Towle, D. K. J. Chem. Soc., Chem. Commun. 1987, 1659.
- 290 Towle, D. K.; Botsford, C. A.; Hodgson, D. J. Inorg. Chim. Acta 1988, 141, 167.
- 291 Oki, A. R.; Glerup, J.; Hodgson, D. J. Inorg. Chem. 1990, 29, 2435.
- 292 Goodson, P. A.; Hodgson, D. J.; Michelsen, K. Inorg. Chim. Acta 1990, 172, 49.
- 293 Goodson, P. A.; Glerup, J.; Hodgson, D. J.; Michelsen, K.; Pedersen, E. Inorg. Chem. 1990, 29, 503.
- 294 Goodson, P. A.; Glerup, J.; Hodgson, D. J.; Michelsen, K.; Weihe, H. Inorg. Chem. 1991, 30, 4909.
- 295 Suzuki, M.; Tokura, S.; Suhara, M.; Uehara, A. Chem. Lett. 1988, 477.
- 296 Suzuki, M.; Senda, H.; Kobayashi, Y.; Oshio, H.; Uehara, A. Chem. Lett. 1988, 1763.
- 297 Brewer, K. J.; Liegeois, A.; Otvos, J. W.; Calvin, M.; Spreer, L. O. J. Chem. Soc., Chem. Commun. 1988, 1219.
- 298 Brewer, K. J.; Calvin, M.; Lumpkin, R. S.; Otvos, J. W.; Spreer, L. O. Inorg. Chem. 1989, 28, 4446.

- 299 Hagen, K. S.; Armstrong, W. H.; Hope, H. Inorg. Chem. 1988, 27, 967.
- 300 Rush, J. D.; Maskos, Z. Inorg. Chem. 1990, 29, 897.
- 301 Renger, G.; Wydrzynski, T. Biol. Met. 1991, 4, 73.
- 302 Guiles, R. D.; Zimmermann, J. -L.; McDarmott, Ann. E.; Yachandra, V. K.; Cole, J. L.; Dexheimer, S. L.; Britt, R. D.; Wieghardt, K.; Bossek, U.; Sauer, K.; Klein, M. P. Biochem. 1990, 29, 471 and references therein.
- 303 Wieghardt, K.; Bossek, U.; Zsolnai, L.; Huffner, G.; Blondin, G.; Girerd, J. J.; Babonneau, F. J. Chem. Soc. Chem. Commun. 1987, 651.
- 304 Baskin, J. S.; Schake, A. R.; Vincent, J. B.; Chang, H.-R.; Li, Q.; Huffman, J. C.; Christou, G. J. Chem. Soc. Chem. Commun. 1988, 700.
- 305 Pal, S.; Gohdes, J. W.; Wilisch, W. C. A.; Armstrong, W. H. Inorg. Chem. 1992, 31, 713.
- 306 Morrison, M. M.; Sawyer, D. T. J. Am. Chem. Soc. 1977, 99, 257.
- 307 Ramaraj, R.; Kira, A.; Kaneko, M. Angew. Chem. Int. Ed. Engl. 1986, 25, 825.

Table I: Anisotropic Thermal Parameters for  $[\text{Fe}(\text{H}_2\text{Me}_2\text{bpp})_2](\text{ClO}_4)_2$

ATOM	U11	U22	U33	U12	U13	U23
Fe	0.0345(3)	0.0375(4)	0.0373(3)	0.0018(4)	0.0069(3)	0.0017(4)
Cl(1)	0.068(1)	0.109(1)	0.111(1)	0.024(1)	0.032(1)	0.031(1)
Cl(2)	0.074(1)	0.061(1)	0.103(1)	-0.022(1)	-0.001(1)	-0.011(1)
O(11)	0.128(6)					
O(12)	0.124(7)					
O(13)	0.081(5)					
O(14)	0.152(5)					
O(15)	0.116(4)					
O(16)	0.127(6)					
O(17)	0.118(4)					
O(18)	0.087(7)					
O(19)	0.030(6)					
O(21)	0.110(7)					
O(22)	0.071(3)					
O(23)	0.099(2)					
O(24)	0.107(4)					
O(25)	0.096(2)					
O(26)	0.118(3)					
O(27)	0.050(4)					
O(28)	0.060(8)					
O(110)	0.091(6)					
O(111)	0.038(3)					
O(112)	0.14(1)					
O(113)	0.113(8)					
N(1A)	0.034(2)	0.046(3)	0.041(3)	0.001(2)	-0.001(2)	-0.001(2)
N(1B)	0.043(2)	0.034(2)	0.041(2)	0.002(2)	0.008(2)	0.004(2)
N(1C)	0.037(2)	0.053(3)	0.049(3)	-0.003(2)	0.007(2)	0.005(2)
N(1D)	0.045(3)	0.052(3)	0.049(3)	0.009(2)	0.017(2)	0.007(2)
N(1E)	0.058(3)	0.045(3)	0.043(3)	0.002(2)	0.010(2)	0.001(2)
N(1F)	0.040(2)	0.037(2)	0.042(3)	0.004(2)	0.002(2)	0.003(2)
N(2C)	0.034(2)	0.061(3)	0.064(3)	-0.004(2)	0.011(2)	0.002(3)
N(2D)	0.045(3)	0.052(3)	0.055(3)	-0.002(2)	0.015(2)	0.013(2)
N(2E)	0.053(3)	0.040(3)	0.054(3)	-0.000(2)	0.004(2)	-0.007(2)
N(2F)	0.045(3)	0.042(3)	0.039(3)	-0.007(2)	0.001(2)	-0.001(2)
C(1)	0.039(3)	0.076(4)	0.056(4)	-0.006(3)	-0.007(3)	-0.006(4)

Table I (contd.)

ATOM	U11	U22	U33	U12	U13	U23
C(2)	0.056(4)	0.035(3)	0.059(4)	-0.000(3)	0.010(3)	0.009(3)
C(2A)	0.040(3)	0.057(4)	0.042(3)	0.002(3)	0.002(3)	-0.001(3)
C(2B)	0.041(3)	0.051(3)	0.043(3)	0.008(3)	0.011(3)	0.008(3)
C(3)	0.074(4)	0.037(3)	0.055(4)	-0.005(3)	0.015(3)	0.003(3)
C(3A)	0.050(4)	0.079(5)	0.060(4)	0.011(4)	-0.009(3)	0.002(4)
C(3B)	0.050(4)	0.065(4)	0.060(4)	0.008(3)	-0.001(3)	0.014(3)
C(3C)	0.041(3)	0.082(5)	0.091(5)	-0.004(3)	0.023(3)	0.012(4)
C(3D)	0.052(3)	0.079(4)	0.064(4)	-0.014(3)	0.020(3)	0.020(3)
C(3E)	0.072(4)	0.052(4)	0.068(4)	0.002(3)	-0.005(4)	-0.017(4)
C(3F)	0.060(4)	0.054(3)	0.040(3)	-0.012(3)	0.003(3)	0.002(3)
C(4)	0.037(3)	0.048(4)	0.058(4)	-0.003(3)	-0.003(3)	0.004(3)
C(4A)	0.073(4)	0.075(5)	0.067(4)	0.025(4)	-0.013(4)	0.015(4)
C(4B)	0.074(4)	0.054(4)	0.069(4)	0.030(3)	0.009(4)	0.017(3)
C(4C)	0.070(4)	0.086(5)	0.080(5)	-0.001(4)	0.040(4)	0.019(4)
C(4D)	0.057(4)	0.096(5)	0.075(5)	0.006(4)	0.034(3)	0.007(4)
C(4E)	0.074(4)	0.080(5)	0.050(4)	0.015(4)	-0.002(4)	-0.024(4)
C(4F)	0.097(5)	0.051(4)	0.046(4)	-0.003(4)	0.021(3)	-0.013(3)
C(5A)	0.079(4)	0.050(4)	0.061(4)	0.015(3)	0.017(3)	0.012(3)
C(5B)	0.077(4)	0.049(4)	0.057(4)	0.016(3)	0.012(3)	0.010(3)
C(5C)	0.053(3)	0.061(4)	0.054(4)	-0.002(3)	0.012(3)	0.002(3)
C(5D)	0.040(3)	0.070(4)	0.060(3)	0.007(3)	0.019(3)	0.008(4)
C(5E)	0.064(4)	0.067(4)	0.044(4)	0.007(3)	0.007(3)	0.002(3)
C(5F)	0.052(3)	0.034(3)	0.049(3)	0.001(3)	0.015(3)	-0.001(3)
C(6A)	0.047(3)	0.047(3)	0.040(3)	0.007(3)	0.006(3)	-0.003(3)
C(6B)	0.054(3)	0.042(3)	0.036(3)	0.002(3)	0.014(3)	0.001(3)
C(6D)	0.109(5)	0.099(6)	0.135(7)	-0.012(5)	0.064(5)	0.043(5)
C(6F)	0.103(6)	0.110(7)	0.061(5)	-0.021(5)	-0.020(5)	-0.013(5)
C(7D)	0.080(5)	0.096(6)	0.106(6)	0.039(4)	0.042(4)	0.014(5)
C(7F)	0.080(4)	0.058(4)	0.086(5)	0.026(3)	0.023(4)	-0.011(4)
H(3A)	0.10(2)					
H(3B)	0.05(1)					
H(3C)	0.05(1)					
H(3E)	0.03(1)					
H(4A)	0.08(2)					
H(4B)	0.06(2)					
H(4C)	0.06(2)					



ATOM	U11	U22	U33	U12	U13	U23
H(4D)	0.07(2)					
H(4E)	0.06(2)					
H(4F)	0.02(1)					
H(5A)	0.07(2)					
H(5B)	0.07(2)					
H(5C)	0.06(2)					
H(5E)	0.05(1)					
H(6DA)	0.11(2)					
H(6DB)	0.1247					
H(6FA)	0.09(2)					
H(6DC)	0.1071					
H(6FB)	0.10(2)					
H(6FC)	0.11(2)					
H(7DA)	0.1095					
H(7DB)	0.11(2)					
H(7FA)	0.0899					
H(7DC)	0.08(2)					
H(7FB)	0.05(2)					
H(7FC)	0.1254					
H(11)	0.05(1)					
H(12)	0.06(2)					
H(21)	0.05(1)					
H(22)	0.05(2)					
H(31)	0.05(1)					
H(32)	0.05(1)					
H(41)	0.07(2)					
H(42)	0.07(2)					

Table II: Table of Least-Squares Planes

## ----- Plane number 1 -----

Atoms Defining Plane	Distance	esd
N1A	-0.0075	0.0040
C2A	0.0065	0.0053
C3A	-0.0012	0.0064
C4A	0.0014	0.0069
C5A	-0.0083	0.0060
C6A	0.0116	0.0051

Mean deviation from plane is 0.0061 angstroms  
 Chi-squared: 11.4

## ----- Plane number 2 -----

Atoms Defining Plane	Distance	esd
N1B	-0.0056	0.0040
C2B	0.0016	0.0052
C3B	0.0064	0.0061
C4B	-0.0050	0.0063
C5B	-0.0060	0.0062
C6B	0.0103	0.0051

Mean deviation from plane is 0.0058 angstroms  
 Chi-squared: 8.3

Dihedral angles between least-squares planes  
                   plane  plane  angle  
                   2      1     26.98

## ----- Plane number 3 -----

Atoms Defining Plane	Distance	esd
N1C	-0.0003	0.0041
N2C	-0.0006	0.0043
C3C	0.0027	0.0066
C4C	-0.0032	0.0068
C5C	0.0017	0.0059

Mean deviation from plane is 0.0017 angstroms  
 Chi-squared: 0.5

Dihedral angles between least-squares planes  
                   plane  plane  angle  
                   3      1     120.80  
                   3      2     98.53

Table of Least-Squares Planes (continued)

## ----- Plane number 4 -----

Atoms Defining Plane	Distance	esd
N1D	0.0034	0.0041
N2D	-0.0053	0.0041
C3D	0.0095	0.0057
C4D	-0.0070	0.0064
C5D	-0.0004	0.0053

Mean deviation from plane is 0.0051 angstroms  
 Chi-squared: 5.9

## Dihedral angles between least-squares planes

plane	plane	angle
4	1	121.30
4	2	98.17
4	3	60.40

## ----- Plane number 5 -----

Atoms Defining Plane	Distance	esd
N1E	-0.0005	0.0042
N2E	0.0006	0.0042
C3E	-0.0010	0.0062
C4E	0.0004	0.0063
C5E	0.0003	0.0057

Mean deviation from plane is 0.0006 angstroms  
 Chi-squared: 0.1

## Dihedral angles between least-squares planes

plane	plane	angle
5	1	76.81
5	2	59.60
5	3	92.14
5	4	46.12

Table of Least-Squares Planes (continued)

-----

----- Plane number 6 -----

Atoms Defining Plane	Distance	esd
N1F	0.0008	0.0039
N2F	-0.0015	0.0040
C3F	0.0027	0.0053
C4F	-0.0024	0.0062
C5F	0.0002	0.0050

Mean deviation from plane is 0.0015 angstroms  
Chi-squared: 0.6

Dihedral angles between least-squares planes

plane	plane	angle
6	1	73.25
6	2	49.27
6	3	49.27
6	4	73.86
6	5	68.45

## FUTURE SCOPE OF THIS WORK

In the first part of this thesis (Chapters 2-4) we have addressed a fundamental research problem of identifying steric/electronic effect. Systematic identification of steric effect was not studied before the present work. We have identified the predominance of incremental contribution of steric factor over electronic or vice versa using absorption spectroscopy and electrochemistry as experimental tools. Systematic changes in bond lengths from X-ray structures could also be employed for precise identification of these effects. If one solves crystal structure for all three bis chelates of any series, the observed M-N bond distances will provide substantial information in this field. However, we were able to solve the crystal structure of only one of the bis chelates of iron(II) in this thesis work. Proper manipulation of the ligand framework can also be employed to separate out steric and electronic factors. Efforts are on, in this laboratory, along those lines. More informations could be gathered if one solves crystal structure of iron(II) spin-equilibrium complex at room temperature as well as at low temperature.

The second aspect of the thesis (Chapters 5-7) deals with dinuclear core formation using tridentate nitrogenous capping ligands. Obviously, a lot can be done on these systems. The present report is just an initiation from this laboratory. The uniqueness of our ( $\mu$ -oxo)( $\mu$ -carboxylato)diiron(III) complexes is their somewhat enhanced antiferromagnetic exchange coupling compared to many related systems reported in the literature. X-ray structure of any of our oxo-bridged diiron complexes will

provide information about the disposition of unsymmetrical chelate rings around the coordination sphere of iron.

Dinuclear oxo-bridged ruthenium complex has a novel reactivity property of oxidizing water stoichiometrically. More interesting results will come out from critical studies on this compound. The high positive potential of  $\text{Ru}^{\text{IV}}\text{Ru}^{\text{III}}/\text{Ru}_2^{\text{III}}$  couple has made the diruthenium(III) state more stable and thus isolation of one electron oxidized species has not been achieved in this work. However, proper manipulation of the field strength of terminal ligands will help to isolate the diruthenium(IV,III) species more easily. Reactivity properties of the bis( $\mu$ -oxo)( $\mu$ -acetato)dimanganese(IV,III) complex would be of significant interest as the bridging acetate is labile in nature. X-ray structures of these complexes would be of paramount importance.